Electron Transfer at Biologically Modified Electrodes

By

Kody D. Wolfe

Dissertation

Submitted to the Faculty of the

Graduate School of Vanderbilt University

in partial fulfillment of the requirements

for the degree of

DOCTOR OF PHILOSOPHY

in

Interdisciplinary Materials Science

August 31, 2021
Nashville, Tennessee

Approved:

G. Kane Jennings, Ph.D.

David E. Cliffel, Ph.D.

Paul E. Laibinis, Ph.D.

Timothy P. Hanusa, Ph.D.

Kelsey B. Hatzell, Ph.D.

To Keri,

my best friend, whom I would do anything

with and nothing without,

&

To my parents,

Joseph A. Wolfe and BettyAnn L. Wolfe,

and grandparents,

Joseph D. Loftis & Cora A. Loftis,

for fostering and continuously

supporting my education.

Acknowledgments

First, I want to thank Dr. G. Kane Jennings for helpful discussions, guidance, and advice and Dr. David E. Cliffel for inspiring me to continue exploring the field of electrochemistry. I truly appreciated having these great professors as co-advisors and could not imagine how I would have navigated graduate school without them. A great thanks goes to Dr. Paul E. Laibinis for group meeting conversations and his eye for detail. And I thank my remaining committee members, Dr. Timothy P. Hanusa and Dr. Kelsey B. Hatzell, for their helpful discussion and intriguing graduate courses. I also thank the Interdisciplinary Materials Science Department staff for their support and help navigating graduate school.

The work presented in this dissertation could not have been possible without the generous funding provided by the National Science Foundation (DMR-1507505), the United States Department of Agriculture (2019-67021-29857), and the National Renew. Energy Laboratory (subcontract number XEJ-9-92257-01 under prime contract number DE-AC36-08GO28308). I thank the Vanderbilt Institute of Nanoscience & Engineering (VINSE) for the use of analytical equipment and training sessions provided by their staff, the Russell G. Hamilton Graduate Leadership Institute for providing a Professional Development & Training Grant that allowed me to train on equipment I would otherwise could not have accessed, the Graduate Student Council for awarding travel funding and holding amazing events for graduate students, and the Vanderbilt Center for Teaching for their excellent training through the College Teaching Certificate Program and courses specific to teaching online and STEM classes. Altogether, the training I have received as a student and researcher at Vanderbilt have been invaluable.

Finally, I thank my family for their support before and throughout graduate school. I would never have made it without them behind me. A special thanks goes to Zachary “Billy” Manuel for always being on the other end of the phone when I call him and for conversations about family, work, and life. I include my “graduate school family”; my lab mates and classmates who have become some of my best friends. I will deeply miss lab lunches at McDougal’s, lively discussions in the office, jamming to Jimmy Buffet in the lab, and late nights at the Villager.

My greatest thanks go to Keri, to whom I dedicate this dissertation. There is no doubt that she has heard more about my courses, research, and graduate school struggles than anyone else. She is always by my side when I need her; if I need quiet time, a good talk on a run, or to take on a ridiculous DIY project together. I am so grateful for the opportunity to live my life with her.

Table of Contents

Page

List of Tables

List of Figures

Appendix

Chapter 1 – Bioelectrodes: A Brief History & Introduction

The overarching theme of the projects described in this dissertation is the study of bioelectrodes for energy conversion applications. Bioelectrodes, or biologically modified electrodes, are created by the coupling of some biomaterial to a conductive electrode material.[1-2] The careful preparation of bioelectrodes enables analytical studies at the convergence of biology, chemistry, biochemistry, and electrochemistry. Many will agree that the initial motivation for the study of bioelectrochemistry took place in Bologna, Italy in 1791 when Luigi Galvani probed a deceased frog with two dissimilar metals, connected electrically, and observed a jerking motion produced within the muscle of the frog.[3-4] While Galvani intended to study "animal electricity", the notion that electricity was produced by living beings, he had actually prepared what was possibly the earliest form of a bioelectrode. Coincidentally, the groundwork for the field of electrochemistry was simultaneously being laid by Galvani's critic and collaborator Allessandro Volta who keenly observed that Galvani's results were brought about by using two dissimilar metals and not by innate forces within the frog itself.[4] His "electric pile" and contributions regarding dissimilar metals created a foundation for advancement in all fields regarding the transfer of electrons among materials.[4]

Since the time of Galvani, the coupling of complex biological systems with electrochemical cells has proven to be a greatly beneficial endeavor.[2, 5] Biological redox reactions are ubiquitous in nature and, therefore, have wide ranging applications in the fields of biology and engineering.[6] The influences of bioelectrochemistry can be seen in the fields of medicine, agriculture, manufacturing, chemical sensing, and energy conversion, among others.[2, 5, 7-8] In fact, many common and valuable products contain a bioelectrode. For example, blood glucose sensors, a lifesaving resource for those suffering from diabetes, implement an enzyme-based bioelectrode to detect glucose within a small blood sample in a very short time.[9] Bioelectrochemistry is also prevalent in waste remediation, biosynthesis, and biohybrid energy technologies.[10-12] Due to its expansive range of applications, low-cost, and natural biocompatibility, there is no doubt that bioelectrochemistry will continue to improve the wellbeing of people around the world and aid in mitigating society's impact on the natural world.

Humanity is facing a daunting challenge with global energy use rapidly increasing and the looming dangers of climate change closely tied to our use of fossil fuels. The National Renew. Energy Laboratory's recent technical report on electrification in the U.S. states that by 2050 the capacity for domestic energy production and distribution will need to be doubled and that new Renew. Energy projects will be critical in achieving widespread electrification.[13] Recently, researchers have turned to bioelectrochemistry for both inspiration and innovation in the field of clean and Renew. Energy technology.[12, 14] Because biological redox reactions have been refined through years of evolutionary adaptation, they promise both high efficiencies and high specificity.[2] Production of bioenergy can also be used as a means of CO_2 sequestration, furthering its benefits for reducing the progression of global climate change.[11, 15] So, efforts are being made to leverage bioelectrochemical reactions to solve problems related to energy production. The goal of the projects reported herein is to develop new technologies that will aid in the transition from a fossil fuel-based energy economy. [7, 16-19] First, biohybrid solar cells utilizing plant proteins to harvest solar energy are investigated (Chapters 3 – 6). Secondly, the electrochemical regeneration of enzymatic cofactors used to produce commodity chemicals typically produced via crude oil refining (Chapters 7 – 9) is studied. Eliminating fossil fuels is a critical step in developing a clean energy economy and efforts in the field of bioelectrochemistry can provide the scientific insight necessary to develop clean or Renew. Energy technologies.

While the value of bioelectrochemistry remains unchallenged and interest in the field is rapidly growing, the underlying mechanisms of electron transfer at the interface of many biomaterials and electrodes is not well understood.[5, 17] In fact, the mechanisms of electron transfer of only a few simple bioelectrochemical reactions can be explained in detail. Therefore, major gaps remain in our understanding of the complex electrochemistry of enzymes, proteins, and their organometallic reaction centers. The purpose of this dissertation research is to provide insight into the modes of electron transfer from specified biomolecules to an electrode. Two bioelectrochemical systems will be discussed: photosystem I (PSI) protein complex-based bioelectrodes (Chapters 3 – 6) and bioelectrodes for the reduction of NAD^+ to NADH (Chapters 7 – 9). Topics will include electron transfer pathways, fundamental limitations and methods of improvement, and discussions of important bioloelectrochemical topics including direct vs.

mediated electron transfer, mediator diffusion, and kinetic equilibrium limitations. Improving the transfer of electrons at the bioelectrode interface can improve the total efficiency of lab-scale devices and bridge large gaps in developing commercially viable technologies. This is the motivation for the work to follow and, with a great deal of effort and luck, will be the motivation humankind needs to redevelop our use of energy to solve both local and global challenges.

The following section gives a short introduction to the theory of electron transfer at bioelectrodes. Chapter 2 will give general experimental procedures used across many of the research chapters. Several more detailed (and adaptable) experimental procedures are given in the appendices including a detailed extraction procedure for obtaining PSI protein complexes and a procedure for fabricating porous, translucent, and conductive indium tin oxide electrodes, among others. The bulk of this dissertation is contained in Chapters 3 – 6, in which projects regarding the use of the plant protein complex, PSI, as a means of harvesting solar energy are discussed. Chapters 7 – 9 describe projects related to the stability of nicotinamide cofactors in aqueous buffers and the electrochemical regeneration of enzymatic cofactor NADH, respectively. Lastly, Chapter 10 summarizes the critical findings and general themes of the dissertation research and is followed by the appendices.

Fundamental Principles of Electron Transfer at Bioelectrode Interfaces

In biological systems, redox chemistry governs energy transfer, storage, the transport of nutrients, and the activity of critical processes including enzymatic reactions.[18, 20-22] Unsurprisingly, many types of biomolecules are redox-active; amino acids, proteins, enzymes, and some metabolites are continuously reduced and/or oxidized *in vivo*.[1] Redox-active biomolecules are involved in cell signaling, electron shuttling, and many other task specific bioelectrochemical reactions. Certain biomolecules have evolved to convert specific forms of energy, others are capable of efficiently catalyzing chemical reactions, and all electroactive biomolecules are interrelated in a web of electron transfers throughout entire organisms.

The capability of biomolecules to exchange electrons is crucial to their function, and therefore, understanding the redox activity of biomolecules is highly beneficial to the study of fields related to or within biology.[5] The investigation of redox-active biomolecules via electrochemistry enables the determination of the presence of specific biomolecules (biosensing), studies of the energetics and kinetics of bioelectrochemical reactions, and methods to employ biomolecules for novel purposes or tasks (bioengineering).[1-2, 5] Because biomolecules are highly specific, elucidating an electrochemical response, or electron transfer, at an electrode surface is nontrivial and often requires a more elaborate electrode design than the traditional electrodes used for simpler heterogeneous electron transfer studies of solvated molecules.[7]

Biomolecules are typically found in much lower concentrations than traditionally used in electrochemical testing. These low concentrations are impractical for electrochemical cells as they result in miniscule signal.[2] To improve the interaction between a biomolecule and an electrode, the molecule may be immobilized on the electrode surface.[2, 5, 14, 23-24] Immobilization improves the electrochemical signal by eliminating diffusional limitations and increasing the surface concentration of the biomolecule. Such an electrode with an immobilized biomolecule is deemed a biologically modified electrode or bioelectrode. Biologically modified electrodes vary widely in application and have become an increasingly prominent area in electrochemical research. Examples of three-electrode electrochemical cells employed as bioelectrochemical cells are shown in Figure 1.1. The biomaterial may be immobilized in a very thin, invisible film on the working electrode (Figure 1.1.A), found freely dissolved within the electrolyte (Figure 1.1.B), or immobilized within a composite biofilm on the working electrode (Figure 1.1.C). The working electrode is polarized or subjected to various electrical waveforms to study the transfer of electrons to and from the biomaterial. Many variations of the simplified cells shown in Figure 1.1 exist including flow cells, rotating disk electrodes, and two electrode devices, among others. The common goal of preparing bioelectrodes is to study, better understand, and improve electron transfer across the biomolecule/electrode interface.

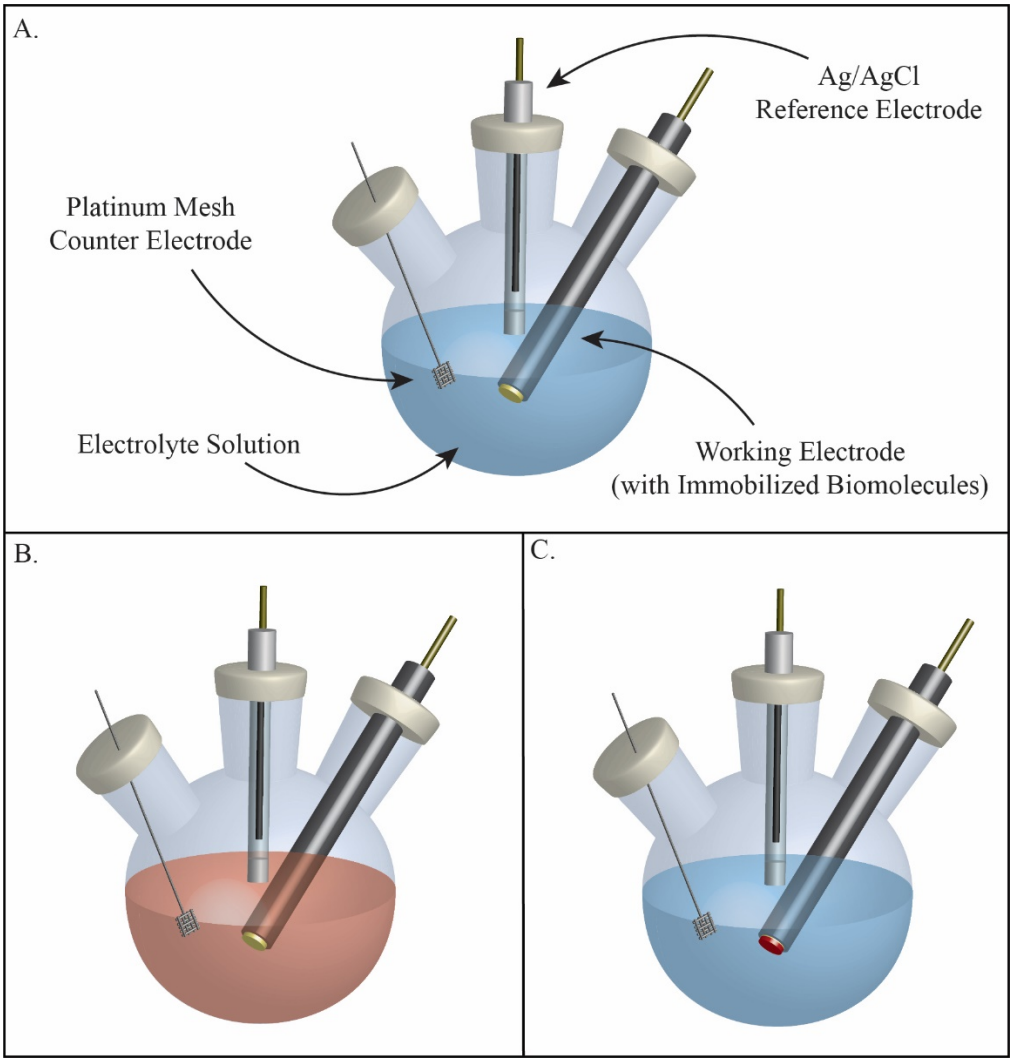

Figure 1.1. *Typical bioelectrochemical cells used for studying electron transfer of biomolecules. A.) A three-neck, round bottom electrochemical cell containing a biomolecule immobilized in a thin, invisible film on the working electrode. B.) An electrochemical cell with similar working components, except the biomolecule is dissolved in the bulk electrolyte instead on being immobilized. C.) A bioelectrochemical cell in which the biomolecule is immobilized in a composite film that is visible on the working electrode.*

Achieving heterogeneous electron transfer between a biomolecule and an inorganic electrode is much more difficult than achieving electron transfer between biomolecules that have evolved to react with one another. The electron transfer reaction may occur at a complex reaction

site or via the redox activity of a functional group on the molecule.[2, 5] This transfer creates many challenges in developing functional and efficient bioelectrodes that can mimic the natural electron donor or acceptor molecule chemistries. Shown in Figure 1.2, biomolecules have been found to interact with electrodes via two non-discrete electron transfer classifications: direct electron transfer (DET) or mediated electron transfer (MET).[25] MET involves the incorporation of another electrochemically active species that is dissolved in the electrolyte and may or may not be biologically derived. The mediator effectively shuttles charge from the biomolecule's reaction site to the electrode, and because the mediator is freely dissolved, the electron transfer distance can be micrometers in length due to diffusion of the mediator. However, MET is inherently mass transfer limited.[2, 23, 25-26] DET is considered superior in performance (rate and efficiency) but is difficult to achieve. A common theme throughout this dissertation will be the discussion of MET vs. DET in bioelectrochemical systems and their implications on the performance of the bioelectrode.

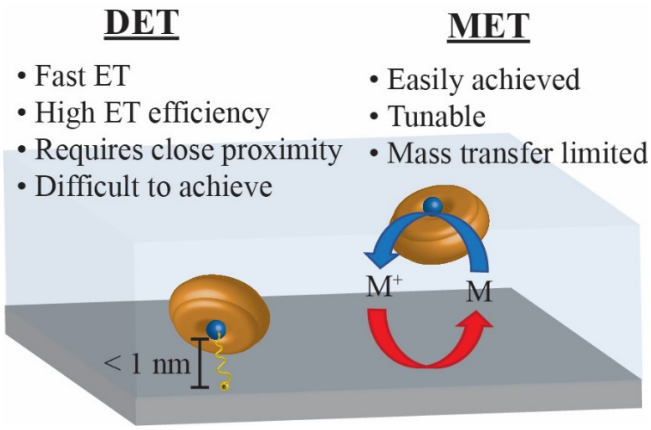

Figure 1.2. *Comparison of direct electron transfer (DET) and mediated electron transfer (MET) along with some of their characteristic properties and limitations.*

In the research chapters of this dissertation biologically modified electrodes will be introduced, the electron transfer pathway (DET or MET) will be discussed, methods for testing electron transfer will be employed, the electron transfer will be improved and/or optimized, and concluding remarks will be given. While much recent effort has been focused on providing DET at biologically modified electrodes, there are cases in which MET is preferred or present due to other limitations.[25] Chapters 4 – 6 primarily discuss MET in PSI-modified bioelectrodes while

Chapter 9 discusses direct reduction of NAD^+ to NADH at an electrode. The importance of acknowledging and studying the differences in testing DET and MET at bioelectrodes cannot be understated and is fundamental to the findings given in this dissertation.

References

1. Bartlett, P. N., Bioelectrochemistry : fundamentals, experimental techniques and applications / edited by P.N. Bartlett. John Wiley & Sons: Chichester, England. **2008**.
2. Bard, A. J., Electrochemical methods : fundamentals and applications / Allen J. Bard, Larry R. Faulkner. Wiley: New York, New York. **1980**.
3. An Account of the Experiments and Discoveries of Lewis Galvani, Professor of Anatomy at Bologna, Relative to the Powers of Electricity in Muscular Motion: Vide Aloysii Galvani de Viribus Electricitatis in Motu Musculari Commentarium. 4to. Bologna, 1791. *Medical facts and observations* **1792,** *3*, 180-190.
4. Piccolino, M., Luigi Galvani and animal electricity: two centuries after the foundation of electrophysiology. *Trends Neurosci.* **1997,** *20* (10), 443-448.
5. Marcus, R. A.; Sutin, N., Electron transfers in chemistry and biology. *Biochim. Biophys. Acta Bioenerg.* **1985,** *811* (3), 265-322.
6. Ostwald, W., *Electrochemistry : history and theory / Wilhelm Ostwald*. Smithsonian Institution and the National Science Foundation, Amerind Pub. Co.: New Delhi. **1980**.
7. Kimmel, D. W.; LeBlanc, G.; Meschievitz, M. E.; Cliffel, D. E., Electrochemical sensors and biosensors. *Anal. Chem.* **2012,** *84* (2), 685-707.
8. Milazzo, G., Applications of bioelectrochemistry in medicine. *Bioelectrochem. Bioenerg.* **1988,** *19* (2), 191-205.
9. Villena Gonzales, W.; Mobashsher, A. T.; Abbosh, A., The Progress of Glucose Monitoring-A Review of Invasive to Minimally and Non-Invasive Techniques, Devices and Sensors. *Sensors (Basel)* **2019,** *19* (4), 800.
10. Bajracharya, S.; Sharma, M.; Mohanakrishna, G.; Dominguez Benneton, X.; Strik, D. P. B. T. B.; Sarma, P. M.; Pant, D., An overview on emerging bioelectrochemical systems (BESs): Technology for sustainable electricity, waste remediation, resource recovery, chemical production and beyond. *Renew. Energy* **2016,** *98*, 153-170.
11. Cravens, A.; Payne, J.; Smolke, C. D., Synthetic biology strategies for microbial biosynthesis of plant natural products. *Nature Comm.* **2019,** *10* (1), 2142.

12. Wey, L. T.; Bombelli, P.; Chen, X.; Lawrence, J. M.; Rabideau, C. M.; Rowden, S. J. L.; Zhang, J. Z.; Howe, C. J., The Development of Biophotovoltaic Systems for Power Generation and Biological Analysis. *ChemElectroChem* **2019,** *6* (21), 5375-5386.

13. Murphy, C., Trieu Mai, Yinong Sun, Paige Jadun, Matteo Muratori, Brent Nelson, and Ryan Jones *Electrification Futures Study: Scenarios of Power System Evolution and Infrastructure Development for the United States*; National Renew. Energy Laboratory: Golden, CO, **2021**.

14. Ma, S.; Ludwig, R., Front Cover: Direct Electron Transfer of Enzymes Facilitated by Cytochromes. *ChemElectroChem* **2019,** *6* (4), 953-953.

15. Creutzig, F.; Ravindranath, N. H.; Berndes, G.; Bolwig, S.; Bright, R.; Cherubini, F.; Chum, H.; Corbera, E.; Delucchi, M.; Faaij, A.; Fargione, J.; Haberl, H.; Heath, G.; Lucon, O.; Plevin, R.; Popp, A.; Robledo-Abad, C.; Rose, S.; Smith, P.; Stromman, A.; Suh, S.; Masera, O., Bioenergy and climate change mitigation: an assessment. *GCB Bioenergy* **2015,** *7* (5), 916-944.

16. Falk, M.; Psotta, C.; Cirovic, S.; Shleev, S., Non-Invasive Electrochemical Biosensors Operating in Human Physiological Fluids. *Sensors (Basel)* **2020,** *20* (21), 6352.

17. Otero, F.; Magner, E., Biosensors-Recent Advances and Future Challenges in Electrode Materials. *Sensors (Basel)* **2020,** *20* (12), 3561.

18. Arshi, S.; Nozari-Asbemarz, M.; Magner, E., Enzymatic Bioreactors: An Electrochemical Perspective. *Catalysts* **2020,** *10* (11).

19. Nguyen, K.; Bruce, B. D., Growing green electricity: Progress and strategies for use of Photosystem I for sustainable photovoltaic energy conversion. *Biochim. Biophys. Acta Bioenerg.* **2014,** *1837*, 1553-1566.

20. Badura, A.; Kothe, T.; Schuhmann, W.; Rögner, M., Wiring photosynthetic enzymes to electrodes. *Energy Environ. Sci.* **2011,** *4*, 3263-3274.

21. Chenault, H. K.; Simon, E. S.; Whitesides, G. M., Cofactor Regeneration for Enzyme-Catalysed Synthesis. *Biotechnol. Genet. Eng. Rev.* **1988,** *6* (1), 221-270.

22. Habermüller, K.; Mosbach, M.; Schuhmann, W., Electron-transfer mechanisms in amperometric biosensors. *Fresenius J. Anal. Chem.* **2000,** *366*, 560-568.

23. Wolfe, K. D.; Dervishogullari, D.; Passantino, J. M.; Stachurski, C. D.; Jennings, G. K.; Cliffel, D. E., Improving the stability of photosystem I–based bioelectrodes for solar energy conversion. *Curr. Opin. Electrochem.* **2020,** *19*, 27-34.

24. Friebe, V. M.; Millo, D.; Swainsbury, D. J. K.; Jones, M. R.; Frese, R. N., Cytochrome c Provides an Electron-Funneling Antenna for Efficient Photocurrent Generation in a Reaction Center Biophotocathode. *ACS Appl. Mater. Interfaces* **2017,** *9* (28), 23379-23388.

25. Morlock, S.; Subramanian, S. K.; Zouni, A.; Lisdat, F., Scalable Three-Dimensional Photobioelectrodes Made of Reduced Graphene Oxide Combined with Photosystem I. *ACS Appl. Mater. Interfaces* **2021,** *13* (9), 11237-11246.

26. Wolfe, K. D.; Dervishogullari, D.; Stachurski, C. D.; Passantino, J. M.; Kane Jennings, G.; Cliffel, D. E., Photosystem I Multilayers within Porous Indium Tin Oxide Cathodes Enhance Mediated Electron Transfer. *ChemElectroChem* **2020,** *7* (3), 596-603.

Chapter 2 – Experimental Methods

The following sections describe experimental procedures and analytical techniques used throughout this dissertation and direct the reader to research chapters in which these methods were employed. Many of the same experimental setups and analytical methods were used throughout several of the research projects and therefore, for brevity, this chapter (along with the Appendix) gives the experimental details for the work in the entire dissertation. The experimental methods are organized into three categories: Cleaning & Sample Preparations, Electrochemical Analyses, and Analytical Testing. In the appendices, methods are given for specific, more detailed procedures mentioned in the research chapters including:

- Extraction and Quantification of Photosystem I – Appendix A
- Preparation of Porous Indium Tin Oxide Electrodes – Appendix B
- Layer-by-Layer Assembly of Photosystem I and PEDOT:PSS – Appendix C

Sample Preparation

Photosystem I Extraction and Modification (Chapters 4-6)

Photosystem I protein complexes were extracted from deveined baby spinach (*Spinacia* oleracea) leaves via a modification of previously reported extraction protocols.[1-5] Appendix A gives a thorough protocol for the extraction of PSI. For the modification of the stromal side lysine residues (Chapter 5), either 2-iminothiolane (Thermo Fisher Scientific) or methyl-PEG_4-NHS Ester (Thermo Fisher Scientific) was added to the resuspended pellet (50 mg in a total volume of ~50 mL). After 12 h, the solution was again centrifuged at 8,000X and washed twice to remove the soluble reactants. The washed pellet was resuspended and mixed vigorously in a Triton X-100 (Millipore Sigma) lysing buffer to lyse the thylakoid membrane. The solution was then centrifuged at 20,000X and the supernatant was collected, and the pellet discarded. The remainder of the extraction was performed as described in Appendix A. The concentration of collected PSI was quantified via a UV-Vis assay for P700 reported by Baba et al. and is also described in Appendix A.[5] Unless otherwise noted, PSI concentration is typically between 0.5-1.0 mg/mL.

Fabrication of Mesoporous Indium Tin Oxide (meso-ITO) Electrodes (Chapter 4)

The procedure for the porous ITO electrode fabrication was adapted from previously reported methods and is reported in detail in Appendix B.[6] Briefly, conductive ITO-coated glass (Sigma-Aldrich) was cut into 2 cm x 1 cm pieces and sonicated (for 5 min each) in acetone, nitric acid (30%), ethanol (99%), and DI water, respectively. The ITO-coated sides of the dried glass pieces were then masked with electrochemical masking tape (Gamry) to yield an exposed area of 0.708 cm^2 (geometric surface area). The isopropanol from the original dispersion was removed in a rotary evaporator at 60 ˚C, and the collected ITO-nanoparticles (Sigma-Aldrich, ~100 nm particle size, 30 wt. % in isopropanol) (2.5 g equivalent of nanoparticle mass only) were dispersed in 10.7 mL terpineol (Sigma-Aldrich, 90% technical grade). The resulting ITO nanoparticle-terpineol mixture was tape-cast onto the exposed area of the masked ITO electrodes. The nanoparticle film was first dried under ambient conditions for 48 h and then sintered in a tube furnace at 550 ˚C for 15 min under argon flow. The tube furnace was ramped to the final temperature through a stepwise ramping procedure, never exceeding 5 ˚C min^{-1}.

Fabrication of Macroporous ITO (macro-ITO) Electrodes (Chapter 4)

The fabrication protocol for porous ITO electrodes is given in detail in Appendix B. Briefly, diluted (1:13) aqueous polystyrene (PS) dispersion (Sigma-Aldrich, Size: 5 μm, 10 wt %) was drop-cast onto the exposed area of the masked ITO-coated glass and allowed to dry in ambient conditions (5-6 h). The slides were then placed on an electric hotplate set to 85 ˚C for 18 h to sinter the PS spheres. The ITO nanoparticle-terpineol mixture used in the fabrication of meso-ITO electrodes was drop-cast onto the dried and sintered PS-template. The mixture was allowed to dry under ambient conditions again for 48 h, then sintered in a tube furnace at 550 ˚C for 30 min under argon flow. The tube furnace was ramped to the final temperature through a stepwise ramping procedure, never exceeding 5 ˚C min^{-1}.

Modification of ITO electrodes with Photosystem I Multilayers (Chapter 4)

Prior to deposition, PSI extract was dialyzed (1:1000) against deionized water using a regenerated cellulose membrane (Spectrum Labs, MWCO: 8-10 kDa) to minimize the concentrations of excess surfactant and buffer salts. For deposition, a controlled amount of dialyzed PSI extract was pipetted onto the exposed area of the ITO substrate, and vacuum was applied to evaporate the solvent and leave behind a dry PSI multilayer film.[7] Due to the low surfactant concentration in the protein suspension, the resulting protein film was no longer soluble in water and could withstand electrochemical characterizations in aqueous electrolyte solutions.

Photosystem I Monolayer Deposition (Chapter 5)

Monolayers were prepared via solution deposition.[8] Gold-coated wafers were prepared through thermal vapor deposition onto p-type silicon [100] wafers. An adhesion layer of 10 nm of chromium was first deposited at a rate of 0.1 Å/s, followed by a 125 nm layer of gold deposited at 1.0 Å/s. The wafers were cut into samples approximately 0.75 cm x 1.5 cm and were cleaned with piranha solution (3:1 concentrated sulfuric acid to 30% hydrogen peroxide) for 30 s then rinsed with deionized water and dried under N_2. Samples were immediately submerged into a diluted solution of either phosphate buffer, unmodified PSI, thiol-modified PSI (T-PSI), or PEG-modified PSI (P-PSI). The solutions were diluted to obtain approximately 0.5 mg/mL PSI. With the exception of deposition rate studies, samples were left in solution for 1000 m (~16.7 h). After the deposition samples were rinsed with deionized water and dried under N_2.

PSI-PEDOT:PSS Layer-by-Layer Deposition (Chapter 6)

A more detailed protocol for the LBL deposition is given in Appendix C. Chromium (10 nm) and gold (125 nm) were sequentially deposited onto silicon (100) wafers, via physical vapor deposition as described previously.[8] Gold-coated wafers were cut into 1.5 cm x 1.4 cm or 2.3 cm x 1.4 cm samples and cleaned with three alternating rinses of ethanol and deionized water. Samples were then dried under a stream of N_2 and placed into a solution of 1 mM aminoethanethiol (AET) (Thermo Scientific) in ethanol for 1 h. The result is a positively charged amine-terminated self-assembled monolayer (SAM) on the gold surface. Next, samples were again rinsed with ethanol

and dried under N_2. For the LBL deposition solutions, PEDOT:PSS solution (Sigma-Aldrich, 1.1 wt %) was diluted to 0.5 mg/mL, and 0.15 M NaCl was added to the diluted PEDOT:PSS solution. Aliquots of PSI solution were used as extracted (0.5 mg PSI/mL in 200 mM sodium phosphate buffer at pH = 7.0 and containing 1 wt % Triton X-100). The AET SAM-modified gold substrates were first exposed to the PEDOT:PSS solution for 15 min and then to the PSI solution for 30 min. After each deposition step, the samples were rinsed with deionized water and dried under N_2. The depositions of PEDOT:PSS and PSI were performed repeatedly until the desired number of bilayers was reached.

Gold Deposition onto Carbon Paper (Chapter 9)

First, the hydrophilicity of the carbon paper should be checked and if a small drop of water beads on the carbon paper surface, the PTFE coating needs to be removed by flame treatment (to burn off the PTFE coating). Carbon fiber paper was cut into 1 cm x 2 cm electrodes, then a copper tape connection was added, and electrochemical masking tape (Gamry) was used to cover the copper tape, leaving a 1 cm x 1 cm area exposed. The electrode was then cycled (using cyclic voltammetry) in 1 M sulfuric acid from +1.0 to -1.0 V vs. Ag/AgCl for ten cycles. The surface area of the cleaned electrodes can be tested by cycling in 100 mM KCl solution and comparing the capacitive current obtained.[9]

The gold acid solution was prepared by dissolving 19 mg of $HAuCl_4 \bullet 3H_2O$, 29 mg sodium nitrate, and 135 mg of 25 wt % cetyltrimethylammonium chloride (CTAC) in deionized water, diluted to 10 mL total volume with deionized water, and sonicated for several minutes.[10] The solution should be a cloudy yellow color and can be stored for repeated use in a refrigerator as long as it is brought to room temperature prior to the deposition. For the deposition, a graphite rod was used as both the counter and reference electrode in a 10 mL beaker. The carbon paper electrode was immersed into the solution, connected as the working electrode, and a potentiostatic deposition was conducted via chronoamperometry. Note that other electrochemical methods can be used, such as pulsed deposition (using potentiostatic steps). After the deposition, the electrode was rinsed and dried. Scanning electron microscopy can be used to verify that the deposition procedure was successful.

Copper UPD & Electroless Exchange for Platinum (Chapter 9)

A copper salt solution was prepared at a concentration of 50 mM copper(II) sulfate in 0.1 M sulfuric acid. The cleaned carbon paper electrode was then immersed in the copper salt solution and underpotential deposition (UPD) of copper was performed by applying a potentiostatic hold at a potential sufficient for UPD but not negative enough to allow bulk copper reduction. Cyclic voltammetry in the copper salt solution can be used to determine the correct potential for UPD and to check that copper UPD occurs on the electrode. For UPD, a Ag/AgCl reference electrode and a platinum mesh counter electrode were used. Figures 9.7 and 9.8 in Chapter 9 describe the method for determining the UPD potential. For carbon paper electrodes with gold nanostructures, a potential of 0.3 V was applied for 100 s (see Figure 9.9) The electrode can then be rinsed and dried or used for electroless exchange with platinum.

For electroless exchange of platinum, a 1 mM chloroplatinic acid (H_2PtCl_6) solution was prepared containing 10 mg H_2PtCl_6 in 25 mL of 0.1 M sulfuric acid.[11] The platinum salt solution was then well deoxygenated by purging with N_2 for approximately 30 min. The solution was kept covered and purging was continued throughout the electroless exchange. After performing copper UPD, the electrode was immediately rinsed with deionized water and then immersed in the deoxygenated platinum salt solution for 30 s. As there is no visible evidence of the electroless exchange, verification was done by measuring the potential onset of the oxygen reduction reaction in sulfuric acid (see below). For generation of a full or nearly full monolayer of platinum, the copper UPD and electroless exchange required repeating several times.[12] In Chapter 9, the process is repeated 3 times.

Electrochemical Analyses

Electrochemical data were collected using the CH Instruments (Austin, TX) CHI 660a electrochemical workstation. Unless otherwise stated, the reference electrode used was a 1 M Ag/AgCl reference, CH Instruments (Austin, TX). For cyclic voltammetry, the scan rate was 100 mV/s unless stated otherwise.

Cyclic Voltammetry

Cyclic voltammetry was used throughout all research chapters of this dissertation (except for Chapter 8). Conditions for cyclic voltammetry are reported in the respective sections. Impotantly, the U.S. convention for plotting cyclic voltammograms was used for this dissertation. That is, cathodic current is consider positive on the y-axis and the potential is plotted from positive to negative (left to right) on the x-axis. The scan direction, therefore, is always clockwise. Figure 2.1 shows the U.S. convention in comparison to the IUPAC convention for a cyclic voltammogram beginning with a negative scan direction. The fundamental parts of the cyclic voltammogram are labelled as well.[13]

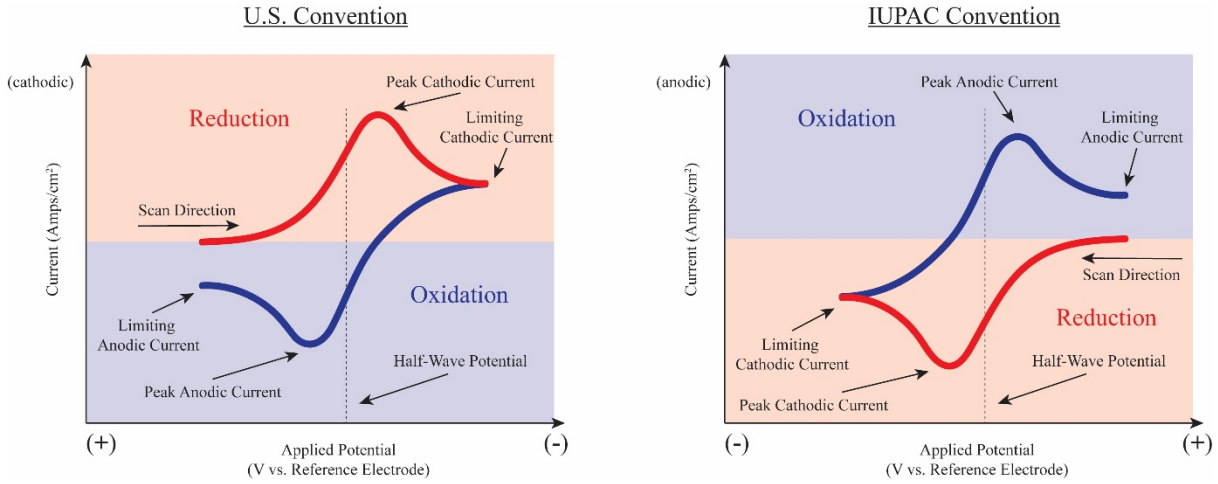

Figure 2.1. *Cyclic voltammogram plotting conventions. The cyclic voltammograms shown throughout this dissertation use the U.S. convention.*

Photochronoamperometric (Photocurrent) Testing (Chapters 4-6)

Photoelectrochemical testing was performed using a homemade photo-electrochemical sample holder with an electrolyte pathlength of 1 cm and a 250 W cold light source (Leica KL 2500 LCD) with an intensity of 100 mW/cm^2 (white light). The electrolyte solution always contained 100 mM KCl as a supporting electrolyte; however, the electrochemical mediator varied between chapters and individual tests. Details about photochronoamperometry (PCA) are given in the individual chapters. A brief experimental description is given for each PSI chapter below.

PCA in Chapter 4 (Porous ITO Cathodes). Photochronoamperometric studies were conducted in a three-electrode system with a Ag/AgCl (sat'd KCl) reference electrode, a platinum mesh counter electrode, and a PSI-modified planar or porous ITO working electrode. The dark open circuit potential (OCP) was measured and set as the applied voltage during photochronoamperometry scans. A 10 s period of dark baseline current was first recorded before samples were illuminated. Stirred photochronoamperometry scans (Figure 4.13) were taken by placing the sample in a 10 mL beaker containing the electrolyte and a small stir bar. Note that the stir plate introduces electromagnetic noise to the chronoamperometry data. For the summarized photochronoamperometric data in Figure 4.15, the cathodic photocurrent density values reported were determined by taking the difference between the initial peak current under illumination and the average dark current, divided by either the geometric surface area of the electrode (0.71 cm^2) or the electrochemically determined active surface area. Reported photocurrent density values are the average from replicates of the same device type, with error bars representing the standard deviation from the average (n = 10). The electrochemical mediator solution used in all photochronoamperometric studies in Chapter 4 (unless otherwise stated) consisted of a mixture of 1 mM 2,6-dichlorophenolindophenol (DCPIP) and 5 mM sodium ascorbate (NaAscH) dissolved in an aqueous solution of 100 mM potassium chloride (KCl).

PCA in Chapter 5 (Stromal-Side Modified PSI). For PCA testing of PSI monolayers (Figure 5.9), only dissolved oxygen was used as a mediator in the 100 mM KCl supporting electrolyte. Note that for PSI monolayers, a low sensitivity value (0-100 nA range) is necessary due to the low current response of monolayer films.

PCA in Chapter 6 (PSI-PEDOT:PSS LBL). All electrolytes contained 100 mM KCl in addition to any electrochemical mediator (mentioned where applicable). Both methyl viologen (Acros-Organics) and ubiquinone-0 (2,3-dimethoxy-5-methyl-1,4-benzoquinone from Acros-Organics) were tested at a concentration of 2 mM. For all PCA data the open circuit potential of the sample was first measured in the dark, and the sample was held at the measured open-circuit potential

during the photocurrent measurement. The sample was then illuminated with a 100 mW/cm^2 white light source for some time interval (typically 20 s) before the light was turned off.

Photopotentiometry (Chapters 4-6)

Potentiometry with illumination (photopotentiometry) was performed throughout the PSI chapters to determine the potential of the electrode upon illumination and to determine driving forces for the production of photocurrent. Photopotentiometry was performed under the same conditions as PCA in each chapter (see above).

Electrochemically Active Surface Area Determination via Cyclic Voltammetry (Chapter 4)

Cyclic voltammetry of planar, meso- and macro-ITO electrodes for active surface area determination were conducted in an aqueous solution of 0.5 M KCl at varying scan rates (50, 100, 150, 200, 250 mV s^{-1}) (Figure 4.9). The method reported by Voiry et al. was used to determine the electrochemically active surface area factor (ECASF).[9]

Electrochemical Impedance Spectroscopy (Chapter 6)

Electrochemical impedance spectroscopy (EIS) was conducted on a CHI 660 potentiostat. A three-electrode cell was used with a platinum counter electrode, Ag/AgCl reference electrode (CH Instruments), and the LBL-coated gold sample as the working electrode using a custom-built sample holder. The electrochemically accessible area was constrained to an exposed area of 0.21 cm^2. All measurements were performed in an aqueous solution of 100 mM KCl (Fisher Chemical). EIS tests were performed from 10,000 to 0.1 Hz at the sample's open-circuit potential and a potential amplitude of 5 mV.

Oxygen Reduction Reaction Check for Platinum Activity (Chapter 9)

The successful deposition of platinum monolayers via copper UPD and electroless exchange can be checked by cycling the electrode in 0.1 or 1 M sulfuric acid and comparing the onset potential of the oxygen reduction reaction (ORR) to a control electrode without platinum. Figure 9.10 shows the onset potential for various electrodes used in Chapter 9. The onset potential

shifts positive when platinum is present because active adsorbed protons on the platinum surface catalyze the ORR. Achieving an onset potential near that of bulk platinum is possible on gold nanostructures deposited onto carbon paper electrodes.

Batch Electrolysis of NAD^+ (Chapter 9)

NAD^+ reduction was performed in a 2 mM NAD^+ solution prepared in 50 mM tris buffer with the pH adjusted to 8.5. Typically, 50 mL of NAD^+ solution was prepared and deoxygenated in a sealed round bottom flask for at least 30 min. A sufficient amount should be prepared for the number of electrolysis experiments to be performed. For the experiments discussed in Chapter 9, 10 mL of solution was used for each experiment. The reaction vessel was a 3-neck round bottom flask sealed with septa. A Ag/AgCl reference electrode was placed in the center neck, a platinum mesh counter was placed on one side, and a carbon paper electrode was placed on the opposite side. All electrodes were passed through the septa so the round neck flask could be sealed and deoxygenated. The carbon paper working electrode was connected to the potentiostat via a wire and alligator clip passed through the septa (with the alligator clip inside the 3-neck flask). A stir bar was placed in the bottom of the 3-neck flask. Figure 9.12 shows an image of the setup. An inlet stream of N_2 was entered through a needle in one septum and an outlet from another. The outlet led to a positive flow assurance bubbler (a beaker with water in which the end of the outlet is submerged and bubbles show positive pressure). The vessel was purged with N_2 for several minutes with all electrodes in place before the reaction solution was introduced.

An aliquot (10 mL) of the reaction solution was transferred via syringe from the round bottom flask where it was continuously being deoxygenated to the reaction vessel where it was then purged for several more minutes. During the batch electrolysis, a positive pressure of N_2 was kept in the reaction vessel by flowing N_2 over the reaction solution at a slow rate (the inlet was not submerged, so that no bubbles were formed). The stir bar was set to 600 rpm and positioned so it would not touch any of the electrodes. For the experiments discussed in Chapter 9, a potential of 1.2 V vs. Ag/AgCl was applied to the working electrode for variable amounts of time (typically 10 min). The reaction effluent was then collected for analysis and stored in a 15 mL centrifuge tube or vial. Before a second reaction the reaction vessel was washed and thoroughly dried.

Analytical Testing

Scanning Electron Microscopy (SEM) (Chapter 4)

SEM images of porous indium tin oxide electrodes used in Chapter 4 were taken with a Zeiss Merlin Scanning Electron Microscope using an accelerating voltage of either 0.5 or 5.0 keV, a working distance of 5 mm, and the InLens secondary electron detector. The low accelerating voltage of 0.5 keV was necessary for imaging the bare polystyrene beads shown in Figures A.5 & A.6 (Appendix B). At higher accelerating voltages, the non-conductive beads charge and the resulting image is distorted. Energy dispersive spectroscopy (EDS) was performed using a Zeiss Merlin Scanning Electron Microscope equipped with an EDS detector (Figures 4.11 and 4.12). EDS samples were sputter coated with gold, and EDS spectra were taken at an accelerating voltage of 20 keV and 3 nA probe current.

Powder X-Ray Diffraction (XRD) (Chapter 4)

XRD of porous indium tin oxide electrodes used in Chapter 4 was performed using a Rigaku Smart Lab X-Ray Diffractometer with a scan time of 10 min from 20 to 70 degrees using a Cu-Kα x-ray source (Figure 4.8). The sample material for XRD was recovered from prepared ITO cathodes by scraping material from the cathode onto the XRD well plate.

Stylus Profilometry (Chapter 4)

Stylus profilometry was utilized to determine the cathode thickness in Chapter 4 using a Veeco Dektak 150 Stylus Profilometer (Figure 4.7). Scans were taken over 1000 μm with the stylus beginning on the bare ITO-coated glass substrate and ending after scanning across approximately 800 μm of the electrode. The average step height was calculated and taken to be representative of the cathode thickness. The coffee-ring effect was observed and was mitigated by scanning over a larger portion of the cathode and taking the average step height.

Four-Point Probe (Chapter 4)

Sheet resistance was determined using an Ossila Four-Point Probe at ambient conditions on electrodes cast onto non-conductive glass substrates (Table 4.2). Each sample was tested at three locations or orientations of the four-point probe. In the event that the probe contacts mechanically damaged the cathode, the data point was discarded and recollected.

Transmission-Absorbance Ultraviolet-Visible Spectroscopy (Chapter 4)

Transmittance-absorbance spectroscopy of porous ITO – PSI cathodes (Chapter 4) was performed using a Varian Cary 5000 UV-VIS-NIR spectrophotometer (Figure 4.10). Scans were performed from 800 to 400 nm at a rate of 600 nm min^{-1} and a sampling frequency of 1 nm. Samples were mounted to a transmittance absorbance holder and a 100% transmittance blank sample (air) was used for baseline subtraction.

Sessile Drop Contact Angle Measurements (Chapter 5)

Sessile drop contact angle measurements of water on PSI monolayers (Figure 5.8.D-G) were taken on a Ramé-Hart Instruments (Succasunna, NJ) goniometer fitted with a camera and a droplet volume of approximately 1 μL of distilled water.

Spectroscopic Ellipsometry for Monolayer Presence (Chapter 5)

Ellipsometric thicknesses of PSI monolayers (Figures 5.8.A & 5.8.B) were obtained using a J.A. Woollam M-2000VI Spectroscopic Ellipsometer (Lincoln, NE) at incident angles of 65° and 75°. On gold substrates, a Cauchy film model, a refractive index of 1.45, and an initial estimated thickness of 10 nm were used. The sample size was 5 (n = 5) for all ellipsometric studies and a background scan of the freshly cleaned gold wafers was taken and subtracted to determine absolute changes in film thickness.

Fourier Transform Infrared Spectroscopy (Chapters 5 & 6)

Phase-modulated infrared reflectance absorbance spectroscopy (PM-IRRAS) was conducted using a Bruker Tensor 27 Fourier transform infrared spectrometer with a liquid

nitrogen-cooled, mercury-cadmium-telluride detector and an incident beam angle of 80° from the substrate surface normal.

Individual LBL Layer Thickness Measurements (Chapter 6)

Ellipsometric measurements were obtained on a JA Woollam Co. M-2000VI variable angle spectroscopic ellipsometer with WVASE32 software for modeling. Each sample was measured at two incident angles of 65° and 75° using a 632 nm HeNe laser. Film thickness was fit from these measurements by using a one-term Cauchy layer model with a refractive index of 1.45.

Water Contact Angles (Chapter 6)

Contact angles of deionized water in ambient conditions were measured on static water drops (1 μL) using a Ramé-Hart goniometer. The needle remained inside the liquid drop during measurements.

UV-Vis Absorbance Spectroscopy (Chapter 6)

UV-Vis absorbance spectroscopy was performed on extracted solutions of PSI using a Varian (now Agilent Technologies (Santa Clara, CA)) Cary 5000 UV-VIS-NIR spectrophotometer. The solutions were placed in disposable cuvettes and scanned from 800 to 450 nm. A background absorbance spectrum was taken of a cuvette with elution buffer and this spectrum was subtracted from the PSI-containing sample's spectra.

UV-Vis Spectroscopy for NADH Quantification (Chapters 8 & 9)

As the dihydropyridine ring of NADH can be observed via absorbance measurement at a wavelength of 340 nm and NAD^+ does not absorb at 340 nm,.[14] UV-visible spectroscopy provided a method for analyzing the reaction effluent from batch electrochemical reduction of NAD^+. The reaction effluent was scanned from 500 to 250 nm against a background of the reaction solution (2 mM NAD^+ in tris buffer). The absorbance maximum at 340 nm was checked against a NADH calibration curve taken in tris buffer (see Figure 9.13.B). When the absorbance was above the measurable range (between 0.20-0.80 a.u.), the reaction solution was diluted. When the absorbance

was below the measurable range, the electrolysis reaction was performed for a longer amount of time. 100 μM NADH (cuvette concentration) absorbs 0.58 a.u. at 340 nm.

NOX Enzymatic Assay (Chapters 8 & 9)

As the UV-vis method for NADH quantification did not test the biological activity of the NADH, an enzymatic assay was used to validate biological activity through the consumption of NADH by an enzyme and the measurement of the loss of absorbance at 340 nm. For the work in this dissertation, a NADH oxidase (NOX) enzyme was used. Marcus Alahuhta (staff scientist at NREL) produced and purified the NOX and shipped it to Vanderbilt for use. The NOX was 29.43 mg/mL as received, and a dilution series was first performed with tris buffer to determine the necessary NOX concentration for use in an enzymatic assay with 3 mL total cuvette volume and a concentration of 100 μM NADH. Dilution series were also performed in HEPES and phosphate buffers and Figure 8.11 shows resulting curves at a NOX concentration of 150 ng/mL. Note that the NOX was first diluted to 15 μg/mL and this solution was labeled NOX dilutant.

For the enzymatic assay, reaction effluent or freshly prepared NADH solution was diluted to approximately 100 μM in a cuvette and either scanning kinetics test from 450 to 250 nm wavelengths was begun (see Figure 8.11) or the absorbance at 340 nm was continuously measured (see Figure 8.12). After 1 scan in the scanning kinetics test or 30 s in the 340 nm continuous measurement, the NOX dilutant was spiked into the cuvette and the absorbance was measured over several minutes. The typical cuvette contents were 2,820 μL of buffer, 150 μL of 2 mM NADH solution in buffer, and 30 μL of NOX dilutant (15 μg/mL). Note that for reaction effluent testing, the NADH concentration is dependent on the reaction time and, therefore, buffer is not used to dilute the reaction effluent in the cuvette (i.e. 2,970 μL reaction effluent + 30 μL NOX dilutant). When the reaction effluent was determined to be too concentrated, it was diluted.

References

1. Reeves, S. G.; Hall, D. O. Higher plant chloroplasts and grana: General preparative procedures. *Photosynthesis and Nitrogen Fixation - Part C*, Ed. Academic Press: San Pietro. **1980**; Vol. 69, pp 85-94.

2. Shiozawa, J. A.; Alberte, R. S.; Thornber, J. P., The P700-chlorophyll a-protein: Isolation and some characteristics of the complex in higher plants. *Arch. Biochem. Biophys.* **1974,** *165* (1), 388-397.

3. Kincaid, H. A.; Niedringhaus, T.; Ciobanu, M.; Cliffel, D. E.; Jennings, G. K., Entrapment of Photosystem I within Self-Assembled Films. *Langmuir* **2006,** *22* (19), 8114-8120.

4. Millsaps, J. F.; Bruce, B. D.; Lee, J. W.; Greenbaum, E., Nanoscale photosynthesis: Photocatalytic production of hydrogen by platinized photosystem I reaction centers. *Photochem. Photobiol.* **2001,** *73* (6), 630-635.

5. Baba, K.; Itoh, S.; Hastings, G.; Hoshina, S., Photoinhibition of Photosystem I electron transfer activity in isolated Photosystem I preparations with different chlorophyll contents. *Photosynth. Res.* **1996,** *47*, 121-130.

6. Wenzel, T.; Härtter, D.; Bombelli, P.; Howe, C. J.; Steiner, U., Porous translucent electrodes enhance current generation from photosynthetic biofilms. *Nature Comm.* **2018,** *9*, 1299.

7. Ciesielski, P. N.; Faulkner, C. J.; Irwin, M. T.; Gregory, J. M.; Tolk, N. H.; Cliffel, D. E.; Jennings, G. K., Enhanced Photocurrent Production by Photosystem I Multilayer Assemblies. *Adv. Funct. Mater.* **2010,** *20*, 4048-4054.

8. Ciobanu, M.; Kincaid, H. A.; Lo, V.; Dukes, A. D.; Kane Jennings, G.; Cliffel, D. E., Electrochemistry and photoelectrochemistry of photosystem I adsorbed on hydroxyl-terminated monolayers. *J. Electroanal. Chem.* **2007,** *599* (1), 72-78.

9. Voiry, D.; Chhowalla, M.; Gogotsi, Y.; Kotov, N. A.; Li, Y.; Penner, R. M.; Schaak, R. E.; Weiss, P. S., Best Practices for Reporting Electrocatalytic Performance of Nanomaterials. *ACS Nano* **2018,** *12*, 9635-9638.

10. Tung, S.-P.; Huang, T.-K.; Lee, C.-Y.; Chiu, H.-T., Electrochemical growth of gold nanostructures on carbon paper for alkaline direct glucose fuel cell. *RSC Advances* **2012,** *2* (3), 1068-1073.

11. Mohl, M.; Dobo, D.; Kukovecz, A.; Konya, Z.; Kordas, K.; Wei, J.; Vajtai, R.; Ajayan, P. M., Formation of CuPd and CuPt Bimetallic Nanotubes by Galvanic Replacement Reaction. *J. Phys. Chem. C* **2011,** *115* (19), 9403-9409.

12. Khosravi, M.; Amini, M. K., Carbon paper supported Pt/Au catalysts prepared via Cu underpotential deposition-redox replacement and investigation of their electrocatalytic

activity for methanol oxidation and oxygen reduction reactions. *Int. J. Hydrogen Energy* **2010,** *35* (19), 10527-10538.

13. Bard, A. J., Electrochemical methods : fundamentals and applications / Allen J. Bard, Larry R. Faulkner. Wiley: New York, New York. **1980**.

14. Rover, L.; Fernandes, J. C. B.; Neto, G. d. O.; Kubota, L. T.; Katekawa, E.; Serrano, S. l. H. P., Study of NADH Stability Using Ultraviolet–Visible Spectrophotometric Analysis and Factorial Design. *Anal. Biochem.* **1998,** *260* (1), 50-55.

Chapter 3 – Introduction to Photosystem I

The efficient harvesting and storage of energy via photosynthesis has inspired the study of photoactive protein complexes as active components in biohybrid solar energy conversion devices. To date, photoactive protein complexes involved in oxygenic photosynthesis have been used in a wide range of research efforts.[1] In nature, the two photoactive protein complexes, Photosystem I (PSI) and Photosystem II (PSII), facilitate the transfer of electrons during photosynthesis (Figure 3.1).[2-4] The electrons gain energy through photoexcitation and are transferred across the thylakoid membrane where they are accepted by an electron carrier or mediator. In particular, the excitation of electrons by PSI (shown inside a dashed box) is of great technological interest for use in bio-hybrid solar energy conversion devices.[5-7]

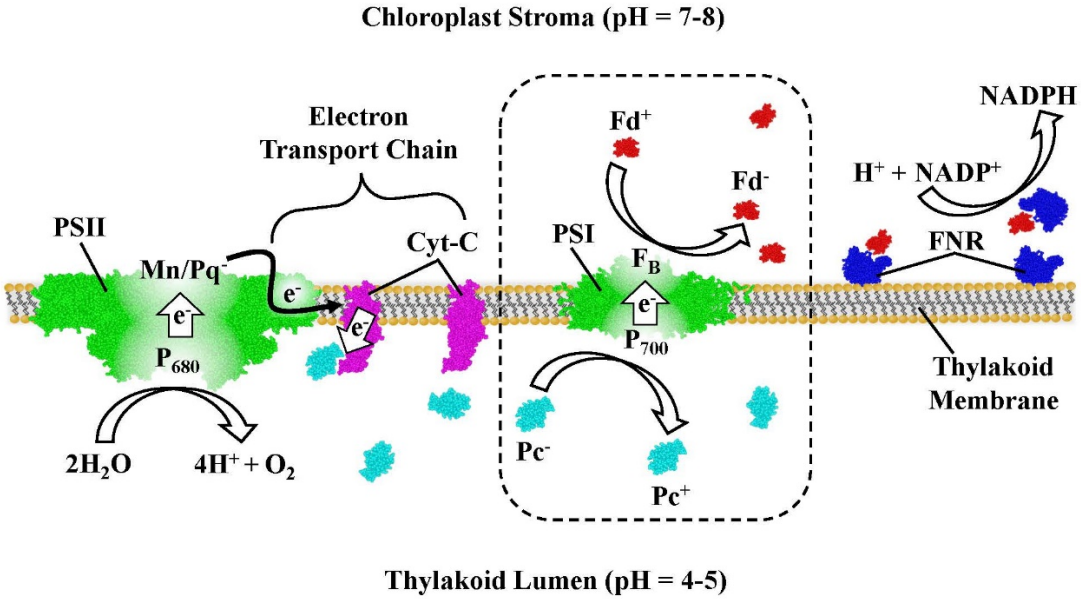

Figure 3.1. *Scheme showing the electron transport chain of photosynthesis. Photosystem I (PSI), the protein complex used in the following experimental chapters, is shown within the dashed box along with its natural electron donor, plastocyanin (Pc), and electron acceptor, ferredoxin (Fd).*

Photosystem I (PSI) can be found within plants, algae, and cyanobacteria. *In vivo*, PSI acts as a photodiode that facilitates the photo-excitation and transport of electrons ultimately necessary for the reduction of $NADP^+$.[8-9] When illuminated, PSI funnels photons captured by chlorophyll antennae to a reaction center in the lumen composed of a special chlorophyll pair, called P_{700}.[10]

An electron hole pair, or exciton, is produced and the electron is transferred ~10 nm to a series of iron-sulfur clusters on the stromal side, with the terminal cluster called the F_B reaction site.[4, 10] This exciton is later utilized to reduce the primary energy storage molecule, $NADP^+$, to drive photosynthesis.[4, 11] Figure 3.2 shows PSI within the thylakoid membrane and depicts the electron transfer across the membrane from the native electron donor protein, plastocyanin (PC), to the electron acceptor, ferredoxin (FD).[10, 12-13] The inset shows an energetic diagram of the electron transfer.

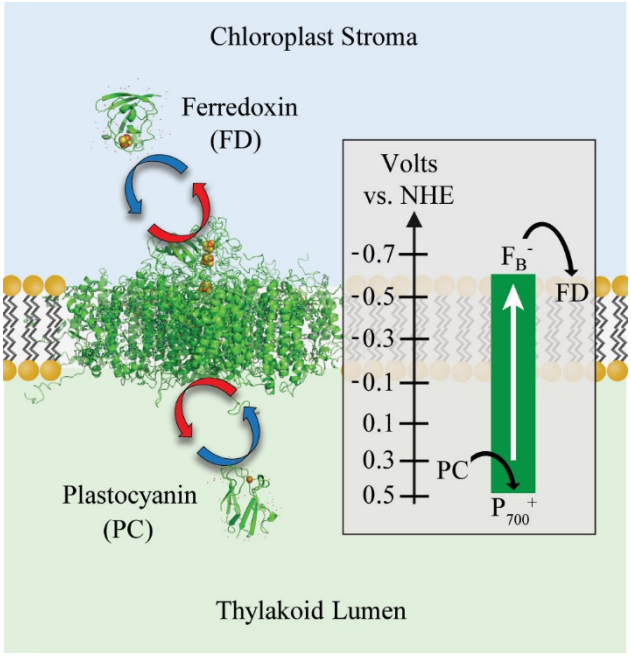

Figure 3.2. *Schematic of PSI operation in vivo. A Photosystem I (PSI) complex is shown within the thylakoid membrane. PSI accepts an electron from plastocyanin (PC), photoexcites the electron from the P_{700} reaction center to the terminal iron-sulfur cluster, F_B, and donates the electron to ferredoxin (FD). The inset shows the absolute energy of the electron at each step, with a net potential gain of approximately 1.1 V from plastocyanin (PC) to ferredoxin (FD). Crystal structures of PSI, plastocyanin, and ferredoxin reproduced from Protein Database files produced by Amunts et al., Xue et al., and Mutoh et al., respectively.*[10, 12,13]

PSI is of great interest for use in solar energy conversion devices because it generates excitons with a net potential difference of 1.1 eV at an internal efficiency near unity.[5] The photo-induced exciton may be leveraged to produce efficient and low-cost biohybrid solar cells, increase the performance of dye-sensitized solar cells (DSSCs), or be utilized for the photocatalysis of

chemical fuel products.[5-7, 14] The natural abundance of PSI, the facile extraction procedure, and its stability outside of its native environment make PSI a prime candidate for development of biohybrid solar energy conversion technologies.[7, 14] For these reasons, PSI can be inexpensively extracted and used to create a variety of lab-scale bio-hybrid photovoltaic cells. Both liquid and solid-state photoelectrochemical cells have been reported.[15-24] Methods of producing useable fuel, such as hydrogen, through PSI photocatalysis have also been proven.[25-31] Many ongoing research efforts continue to probe the fundamental challenges associated with PSI-based devices with the goal of developing the first prototype PSI solar energy conversion technology.

To achieve charge transfer in PSI-based biohybrid systems, the soluble redox-active proteins that interact with PSI in plants are replaced with electrochemical mediators and metal, semi-metal, or semiconducting electrode materials.[5-6, 32-37] Early PSI research studies focused on improving the electrical current produced by the PSI bioelectrodes by choosing the best combination of electrode material, PSI deposition method, and electrochemical mediator species.[18, 32-33, 38-40] Throughout the early 2000's and up to 2010, the work on PSI revealed which electrochemical mediators could be used and their general behavior when in the presence of PSI.[33] Robinson et al. showed that the interactions between simple electrochemical mediators and PSI is governed by imbalanced reaction kinetics at the two PSI reaction sites, resulting in the production of an excess of either reduced (R) or oxidized (O) mediator species (Figure 3.3.A).[37] Briefly, if a mediator or mediator system (R_1 and O_1) reacts faster at the F_B^- site of PSI, an excess of R_1 will be produced (Figure 3.3.A). The excess R_1 will then be oxidized at the underlying electrode and the resulting current into the electrode is called anodic photocurrent. In the opposite case, there is a production of excess oxidized mediator and cathodic photocurrent as shown in Figure 3.3.B. The unbalanced reaction kinetics are believed to depend largely on the half-wave potential of the mediator.[37, 41]

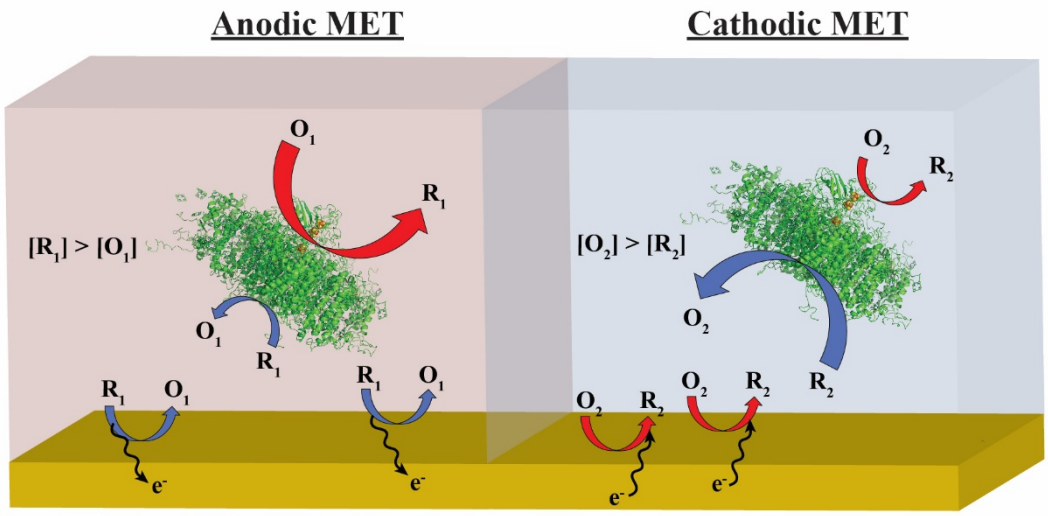

Figure 3.3. *Schematic representation of the effect of imbalanced reaction kinetics at the reaction sites of PSI resulting in either anodic MET (left) or cathodic MET (right).*

Another early advance in knowledge came regarding deposition methods for preparing PSI films. Examples of these methods include rapid PSI adsorption to self-assembled monolayers (SAMs), cross-linking of PSI multilayer films, vacuum-assisted deposition, and PSI trapping within electropolymerized conductive polymers.[7] Some of the highest performing PSI bioelectrodes from this time period include LeBlanc et al.'s PSI multilayers on p-doped silicon that achieved 875 μA/cm^2 and Mershin et al.'s PSI based biophotovoltaic device that yielded 362 μA/cm^2.[18, 32] A major shortcoming of these deposition methods has been a lack of control over exact PSI location, orientation, and film morphology.[7, 14] More recent studies have pursued these issues through means such as genetic engineering of the protein complex to express reactive sites, coupling with smaller redox proteins, and tailoring the electrode surface to interact specifically with PSI.[29,38,42-44] While advancements have been made, the lack of direct and convincing evidence of individual protein complex control in the literature provided motivation for the research chapters that follow.

More recently, attention has moved toward solid-state PSI devices, developing improved means of immobilizing PSI, and understanding the role of dissolved oxygen in mediated PSI devices (Figure 3.4).[7, 14, 17, 19, 24, 45-47] While understanding the role of oxygen is primarily a

concern of PSI stability, efforts toward developing solid state PSI devices and finding new PSI linking strategies have been aimed to improve the performance of PSI devices. The move toward solid state devices and faster electron transfer via better PSI immobilization has increased attention to the concept of direct (DET) versus mediated electron transfer (MET).[7, 48] As mentioned in the general introduction section, DET is desirable due to its faster electron transfer rates, but it is difficult to achieve in bioengineered applications. Few research efforts have claimed to achieve solely or even mostly DET in a PSI bioelectrode.[48-51] One area of promise in achieving DET is using the smaller redox protein, cytochrome C. The use of cyt C with PSI has been extensively studied with a recent report of cyt c and PSI within porous graphene oxide electrodes yielding 14 $\mu A/cm^2$.[20-22, 48-50, 52] To date, PSI bioelectrodes based on either DET or MET cannot outperform other solar energy conversion technologies. Fundamental research on improving PSI electron transfer is necessary to push PSI bioelectrodes forward toward viable small-scale prototypes.

With the promise of achieving efficient DET in PSI devices still out of reach, another direction toward improving PSI bioelectrode performance is to increase the activity and loading of PSI on the active electrode. Solid state PSI devices have suffered from low PSI loadings and traditional deposition procedures for achieving high loadings of protein complexes (PSI multilayers) result in random orientation and morphology. The following research chapters address the challenges of low PSI loading and activity through the development of specially designed 3-dimensional electrodes and deposition procedures based on molecular interactions. While these directions still rely on MET, the improvements in performance may solve fundamental problems and translate into solid-state device development or the use of PSI bioelectrodes for biohybrid solar catalysis.

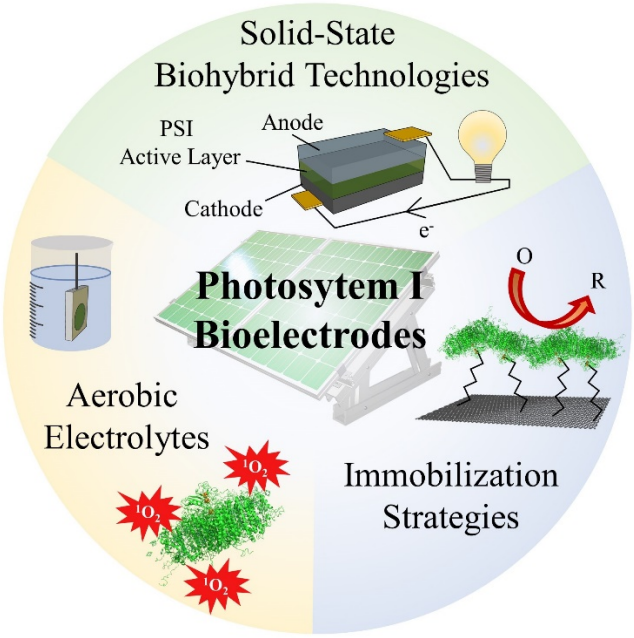

Figure 3.4. *Areas of recent interest in improving the performance of PSI-based bioelectrodes including the development of solid-state PSI devices, discovery of new immobilization strategies for improving electron transfer, and understanding the effects of dissolved oxygen on PSI. Modified and reproduced from Wolfe et al., Curr. Opin. Electrochem.* ***2020,*** *(19), 27-34.*

The following chapters of this dissertation discuss work related to improving mediated photocurrent generation through the development of 3-dimensional PSI electrode architectures and specialized PSI deposition techniques. Chapter 4 discusses the development and study of porous indium tin oxide electrodes that dramatically increase the active surface area and promote high areal loadings of PSI. Chapter 5 changes focus and discusses a strategy for modifying the PSI protein complex during extraction from spinach to produce PSI monolayer films with distinct surface functionalities. PSI was modified with either thiol terminated functional groups or PEG terminated groups by reaction with primary amines located on the lysine residues of PSI's stromal side. Lastly, Chapter 6 highlights the ability to deposit PSI and the conducting polymer PEDOT:PSS sequentially using layer-by-layer assembly. The layers are highly reproducible and yield an increase in PSI activity up to 6-layer pairs or twelve total layers. In all, the following chapters add to our current understanding of mediated electron transfer between PSI and a nearby

electrode. Focus and detail are given on the effects of oxygen, activity of PSI, mechanism of electron transfer, and the mass transfer of mediator from the protein complex to the electrode.

References

1. McCormick, A. J.; Bombelli, P.; Bradley, R. W.; Thorne, R.; Wenzel, T.; Howe, C. J., Biophotovoltaics: oxygenic photosynthetic organisms in the world of bioelectrochemical systems. *Energy Environ. Sci.* **2015,** *8*, 1092-1109.
2. Ko, K., Photosynthesis: A Comprehensive Treatise. A. S. Raghavendra. *Quart. Rev. Bio.* **1998,** *73*, 356-357.
3. Amunts, A.; Nelson, N., Functional organization of a plant Photosystem I: Evolution of a highly efficient photochemical machine. *Plant Physiol. Biochem.* **2008,** *46*, 228-237.
4. Nelson, N.; Junge, W., Structure and Energy Transfer in Photosystems of Oxygenic Photosynthesis. *Annu. Rev. Biochem* **2015,** *84*, 659-683.
5. Nguyen, K.; Bruce, B. D., Growing green electricity: Progress and strategies for use of Photosystem I for sustainable photovoltaic energy conversion. *Biochim. Biophys. Acta Bioenerg.* **2014,** *1837*, 1553-1566.
6. Friebe, V. M.; Frese, R. N., Photosynthetic reaction center-based biophotovoltaics. *Curr. Opin. Electrochem.* **2017,** *5*, 126-134.
7. Wolfe, K. D.; Dervishogullari, D.; Passantino, J. M.; Stachurski, C. D.; Jennings, G. K.; Cliffel, D. E., Improving the stability of photosystem I–based bioelectrodes for solar energy conversion. *Curr. Opin. Electrochem.* **2020,** *19*, 27-34.
8. Hogewoning, S. W.; Wientjes, E.; Douwstra, P.; Trouwborst, G.; van Ieperen, W.; Croce, R.; Harbinson, J., Photosynthetic Quantum Yield Dynamics: From Photosystems to Leaves. *The Plant Cell* **2012,** *24*, 1921 LP - 1935.
9. Shinkarev, V. P.; Vassiliev, I. R.; Golbeck, J. H., A Kinetic Assessment of the Sequence of Electron Transfer from FX to FA and Further to FB in Photosystem I: The Value of the Equilibrium Constant between FX and FA. *Biophys. J.* **2000,** *78*, 363-372.
10. Amunts, A.; Toporik, H.; Borovikova, A.; Nelson, N., Structure determination and improved model of plant photosystem I. *J. Bio. Chem.* **2010,** *285*, 3478-3486.
11. Golbeck, J. H., *Photosystem I: The Light-Driven Plastocyanin: Ferredoxin Oxidoreductase*. Springer Netherlands: **2007**.
12. Xue, Y.; Ökvist, M.; Hansson, Ö.; Young, S., Crystal structure of spinach plastocyanin at 1.7 Å resolution. *Protein Sci.* **1998,** *7* (10), 2099-2105.
13. Mutoh, R.; Muraki, N.; Shinmura, K.; Kubota-Kawai, H.; Lee, Y.-H.; Nowaczyk, M. M.; Rögner, M.; Hase, T.; Ikegami, T.; Kurisu, G., X-ray Structure and Nuclear Magnetic

Resonance Analysis of the Interaction Sites of the Ga-Substituted Cyanobacterial Ferredoxin. *Biochemistry* **2015,** *54* (39), 6052-6061.

14. Teodor, A. H.; Bruce, B. D., Putting Photosystem I to Work: Truly Green Energy. Trends Biotechnol. **2021**, 11, 1000122.

15. Ciesielski, P. N.; Hijazi, F. M.; Scott, A. M.; Faulkner, C. J.; Beard, L.; Emmett, K.; Rosenthal, S. J.; Cliffel, D.; Kane Jennings, G., Photosystem I – Based biohybrid photoelectrochemical cells. *Bioresour. Technol.* **2010,** *101*, 3047-3053.

16. Robinson, M. T.; Armbruster, M. E.; Gargye, A.; Cliffel, D. E.; Jennings, G. K., Photosystem I Multilayer Films for Photovoltage Enhancement in Natural Dye-Sensitized Solar Cells. *ACS Appl. Energy Mater.* **2018,** *1*, 301-305.

17. Gizzie, E. A.; Scott Niezgoda, J.; Robinson, M. T.; Harris, A. G.; Kane Jennings, G.; Rosenthal, S. J.; Cliffel, D. E., Photosystem I-polyaniline/TiO2solid-state solar cells: Simple devices for biohybrid solar energy conversion. *Energy Environ. Sci.* **2015,** *8*, 3572-3576.

18. Mershin, A.; Matsumoto, K.; Kaiser, L.; Yu, D.; Vaughn, M.; Nazeeruddin, M. K.; Bruce, B. D.; Graetzel, M.; Zhang, S., Self-assembled photosystem-I biophotovoltaics on nanostructured TiO2 and ZnO. *Scientific Reports* **2012,** *2*, 234.

19. Kazemzadeh, S.; Riazi, G.; Ajeian, R., Novel Approach of Biophotovoltaic Solid State Solar Cells Based on a Multilayer of PS1 Complexes as an Active Layer. *ACS Sustain. Chem. Eng.* **2017,** *5*, 9836-9840.

20. Ciornii, D.; Riedel, M.; Stieger, K. R.; Feifel, S. C.; Hejazi, M.; Lokstein, H.; Zouni, A.; Lisdat, F., Bioelectronic Circuit on a 3D Electrode Architecture: Enzymatic Catalysis Interconnected with Photosystem I. *J. Am. Chem. Soc.* **2017,** *139* (46), 16478-16481.

21. Stieger, K. R.; Ciornii, D.; Kölsch, A.; Hejazi, M.; Lokstein, H.; Feifel, S. C.; Zouni, A.; Lisdat, F., Engineering of supramolecular photoactive protein architectures: the defined co-assembly of photosystem I and cytochrome c using a nanoscaled DNA-matrix. *Nanoscale* **2016,** *8*, 10695-10705.

22. Stieger, K. R.; Feifel, S. C.; Lokstein, H.; Hejazi, M.; Zouni, A.; Lisdat, F., Biohybrid architectures for efficient light-to-current conversion based on photosystem i within scalable 3D mesoporous electrodes. *J. Mater. Chem. A* **2016,** *4*, 17009-17017.

23. Wolfe, K. D.; Dervishogullari, D.; Stachurski, C. D.; Passantino, J. M.; Kane Jennings, G.; Cliffel, D. E., Photosystem I Multilayers within Porous Indium Tin Oxide Cathodes Enhance Mediated Electron Transfer. *ChemElectroChem* **2020,** *7* (3), 596-603.

24. Gordiichuk, P. I.; Wetzelaer, G. J. A. H.; Rimmerman, D.; Gruszka, A.; De Vries, J. W.; Saller, M.; Gautier, D. A.; Catarci, S.; Pesce, D.; Richter, S.; Blom, P. W. M.; Herrmann, A., Solid-state biophotovoltaic cells containing photosystem i. *Adv. Mater.* **2014,** *26*, 4863-4869.

25. Lubner, C. E.; Knorzer, P.; Silva, P. J. N.; Vincent, K. A.; Happe, T.; Bryant, D. A.; Golbeck, J. H., Wiring an [FeFe]-Hydrogenase with Photosystem I for Light-Induced Hydrogen Production. *Biochemistry* **2010,** *49* (48), 10264-10266.

26. Millsaps, J. F.; Bruce, B. D.; Lee, J. W.; Greenbaum, E., Nanoscale photosynthesis: Photocatalytic production of hydrogen by platinized photosystem I reaction centers. *Photochem. Photobiol.* **2001,** *73* (6), 630-635.

27. Walters, K. A.; Golbeck, J. H., Designing a modified clostridial 2[4Fe-4S] ferredoxin as a redox coupler to directly link photosystem I with a Pt nanoparticle. *Photosynth. Res.* **2019**.

28. Zhao, F. Y.; Conzuelo, F.; Hartmann, V.; Li, H. G.; Nowaczyk, M. M.; Plumere, N.; Rogner, M.; Schuhmann, W., Light Induced H-2 Evolution from a Biophotocathode Based on Photosystem 1-Pt Nanoparticles Complexes Integrated in Solvated Redox Polymers Films. *J. Phys. Chem. B* **2015,** *119* (43), 13726-13731.

29. Zhao, F.; Wang, P.; Ruff, A.; Hartmann, V.; Zacarias, S.; Pereira, I. A. C.; Nowaczyk, M. M.; Rögner, M.; Conzuelo, F.; Schuhmann, W., A photosystem I monolayer with anisotropic electron flow enables Z-scheme like photosynthetic water splitting. *Energy Environ. Sci.* **2019,** *12* (10), 3133-3143.

30. Badura, A.; Guschin, D.; Kothe, T.; Kopczak, M. J.; Schuhmann, W.; Rögner, M., Photocurrent generation by photosystem 1 integrated in crosslinked redox hydrogels. *Energy Environ. Sci.* **2011,** *4*, 2435-2440.

31. LeBlanc, G.; Chen, G. P.; Jennings, G. K.; Cliffel, D. E., Photoreduction of Catalytic Platinum Particles Using Immobilized Multilayers of Photosystem I. *Langmuir* **2012,** *28* (21), 7952-7956.

32. LeBlanc, G.; Chen, G.; Gizzie, E. A.; Jennings, G. K.; Cliffel, D. E., Enhanced Photocurrents of Photosystem I Films on p-Doped Silicon. *Adv. Mater.* **2012,** *24*, 5959-5962.

33. Robinson, M. T.; Gizzie, E. A.; Mwambutsa, F.; Cliffel, D. E.; Jennings, G. K., Mediated approaches to Photosystem I-based biophotovoltaics. *Curr. Opin. Electrochem.* **2017,** *5*, 211-217.

34. Carmeli, I.; Frolov, L.; Carmeli, C.; Richter, S., Photovoltaic Activity of Photosystem I-Based Self-Assembled Monolayer. *J. Am. Chem. Soc.* **2007,** *129*, 12352-12353.

35. Petrova, A.; Mamedov, M.; Ivanov, B.; Semenov, A.; Kozuleva, M., Effect of artificial redox mediators on the photoinduced oxygen reduction by photosystem I complexes. *Photosynth. Res.* **2018,** *137*, 421-429.

36. Buesen, D.; Hoefer, T.; Zhang, H.; Plumeré, N., A kinetic model for redox-active film based biophotoelectrodes. *Faraday Discuss.* **2019,** *215*, 39-53.

37. Robinson, M. T.; Cliffel, D. E.; Jennings, G. K., An Electrochemical Reaction-Diffusion Model of the Photocatalytic Effect of Photosystem I Multilayer Films. *J. Phys. Chem. B* **2018,** *122* (1), 117-125.

38. Ciobanu, M.; Kincaid, H. A.; Lo, V.; Dukes, A. D.; Kane Jennings, G.; Cliffel, D. E., Electrochemistry and photoelectrochemistry of photosystem I adsorbed on hydroxyl-terminated monolayers. *J. Electroanal. Chem.* **2007,** *599* (1), 72-78.

39. Kincaid, H. A.; Niedringhaus, T.; Ciobanu, M.; Cliffel, D. E.; Jennings, G. K., Entrapment of Photosystem I within Self-Assembled Films. *Langmuir* **2006,** *22* (19), 8114-8120.

40. Beam, J. C.; LeBlanc, G.; Gizzie, E. A.; Ivanov, B. L.; Needell, D. R.; Shearer, M. J.; Jennings, G. K.; Lukehart, C. M.; Cliffel, D. E., Construction of a Semiconductor–Biological Interface for Solar Energy Conversion: p-Doped Silicon/Photosystem I/Zinc Oxide. *Langmuir* **2015,** *31*, 10002-10007.

41. Bard, A. J., Electrochemical methods : fundamentals and applications / Allen J. Bard, Larry R. Faulkner. Wiley: New York, New York. **1980**.

42. Gordiichuk, P.; Pesce, D.; Ocampo, O. E. C.; Marcozzi, A.; Wetzelaer, G.-J. A. H.; Paul, A.; Loznik, M.; Gloukhikh, E.; Richter, S.; Chiechi, R. C.; Herrmann, A., Orientation and Incorporation of Photosystem I in Bioelectronics Devices Enabled by Phage Display. *Adv. Sci.* **2017,** *4*, 1600393.

43. Kiliszek, M.; Harputlu, E.; Szalkowski, M.; Kowalska, D.; Unlu, C. G.; Haniewicz, P.; Abram, M.; Wiwatowski, K.; Niedziółka-Jönsson, J.; MaćKowski, S.; Ocakoglu, K.; Kargul, J., Orientation of photosystem i on graphene through cytochrome: C 553 leads to improvement in photocurrent generation. *J. Mater. Chem. A* **2018,** *6*, 18615-18626.

44. Trammell, S. A.; Spano, A.; Price, R.; Lebedev, N., Effect of protein orientation on electron transfer between photosynthetic reaction centers and carbon electrodes. *Biosens. Bioelectron.* **2006,** *21* (7), 1023-1028.

45. Barhom, H.; Carmeli, C.; Carmeli, I., Fabrication of Electronic Junctions between Oriented Multilayers of Photosystem I and the Electrodes of Optoelectronic Solid-State Devices. *J. Phys. Chem. B* **2021,** *125* (3), 722-728.

46. Das, R.; Kiley, P. J.; Segal, M.; Norville, J.; Yu, A. A.; Wang, L.; Trammell, S. A.; Reddick, L. E.; Kumar, R.; Stellacci, F.; Lebedev, N.; Schnur, J.; Bruce, B. D.; Zhang, S.; Baldo, M., Integration of Photosynthetic Protein Molecular Complexes in Solid-State Electronic Devices. *Nano Lett.* **2004,** *4*, 1079-1083.

47. Zeynali, A.; Ghiasi, T. S.; Riazi, G.; Ajeian, R., Organic solar cell based on photosystem I pigment-protein complex, fabrication and optimization. *Org. Electron.* **2017,** *51*, 341-348.

48. Morlock, S.; Subramanian, S. K.; Zouni, A.; Lisdat, F., Scalable Three-Dimensional Photobioelectrodes Made of Reduced Graphene Oxide Combined with Photosystem I. *ACS Appl. Mater. Interfaces* **2021,** *13* (9), 11237-11246.

49. Ciornii, D.; Kölsch, A.; Zouni, A.; Lisdat, F., A precursor-approach in constructing 3D ITO electrodes for the improved performance of photosystem I-cyt c photobioelectrodes. *Nanoscale* **2019**.

50. Feifel, S. C.; Stieger, K. R.; Hejazi, M.; Wang, X.; Ilbert, M.; Zouni, A.; Lojou, E.; Lisdat, F., Dihemic c4-type cytochrome acting as a surrogate electron conduit: Artificially interconnecting a photosystem I supercomplex with electrodes. *Electrochem. Commun.* **2018,** *91*, 49-53.

51. Lopez-Martinez, M.; Lopez-Ortiz, M.; Antinori, M. E.; Wientjes, E.; Nin-Hill, A.; Rovira, C.; Croce, R.; Diez-Perez, I.; Gorostiza, P., Electrochemically Gated Long-Distance Charge Transport in Photosystem I. *Angew. Chem. Int. Ed.* **2019,** *58* (38), 13280-13284.

52. Kölsch, A.; Hejazi, M.; Stieger, K. R.; Feifel, S. C.; Kern, J. F.; Müh, F.; Lisdat, F.; Lokstein, H.; Zouni, A., Insights into the binding behavior of native and non-native cytochromes to photosystem I from Thermosynechococcus elongatus. *J. Biol. Chem.* **2018,** *293*, 9090-9100.

Chapter 4 – Photosystem I Multilayers within Porous Indium Tin Oxide Cathodes

The following work on producing and testing porous and transparent indium tin oxide cathodes with PSI was a collaborative effort led by the author (Kody D. Wolfe) and Dr. Dilek Dervishogullari. The contents of this chapter were first published in ChemElectroChem (Wolfe et al., ChemElectroChem **2020**, *7* (3), 596-603).[1] Dr. Christopher D. Stachurski and Joshua M. Passantino assisted in editing and experimental planning. Additional thanks go to the Rosenthal Lab at Vanderbilt University for the use of their tube furnace. Funding for the following work was provided by the National Science Foundation (DMR-1507505) and the United States Department of Agriculture (2019-67021-29857).

Introduction

One limiting factor within PSI-based bioelectrodes is the slow electron transfer from PSI's reaction centers to the electrode materials, which ultimately limits the produced photocurrent.[2-5] Electron transfer in PSI bioelectrodes can be categorized into two broad groups: direct electron transfer (DET) and mediated electron transfer (MET).[2] DET is achieved through transfer of electrons or holes from the electrode into the protein via electron tunneling.[6] MET involves the use of an electrochemical mediator to shuttle charge between either of the two active sites, P_{700}^{+} or F_B^{-}, of PSI and an electrode through a diffusion-reaction pathway.[4, 6] While DET is favorable in regards to its elimination of intermediate species and associated mass transfer steps, it requires close proximity of the protein active site to the electrode.[6] Many strategies have been explored with aims of maximizing electron transfer between PSI and its host electrode.[2-5] To enable DET, monolayers of PSI protein complexes have been coupled with various linking molecules and proteins, which help minimize the electrode-protein separation distance and also provide an energetically favorable pathway for electron transfer.[3, 7-18] Most notably, the cytochrome complex (cyt c) has been used to incorporate PSI onto a variety of electrode materials.[13]

Alternatively, significant improvements in mediated photocurrent generation have been achieved by drop-casting thick multilayer films of PSI onto silicon, gold, and graphene electrodes.[19-23] Applying thicker films of PSI increases overall light absorption by providing a

higher areal protein loading and increases the total amount of converted mediator.[4] However, multilayer PSI assemblies are limited by both the diffusion rate of the mediator and the distance from individual PSI protein complexes to the electrode surface.[24-25]

Three-dimensional electrodes offer another avenue for increasing the areal protein loading.[7, 11, 26-29] Ciesielski et al. modified nanoporous gold leaf electrodes with PSI monolayers and achieved a 300% increase in photocurrent.[27] The improvement was credited to an increase in the electrochemically active surface area, which allowed for an increase in mediated photocurrent response. Examples of other high surface area PSI bioelectrodes include a gold nanoparticle-based approach, and a nanostructured TiO_2 and ZnO device.[30-31] In each case, the increase in photocurrent density is primarily attributed to an increase in the active electrode surface area, regardless of the prescribed electron transfer pathway. Increasing the active surface area will impact both the DET and MET response of the bioelectrode because it provides a higher surface area for either protein-electrode interaction or for mediator electron transfer.

Recently, methods for producing three-dimensional, transparent, and conductive ITO electrodes have spurred interest in their application to biohybrid photovoltaics. Wenzel et al. showed that photocurrents generated from photosynthetic biofilms composed of either *Nostoc punctiforme* or *Synechocystis sp*. on porous ITO electrodes are two orders of magnitude larger than those on planar ITO.[28] Stieger et al. utilized porous ITO with isolated PSI by wiring *T. elongatus*-derived PSI via cyt c to the surface of 460 nm ITO pores, resulting in a 150 μA cm^{-2} photocurrent density with an applied potential of 100 mV vs. Ag/AgCl.[11] Additionally, Ciornii et al. found that porous ITO electrodes incorporating cyt c as a linking agent show a maximum performance of 270 μA cm^{-2} at the 460 nm pore size (compared to pore sized up to 3 μm) with an applied potential of 200 mV vs. Ag/AgCl.[7] The maximum is attributed to a maximum areal loading of cyt c and PSI on the ITO surface due to a higher protein binding capacity within smaller pores. These reports have shown that porous ITO is an effective cathode material for PSI-based bioelectrodes in conjunction with cyt c and an applied potential to drive DET. In contrast to our work, PSI was confined to the surface through the use of cyt c as a post-deposition linking agent and is therefore limited by the surface area of the porous electrode and the capacity for areal loading of PSI and cyt c.[22, 32]

Multilayers of PSI within pores can be expected to undergo mediated photocurrent production, and, therefore, may surpass the pore size limitation of previous monolayer studies. Many electrochemical mediators have been studied within PSI bioelectrodes to achieve high rates of MET.[33-34] One particularly high-performing mediator pair is 2,6-dichlorophenolindophenol (DCPIP) and ascorbate (AscH).[33, 35] Upon dissolution of sodium ascorbate salt into deionized water, AscH is protonated, forming ascorbic acid ($AscH_2$). $AscH_2$ then undergoes a heterogeneous reaction (Rxn 4.1) in which two electrons and two protons are transferred to DCPIP, forming $DCPIPH_2$ and dehydroascorbate (DHA).[36] $DCPIPH_2$ is a fast electron donor to P_{700}^+, making it an ideal mediator species for shuttling charge between the P_{700}^+ reaction center and the cathode material.[33, 35] Herein, $DCPIPH_2$ is used to ensure fast electron transfer from ITO to PSI multilayers in order to study the effect of the porous ITO morphology on MET.

$$DCPIP + AscH_2 \rightarrow DCPIPH_2 + DHA \qquad \text{(Rxn 4.1)}$$

We used ITO nanoparticles to produce two different three-dimensional electrode morphologies: mesoporous and macroporous ITO (meso-ITO and macro-ITO). The meso-ITO electrodes bear cavities of approximately 20-100 nm, which is slightly larger than the crystallographic dimensions of the PSI protein complex and is hypothesized to increase the PSI-ITO contact area.[37] Macro-ITO prepared via an ITO-coated polystyrene templating procedure (See Appendix B) provided much larger pore sizes (~5 μm). The electrochemically active surface area of both electrode morphologies was determined via capacitance cyclic voltammetry (CV).[38] These electrodes were then modified with PSI multilayer films of various mass loadings and tested in a photoelectrochemical cell.

Our findings show that by entrapping PSI protein complexes in larger pores, an increase in mediated photocurrent is observed (Figure 4.1). Macro-ITO produced 42 μA cm^{-2}, approximately 3 times more photocurrent than meso-ITO and 40 times more than the planar ITO at a PSI loading of 66 μg cm^{-2}. Macropores increase photocurrent by allowing multilayers of PSI to deposit along

pore walls, which increases mediator conversion within a single pore and results in an increase in MET. We discuss the effects of electrode conductivity, electrode translucency, protein loading, and electrochemical surface area in multilayer PSI-modified meso- and macro-ITO cathodes to draw conclusions about both charge transfer pathways and routes for optimizing porous bioelectrode interfaces by incorporating mediated electron transfer. Finally, this work highlights the ability of porous ITO-PSI biocathodes to improve MET at the dark open circuit potential (OCP), achieving appreciable photocurrent in the absence of surface linking agents and an applied overpotential.

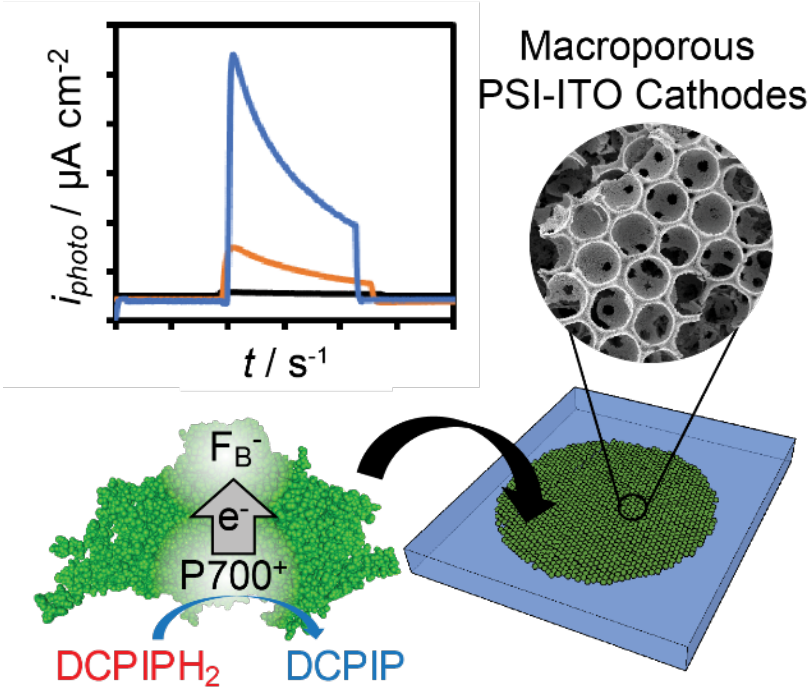

Figure 4.1. *Schematic representation of the fabrication and testing of a PSI Macro-ITO cathode for enhanced mediated photocurrent production.*

Results & Discussion

First, the mediated electron transfer between PSI, $DCPIPH_2$, and ITO was investigated using photochronoamperometry (Figure 4.2). A multilayer film of PSI on an ITO-coated glass slide was illuminated under a 100 mW cm^{-2} white light source in the presence of 1 mM DCPIP and 5 mM AscH (green), 5 mM AscH (red), and 1 mM DCPIP (blue), while the ITO was held at the dark OCP. Of these conditions, a 1:5 ratio of DCPIP to AscH produced a much greater photocurrent in comparison to AscH only or DCPIP only solutions. In either the DCPIP only or AscH only solutions, the photocurrent is much lower and is limited by a reaction at one of the PSI active sites, evidenced by the flat photocurrent responses, Figure 4.2. A schematic representation of the mediated electron transfer process is given in Figure 4.3. At the P_{700}^{+} reaction site, $DCPIPH_2$ is electrochemically oxidized via Reaction 4.2. The final oxidized product (DCPIP) may then react at the cathode or be chemically reduced to $DCPIPH_2$ (Rxn 4.1, see in introduction section). Excess AscH is necessary to increase the concentration of $AscH_2$, which regenerates the local concentration of $DCPIPH_2$. A steady state rate is reached and is limited by the diffusion of $AscH_2$ into the multilayer film to replenish $DCPIPH_2$.[24-25] In conclusion, $DCPIPH_2$ is capable of rapidly reducing the P_{700}^{+} site, and PSI multilayers in the presence of $DCPIPH_2$ and excess AscH on an ITO electrode produce cathodic photocurrent.

$$DCPIPH_2 \leftrightarrow DCPIP + 2e^- + 2H^+ \qquad \text{(Rxn 4.2)}$$

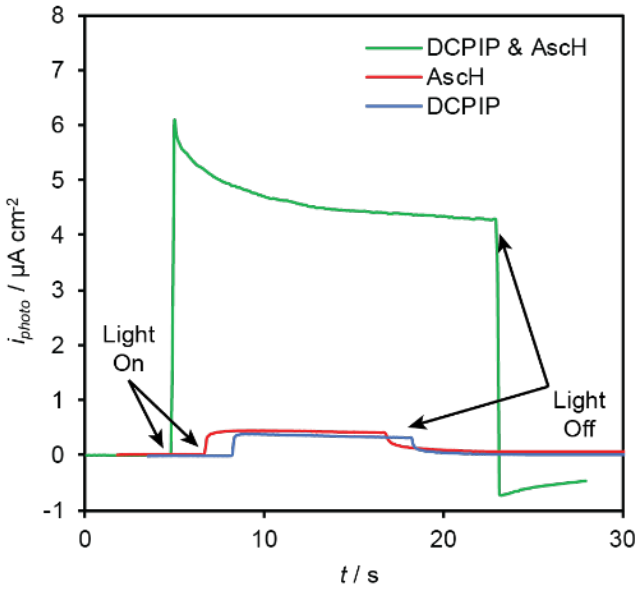

Figure 4.2. *Photoelectrochemical studies of DCPIP and AscH. Photochronoamperometry scans taken on a planar ITO electrode with a PSI multilayer in the presence of 1 mM DCPIP and 5 mM AscH (green) 5 mM AscH (red), and 1 mM DCPIP (blue). Photochronoamperometry studies were performed in a 100 mM KCl supporting electrolyte containing the mediator species and the sample was illuminated with a 100 mW cm^{-2} white light source with the planar ITO electrode held at the dark open circuit potential (OCP).*

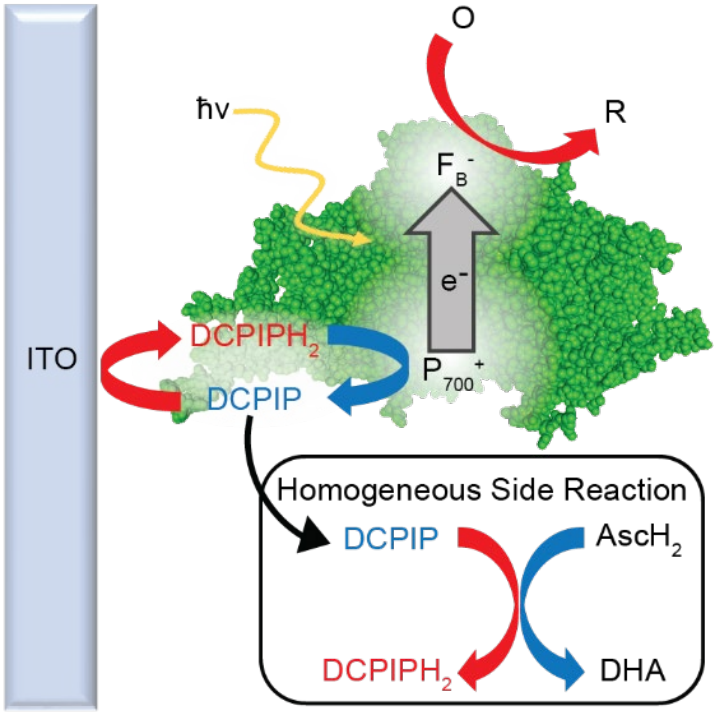

Figure 4.3. *Proposed mediated electron transfer mechanism by PSI in the presence of AscH and DCPIP. Photocurrent generation is driven by the local production of DCPIP by PSI near the electrode surface, where it can be reduced to $DCPIPH_2$ by the electrode, producing cathodic current. The homogeneous side reaction competes with the production of DCPIP by P_{700} but also sets the solution potential and the dark OCP to a fully reduced state (all $DCPIPH_2$) so that when the light is turned on, PSI provides a driving force for cathodic photocurrent generation (production of excess DCPIP near the electrode).*

In the absence of an electrochemical mediator, the achieved photocurrent is negligible as seen in Figure 4.4. In contrast, in the presence of a mediator, the PSI-modified ITO cathodes yield a significant cathodic current, while in the absence of mediator a negligible current is observed. This shows that mediated electron transfer (MET) is the primary means of electron transfer at the PSI-ITO interface.

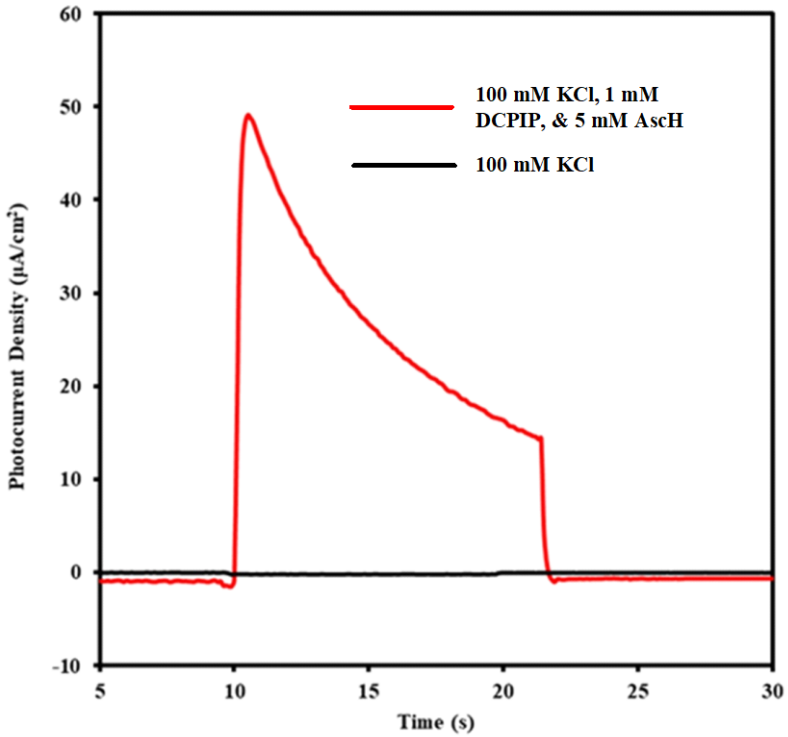

Figure 4.4. *Chronoamperometric scans of a PSI macro-ITO cathode with (red) and without (black) the electrochemical mediator, DCPIP and AscH. The PSI-modified (125 μL PSI solution) macro-ITO cathodes were immersed in an aqueous solution of 1 mM DCPIP, 5 mM NaAsc and 100 mM KCl and illuminated with a 100 mW* cm^{-2} *whit light source.*

Mesoporous ITO electrodes were prepared by tape-casting an aliquot of suspended ITO nanoparticles onto a cleaned ITO-coated glass slide. The nanoparticles were then sintered under an argon environment to produce translucent and conductive mesoporous electrodes. Similarly, macroporous ITO electrodes were prepared by tape-casting ITO nanoparticles onto a polystyrene template and simultaneously sintering the ITO nanoparticles and removing the polystyrene spheres. The polystyrene template was prepared by drop-casting polystyrene spheres onto a cleaned ITO-coated electrode and sintering the spheres at 85 °C. After the porous electrode fabrication, both meso- and macro-ITO electrodes were imaged to assess successful ITO nanoparticle sintering and electrode quality using scanning electron microscopy (SEM). SEM also verified the removal of the polystyrene spheres, during the sintering process of the macro-ITO

samples. Figure 4.5 shows top down and cross-sectional SEM micrographs of the meso- and macro-ITO electrodes. Within the meso-ITO, the ITO nanoparticles pack randomly and densely, forming pore sizes between 20 and 100 nm (Figures 4.5.A and 4.5.B). These mesopores are on the scale of the crystallographic PSI protein complex unit cell dimensions, approximately 12 nm x 13 nm x 19 nm.[37] The dense porous structure extends uniformly to the substrate surface, as shown in the cross-sectional SEM (Figure 4.5.C). The macro-ITO electrodes yield hierarchical nanostructured pores, with larger macropores created by the polystyrene template (Figures 4.5.D and 4.5.E) and smaller mesopores created by the sintered ITO nanoparticles that make up the macropore walls (Figure 4.6). The intrapore connections formed by sintering the polystyrene spheres prior to the deposition of ITO nanoparticles can be clearly observed in both Figure 4.5.E and the cross-sectional SEM in Figure 4.5.F.[28]

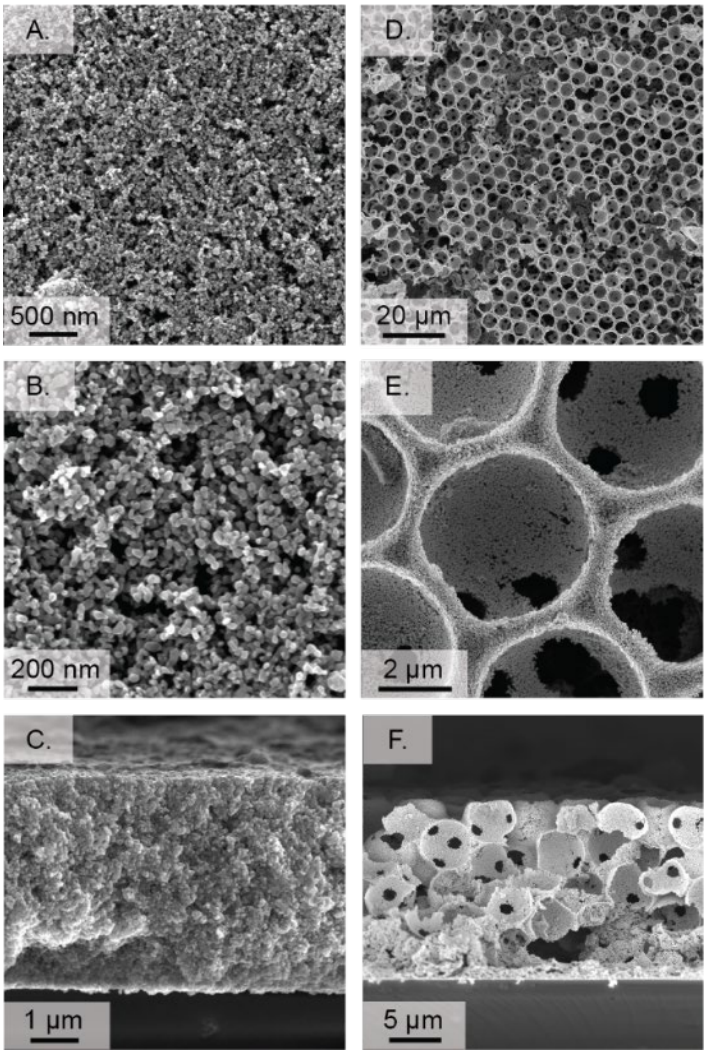

Figure 4.5. *Scanning electron microscopy (SEM) micrographs of: (A) Meso-ITO electrode surface, (B) Meso-ITO electrode pores on the order of 20-100 nm, (C) Cross-sectional SEM of the meso-ITO, (D) Macro-ITO electrode surface showing the inverse opal structure, (E) Individual macropores with intrapore connections, and (F) Macro-ITO electrode cross-sectional image. A high magnification image of the macro-ITO pore wall is given in Figure 4.6, highlighting the mesoporous structure of the sintered nanoparticle walls. All images are taken at 5.0 keV and a working distance of 5 mm using a secondary electron detector.*

The hierarchical structure of the macro-ITO electrodes can be described as an inverse opal macropore (created via the PS sphere template procedure detailed in Appendix B) structure created by mesoporous walls.[28] Figure 4.6 shows a high magnification electron micrograph of the outer pore wall of a macropore which is composed of the sintered ITO nanoparticles.

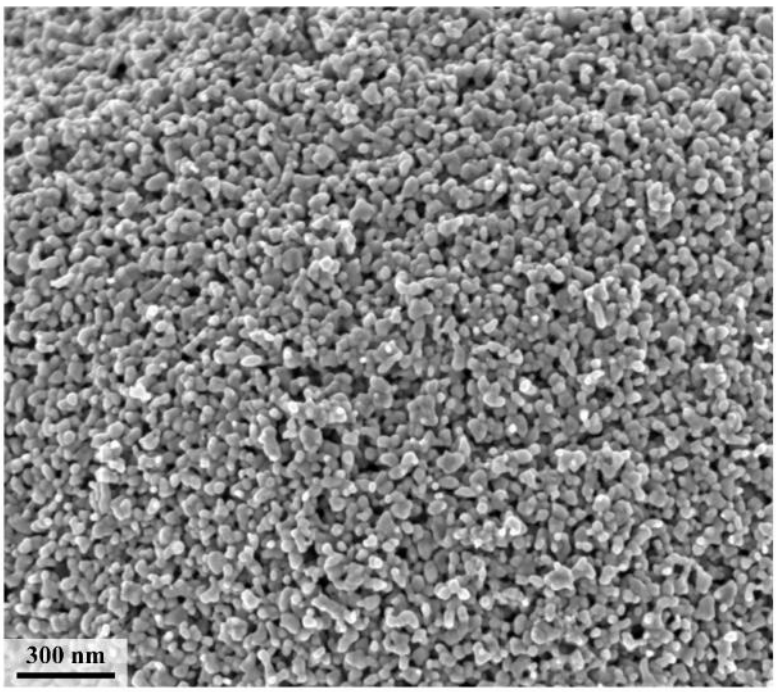

Figure 4.6. *A high magnification scanning electron micrograph of the surface of a macropore wall (macropores seen in Figures 4.5.D, E, and F). The mesoporous structure making up the macropore walls increases the active surface area of the macro-ITO electrodes. Image taken at 5.0 keV and a working distance of 5 mm using a secondary electron detector.*

The fabricated meso-ITO electrodes have a thickness of 4.6 ± 1.3 μm (Figure 4.7.A), and the macro-ITO electrodes have a thickness of 9.4 ± 2.0 μm as measured via profilometry (Figure 4.7.B). The profilometry scans began on the bare ITO-coated glass surface for approximately 200 μm and proceeded onto to the porous electrode for approximately 800 μm. As a coffee ring effect was observed on all electrodes, the average step-height was taken over the 800 μm electrode scan length to obtain a representative value. The average step height for 5 samples was measured and the average value is represented by a dashed line.

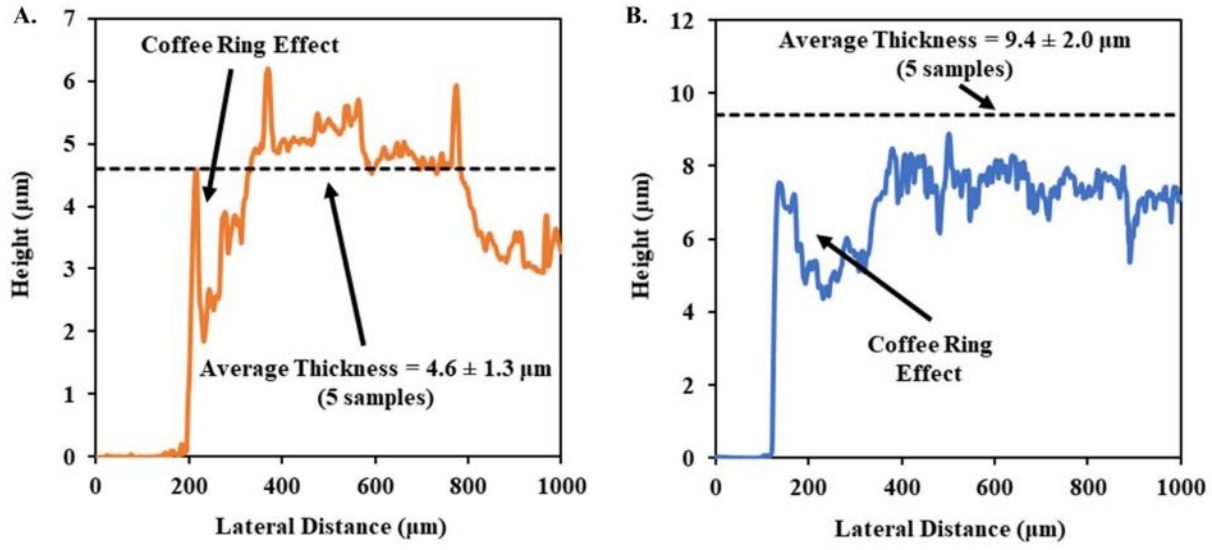

Figure 4.7. *Stylus profilometry scans for unmodified (A) meso- and (B) macro-ITO electrodes.*

Importantly, both the conductivity and optical band gap of ITO depend on the crystal structure and the tin dopant concentration.[39-40] Therefore, to ensure the quality and performance of the electrodes, the ITO must remain in its body-centered cubic structure (space group = Ia-3(No. 206)) after sintering.[39] Figure 4.8 shows powder x-ray diffraction (XRD) spectra for ITO recovered from sintered meso- and macro-ITO electrodes and indicates that the crystal structure is unaffected by the sintering process and the polystyrene templating procedure. The observed peaks correspond to the desired cubic ITO phase, with peak assignments given in Table 4.1.[39]

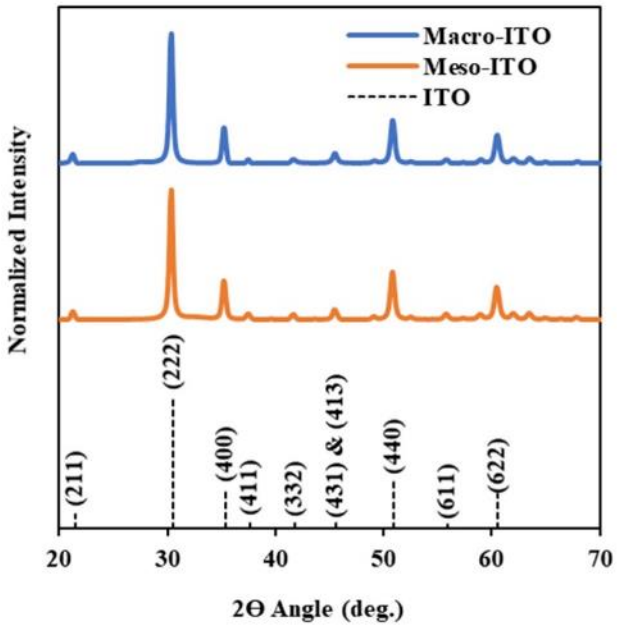

Figure 4.8. *Powder X-ray diffraction (XRD) spectra for macro- (blue) and meso-ITO (orange) recovered from fabricated electrodes. The characteristic spectra for the body-centered cubic phase of ITO is given by the dashed lines (with relative intensity and crystallographic plane assignments). The characteristic spectral data is also tabulated below in Table 4.1.* [39]

Table 4.1. XRD peak assignments of ITO nanoparticles recovered from porous electrodes. The peaks correspond to the body-centered cubic phase, space group Ia-3(No. 206).[39]

Crystal Plane (hkl)	2Θ Angle (deg.)	Relative Intensity (%)
211	21.46	11.0
222	30.54	100.0
400	35.41	30.4
411	37.63	5.2
332	41.78	4.5
431 & 413	45.61	3.9 & 4.5
440	50.94	36.6
611	55.89	3.3
622	60.56	26.5

The electrical conductivity, or, inversely, resistivity, of the electrodes is critical to the electrode performance and was measured via a four-point probe sheet resistance test. Sintering the ITO nanoparticles under an argon atmosphere resulted in highly conductive electrodes. Table 4.2 gives a summary of the electrode sheet resistance measurements and highlights the exceptional decrease in sheet resistance upon sintering for both electrode morphologies. For these measurements, electrodes were cast onto non-conductive bare glass substrates. Sheet resistances are reported (instead of resistivity values) to avoid the incorrect assumption that the electrodes are a continuous bulk material, which is a requisite for the determination of resistivity or conductivity.

Table 4.2. Sheet resistance measurements pre and post sintering for meso- and macro-ITO electrodes.

Electrode Morphology	Unannealed Sheet Resistance (kΩ/sq)	Post Annealed Sheet Resistance (kΩ/sq)
Meso-ITO	2400 ± 1300	1.4 ± 0.2
Macro-ITO	900 ± 600	3.5 ± 1.9

In electrochemical reactions, the active surface area can be directly related to the reaction rate.[12] Therefore, to better understand the MET achieved within porous electrodes, the electrochemically active surface area should be considered. Following the procedure reported by Voiry et al., we determined the electrochemical surface area factor (ECSAF) of the macro- and meso-ITO electrodes and used these values to approximate the active surface area.[38] By measuring the ECSAF of the electrodes, the area in which a species in solution can react at the electrode surface can be studied.[38] The ECSAF was determined by plotting the capacitive current vs. the scan rate in a linear potential sweep test, such as CV.[38] The capacitive current, i_c (A), is known to vary linearly with respect to scan rate, v (V s^{-1}) (Eq. 4.1).[41]

$$|i_c| = AC_d v \qquad \text{(Eq. 4.1)}$$

To measure the non-faradaic current, the test is conducted in a supporting electrolyte solution in the absence of any electrochemically active species. The produced current is a result of the formation of the electric double layer at the electrode surface. Figures 4.9.A-C show the large

increase in non-faradaic current with respect to the scan rate for A) a planar ITO electrode, B) a meso-ITO electrode, and C) a macro-ITO electrode. A dramatic increase is shown in the magnitude of current for the porous electrodes in Figures 4.9.B and 4.9.C. The current at various scan rates was then plotted, and the slope was used to determine the ECSAF. In Figure 4.9.D, the ECSAF was determined for the meso- and macro-ITO electrodes by normalizing their slopes to that found for the planar electrode, which was taken to have an area equivalent to the geometric surface area and was thus assigned an ECSAF of one. After multiplying the respective ECSAF by the known surface area of the planar electrode (0.708 cm^2), we approximated that the meso-ITO electrodes had an active surface area of 139 ± 5 cm^2, while the macro-ITO electrodes had a much greater active surface area of 285 ± 5 cm^2. The increased active surface area in the macro-ITO electrodes is due to the decrease in nanoparticle packing efficiency on the polystyrene template, which resulted in a hierarchical porous structure and an increase in electrode thickness.

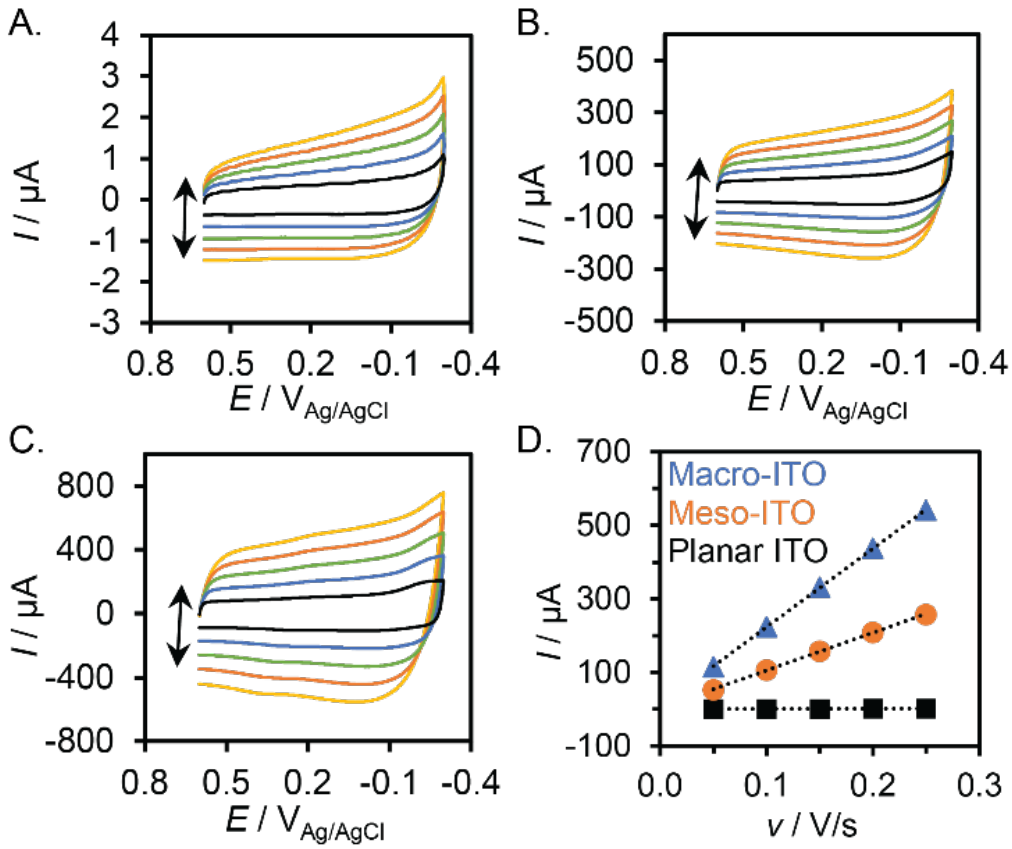

Figure 4.9. *Cyclic voltammetry (CV) scans of (A) planar ITO, (B) meso-ITO and (C) macro-ITO electrodes in an aqueous solution of 0.5 M KCl at increasing scan rates (50, 100, 150, 200, 250 mV s^{-1}, black to yellow respectively). (D) Scan rate (V s^{-1}) plotted against the current response (µA) at 0.0 V vs Ag/AgCl (Square = planar ITO, circle = meso-ITO and triangle = macro-ITO) with n = 10. From the capacitive charging current at 0.0 V vs Ag/AgCl for various scan rates, the value of AC_D can be extracted from the slopes of the linear fits shown in panel D. The slope for meso- and macro-ITO is then divided by the slope for a planar electrode that has a known surface area of 0.708 cm^2. The ratio of the slopes is the ECSAF and the respective ECSAFs can then be multiplied by the known surface area of the planar electrode to find the active surface area. Meso- and macro-ITO electrodes were found to have an active surface area of 139 ±5 cm^2 and 285 ±5 cm^2, respectively.*[39,40]

PSI was introduced into the porous electrodes via sequential drop-casting of 13.2 µg cm^{-2} PSI under low pressure until the desired mass loading was obtained. Transmission-absorbance spectroscopy was used to characterize the ability of the prepared electrodes to transmit light within the absorption region of PSI. PSI absorbs strongly at wavelengths of 680 and 450 nm.[42] Figures 4.10.A and 4.10.B show transmission spectra for planar ITO-coated glass, meso-ITO, and macro-

ITO, without and with PSI, respectively. As seen in Figure 4.10.A, the planar and meso-ITO electrodes without PSI show high transmission. In the macro-ITO electrodes, much of the transmission is lost to scattering. In Figure 4.10.B the characteristic absorption peak of PSI at 680 nm is clearly distinguishable in each electrode morphology; this peak is evidence that PSI is present and active.

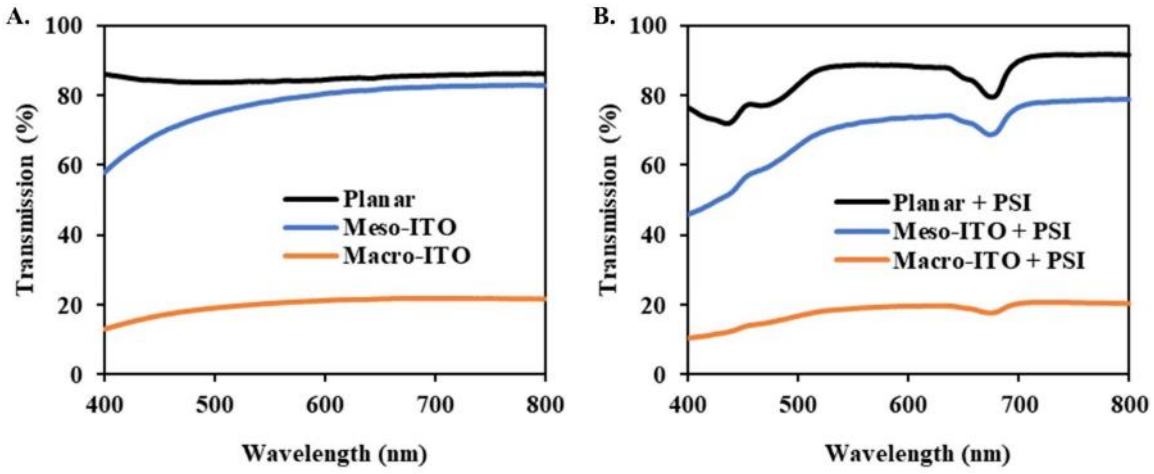

Figure 4.10. *Transmission of (A) planar, meso-, and macro-ITO electrodes without PSI. (B) Planar, meso-, and macro-ITO spectra with 53 μg cm^{-2} PSI. A characteristic absorbance peak for PSI can be seen in panel B at 680 nm in each spectrum, verifying that PSI is present and absorbing light.*

The location of PSI protein complexes was investigated using energy dispersive spectroscopy (EDS). Figure 4.11 shows a cross-sectional scanning electron micrograph (SEM) of a meso-ITO electrode with 52 μg cm^{-2} of PSI deposited. To the right of the electron micrograph are EDS maps for indium (In), tin (Sn), oxygen (O), silicon (Si), carbon (C), and a composite map. The indium, tin and oxygen are found in the ITO electrode. The silicon and additional oxygen compromise the glass substrate. The carbon-rich layer in the upper ~1 μm of the meso-ITO electrode is attributed to the deposited PSI protein complexes. The presence of this carbon-rich layer indicates that agglomeration or pore blockage prevents PSI from fully penetrating the meso-ITO electrodes.

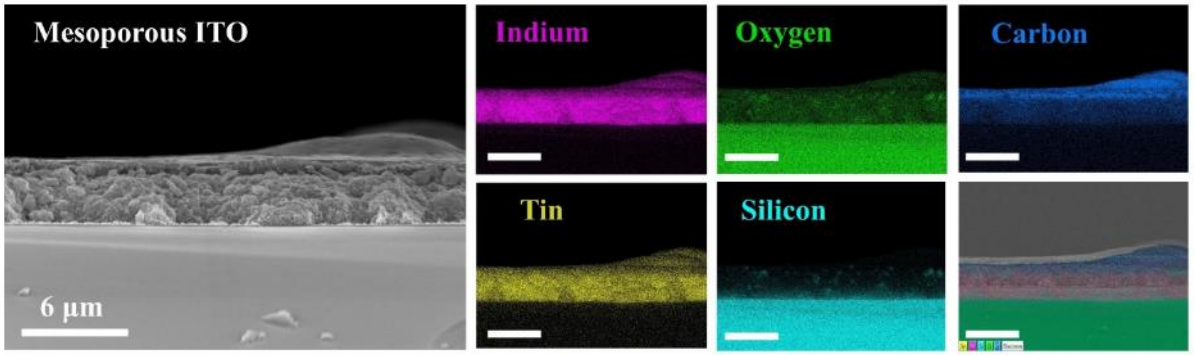

Figure 4.11. *Energy dispersive spectroscopy (EDS) mapping of a meso-ITO electrode with 53 µg cm^{-2} of PSI protein complexes deposited. Left: scanning electron micrograph (SEM). Right: EDS maps for indium (In), tin (Sn), oxygen (O), silicon (Si), carbon (C), and a composite map.*

Figure 4.12 shows a cross-sectional scanning electron micrograph (SEM) of a macro-ITO electrode with 53 µg cm^{-2} of PSI deposited. To the right of the electron micrograph are EDS maps for indium (In), tin (Sn), oxygen (O), silicon (Si), carbon (C), and a composite map. The carbon EDS map of the macro-ITO electrode with 52 µg cm^{-2} of PSI did not reveal a carbon-rich area stratified near the upper region of the electrode. Instead, the carbon is uniformly distributed throughout the porous structure, with the exception of the intrapore connections. We hypothesize that this carbon signal is because the PSI multilayers are deposited onto the inner surface of the macropores. These results suggest that, within the macro-ITO electrodes, PSI multilayers assemble along the macropore surface, allowing a greater PSI mass loading without blocking intrapore connections.

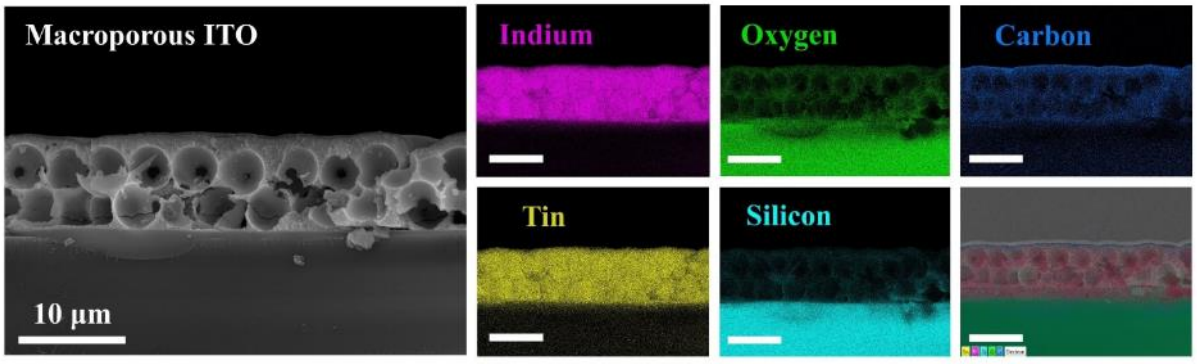

Figure 4.12. *Energy dispersive spectroscopy (EDS) mapping of a macro-ITO electrode with 53 µg cm^{-2} of PSI protein complexes deposited. Left: scanning electron micrograph (SEM). Right: EDS maps for indium (In), tin (Sn), oxygen (O), silicon (Si), carbon (C), and a composite map.*

The photoelectrochemical performance of the cathodes was studied using photochronoamperometry in the 1:5 DCPIP:AscH mediator (Figure 4.13). Both meso- and macro-ITO cathodes improve the produced photocurrent measured at the dark OCP. The cathodes were tested at the dark OCP to eliminate any current driven by external forces such as an applied overpotential. The macro-ITO cathodes achieve a peak cathodic photocurrent of 42 ± 5 μA cm^{-2}, the meso-ITO yield 11 ± 1 μA cm^{-2}, and the planar ITO provides 1 ± 1 μA cm^{-2} at a PSI loading of 66 μg cm^{-2}. The dashed photochronoamperometry curves in Figure 4.13, taken with a stirred electrolyte, show that a steady-state photocurrent can be achieved when the mass transport limitations within the bulk solution are eliminated. This result shows that intrapore diffusion is not the cause of the large diffusional loss.

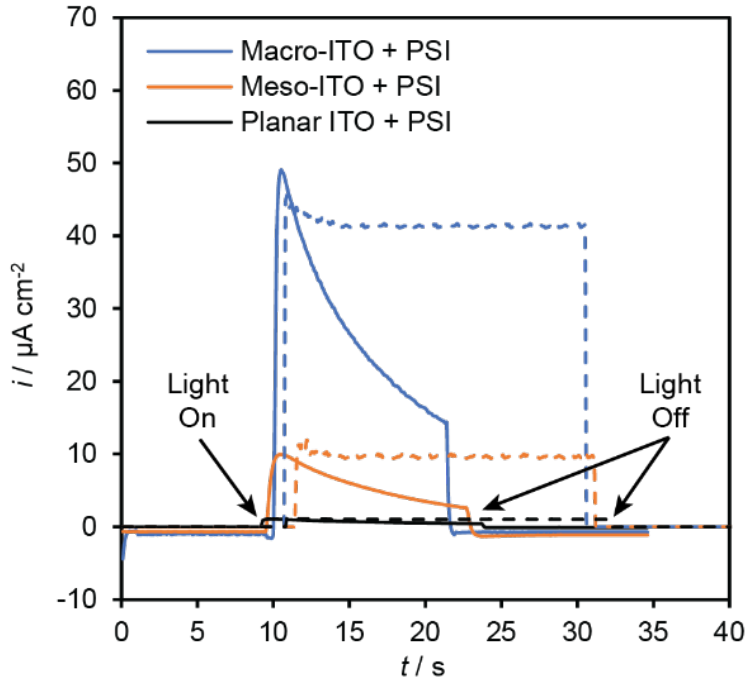

Figure 4.13. *Photochronoamperometric scans of PSI-modified (66 μg cm^{-2} PSI loading) macro-, meso- and planar ITO cathodes in an aqueous solution of 1 mM DCPIP, 5 mM AscH and 100 mM KCl. Dashed lines indicate stirring of the solution. Samples were illuminated under a 100 mW cm^{-2} white light source for a variable amount of time and the ITO electrodes were held at the dark open circuit potential (OCP).*

We also tested porous PSI-ITO cathodes with pore sizes of 500 nm because similar pore sizes have been shown to be optimal for photocurrent generation by PSI and cyt c.[7] However, the

500 nm pore cathodes produced photocurrent values lower than the meso-ITO (Figure 4.14). We attribute the low value for the 500 nm pore size to the need for additional fabrication and deposition optimization and suspect that the optimum value would fall between that of meso-ITO and macro-ITO The achieved photocurrent for macro-ITO is high in comparison to other PSI multilayer studies on metal and metal-like substrates and shows that MET within translucent and porous ITO electrodes can improve PSI-based photoelectrochemical cells.[20, 33]

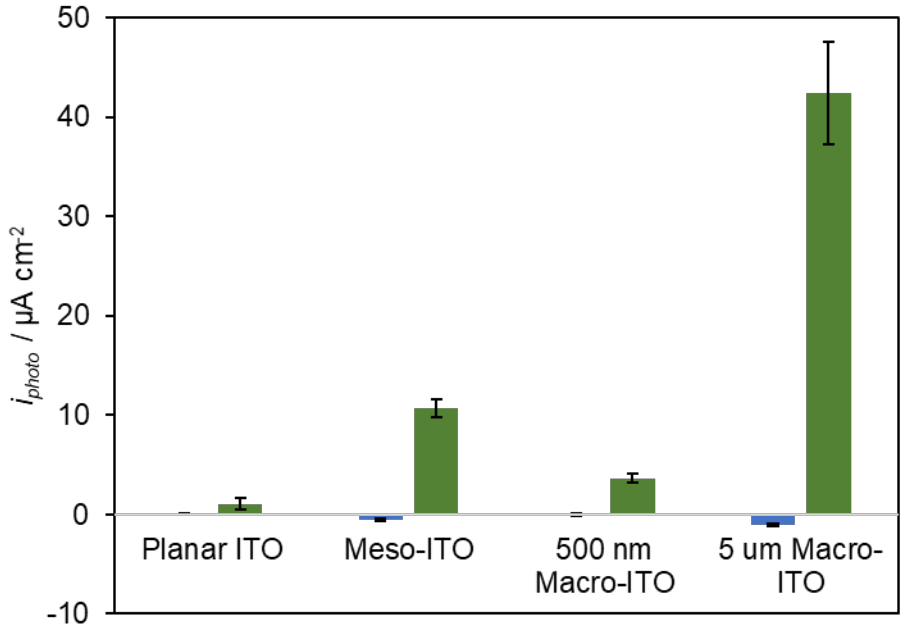

Figure 4.14. *Data from photochronoamperometric scans of meso-ITO, 500 nm pore size macro-ITO, and 5 µm macro-ITO with 0 µg cm^{-2} PSI (blue) and with 66 µg cm^{-2} PSI (green). The photocurrents are normalized to geometric surface area and were taken in a 100 mM KCl, 1 mM DCPIP and 5 mM AscH electrolyte using a 100 mW cm^{-2} white light source. Note that n=3 for the 500 nm Macro-ITO while n=10 for all other data points.*

Geometric surface area is crucial to the practicality of photovoltaics because it is used to determine the footprint area needed to produce a specific amount of power. The areal loading of PSI per geometric surface area is also known to greatly influence PSI biohybrid electrode performance. By incorporating a greater quantity of PSI protein complexes, the concentration of the reacted mediator is increased locally, resulting in a greater photocurrent.[4, 24, 43] Figure 4.15 shows that increasing the PSI loading in the fabricated cathodes increases the produced

photocurrent until a saturation point is reached, as denoted by asterisks. The macro-ITO cathodes yield the highest saturation point between 53 and 79 μg cm^{-2} of PSI. The meso-ITO cathodes become saturated between 40 and 66 μg cm^{-2}, and the planar ITO cathodes show the lowest saturation point between 26 and 53 μg cm^{-2}. At the saturation loading of the macro-ITO cathodes, the macro-ITO produces 3 times more photocurrent than the meso-ITO and 40 times more than the planar ITO. The cause of this protein saturation point can be attributed to both the absorption of usable radiation and the total pore volume available for PSI protein complexes.

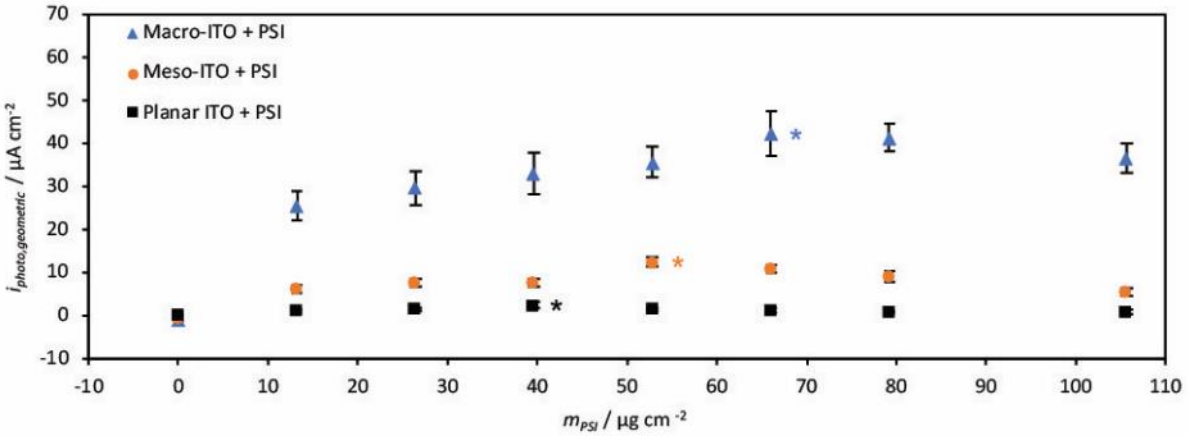

Figure 4.15. *Summary of photocurrent production as a function of PSI mass loading on ITO electrodes in the presence of a 1 mM DCPIP, 5 mM AscH, and 100 mM KCl electrolyte. Asterisks denote the maximum photocurrent achieved for an electrode morphology (planar, meso-, or macro-ITO). Samples were illuminated using a 100 mW cm^{-2} white light source and the ITO electrodes were held at the dark open circuit potential (OCP) (n = 10).*

The rate of faradaic reactions, involving charge transfer between electrochemically active species and the electrode, increases linearly with respect to active surface area.[41] Therefore, by increasing the active surface area, an increase in photocurrent should follow. To analyze how well the meso- and macro-ITO cathodes utilize their respective increase in active surface area, we defined a photocurrent factor (PCF) to be compared to the ECSAF. The PCF is simply the photocurrent produced by either the meso- or macro-ITO cathodes divided by the photocurrent produced by the planar ITO cathode at the same PSI mass loading. The ECSAFs of the meso-ITO and the 5 μm macro-ITO were determined to be 197 ± 7 and 406 ± 6, respectively. In an ideal system the PCF would be equal to the ECSAF, and the cathode would then achieve a 100% usage

of available active surface area. We found that, on average, the meso-ITO cathodes utilized 3.8 ± 1.3 % of the total active surface area and the macro-ITO utilized 7.9 ± 3.3 %. Below an example calculation is provided for the meso- and macro-ITO cathodes at a PSI mass loading of 66 µg cm^{-2}. The standard deviation was carried through the calculation as a standard error to determine the final error in the calculated active surface area utilization value. The active surface area utilized during photocurrent production by the macro-ITO cathodes was over double that of the meso-ITO cathodes for all PSI mass loadings. This result conveys that the increase in active surface area is not the only factor involved in the increase in mediated photocurrent achieved with the macro-ITO cathodes.

Meso-ITO with 66 µg cm^{-2} PSI mass loading:

$$PCF_{meso} = \frac{i_{meso}}{i_{planar}} = \frac{10.69\ \mu A\ cm^{-2}}{1.09\ \mu A\ cm^{-2}} = 9.83$$

$$Mesoporous\ ITO\ Active\ Surface\ Area\ Utilization = \frac{PCF_{meso}}{ECSAF_{meso}} = \frac{9.83}{196.8} = 0.050 = 5.0\%$$

Macro-ITO with 66 µg cm^{-2} PSI mass loading:

$$PCF_{macro} = \frac{i_{macro}}{i_{planar}} = \frac{42.39\ \mu A\ cm^{-2}}{1.09\ \mu A\ cm^{-2}} = 38.97$$

$$Macroporous\ ITO\ Active\ Surface\ Area\ Utilization = \frac{PCF_{macro}}{ECSAF_{macro}} = \frac{38.97}{405.6} = 0.096 = 9.6\%$$

Conclusions

The macro-ITO electrodes fabricated in this study increase the photocurrent produced by PSI multilayers via MET using a DCPIP and AscH mediator from 11± 1 μA cm^{-2} in meso-ITO to 42 ± 5 μA cm^{-2} in macro-ITO. We determined that the increase in active surface area was not the sole contributor to the increase in photocurrent between the meso- and macro-ITO morphologies. PSI-modified macro-ITO cathodes were capable of utilizing double the available active surface area, when compared to meso-ITO cathodes with the same PSI mass loading. Our findings show that if MET alone is considered, 5 μm pores outperformed their mesoporous ITO equivalent, while other studies that report a DET-based mechanism find that pores on the scale of hundreds of nanometers are optimal.[7] We conclude that this difference in findings is due to the difference between the electron transfer pathways. In future studies, an MET approach could be incorporated in conjunction with DET strategies to further improve photocurrent within porous ITO architectures.

We conclude that the geometry of the hierarchical pore structure and the location of the PSI protein complexes allow for higher loadings of PSI to further increase the photocurrent in the macro-ITO electrodes. PSI multilayers adhered to the inner walls of the macropores produce converted mediator, which can then react at both the pore wall under the multilayer and also diffuse through the pore to all other areas of the pore wall. Within meso-ITO, the PSI multilayers are concentrated near the electrode/bulk electrolyte interface (Figure 4.11), and therefore, reacted mediator can escape into the bulk solution more easily than in macro-ITO pores, decreasing the maximum achievable photocurrent through MET and resulting in less efficient use of the active electrode surface area. Our findings show that hierarchical pore structures on the micrometer scale are advantageous in comparison to smaller pore sizes for MET within PSI multilayers, due to an increase in PSI loading and higher concentration of converted mediator reaching the active electrode surface.

References

1. Wolfe, K. D.; Dervishogullari, D.; Stachurski, C. D.; Passantino, J. M.; Kane Jennings, G.; Cliffel, D. E., Photosystem I Multilayers within Porous Indium Tin Oxide Cathodes Enhance Mediated Electron Transfer. *ChemElectroChem* **2020,** *7* (3), 596-603.

2. Friebe, V. M.; Frese, R. N., Photosynthetic reaction center-based biophotovoltaics. *Curr. Opin. Electrochem.* **2017,** *5*, 126-134.

3. Nguyen, K.; Bruce, B. D., Growing green electricity: Progress and strategies for use of Photosystem I for sustainable photovoltaic energy conversion. *Biochim. Biophys. Acta Bioenerg.* **2014,** *1837*, 1553-1566.

4. Robinson, M. T.; Gizzie, E. A.; Mwambutsa, F.; Cliffel, D. E.; Jennings, G. K., Mediated approaches to Photosystem I-based biophotovoltaics. *Curr. Opin. Electrochem.* **2017,** *5*, 211-217.

5. Wolfe, K. D.; Dervishogullari, D.; Passantino, J. M.; Stachurski, C. D.; Jennings, G. K.; Cliffel, D. E., Improving the stability of photosystem I–based bioelectrodes for solar energy conversion. *Curr. Opin. Electrochem.* **2020,** *19*, 27-34.

6. Habermüller, K.; Mosbach, M.; Schuhmann, W., Electron-transfer mechanisms in amperometric biosensors. *Fresenius J. Anal. Chem.* **2000,** *366*, 560-568.

7. Ciornii, D.; Kölsch, A.; Zouni, A.; Lisdat, F., A precursor-approach in constructing 3D ITO electrodes for the improved performance of photosystem I-cyt c photobioelectrodes. *Nanoscale* **2019**.

8. Olmos, J. D. J.; Becquet, P.; Gront, D.; Sar, J.; Dąbrowski, A.; Gawlik, G.; Teodorczyk, M.; Pawlak, D.; Kargul, J., Biofunctionalisation of p-doped silicon with cytochrome c553 minimises charge recombination and enhances photovoltaic performance of the all-solid-state photosystem I-based biophotoelectrode. *RSC Advances* **2017,** *7*, 47854-47866.

9. Kiliszek, M.; Harputlu, E.; Szalkowski, M.; Kowalska, D.; Unlu, C. G.; Haniewicz, P.; Abram, M.; Wiwatowski, K.; Niedziółka-Jönsson, J.; MaćKowski, S.; Ocakoglu, K.; Kargul, J., Orientation of photosystem i on graphene through cytochrome: C 553 leads to improvement in photocurrent generation. *J. Mater. Chem. A* **2018,** *6*, 18615-18626.

10. Mayoral, T.; Martínez-Júlvez, M.; Pérez-Dorado, I.; Sanz-Aparicio, J.; Gómez-Moreno, C.; Medina, M.; Hermoso, J. A., Structural analysis of interactions for complex formation between Ferredoxin-NADP+ reductase and its protein partners. *Proteins: Structure, Function, and Bioinformatics* **2005,** *59*, 592-602.

11. Stieger, K. R.; Feifel, S. C.; Lokstein, H.; Hejazi, M.; Zouni, A.; Lisdat, F., Biohybrid architectures for efficient light-to-current conversion based on photosystem i within scalable 3D mesoporous electrodes. *J. Mater. Chem. A* **2016,** *4*, 17009-17017.

12. Friebe, V. M.; Millo, D.; Swainsbury, D. J. K.; Jones, M. R.; Frese, R. N., Cytochrome c Provides an Electron-Funneling Antenna for Efficient Photocurrent Generation in a Reaction Center Biophotocathode. *ACS Appl. Mater. Interfaces* **2017,** *9* (28), 23379-23388.

13. Feifel, S. C.; Stieger, K. R.; Hejazi, M.; Wang, X.; Ilbert, M.; Zouni, A.; Lojou, E.; Lisdat, F., Dihemic c4-type cytochrome acting as a surrogate electron conduit: Artificially interconnecting a photosystem I supercomplex with electrodes. *Electrochem. Commun.* **2018,** *91*, 49-53.

14. Stieger, K. R.; Ciornii, D.; Kölsch, A.; Hejazi, M.; Lokstein, H.; Feifel, S. C.; Zouni, A.; Lisdat, F., Engineering of supramolecular photoactive protein architectures: the defined co-assembly of photosystem I and cytochrome c using a nanoscaled DNA-matrix. *Nanoscale* **2016,** *8*, 10695-10705.

15. Stieger, K. R.; Feifel, S. C.; Lokstein, H.; Lisdat, F., Advanced unidirectional photocurrent generation via cytochrome c as reaction partner for directed assembly of photosystem I. *Phys. Chem. Chem. Phys.* **2014,** *16*, 15667-15674.

16. Kölsch, A.; Hejazi, M.; Stieger, K. R.; Feifel, S. C.; Kern, J. F.; Müh, F.; Lisdat, F.; Lokstein, H.; Zouni, A., Insights into the binding behavior of native and non-native cytochromes to photosystem I from Thermosynechococcus elongatus. *J. Biol. Chem.* **2018,** *293*, 9090-9100.

17. Efrati, A.; Tel-Vered, R.; Michaeli, D.; Nechushtai, R.; Willner, I., Cytochrome c-coupled photosystem I and photosystem II (PSI/PSII) photo-bioelectrochemical cells. *Energy Environ. Sci.* **2013,** *6*, 2950-2956.

18. Lopez-Martinez, M.; Lopez-Ortiz, M.; Antinori, M. E.; Wientjes, E.; Nin-Hill, A.; Rovira, C.; Croce, R.; Diez-Perez, I.; Gorostiza, P., Electrochemically Gated Long-Distance Charge Transport in Photosystem I. *Angew. Chem. Int. Ed.* **2019,** *58* (38), 13280-13284.

19. LeBlanc, G.; Chen, G.; Gizzie, E. A.; Jennings, G. K.; Cliffel, D. E., Enhanced Photocurrents of Photosystem I Films on p-Doped Silicon. *Adv. Mater.* **2012,** *24*, 5959-5962.

20. Yang, S.; Robinson, M. T.; Mwambutsa, F.; Cliffel, D. E.; Jennings, G. K., Effect of Cross-linking on the Performance and Stability of Photocatalytic Photosystem I Films. *Electrochim. Acta* **2016,** *222*, 926-932.

21. Gunther, D.; LeBlanc, G.; Prasai, D.; Zhang, J. R.; Cliffel, D. E.; Bolotin, K. I.; Jennings, G. K., Photosystem I on Graphene as a Highly Transparent, Photoactive Electrode. *Langmuir* **2013,** *29*, 4177-4180.

22. Ciesielski, P. N.; Faulkner, C. J.; Irwin, M. T.; Gregory, J. M.; Tolk, N. H.; Cliffel, D. E.; Jennings, G. K., Enhanced Photocurrent Production by Photosystem I Multilayer Assemblies. *Adv. Funct. Mater.* **2010,** *20*, 4048-4054.

23. Passantino, J. M.; Wolfe, K. D.; Simon, K. T.; Cliffel, D. E.; Jennings, G. K., Photosystem I Enhances the Efficiency of a Natural, Gel-Based Dye-Sensitized Solar Cell. *ACS Appl. Bio. Mater.* **2020**.

24. Buesen, D.; Hoefer, T.; Zhang, H.; Plumeré, N., A kinetic model for redox-active film based biophotoelectrodes. *Faraday Discuss.* **2019,** *215*, 39-53.

25. Robinson, M. T.; Cliffel, D. E.; Jennings, G. K., An Electrochemical Reaction-Diffusion Model of the Photocatalytic Effect of Photosystem I Multilayer Films. *J. Phys. Chem. B* **2018,** *122* (1), 117-125.

26. Morlock, S.; Subramanian, S. K.; Zouni, A.; Lisdat, F., Scalable Three-Dimensional Photobioelectrodes Made of Reduced Graphene Oxide Combined with Photosystem I. *ACS Appl. Mater. Interfaces* **2021,** *13* (9), 11237-11246.

27. Ciesielski, P. N.; Scott, A. M.; Faulkner, C. J.; Berron, B. J.; Cliffel, D. E.; Jennings, G. K., Functionalized Nanoporous Gold Leaf Electrode Films for the Immobilization of Photosystem I. *ACS Nano* **2008,** *2*, 2465-2472.

28. Wenzel, T.; Härtter, D.; Bombelli, P.; Howe, C. J.; Steiner, U., Porous translucent electrodes enhance current generation from photosynthetic biofilms. *Nature Comm.* **2018,** *9*, 1299.

29. Ciornii, D.; Riedel, M.; Stieger, K. R.; Feifel, S. C.; Hejazi, M.; Lokstein, H.; Zouni, A.; Lisdat, F., Bioelectronic Circuit on a 3D Electrode Architecture: Enzymatic Catalysis Interconnected with Photosystem I. *J. Am. Chem. Soc.* **2017,** *139* (46), 16478-16481.

30. Terasaki, N.; Yamamoto, N.; Hiraga, T.; Sato, I.; Inoue, Y.; Yamada, S., Fabrication of novel photosystem I–gold nanoparticle hybrids and their photocurrent enhancement. *Thin Solid Films* **2006,** *499*, 153-156.

31. Mershin, A.; Matsumoto, K.; Kaiser, L.; Yu, D.; Vaughn, M.; Nazeeruddin, M. K.; Bruce, B. D.; Graetzel, M.; Zhang, S., Self-assembled photosystem-I biophotovoltaics on nanostructured TiO2 and ZnO. *Scientific Reports* **2012,** *2*, 234.

32. Trammell, S. A.; Spano, A.; Price, R.; Lebedev, N., Effect of protein orientation on electron transfer between photosynthetic reaction centers and carbon electrodes. *Biosens. Bioelectron.* **2006,** *21* (7), 1023-1028.

33. Ciesielski, P. N.; Hijazi, F. M.; Scott, A. M.; Faulkner, C. J.; Beard, L.; Emmett, K.; Rosenthal, S. J.; Cliffel, D.; Kane Jennings, G., Photosystem I – Based biohybrid photoelectrochemical cells. *Bioresour. Technol.* **2010,** *101*, 3047-3053.

34. Chen, G.; LeBlanc, G.; Jennings, G. K.; Cliffel, D. E., Effect of Redox Mediator on the Photo-Induced Current of a Photosystem I Modified Electrode. *J. Electrochem. Soc.* **2013,** *160* (6), H315-H320.

35. Petrova, A.; Mamedov, M.; Ivanov, B.; Semenov, A.; Kozuleva, M., Effect of artificial redox mediators on the photoinduced oxygen reduction by photosystem I complexes. *Photosynth. Res.* **2018,** *137*, 421-429.

36. Washko, P. W.; Welch, R. W.; Dhariwal, K. R.; Wang, Y. H.; Levine, M., Ascorbic-Acid and Dehydroascorbic Acid Analyses in Biological Samples. *Anal. Biochem.* **1992,** *204* (1), 1-14.

37. Amunts, A.; Toporik, H.; Borovikova, A.; Nelson, N., Structure determination and improved model of plant photosystem I. *J. Bio. Chem.* **2010,** *285*, 3478-3486.

38. Voiry, D.; Chhowalla, M.; Gogotsi, Y.; Kotov, N. A.; Li, Y.; Penner, R. M.; Schaak, R. E.; Weiss, P. S., Best Practices for Reporting Electrocatalytic Performance of Nanomaterials. *ACS Nano* **2018,** *12*, 9635-9638.

39. González, G. B.; Cohen, J. B.; Hwang, J.-H.; Mason, T. O.; Hodges, J. P.; Jorgensen, J. D., Neutron diffraction study on the defect structure of indium–tin–oxide. *J. Appl. Phys.* **2001,** *89*, 2550-2555.

40. Thirumoorthi, M.; Thomas Joseph Prakash, J., Structure, optical and electrical properties of indium tin oxide ultra thin films prepared by jet nebulizer spray pyrolysis technique. *Journal of Asian Ceramic Societies* **2016,** *4*, 124-132.

41. Bard, A. J., Electrochemical methods : fundamentals and applications / Allen J. Bard, Larry R. Faulkner. Wiley: New York, New York. **1980**.

42. Laisk, A.; Oja, V.; Eichelmann, H.; Dall'Osto, L., Action spectra of photosystems II and I and quantum yield of photosynthesis in leaves in State 1. *Biochim. Biophys. Acta Bioenerg.* **2014,** *1837*, 315-325.

43. Robinson, M. T.; Armbruster, M. E.; Gargye, A.; Cliffel, D. E.; Jennings, G. K., Photosystem I Multilayer Films for Photovoltage Enhancement in Natural Dye-Sensitized Solar Cells. *ACS Appl. Energy Mater.* **2018,** *1*, 301-305.

Chapter 5 – Stromal Side-Selective Modification of Photosystem I

The initial inspiration and preliminary studies for the work presented in this chapter were provided by Dr. Evan Gizzie and Carson J. Bryant. The findings reported herein are based on data produced by the author (Kody D. Wolfe) and thanks are given to Dr. Dilek Dervishogullari, Joshua M. Passantino, and Dr. Christopher D. Stachurski for collaborative discussion, manuscript editing, and general assistance. Funding for the following work was provided by the National Science Foundation (DMR-1507505) and the United States Department of Agriculture (2019-67021-29857).

Introduction

A major challenge in advancing the performance of PSI-electrode interfaces is the random orientation of the protein after it has been removed from the thylakoid membrane and deposited onto a surface.[1-4] In the thylakoid membrane, the PSI protein complex is naturally oriented with the stromal side facing outward (see Figure 5.1.A).[5-7] The directional nature of the exciton along with the physical separation of the lumenal and stromal fluids by the thylakoid membrane results in highly efficient electron transfer *in vivo*.[8] However, during the extraction of PSI, the thylakoid membrane is lysed and regaining control over the orientation becomes challenging for various reasons. One issue is the similarity between the functional groups on the stromal and lumenal faces of the protein complex. For example, Figures 5.1.A and 5.1.B show the distribution of primary amines on the surface of PSI. Although the stromal side contains a greater number of surface amines, the presence of the same functional groups on both faces makes orientation specific deposition difficult.

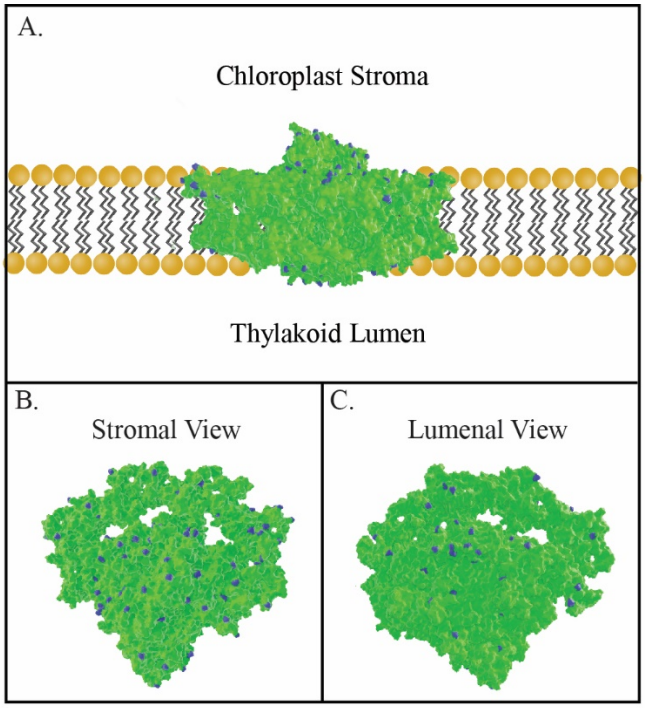

Figure 5.1. *Schematic illustrations of PSI with primary amines labeled blue. A.) PSI in the thylakoid membrane. B.) A stromal view of PSI (top-down view compared to panel A). C.) Lumenal view of PSI (bottom-up view compared to panel A). Structure recreated from data reported by Amunts et al.*[5]

Random orientation is problematic because maximizing performance of PSI monolayers requires both directional orientation of PSI protein complexes upon deposition onto the electrode and efficient transfer of the electrons from PSI to the electrode. Direct electron transfer (DET) from PSI to the electrode via electron tunneling is the preferred electron transfer mechanism as it is fast and is not limited by diffusion of solubilized species between the reaction center and electrode.[9] However, DET is difficult to achieve due to the close proximity necessary for electron tunneling. Lopez-Martinez et al. reported that a distance of approximately 1 nm is needed for efficient electron tunneling at the P_{700} site, determined via electrochemical scanning tunneling microscopy.[10] The tunneling distance creates technical challenges when considering the orientation of a large protein complex such as PSI that has dimensions on the order of 10-20 nm. The issue is further exacerbated by P_{700} being contained within a lumenal pocket, making it very difficult to interact directly with an electrode without modification.[5] Alternatively, mediated

electron transfer (MET) is more often observed in PSI-based biohybrid photovoltaics.[11-13] MET can be achieved through the introduction of electrochemical mediators and greatly enhances charge transfer in multilayer PSI assemblies by leveraging diffusion of the molecules to reach PSI's reaction sites.[11, 14]

The issue of PSI orientation has been previously studied with success utilizing bio-conjugation strategies and electrostatic interactions.[15-22] Recently, Zhao et al. fabricated unidirectional PSI monolayers on osmium-containing polymer coated gold substrates through formation of monolayers at a water-air interface and depositing the monolayers via Langmuir-Blodgett techniques.[21] Many reports have also shown enhancements in electron transfer through the use of the cytochrome complex (cyt c) as a linking agent.[19, 21-30] Cyt c binds to PSI and can provide an electron conduit between PSI's P_{700} reaction center and the underlying electrode.[22] While cyt c provides a great enhancement in observed electron transfer rates, one concern regarding the use of cyt c to promote PSI orientation is that non-native cyt c relies solely on electrostatic interactions between the lumenal side of PSI and cyt c.[22] More direct approaches toward PSI orientation have been investigated, including the preparation of genetically modified PSI mutants that express cysteine residues near the P_{700} site.[31] The cysteine mutants were used to attach the PSI onto gold electrodes, but a great enhancement in photocurrent was not reported. The need for a simple and highly efficient means of simultaneously achieving PSI orientation and enhanced connectivity to the substrate electrode warrants further research in PSI modification strategies.

Herein, a solution-based modification strategy, implemented during the extraction of PSI from spinach, is highlighted as a facile and scalable method for modifying PSI protein complexes and preparing monolayer films. Amines located on stromal-side lysine residues of the protein complex are targeted as reactive centers for modification during extraction.[5, 32] The modification is performed during the PSI extraction, after the cell membrane has been mechanically broken but before the thylakoid membrane is lysed, resulting in selective reaction with stromal side amines. A schematic of the extraction procedure, also shown in Appendix A and adapted from Reeves and Hall, Shiozawa et al., Millsaps et al., and Baba et al., with the modification step shown is given in Figure 5.2.[33-36]

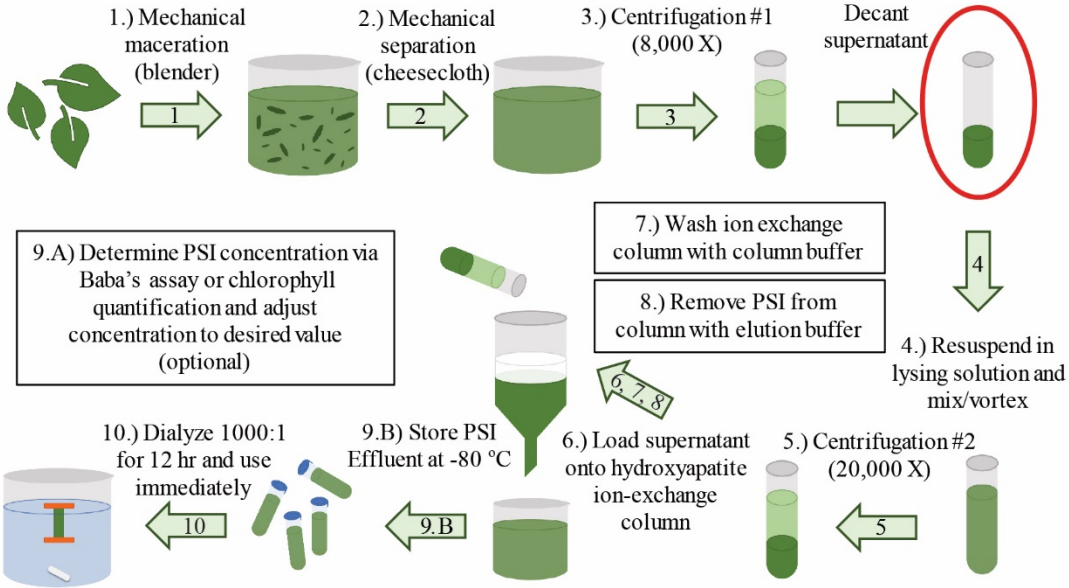

Figure 5.2. *PSI extraction procedure (also described in Appendix A) with the stromal side amine modification step circled in red.*

A general schematic of the PSI extraction step during which the thylakoid membrane is intact and only stromal side amines are exposed is shown in Figure 5.3. The side-selective reaction scheme can be tailored to use various amine reactive molecules to achieve novel surface functionalities on the stromal side of PSI. The resulting modified PSI complexes are then used to obtain oriented monolayer films.

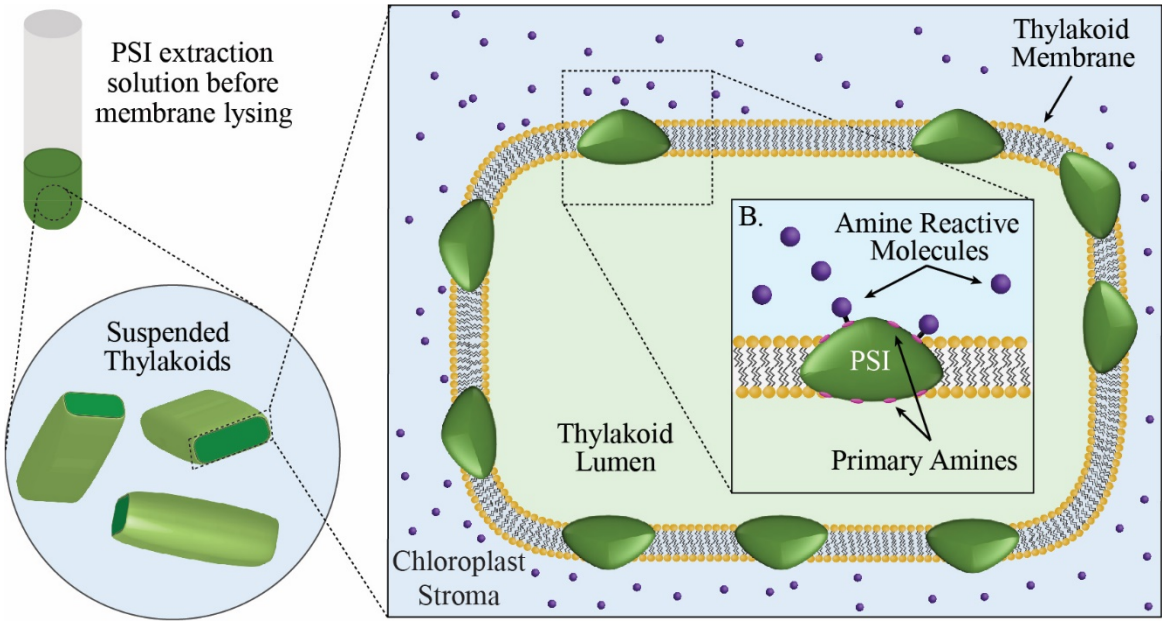

Figure 5.3. *A general stromal-side modification scheme for PSI complexes within the thylakoid membrane. At this step in the extraction procedure thylakoids are suspended in solution and amine reactive molecules are introduced. The thylakoid membrane acts as a physical barrier, resulting in reaction with only stromal-side primary amines exposed to the solution.*

The substrate, in conjunction with the newly introduced functional groups, determines the preferred orientation of the protein complex during a solution-based deposition. In this study we compare PSI-modified with 2-iminothiolane, or Traut's Reagent, (T-PSI) and an NHS-Ester PEG (P-PSI). The reaction schemes resulting in T-PSI and P-PSI are given in Figure 5.4.A & 5.4.B, respectively.

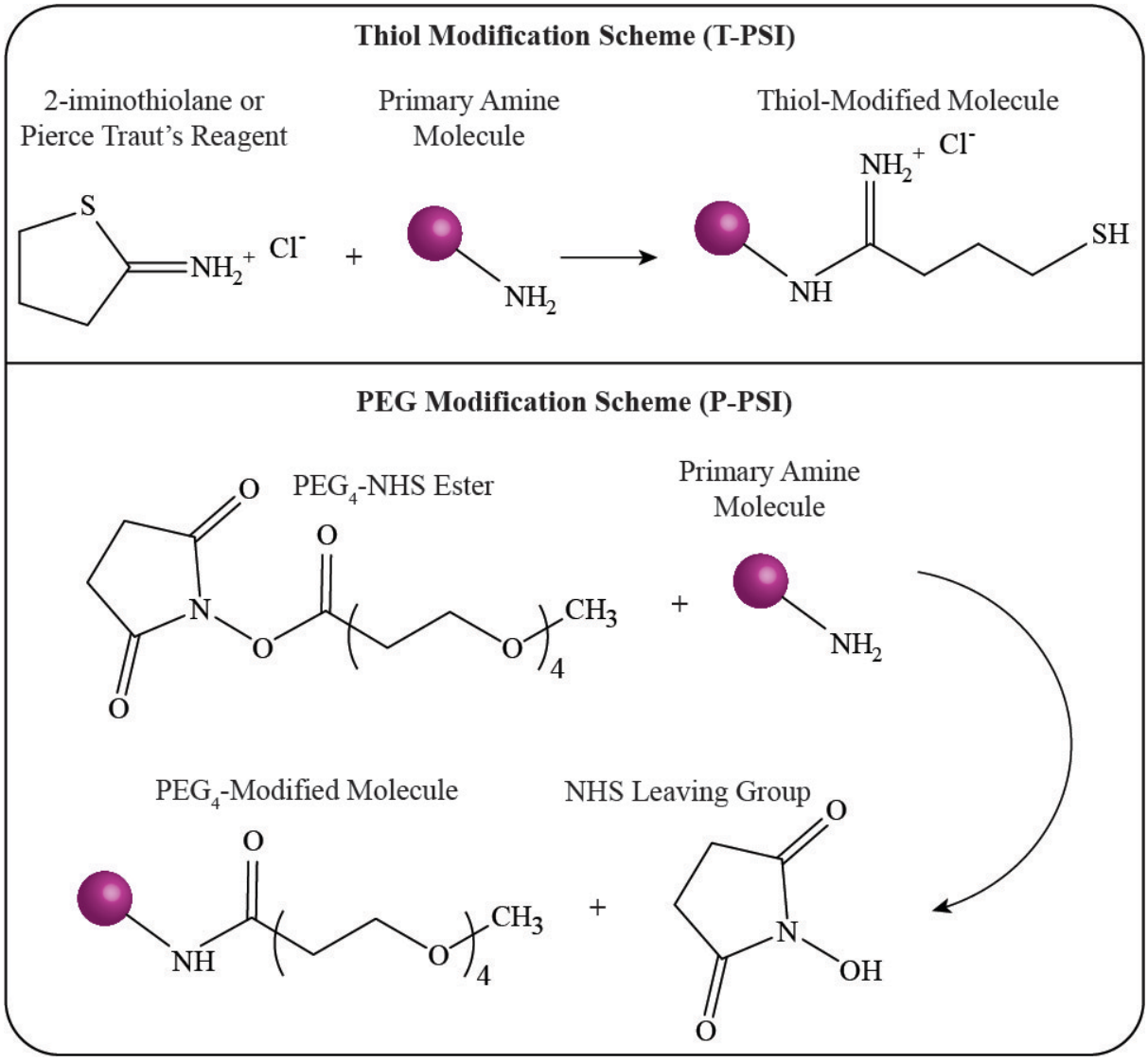

Figure 5.4. *Reaction schemes for PSI modification including A.) a thiol modification scheme using 2-iminothiolane and B.) a polyethylene glycol (PEG) modification scheme utilizing a PEG_4-NHS ester.*

The newly introduced functional groups are hypothesized to interact with a gold electrode, resulting in opposite PSI orientations. As seen in Figure 5.5.A, PSI with stromal-side thiol functionality (T-PSI) will orient itself with the stromal side nearest the gold substrate, subsequently referred to as downward, due to the strong thiol-gold affinity.[31] PSI with stromal-side PEG functionality (P-PSI) will preferentially orient upward because the net neutral charge and hydrophilic screening of the PEG chains prevents the stromal side from adsorbing through electrostatic attraction, Figure 5.4.B. The unmodified amine groups on the lumenal sides of PSI

are expected to adsorb due to electrostatic attraction, and this is the primary method of non-specific deposition of unmodified PSI onto many substrates in other studies.[16-17] Aside from greatly improving electron transfer at the PSI electrode interface and improving overall efficiency through a high net orientation, there are several other potential applications of side-selectively functionalizing PSI, including assembly of a more stable monolayer, modification for attaching to nano-scale catalysts, and the incorporation of the protein into complex frameworks such as conductive polymer matrices.

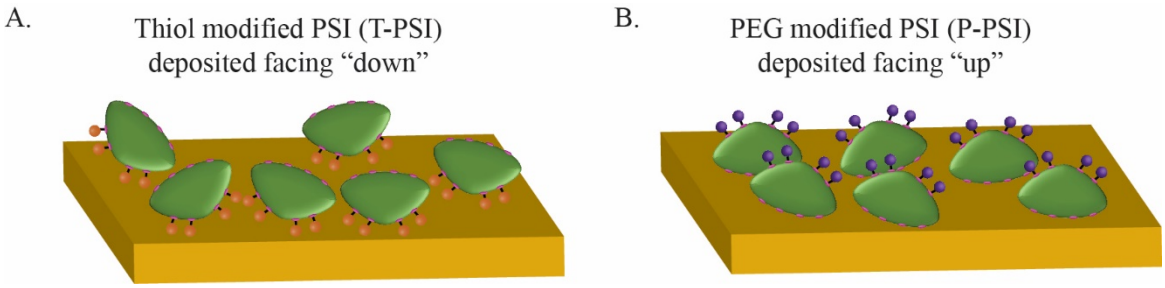

Figure 5.5. *Hypothesized modified PSI monolayer orientations. A.) The hypothesized thiol-modified PSI (T-PSI) orientation on gold. The strong thiol-gold affinity will result in T-PSI complexes with the reacted stromal side facing the gold substrate B.) The hypothesized PEG-modified PSI (P-PSI) orientation on gold. The PEG groups are highly hydrophilic and less likely to interact electrostatically with the gold substrate than positively charged primary amines.*

Results & Discussion

To determine if the PSI complexes are damaged during the stromal-side modification reaction, T-PSI and P-PSI complexes were studied in solution for structure and function properties prior to monolayer preparation. UV-Vis spectroscopy shows that the protein complex's ability to absorb red and blue light is not affected by partial reaction of the stromal side amines, Figure 4.6. PSI strongly absorbs visible light at approximately 430 and 680 nm and has a characteristic absorbance spectrum.[4] The modified protein complexes do show slight changes in absorbance. P-PSI shows a shoulder at both 480 and 650 nm wavelengths. The shoulder may be due to a minor change in the secondary structure of the protein complex due to the reaction of the surface amines. Robinson et al. have reported similar changes including the deconvolution of the Amide I band when PSI is encapsulated by PEDOT via vapor phase polymerization.[37]

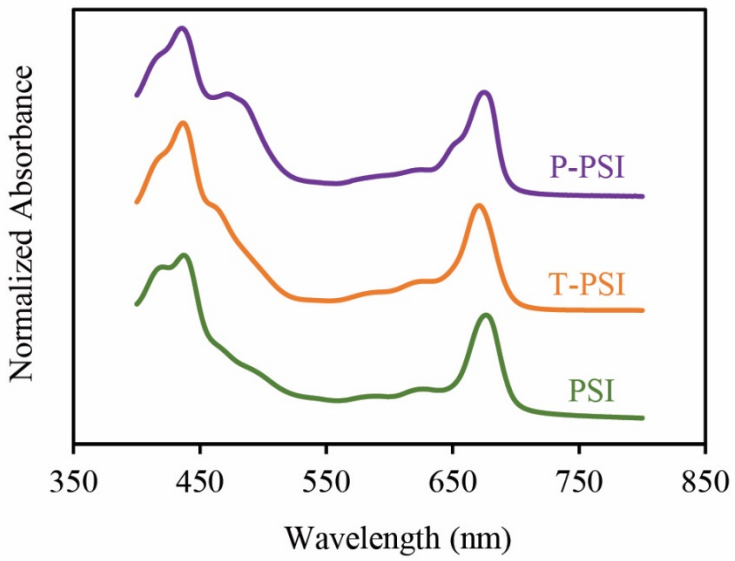

Figure 5.6 *Absorbance spectra of modified PSI complexes in comparison with an unmodifided PSI control show that the protein complexes are present and functional.*

Because the T-PSI solutions maintain homogenous solubility upon visual inspection, the modification procedure at low to moderate 2-iminothiolane (2-IT) concentration does not significantly affect solubility of PSI in the presence of 1.0 wt % Triton X-100 surfactant. However, at high concentrations of 2-IT (500 mg 2-IT/40 mL thylakoid suspension), the resulting modified protein complexes lose their solubility (Figure 5.7). This loss of solubility is attributed to the formation of disulfide linkages between modified protein complexes as reported by Yang et al., which result in protein complex aggregation and precipitation.[38] Note that P-PSI was found to be soluble even at high reactant concentrations.

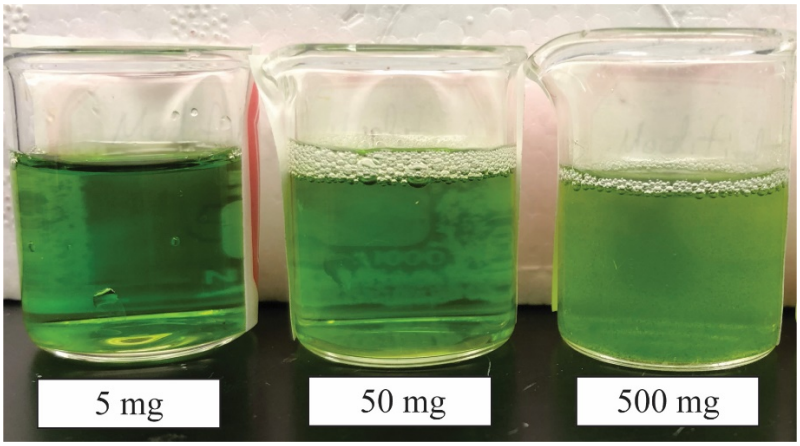

Figure 5.7. *PSI modification with Traut's Reagent (2-iminothiolane) to produce T-PSI was tested with variable concentrations of reactant (5, 50, and 500 mg respectively). At higher concentrations, PSI crosslinking results in loss of solubility (500 mg beaker).*

Figure 5.8 shows the concentration of PSI complexes in solution after modification, determined via Baba's assay for P_{700} concentration.[36] For subsequent experiments and protein depositions, the concentration of PSI was diluted to approximately 0.5 mg/mL (1 μM) for each solution so that we were able to investigate a normalized condition for each type of PSI. The lower concentration of P-PSI is attributed to variation between extraction batches and is not believed to be a consequence of the modification procedure.

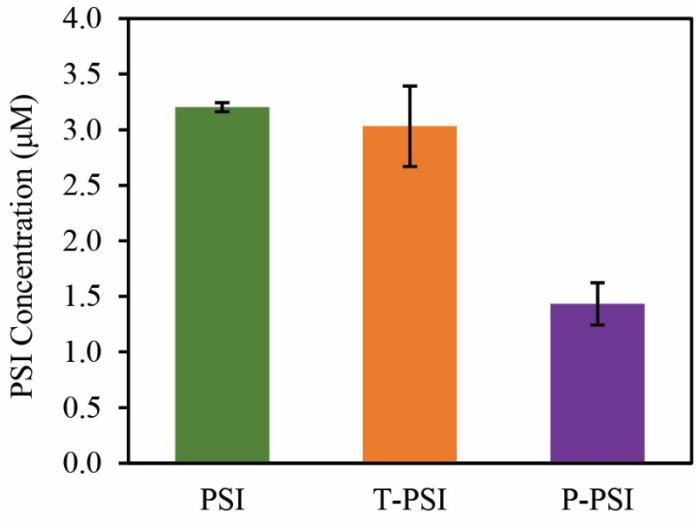

Figure 5.8*. The P_{700} concentration for each PSI type was determined via Baba's Assay and used to adjust concentrations for deposition studies.*

The deposition of PSI monolayers was observed using spectroscopic ellipsometry at various times during the solution deposition process (Figures 5.8.A and 5.8.B). Ellipsometry is a bulk surface technique, and the resulting output is an average height of the protein film across the probed area; therefore, the ellipsometric height can be used to determine the percent coverage of the monolayer. Faulkner et al. demonstrated that a 6-7 nm film corresponds to a dense PSI monolayer.[18] Assuming that a dense monolayer corresponds to approximately 91% coverage, based on the maximum packing efficiency of circles on a surface and previous PSI reports, the solution deposition process used here achieves between 25-45% coverage of PSI.[18] Table 5.1 shows the theoretical percent PSI coverages, ellipsometric thicknesses, equivalent surface coverages, and expected PSI mass per unit area for comparison.[18, 32] The ellipsometric thicknesses and deposition rates are shown in Figures 5.8.A and 5.8.B. The T-PSI deposited significantly faster than the unmodified PSI and P-PSI during the first minute of the deposition (Figure 5.8.B). After 1 min, the deposition rate slows dramatically and is similar for all samples. A larger observed thickness is attributed to a higher packing density in the T-PSI monolayer; a result of the high affinity of the T-PSI for the gold substrate.

Table 5.1. Theoretical percent coverages, ellipsometric thicknesses, equivalent surface concentrations, and PSI mass per unit area. Note that 100% coverage is not achievable due to the maximum packing efficiency (91% for perfect circles on a surface) limitation and the area covered by a single PSI complex is 320 nm^2 based on the reported crystallographic structure. Herein, a 6.5 nm PSI film is considered a dense monolayer.

Approximate Percent Coverage (%)	Ellipsometric Thickness (nm)	Surface Concentration ($pmol/cm^2$)	Expected Mass Density (ng/cm^2)
91	6.5	0.50	250
70	5.0	0.38	192
56	4.0	0.31	154
42	3.0	0.23	115
28	2.0	0.15	77
14	1.0	0.08	38

After the deposition of the PSI complexes, PM-IRRAS spectra were obtained to validate the presence of PSI in the deposited monolayers (Figure 5.8.C). The expected Amide I and Amide II bands at 1667 cm^{-1} and 1546 cm^{-1}, respectively, verify the successful deposition of intact PSI on the gold substrates.[45] Orientation was examined by contact angle measurements. While the T-PSI monolayers and unmodified PSI monolayers yielded the same contact angle of 71 ± 3° and 72 ± 3°, respectively, the P-PSI monolayers showed a decrease in contact angle, 60 ± 2° (Figures 5.8.D-G). These results are consistent with the expected increase in surface hydrophilicity for a P-PSI complex due to PEG groups facing upwards and that both an unmodified PSI complex and a T-PSI complex, with the thiolated stromal side facing the substrate, should result in similar surface compositions of amines, carboxylic acids, and more hydrophobic residues on the surface. Note that a larger change in contact angle would be expected if the PSI surface coverage, which was approximated as 35% for PSI, 28% for P-PSI, and 45% for T-PSI after a 16-h deposition, was more complete (a dense monolayer).

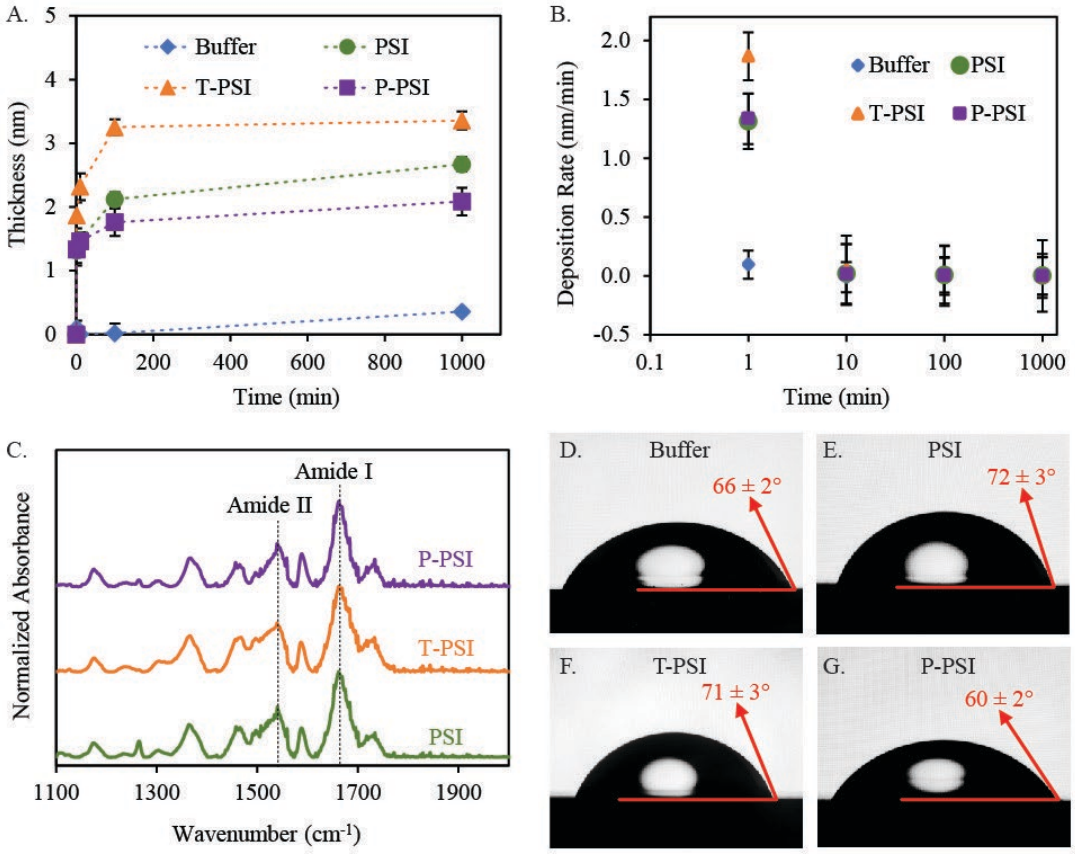

Figure 5.8. *PSI monolayer characterization. (A) Gold substrates were exposed to buffer (blue diamonds), PSI (green circles), T-PSI (orange triangles), or P-PSI (purple squares) solutions and the ellipsometric thickness was taken at various time intervals. (B) The deposition rate was calculated from (A) and plotted versus time, showing that T-PSI deposits significantly faster than PSI or P-PSI in the initial 1 min of the deposition procedure. (C) PM-IRRAS scans of the deposited monolayers verify the presence of PSI through the Amide I and Amide II peaks at 1667 and 1546 cm^{-1}, respectively. (D-G) Sessile drop contact angle measurements of 1 μL distilled water on a sample immersed in buffer (D), PSI (E), T-PSI (F), or P-PSI (G) solutions for 1000 min. The average and standard deviations are reported for n = 24. The contact angle results show that PSI and T-PSI result in monolayers with similar surface compositions, while P-PSI results in a much lower contact angle due to the presence of PEG groups facing away from the gold substrate.*

The potential for an increase in photoelectrochemical performance in oriented PSI monolayers was tested using photochronamperometry (PCA). The samples were held at the dark open circuit potential (OCP_{dark}) and illuminated for 10 s with a ~100 mW/cm^2 white light source in the presence of a supporting electrolyte of 100 mM potassium chloride. Artificial electrochemical mediators were not used in attempt to promote DET between PSI and the

electrode. Ideally, in a PSI monolayer test without mediator, the electrode would donate an electron to P_{700} and oxygen would scavenge an excited electron from F_B, producing cathodic photocurrent. However, only anodic photocurrent was observed (Figure 5.9). The PCA test was repeated after deoxygenating the electrolyte solution by bubbling N_2 for 30 min (dashed lines). The magnitude of the produced photocurrent was the same for each type of PSI monolayer. Additionally, after oxygen was removed, the photocurrent response was lost. The photochronoamperometry results show that an oxygen mediated photocurrent response is dominant in the absence of an artificial mediator or linking agent. We propose that dissolved oxygen is being reduced at F_B, similar to the production of ROS in vivo.[32, 39-40] The reduced oxygen then diffuses to the electrode and is oxidized, producing anodic photocurrent dependent on the presence of dissolved oxygen.

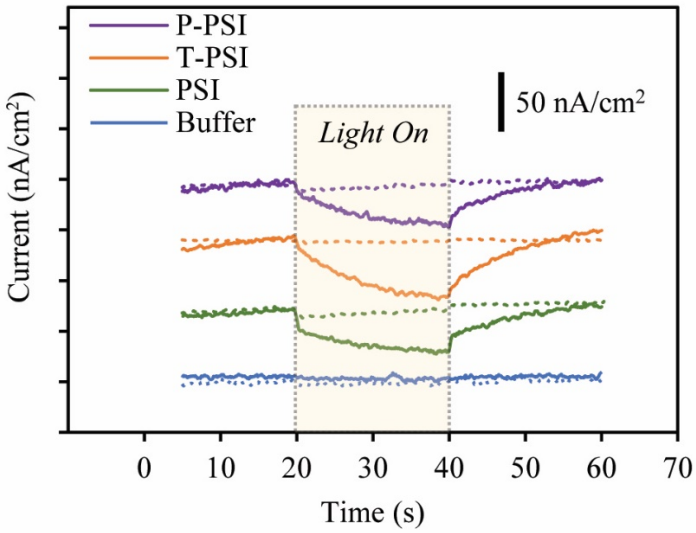

Figure 5.9. *Photochronoamperometric studies of PSI monolayers. Photochronoamperometry (PCA) curves for buffer (blue), PSI (green), T-PSI (orange), and P-PSI (purple) taken in 100 mM KCl with a 20 s illumination by a ~100 mW/cm² white light source. Tests conducted in a deoxygenated electrolyte are denoted by the dashed lines.*

Photochronopotentiometry shows that the local potential at the substrate electrode shifts more negative when the PSI monolayers are illuminated (Figure 5.10). Based on the Nernst equation (Eq 5.1), the behavior observed is explained by an increase in the ratio of reduced (R) to oxidized (O) species at the electrode surface, which causes a negative shift in the potential measured at the electrode, E.[41] The produced reduced species in this case are reduced oxygen

species.[39] We conclude that this shift in potential is the driving force in the production of anodic photocurrent in the PSI, T-PSI, and P-PSI monolayers. In the PCA results (Figure 5.9), this local increase in R results in an anodic photocurrent; the substrate electrode accepts electrons or oxidizes R in solution. The driving force for the anodic photocurrent is the difference in the local solution potential and the substrate's OCP_{dark}, at which the sample is held during PCA tests in Figure 5.9.

$$E = E^{0\prime} - \frac{nF}{RT}\log\left(\frac{[R]}{[O]}\right) \qquad \text{(Eq. 5.1)}$$

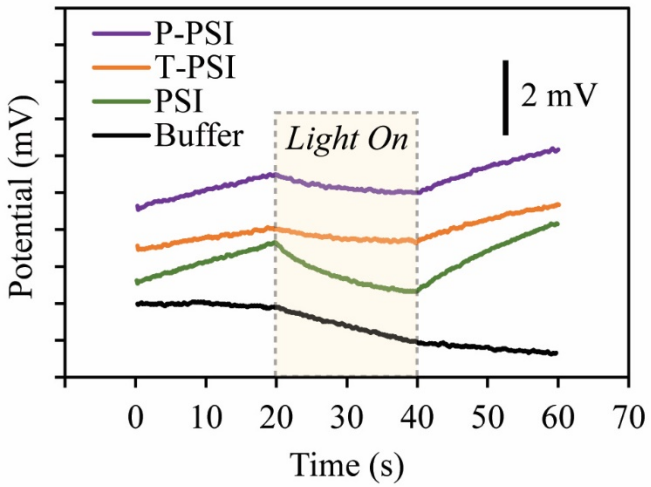

Figure 5.10. *Photopotentiometric studies of PSI monolayers. Curves for buffer (black), PSI (green), T-PSI (orange), and P-PSI (purple) taken in 100 mM KCl with a 10 s illumination by a ~100 mW/cm^2 white light source. Curves for buffer (black), PSI (green), T-PSI (orange), and P-PSI (purple) taken in 100 mM KCl with a 20 s illumination by a ~100 mW/cm^2 white light source.*

Conclusions

T-PSI showed a faster initial deposition rate and a higher degree of surface coverage during the ellipsometric deposition study. This agrees with the proposed deposition mechanism, in which free thiols on the stromal surface of T-PSI should interact strongly with the gold surface. In contrast, P-PSI shows a slower initial deposition rate and a lower surface coverage saturation than

T-PSI but was not significantly different from unmodified PSI. The deposition rate results and the presence of the Amide I and II bands in PM-IRRAS spectra show that the modified PSI complexes deposit on gold electrodes with 25-45% coverage and that T-PSI deposits at a faster rate, presumably due to the presence of free thiols on the stromal side. Further, contact angle measurements reveal that the surface composition of T-PSI is very similar to that of unmodified PSI. We conclude this is because any free thiols on T-PSI should preferentially bind to the gold surface, leaving the unmodified lumenal side of T-PSI facing upward. Therefore, both T-PSI and unmodified PSI can be expected to produce similar surface composition, as was observed. In contrast, P-PSI yielded a more hydrophilic surface, as is expected if the PEG groups on the stromal side inhibit substrate binding and thus, orient the stromal side upward. Through a summative view of these results, we have shown that the facile solution-based modification of the stromal side lysine residues in PSI can be leveraged to produce PSI monolayers with distinct surface compositions.

Photoelectrochemical testing revealed that the photocurrent response of the produced monolayers is dependent on oxygen mediated electron transfer and that modification of PSI did not alter the photocurrent response. Here we would like to note that this was not the anticipated outcome but is still an insightful result. The observed oxygen mediated electron transfer and the lack of any measurable electron transfer upon deaeration implies that the resistance to direct electron transfer (DET) via tunneling is too great in the prepared monolayers and that an electron donor or acceptor may be necessary to study DET. This result is validated by the findings of Lopez-Martinez et al., who determined through scanning tunneling microscopy that a distance of less than 1 nm between PSI's P_{700} site and the active electrode is necessary to achieve DET.[10] We therefore conclude that while the modified PSI monolayers provide a method for altering the surface composition and potentially the orientation of individual PSI complexes, an additional electron transfer conduit is necessary to provide DET, even at the single monolayer level. Further work investigating a combination of facile modification-extraction procedures and the implementation of additional electron transfer entities is needed.

To summarize, manipulating individual PSI complexes is a challenging task but one that may yield advances in the performance of PSI biohybrid energy conversion. A simple solution-

based modification-extraction procedure was developed that allows the tailored modification of the stromal side of PSI. We modified PSI with both thiol and PEG functionalities and produced monolayer films with unique surface compositions that validate the hypothesized orientations of the modified PSI complexes. Yet the modified PSI monolayers did not operate by means of direct electron transfer (DET). Instead, it was found that the produced monolayers were limited to oxygen mediated electron transfer. These results call for further work on the task of both orienting individual PSI complexes and providing a molecular scale electron conduit to promote DET. An alternative means of testing for direct electron transfer, based on square wave voltammetry, between PSI reaction centers and a gold electrode is given in Appendix D. The square wave voltammetry results may indicate some degree of orientation; however, the tests were highly irreproducible and were therefore removed from this chapter. The modification-extraction procedure reported herein opens opportunity for the facile incorporation of modified PSI complexes in combination with methods for achieving high degrees of DET for the future development of PSI biohybrid technologies.

References

1. Nguyen, K.; Bruce, B. D., Growing green electricity: Progress and strategies for use of Photosystem I for sustainable photovoltaic energy conversion. *Biochim. Biophys. Acta Bioenerg.* **2014,** *1837*, 1553-1566.
2. Teodor, A. H.; Bruce, B. D., Putting Photosystem I to Work: Truly Green Energy. Trends Biotechnol. **2021**, 11, 1000122.
3. Wolfe, K. D.; Dervishogullari, D.; Passantino, J. M.; Stachurski, C. D.; Jennings, G. K.; Cliffel, D. E., Improving the stability of photosystem I–based bioelectrodes for solar energy conversion. *Curr. Opin. Electrochem.* **2020,** *19*, 27-34.
4. Friebe, V. M.; Frese, R. N., Photosynthetic reaction center-based biophotovoltaics. *Curr. Opin. Electrochem.* **2017,** *5*, 126-134.
5. Amunts, A.; Toporik, H.; Borovikova, A.; Nelson, N., Structure determination and improved model of plant photosystem I. *J. Bio. Chem.* **2010,** *285*, 3478-3486.
6. Xue, Y.; Ökvist, M.; Hansson, Ö.; Young, S., Crystal structure of spinach plastocyanin at 1.7 Å resolution. *Protein Sci.* **1998,** *7* (10), 2099-2105.

7. Mutoh, R.; Muraki, N.; Shinmura, K.; Kubota-Kawai, H.; Lee, Y.-H.; Nowaczyk, M. M.; Rögner, M.; Hase, T.; Ikegami, T.; Kurisu, G., X-ray Structure and Nuclear Magnetic Resonance Analysis of the Interaction Sites of the Ga-Substituted Cyanobacterial Ferredoxin. *Biochemistry* **2015,** *54* (39), 6052-6061.

8. Nelson, N.; Junge, W., Structure and Energy Transfer in Photosystems of Oxygenic Photosynthesis. *Annu. Rev. Biochem* **2015,** *84*, 659-683.

9. Marcus, R. A.; Sutin, N., Electron transfers in chemistry and biology. *Biochim. Biophys. Acta Bioenerg.* **1985,** *811* (3), 265-322.

10. Lopez-Martinez, M.; Lopez-Ortiz, M.; Antinori, M. E.; Wientjes, E.; Nin-Hill, A.; Rovira, C.; Croce, R.; Diez-Perez, I.; Gorostiza, P., Electrochemically Gated Long-Distance Charge Transport in Photosystem I. *Angew. Chem. Int. Ed.* **2019,** *58* (38), 13280-13284.

11. Robinson, M. T.; Gizzie, E. A.; Mwambutsa, F.; Cliffel, D. E.; Jennings, G. K., Mediated approaches to Photosystem I-based biophotovoltaics. *Curr. Opin. Electrochem.* **2017,** *5*, 211-217.

12. Ciesielski, P. N.; Faulkner, C. J.; Irwin, M. T.; Gregory, J. M.; Tolk, N. H.; Cliffel, D. E.; Jennings, G. K., Enhanced Photocurrent Production by Photosystem I Multilayer Assemblies. *Adv. Funct. Mater.* **2010,** *20*, 4048-4054.

13. Robinson, M. T.; Cliffel, D. E.; Jennings, G. K., An Electrochemical Reaction-Diffusion Model of the Photocatalytic Effect of Photosystem I Multilayer Films. *J. Phys. Chem. B* **2018,** *122* (1), 117-125.

14. Friebe, V. M.; Swainsbury, D. J. K.; Fyfe, P. K.; van der Heijden, W.; Jones, M. R.; Frese, R. N., On the mechanism of ubiquinone mediated photocurrent generation by a reaction center based photocathode. *Biochim. Biophys. Acta Bioenerg.* **2016,** *1857*, 1925-1934.

15. Zhao, F.; Wang, P.; Ruff, A.; Hartmann, V.; Zacarias, S.; Pereira, I. A. C.; Nowaczyk, M. M.; Rögner, M.; Conzuelo, F.; Schuhmann, W., A photosystem I monolayer with anisotropic electron flow enables Z-scheme like photosynthetic water splitting. *Energy Environ. Sci.* **2019,** *12* (10), 3133-3143.

16. Carmeli, I.; Frolov, L.; Carmeli, C.; Richter, S., Photovoltaic Activity of Photosystem I-Based Self-Assembled Monolayer. *J. Am. Chem. Soc.* **2007,** *129*, 12352-12353.

17. Ciobanu, M.; Kincaid, H. A.; Lo, V.; Dukes, A. D.; Kane Jennings, G.; Cliffel, D. E., Electrochemistry and photoelectrochemistry of photosystem I adsorbed on hydroxyl-terminated monolayers. *J. Electroanal. Chem.* **2007,** *599* (1), 72-78.

18. Faulkner, C. J.; Lees, S.; Ciesielski, P. N.; Cliffel, D. E.; Jennings, G. K., Rapid Assembly of Photosystem I Monolayers on Gold Electrodes. *Langmuir* **2008,** *24*, 8409-8412.

19. Stieger, K. R.; Feifel, S. C.; Lokstein, H.; Lisdat, F., Advanced unidirectional photocurrent generation via cytochrome c as reaction partner for directed assembly of photosystem I. *Phys. Chem. Chem. Phys.*. **2014,** *16*, 15667-15674.

20. Stieger, K. R.; Ciornii, D.; Kölsch, A.; Hejazi, M.; Lokstein, H.; Feifel, S. C.; Zouni, A.; Lisdat, F., Engineering of supramolecular photoactive protein architectures: the defined co-assembly of photosystem I and cytochrome c using a nanoscaled DNA-matrix. *Nanoscale* **2016,** *8*, 10695-10705.

21. Friebe, V. M.; Millo, D.; Swainsbury, D. J. K.; Jones, M. R.; Frese, R. N., Cytochrome c Provides an Electron-Funneling Antenna for Efficient Photocurrent Generation in a Reaction Center Biophotocathode. *ACS Appl. Mater. Interfaces* **2017,** *9* (28), 23379-23388.

22. Feifel, S. C.; Stieger, K. R.; Hejazi, M.; Wang, X.; Ilbert, M.; Zouni, A.; Lojou, E.; Lisdat, F., Dihemic c4-type cytochrome acting as a surrogate electron conduit: Artificially interconnecting a photosystem I supercomplex with electrodes. *Electrochem. Commun.* **2018,** *91*, 49-53.

23. Ciornii, D.; Kölsch, A.; Zouni, A.; Lisdat, F., A precursor-approach in constructing 3D ITO electrodes for the improved performance of photosystem I-cyt c photobioelectrodes. *Nanoscale* **2019**.

24. Efrati, A.; Tel-Vered, R.; Michaeli, D.; Nechushtai, R.; Willner, I., Cytochrome c-coupled photosystem I and photosystem II (PSI/PSII) photo-bioelectrochemical cells. *Energy Environ. Sci.* **2013,** *6*, 2950-2956.

25. Feifel, S. C.; Ludwig, R.; Gorton, L.; Lisdat, F., Catalytically Active Silica Nanoparticle-Based Supramolecular Architectures of Two Proteins – Cellobiose Dehydrogenase and Cytochrome c on Electrodes. *Langmuir* **2012,** *28* (25), 9189-9194.

26. Ciornii, D.; Riedel, M.; Stieger, K. R.; Feifel, S. C.; Hejazi, M.; Lokstein, H.; Zouni, A.; Lisdat, F., Bioelectronic Circuit on a 3D Electrode Architecture: Enzymatic Catalysis Interconnected with Photosystem I. *J. Am. Chem. Soc.* **2017,** *139* (46), 16478-16481.

27. Kölsch, A.; Hejazi, M.; Stieger, K. R.; Feifel, S. C.; Kern, J. F.; Müh, F.; Lisdat, F.; Lokstein, H.; Zouni, A., Insights into the binding behavior of native and non-native cytochromes to photosystem I from Thermosynechococcus elongatus. *J. Biol. Chem.* **2018,** *293*, 9090-9100.

28. Kiliszek, M.; Harputlu, E.; Szalkowski, M.; Kowalska, D.; Unlu, C. G.; Haniewicz, P.; Abram, M.; Wiwatowski, K.; Niedziółka-Jönsson, J.; MaćKowski, S.; Ocakoglu, K.; Kargul, J., Orientation of photosystem i on graphene through cytochrome: C 553 leads to improvement in photocurrent generation. *J. Mater. Chem. A* **2018,** *6*, 18615-18626.

29. Olmos, J. D. J.; Becquet, P.; Gront, D.; Sar, J.; Dąbrowski, A.; Gawlik, G.; Teodorczyk, M.; Pawlak, D.; Kargul, J., Biofunctionalisation of p-doped silicon with cytochrome c553 minimises charge recombination and enhances photovoltaic performance of the all-solid-state photosystem I-based biophotoelectrode. *RSC Advances* **2017,** *7*, 47854-47866.

30. Mukherjee, D.; May, M.; Vaughn, M.; Bruce, B. D.; Khomami, B., Controlling the Morphology of Photosystem I Assembly on Thiol-Activated Au Substrates. *Langmuir* **2010,** *26* (20), 16048-16054.

31. Frolov, L.; Rosenwaks, Y.; Carmeli, C.; Carmeli, I., Fabrication of a Photoelectronic Device by Direct Chemical Binding of the Photosynthetic Reaction Center Protein to Metal Surfaces. *Adv. Mater.* **2005,** *17* (20), 2434-2437.

32. Golbeck, J. H., *Photosystem I: The Light-Driven Plastocyanin: Ferredoxin Oxidoreductase*. Springer Netherlands: 2007.

33. Reeves, S. G.; Hall, D. O., [8] Higher plant chloroplasts and grana: General preparative procedures (excluding high carbon dioxide fixation ability chloroplasts). In *Photosynthesis and Nitrogen Fixation - Part C*, Ed. Academic Press: San Pietro, **1980**; Vol. 69, pp 85-94.

34. Shiozawa, J. A.; Alberte, R. S.; Thornber, J. P., The P700-chlorophyll a-protein: Isolation and some characteristics of the complex in higher plants. *Arch. Biochem. Biophys.* **1974,** *165* (1), 388-397.

35. Millsaps, J. F.; Bruce, B. D.; Lee, J. W.; Greenbaum, E., Nanoscale photosynthesis: Photocatalytic production of hydrogen by platinized photosystem I reaction centers. *Photochem. Photobiol.* **2001,** *73* (6), 630-635.

36. Baba, K.; Itoh, S.; Hastings, G.; Hoshina, S., Photoinhibition of Photosystem I electron transfer activity in isolated Photosystem I preparations with different chlorophyll contents. *Photosynth. Res.* **1996,** *47*, 121-130.

37. Robinson, M. T.; Simons, C. E.; Cliffel, D. E.; Jennings, G. K., Photocatalytic photosystem I/PEDOT composite films prepared by vapor-phase polymerization. *Nanoscale* **2017,** *9*, 6158-6166.

38. Yang, S.; Robinson, M. T.; Mwambutsa, F.; Cliffel, D. E.; Jennings, G. K., Effect of Cross-linking on the Performance and Stability of Photocatalytic Photosystem I Films. *Electrochim. Acta* **2016,** *222*, 926-932.

39. Zhao, F.; Hardt, S.; Hartmann, V.; Zhang, H.; Nowaczyk, M. M.; Rögner, M.; Plumeré, N.; Schuhmann, W.; Conzuelo, F., Light-induced formation of partially reduced oxygen species limits the lifetime of photosystem 1-based biocathodes. *Nature Comm.* **2018,** *9*.

40. Zhao, F.; Ruff, A.; Rögner, M.; Schuhmann, W.; Conzuelo, F., Extended Operational Lifetime of a Photosystem-Based Bioelectrode. *J. Am. Chem. Soc.* **2019,** *141*, 5102-5106.

41. Bard, A. J., Electrochemical methods : fundamentals and applications / Allen J. Bard, Larry R. Faulkner. Wiley: New York, New York. **1980**.

Chapter 6 – Photosystem I – PEDOT:PSS Layer-by-Layer Assembly

The research presented in this chapter was started by chemical engineering undergraduate student and researcher Avi Gargye. Further work was completed to produce the following manuscript, which was a collaborative effort between the author (Kody D. Wolfe) and Avi Gargye. At the time of the writing of this dissertation, the contents of this chapter have been submitted for publication in Langmuir and are under peer review. Long Than, undergraduate researcher, and Faustin Mwambutsa, past graduate researcher, assisted in data collection and interpretation. Funding for the following work was provided by the National Science Foundation (DMR-1507505) and the United States Department of Agriculture (2019-67021-29857).

Introduction

In PSI-based electrodes and devices, PSI protein complexes are deposited as a monolayer or multilayer film onto a variety of electrode materials. As mentioned in the introduction, achieving a high loading of active PSI complexes is an area of great research interest. Many methods to immobilize PSI have been reported, including self-assembly, vacuum-assisted drop casting, dip-coating, Langmuir monolayer transfer, spin coating, and copolymerization among others.[1-10] Regardless of the deposition technique, the desired characteristics of a PSI film include high connectivity between protein complexes, high loading of protein complexes, and good connection between the active layers and the electrode. The following work seeks to improve loading and connectivity of PSI by using layer-by-layer assembly to achieve the deposition of individual PSI monolayers between conducting polymer layers.

Conducting polymers offer a promising route towards improving the connectivity between the electrically insulating proteins. Conducting polymers fall into two classes, intrinsic or electron conducting polymers and redox polymers, and both types have been used in conjunction with PSI. Zhao et. al and Badura et al. developed osmium-based redox hydrogels and hydrogel films for use with PSI, showing the promise of redox polymers in the field and resulting in their continued use in recent efforts.[7-8, 11-12] Dervishogullari et al. used a polyviologen redox polymer as an electron transport layer and Yehezkeli et al. used two redox-active polymers to create layered films

incorporating PSI and PSII.[13-14] Intrinsic conducting polymers have also been successfully used in thylakoid membrane-based bioelectrodes and as bulk conducting layers in PSI solid state devices.[15-17]

Recently, efforts in the Cliffel and Jennings research groups has focused on incorporating PSI within intrinsically conducting polymer matrices to fabricate PSI-based biohybrid electrodes.[9-10, 13] Gizzie et al. electropolymerized aniline in the presence of PSI to entrap it, creating an active layer for a PSI-polyaniline film, and later a solid state bio-photovoltaic device.[10, 18] An impressive increase in photocurrent is provided by PSI at low loadings (14.5 ± 2.7 nmol PSI/cm^3); however, obtaining higher loadings of PSI in the devices was not demonstrated due to limitations in the electropolymerization process.[19] In another project, Robinson et al. vapor deposited poly(3,4-ethylenedioxythiophene) (PEDOT) throughout a multilayer of PSI and concluded that PEDOT acted as an extension of the electrode, decreasing photocurrent attenuation for PSI farther from the electrode.[9] Unfortunately, when this grafting technique was used with densely packed PSI multilayers, only a small amount of PEDOT was able to grow near the electrode, limiting electrical connectivity. To address the issue of increasing PSI loading while retaining the beneficial properties of using intrinsically conducting polymer entrapment, we have leveraged electrostatic interactions between PSI and poly(3,4-ethylenedioxythiophene)-polystyrene sulfonate (PEDOT:PSS) to enable the preparation of layered PSI-PEDOT:PSS films. PEDOT:PSS is a polymer salt with PEDOT acting as the positively charged polycation and PSS acting as the polyanion.[20] PSI also bears a mixed charge in solution due to the varied functional groups on its surface. Figure 6.1 schematically depicts the surface of the PSI protein complex and illustrates the position of primary amines and carboxylic acids that contribute a majority of PSI's mixed surface charge. At pH = 7.0 the primary amines (blue) yield a local positive charge while the carboxylic acids (red) yield a local negative charge.[21]

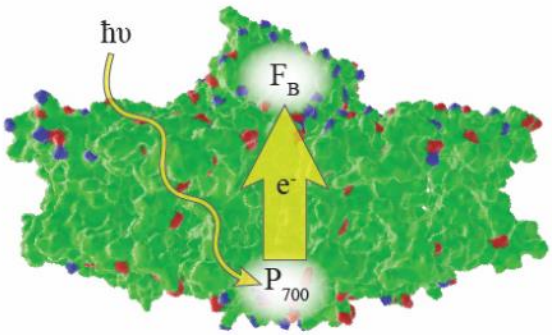

Figure 6.1. *Schematic illustration highlighting PSI's surface-exposed primary amines (blue) and carboxylic acids (red). At pH = 7.0, surface amines yield a local positive charge while carboxylic acids yield a negative charge. The primary amines shown are present in lysine residues while the carboxylic acids are contributed by aspartic and glutamic acid residues. The exposed functional groups on PSI were created using the PyMol molecular visualization software and structural data of Amunts et al.*[21]

One method for creating composite films based on electrostatic interactions is layer-by-layer (LBL) deposition, where films are created by adsorbing nanoscale layers of material with alternating charges. LBL deposition has proven useful for a variety of applications such as membrane fabrication, electrochromism, and biomaterials.[22-26] The benefits of LBL assembly include nanoscale-control of the film thickness, ease of preparation and scalability, high degrees of reproducibility, and high achievable loadings of biomolecules.[23, 27] Several researchers have used LBL deposition to couple PSI/PSII or bacterial photosynthetic reaction centers with polyelectrolytes and examined photocurrents.[25-29] Yehezkeli et al. fabricated up to 3 bilayers of poly-benzyl viologen redox polymer-based LBL films with PSI.[14] The authors did not observe an increase in performance beyond 3 layers of PSI, which they attribute to electrical perturbations causing a loss of communication between the active protein and redox polymer. Stieger et al. used DNA as a polyelectrolyte to build self-assembled PSI:cytochrome c films.[29] The DNA polyelectrolyte was used to improve the stability of PSI and cyt c co-assembled films and the results showed that the high performing electrodes were also stable for many days if stored in dry conditions.[29] This study highlights the importance of the polyelectrolyte to improve loading and stability of active components in biohybrid layered assemblies.

PEDOT:PSS has been studied as a conductive layer in PSI biohybrid films previously. Using a spin-coating technique, Barhom et al. incorporated PEDOT:PSS layers of unreported thickness as an electrode atop PSI multilayers and Kazemzadeh et al. used PEDOT:PSS as an interfacial layer between PSI and indium tin oxide (ITO) to improve the performance of solid state PSI devices.[16-17] Both of these studies capitalized on PEDOT:PSS's flexibility and electrical conductivity to improve the connection between PSI layers and electrodes. Based on the previous successes, our goal is to leverage electrostatic interactions between PSI and PEDOT:PSS to combat limitations with low PSI loadings and ill-defined electrode-conducting polymer interfaces through the fabrication and testing of PSI-PEDOT:PSS LBL films.

In this work, alternating layers of PEDOT:PSS and PSI are deposited onto aminoethanethiol (AET) monolayers on gold electrodes as shown in Figure 6.2. The LBL method circumvents constraints from our group's previous methods for creating PSI/conducting polymer assemblies. It ensures both high PSI loading within the film and protein/conducting polymer interactions throughout the film. During the LBL process, PEDOT:PSS first electrostatically binds to the AET monolayer, producing a thin film of PEDOT:PSS on the electrode. Next, the mixed charge functional groups on PSI's surface promotes the deposition of a well-packed PSI monolayer, creating a bilayer or one layer pair. The deposition is repeated to produce many layer pairs. We then show that through mediated electron transfer (MET) via ubiquinone-0, a linear increase in photocurrent production is achieved with the addition of each layer pair up to a threshold level of 6-layer pairs and that the PSI-PEDOT:PSS LBL films greatly outperform densely packed PSI multilayer films when photocurrent is normalized to protein loading.

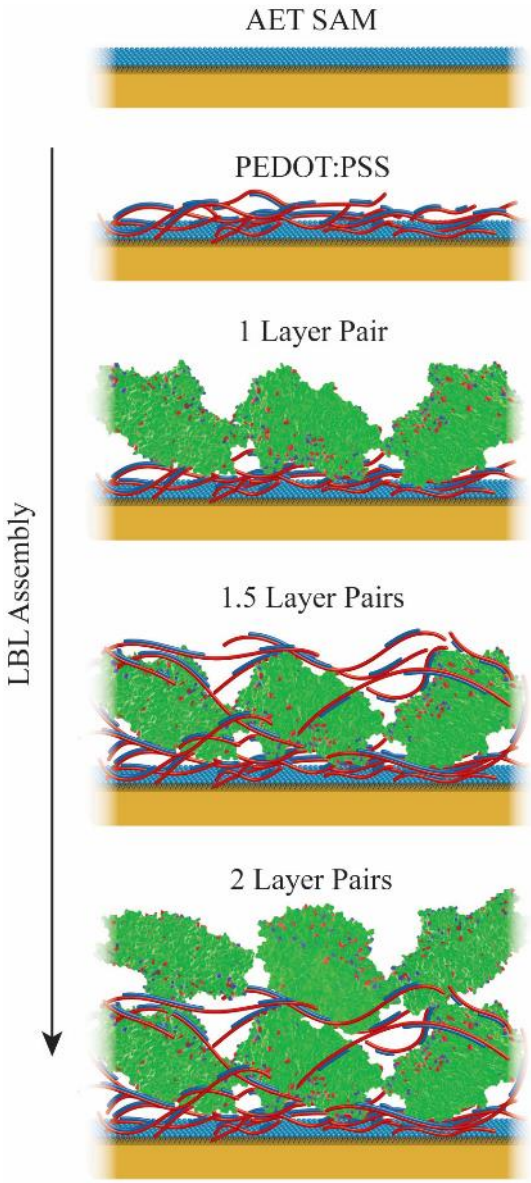

Figure 6.2. *Schematic illustration of the LBL assembly procedure showing the depositions steps required to prepare 2-layer pairs.*

Results & Discussion

During the preparation of the LBL films, advancing contact angle measurements were taken to observe the evolution of film surface composition. The exposed functional groups of PEDOT:PSS and PSI result in a change in contact angle with each layer of the deposition (Figure

6.3). The positively charged amine-terminated SAM yields a reproducible contact angle below 40° due to the strong interaction of water with the charged surface that provides a low solid-liquid interfacial free energy. The deposition of the first layer of PEDOT:PSS does not significantly change the observed contact angle. The dramatic increase in contact angle upon PSI deposition is due to the complex, amphiphilic character of PSI, which contains a hydrophobic "belt" that is typically embedded within the thylakoid membrane.[24] Contact angles for PSI monolayers have been reported as high as 90°, so the values of >80° here are consistent with a surface dominated by the protein.[30] After the PSI surface was exposed to a solution of PEDOT:PSS, the contact angle drops from ~80° to ~60°, indicating the presence of the more hydrophilic polymer at the surface. This contact angle trend is repetitive throughout the LBL deposition steps, signifying that the respective material is adsorbed via each deposition step and that the film maintains an adequate charge to attract the next layer.[31] This consistent deposition behavior is typical of well-behaved LBL systems. On average, PEDOT:PSS layers deposited atop PSI have a contact angle of 61° ± 9°, and PSI layers deposited atop PEDOT have an average contact angle of 82° ± 5°. Spun cast homogeneous PEDOT:PSS films have been reported to provide water contact angles of 25° because the free charges associated with the sulfonate and thiophene groups provide strong ion-dipole interactions with water.[32] In LBL films, the contact angles of water on PEDOT:PSS vary widely from 20° to 80° based on layer thickness, counterion of the salt, and composition of the other polyion.[33-34] The discrepancy shown between the first and subsequent PEDOT:PSS layers here is attributed to the different sublayers, a highly charged AET surface versus a more hydrophobic PSI layer, in which each may be partially exposed. These different sublayers would also affect the structure of the PEDOT:PSS layer. Water is known to be sensitive to surface groups located within ~0.3-0.4 nm of the outermost surface.[35] Thus, given the average thicknesses of the polymer layers (1-2 nm, shown later in Figure 6.5) and the sensitivity of contact angle to the sublayer, the contact angles suggest that intermixing occurs between the polymer and protein layers. A schematic of this behavior is shown in Figure 6.2, in which the PEDOT:PSS polymer penetrates the PSI layers.

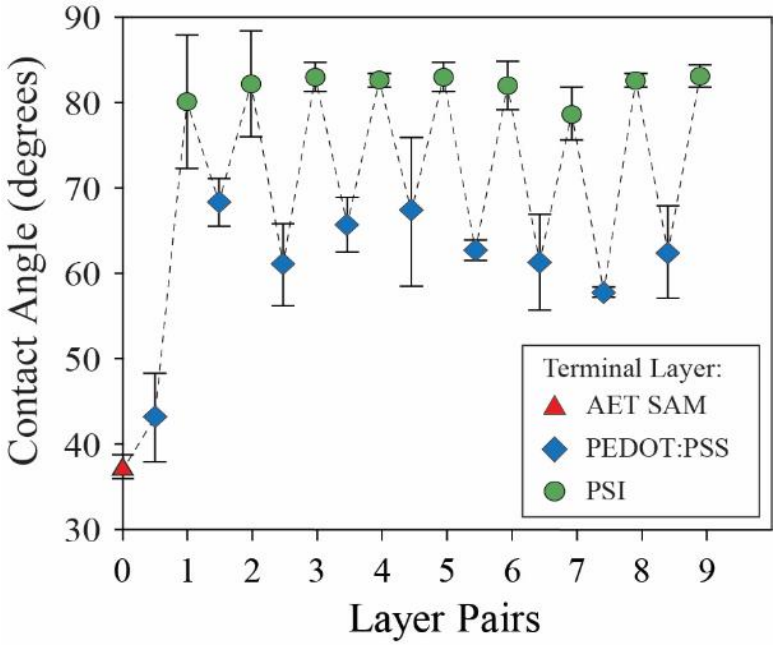

Figure 6.3. *Advancing contact angle measurements taken with deionized water after each deposition step in the LBL assembly.*

The film thickness was also measured between each deposition step using spectroscopic ellipsometry (Figure 6.4). In classical LBL films, alternating layers of oppositely charged polyions are deposited, and the resulting layers are considered as intermingling charged domains with thicknesses on the order of 1-3 nm per layer pair.[23] The PSI and PEDOT:PSS case is much more complex due to the sheer size of the PSI protein complex and the mixed-charge nature of both PSI and PEDOT:PSS.[21] The thickness of the PEDOT:PSS and PSI composite films grows linearly by 8.11 ± 0.14 nm with each additional layer pair. Based on the reproducibility of ellipsometric thickness measurements across many samples, we believe that the films are much more uniform than their thicker drop-cast counterparts.[1]

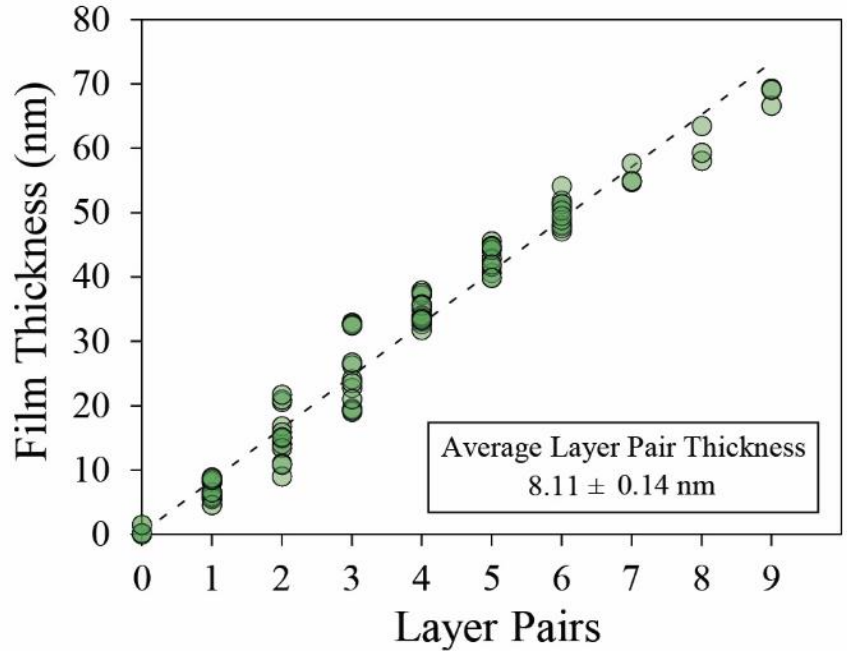

Figure 6.4. *Total film thickness for all whole layer pair samples, obtained via spectroscopic ellipsometry. Note that whole layer pair samples are terminated by PSI. Note that a decrease in opacity of the markers indicates overlapping data points.*

While the step height for whole layer pairs is highly reproducible, the height change of individual PEDOT:PSS or PSI layers is typically within the bounds of error of the previous layer (Figure 6.5). Figure 6.5 shows that the deposition of PEDOT:PSS (blue bars) results in an approximately 1-2 nm increase in thickness while the deposition of PSI (green bars) yields a 6-7 nm increase in thickness. Note that the error between partial layer pairs is large, and therefore, only a qualitative assessment of this data is possible. PEDOT:PSS layers increase the thickness much less than the PSI layers, as is expected based on their molecular sizes. The increase in film thickness during PSI deposition is consistent with the formation of a dense PSI monolayer after only a short deposition time of 30 min.[2] For comparison, Faulkner et al. required 48 h for solution phase assembly to deposit a similar thickness of PSI.[2] We believe the faster deposition onto the PEDOT:PSS polymer is due to the favorable electrostatic interactions between the mixed charges present on PSI along with the positive charge of the PEDOT moiety and the negative PSS counter anion.

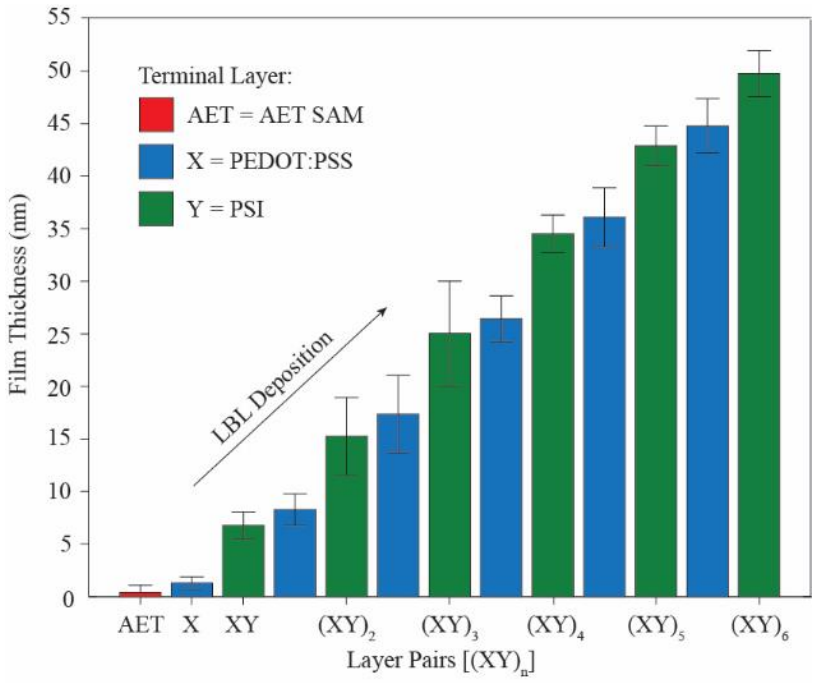

Figure 6.5. *Ellipsometric film thickness values for partial layer depositions. Blue bars denote a PEDOT:PSS-terminated film otherwise called a half layer pair, and the green bars denote PSI-terminated films or full layer pairs.*

FTIR spectroscopy was used to confirm the presence of both PSI and PEDOT:PSS in the film as layers were assembled. PSI's characteristic amide I and amide II peaks appear prominently at 1664 cm^{-1} (I) and 1547 cm^{-1} (II), respectively, in both the 1- and 8-layer pair samples shown in Figure 6.6. The observed amide I and amide II bands align well with the PSI spectra presented by Robinson et al.,[9] indicating that PSI is not only present, but whether in layer 1 or all inclusive, PSI exhibits a secondary structure that is consistent with that of redox-active PSI used in multilayer and polymer composite films. The peaks observed at 1009 cm^{-1} (VII) and 1036 cm^{-1} (VI) are attributed to PSS's S-phenyl bond and the broad peak at 1182 cm^{-1} (IV) is attributed to PSS's S=O vibration.[36-38] The peaks at 1128 and 1219 cm^{-1} (III) correspond to PEDOT's C-O-C bond.[36, 38-39] These peaks, characteristic of PEDOT:PSS, are present in the 1- and 8-layer pair samples as well, indicating that PSI deposition does not remove either PEDOT or PSS during LBL deposition.

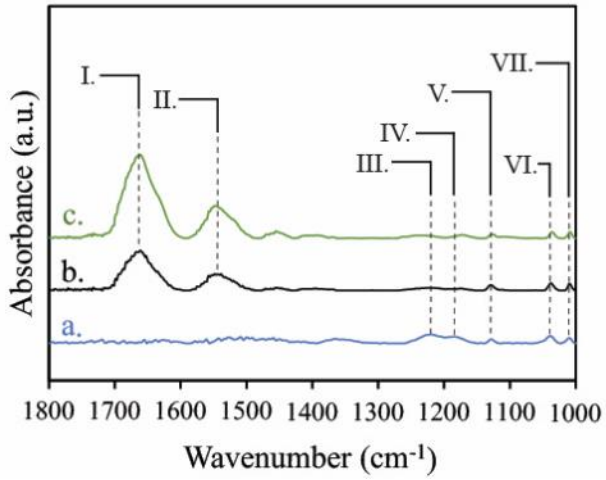

Figure 6.6. *(a) FTIR spectra of a single layer of PEDOT:PSS atop an AET monolayer shown at 25X intensity, (b) a 1-layer pair LBL film shown at 8X intensity, and (c) an 8-layer pair LBL film shown at 1X intensity. Dashed lines and Roman numerals indicate the positions of key absorbance peaks, as described in the text.*

The peaks corresponding to PSS and PEDOT at 1182 and 1219 cm^{-1}, respectively, grow further apart as layers of PSI and the polymer are added repetitively to the film (Figure 6.7 and Table 6.1). Figure 6.7 shows a zoomed in region of Figure 6.6 above, showing these shifted peaks. Dashed lines align with the peaks in the PEDOT:PSS spectrum (a) and the arrows point in the direction of the peak shift in the 8-layer pair sample (c). Spectrum (b) is for a 1-layer pair sample. Table 6.1 gives the wavelength of the peaks in Figure 6.7 for each spectrum. Specifically, the S=O peak (PSS) shifts from 1182 to 1173 cm^{-1} and the C-O-C peak (PEDOT) shifts from 1219 to 1232 cm^{-1} between the PEDOT:PSS film and the 8-layer pair film. These peak shifts may indicate attractive intermolecular interactions between the polymer and PSI. Studies have noted peak shifts during LBL deposition as a result of electrostatic or dipole-dipole interactions.[40-41]

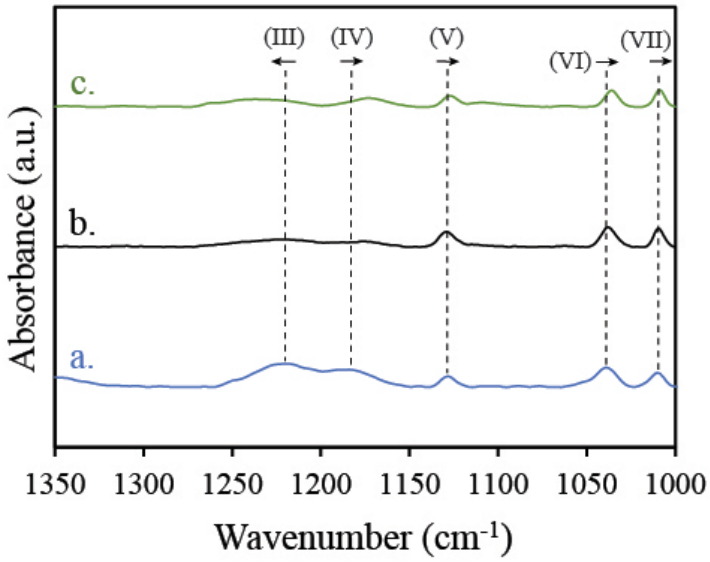

Figure 6.7. *FTIR spectra from Figure 6.6, zoomed into the low wavenumber region to show the shifting of peaks corresponding to PEDOT and PSS. Spectrum a is from a single layer of PEDOT:PSS on an AET self-assembled monolayer, spectrum b is from a single layer pair sample, and spectrum c is from an 8-layer pair sample. Table 6.1 gives the peak wavenumbers for each spectrum.*

Table 6.1. Infrared Peak Assignments for Spectra Shown in Figure 6.7.[36-39]

Wavenumbers for Assigned Peaks from Figure 6.7 (cm^{-1})					
Peak Label	III	IV	V	VI	VII
Contributing Constituent	PEDOT	PSS	PEDOT	PSS	PSS
Chemical Assignment	C-O-C	S=O	C-O-C	S-phenyl	S-phenyl
PEDOT:PSS (a)	1219	1182	1128	1040	1010
1-Layer Pair (b)	1220	1176	1129	1038	1009
8-Layer Pairs (c)	1232	1173	1127	1036	1007

The photoelectrochemical activity of the LBL films was studied using photochronoamperometry (PCA). For all PCA experiments, the open circuit potential (OCP) was first measured in the dark, and the measured OCP value for each individual sample was recorded and used as the applied potential in the PCA experiment. By beginning the test at OCP, the background current is near zero, and any increase in current upon illumination is directly due to reactions within the film and, ultimately, at the electrode surface. Photoelectrochemical performance of 3-layer pair PEDOT:PSS and PSI films were tested in three electrolyte solutions including supporting electrolyte only (100 mM KCl), 2 mM methyl viologen and supporting electrolyte, and 2 mM ubiquinone and supporting electrolyte (Figure 6.8). Tests were conducted at ambient conditions, and the samples were illuminated by a 100 mW/cm^2 white light source from 10 to 20 s. The samples were held at the dark open circuit potential measured just before the test. Anodic photocurrent was produced in the presence of methyl viologen or ubiquinone-0. On average, ubiquinone-0 outperformed methyl viologen by more than a factor of two and was therefore chosen as the mediator for the study of the PSI-PEDOT:PSS LBL system.

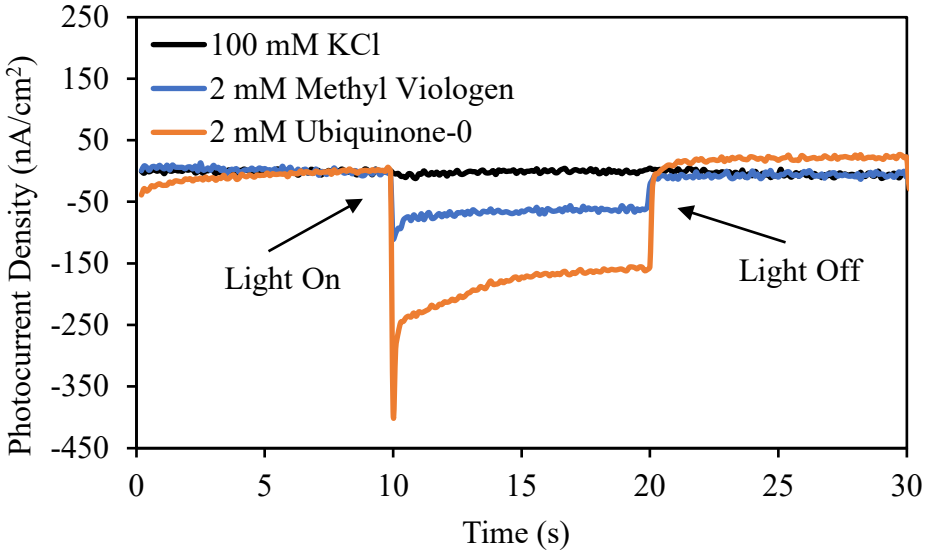

Figure 6.8. *Photochronoamperometry tests with 100 mM KCl(aq) supporting electrolyte only, 2 mM methyl viologen in 100 mM KCl, and 2 mM Ubiquinone-0 in 100 mM KCl. The sample shown has 3 layer pairs of PEDOT:PSS and PSI.*

Control tests were performed using a single layer of PEDOT:PSS atop an AET SAM-modified gold substrate (alternatively described as a 0.5-layer pair film) in the presence of the 2 mM ubiquinone-0 mediator, and the results are shown in Figure 6.9. These controls were taken to ensure that no photocurrent response can be attributed to the underlying electrode. A drifting current response was observed with no change upon illumination.

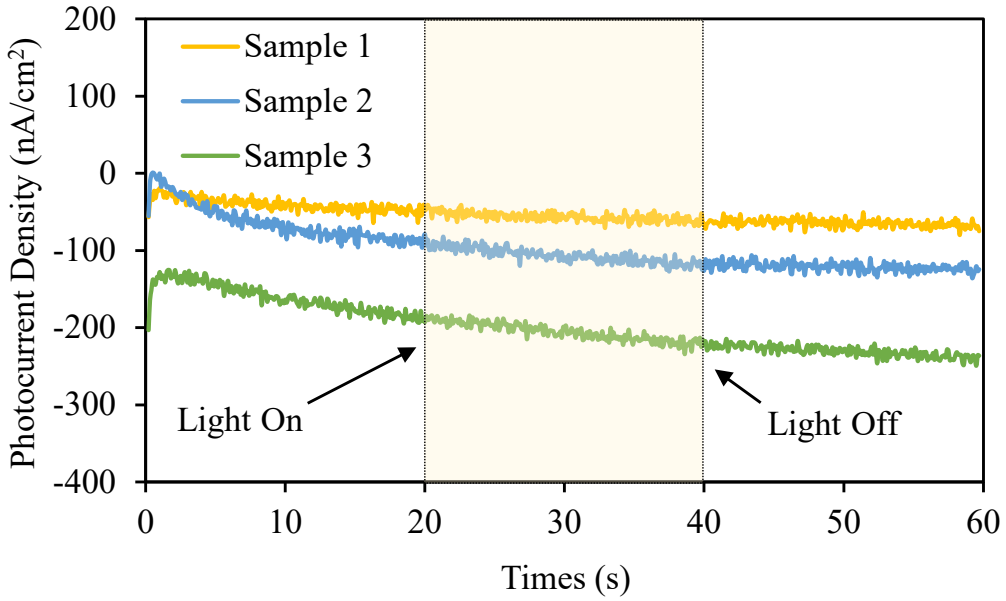

Figure 6.9. *Photochronoamperometric results from a single layer of PEDOT:PSS on top of an AET-modified gold substrate. Tests were performed in 2 mM ubiquinone-0 and 100 mM KCl at the measured dark open circuit potential. Each result represents an independently prepared control film.*

The ubiquinone-0 mediator produced higher photocurrents and was therefore chosen for further study of PSI activity in the LBL films. The films were tested under aerobic conditions and, therefore, the lower photocurrent produced by methyl viologen may be due to competing methyl viologen oxidation by dissolved oxygen species.[42] Ubiquinone-0 has been used as a mediator in PSI bioelectrodes and was shown to mitigate damage by reactive oxygen species during photocurrent production by Zhao et al.[43] Additionally, Friebe et al. have studied direct reductions of ubiquinone-0 by reaction centers of photosynthetic protein complexes.[44] The behavior of

ubiquinone-0 as an electrochemical mediator for PSI in LBL films was studied and the results are summarized in the following paragraphs. First, cyclic voltammetry of the tested mediators is shown in Figure 6.10. The reversible electron transfer process of ubiquinone-0 involves two electrons while the methyl viologen redox couple involves a single electron (evident based on the factor of 2 increase in current density at an equivalent mediator concentration). Additionally, ubiquinone-0 has a more positive half-wave potential ($E_{1/2,\ ubiquinone}$) than methyl viologen ($E_{1/2,\ MV}$). Figure 6.10 also shows why ubiquinone-0's more positive $E_{1/2}$ is significant. The more positive $E_{1/2}$ increases the overpotential for reduction of ubiquinone-0 at the F_B^- site ($\eta_{ubiquinone}$), which results in production of excess reduced ubiquinone-0 within the LBL film. Note that the overpotential for ubiquinone-0 oxidation vs. the P_{700} site is smaller in magnitude. The relationship between the overpotential of an electrochemical reaction and the reaction kinetics is given by the Butler-Volmer equation and the theory of mediated photocurrent generation by PSI is discussed in detail by Robinson et al. for the ferri/ferrocyanide mediator system.[45-46] We believe a similar mode of mediated electron transfer is facilitated by ubiquinone-0. Methyl viologen, however, has a more negative $E_{1/2}$ and a smaller overpotential for reduction vs. $F_B^{-\cdot}$ The lower overpotential for reduction and the competitive reaction of reduced methyl viologen with dissolved oxygen results in a lower anodic photocurrent generation in the presence of methyl viologen. Lastly, the cyclic voltammograms of ubiquinone-0 at varied pH gave nearly identical curves, which indicates that the ubiquinone-0 reduction (under these conditions) does not involve protonation. The mechanisms of quinone electrochemistry are complex and have been studied extensively.[47] To summarize, we believe the greater overpotential and the additional transferred electron result in greater photocurrent with ubiquinone-0 in comparison to methyl viologen.

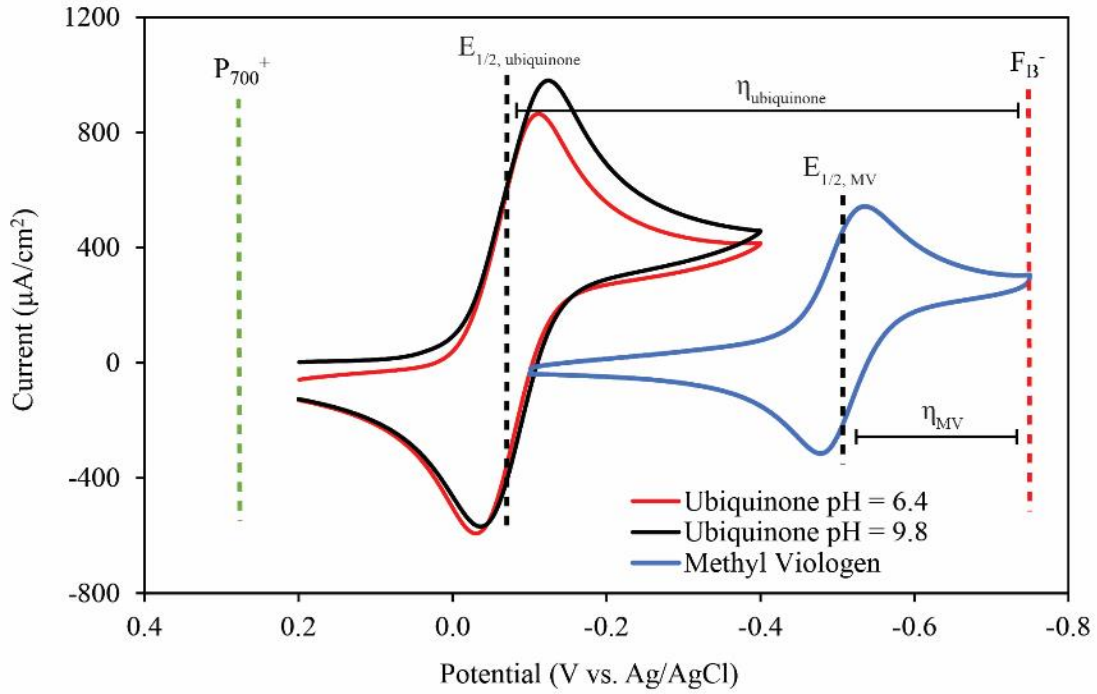

Figure 6.10. *Cyclic voltammograms of 2 mM methyl viologen and 2 mM ubiquinone-0 in 100 mM KCl taken at a scan rate of 100 mV/s on a gold working electrode. Cyclic voltammograms for ubiquinone-0 are given at pH = 6.4 and pH = 9.8. The pH = 9.8 scan was conducted by adjusting the solution pH using dilute NaOH.*

To determine the mode of electron transfer between PSI (within the LBL films) and the underlying gold electrode, the interactions between PSI and ubiquinone-0 were studied by measuring the open circuit potential (OCP) under various conditions. The OCP is the potential at which a near zero current is observed at the working electrode. The near zero current is observed because the electrode potential is at equilibrium with the potential of redox-active species in the solution. The OCP is therefore dependent on the concentrations of redox-active species in solution (as governed by the Nernst equation).[45] We observed that in the presence of even a single layer pair of PSI and PEDOT:PSS, the OCP of the electrode decreases by approximately ~150 mV (Figure 7.11). This finding led us to conclude that in the presence of PSI, the ratio of reduced to oxidized ubiquinone-0 in solution increases, shifting the observed OCP negative.

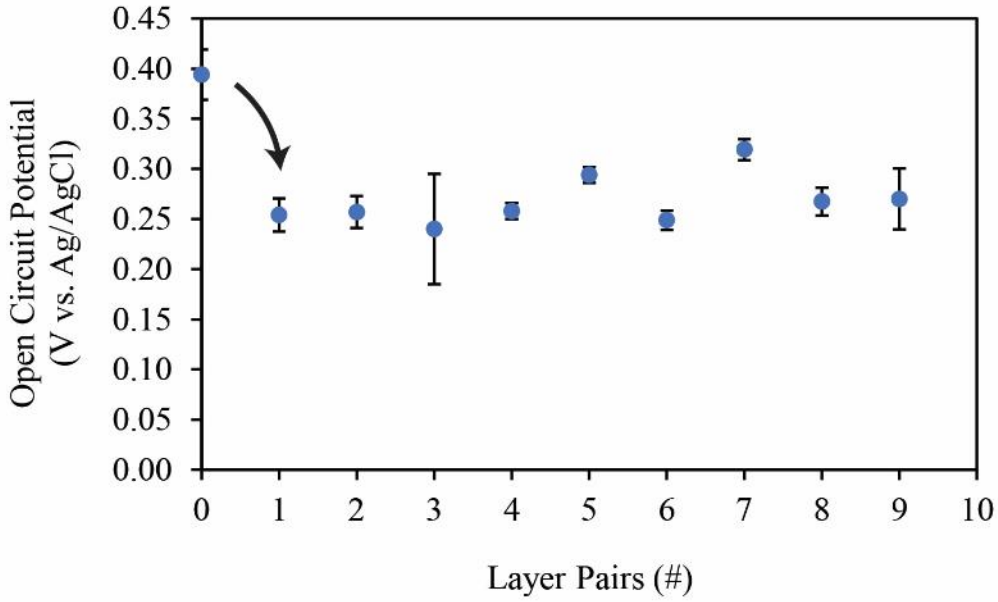

Figure 6.11. *Open-circuit potential (OCP) of LBL films under dark conditions ranging from zero to 9-layer pairs. The arrow denotes the change in solution equilibrium potential caused by the presence of PSI (further studied in Figure 6.12). Conditions are the same as for photochronoamperometric data given in Figures 6.15 and 6.16: 2 mM ubiquinone-0 in 100 mM KCl and atmospheric conditions.*

We then conducted OCP studies of ubiquinone-0 and PSI in solution (Figure 6.12) under dark conditions. These tests were conducted by measuring the OCP at an AET- and PEDOT:PSS-coated gold electrode (alternatively denoted as a 0.5 layer pair LBL film) with 2 mM ubiquinone-0 and 100 mM KCl present. After 120 s, an aliquot (1 mL) of A) PSI solution, B) deoxygenated PSI solution, or C) PSI extraction buffer without PSI was spiked into the electrochemical cell. Note that in the case of deoxygenated PSI (B), the ubiquinone-0 solution was also deoxygenated before the spiked solution was added. Curve D) shows a control of 100 mM KCl (without ubiquinone-0) as the initial solution and was spiked with PSI solution as in A). The results can be summarized by two statements. First, as seen in the OCP measurements of LBL films in Figure 6.11, in the presence of PSI and oxygen, ubiquinone-0 becomes reduced, as evident by the reduction of the OCP. Secondly, the production of reduced species does occur in the absence of PSI but to a lesser extent. We conclude that even under dark conditions, PSI shifts the redox

potential of a ubiquinone-0 mediator solution in the negative direction by producing reduced species and that this process must involve an oxygen intermediate.

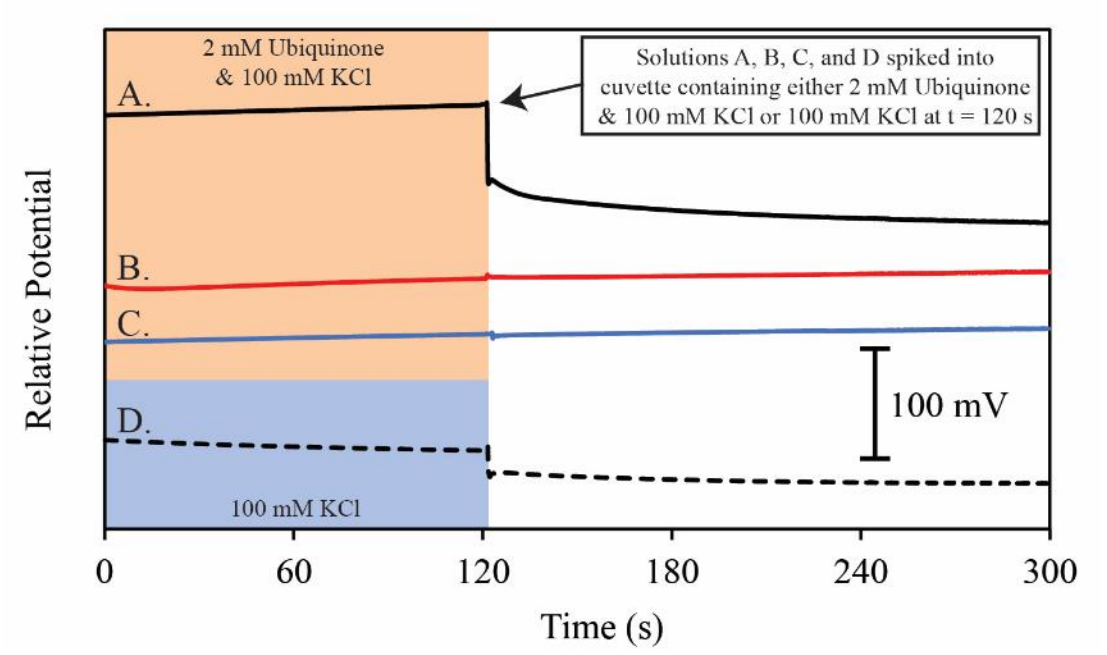

Figure 6.12. *Open-circuit potential (OCP) study of PSI and ubiquinone-0 under dark conditions. The OCP of solutions of either 2 mM ubiquinone-0 in 100 mM KCl (orange area) or 100 mM KCl (blue area) were monitored for 120 s then a 1 mL aliquot of A.) PSI solution, B.) deoxygenated PSI solution, C.) PSI elution buffer without PSI, or D.) PSI solution was spiked into the electrochemical cell. Note that the initial cell volume was 1 mL and the final volume (after addition of a 1 mL aliquot) was 2 mL and that these tests were performed in the dark.*

To show that the photocurrent is driven by the production of excess reduced species and is accelerated by the influx of photons and the excitation of PSI, we conducted chopped light potentiometry (Figure 6.13). Chopped light potentiometry was performed in solution at a gold working electrode with either 1 mL PSI solution and 1 mL 2 mM ubiquinone-0 (black), 1 mL elution buffer and 1 mL 2 mM ubiquinone-0 (blue), or 1 mL PSI and 1 mL 100 mM KCl (black, dashed). When PSI and ubiquinone-0 are present, a greater change in the OCP is observed when the solution is illuminated, compared to either ubiquinone-0 in the presence of elution buffer (the extraction buffer used to elute PSI) or PSI in supporting electrolyte (KCl). These results show that to produce an excess of reduced species, PSI needs ubiquinone-0 to be present, and that while

ubiquinone-0 exhibits some inherent light activity, the reduction of ubiquinone-0 is accelerated in the presence of PSI. These results agree with recent reports on the importance of dissolved oxygen in PSI bioelectrodes and the use of ubiquinone-0 as an electron acceptor from PSI.[19, 43-44, 48] In the chopped light experiment, upon illumination the potential decreases due to the production of reduced species near the electrode surface (resulting in a decrease in the measured chemical potential of the electrolyte solution). Further, because potential is being measured, very little current is allowed to pass through the working electrode and some time is required to reach a steady state equilibrium with respect to diffusion away from the electrode surface. The "saw-tooth" shape is observed because after the light is turned off, the excess reduced species produced by PSI diffuse into the bulk electrolyte. To summarize, the driving force behind the ubiquinone-0 mediated photocurrent is the production of excess reduced species by PSI in the presence of dissolved oxygen. During photochronoamperometry (Figures 6.15 and 6.16), the production of excess reduced species by PSI results in the collection of anodic photocurrent via the oxidation of reduced species at the PEDOT:PSS or the underlying gold electrode. Previous studies by our group have shown that PSI can exhibit unbalanced reaction kinetics with electrochemical mediators, which result in anodic photocurrent generation when an excess of reduced mediator is produced near the electrode.[46]

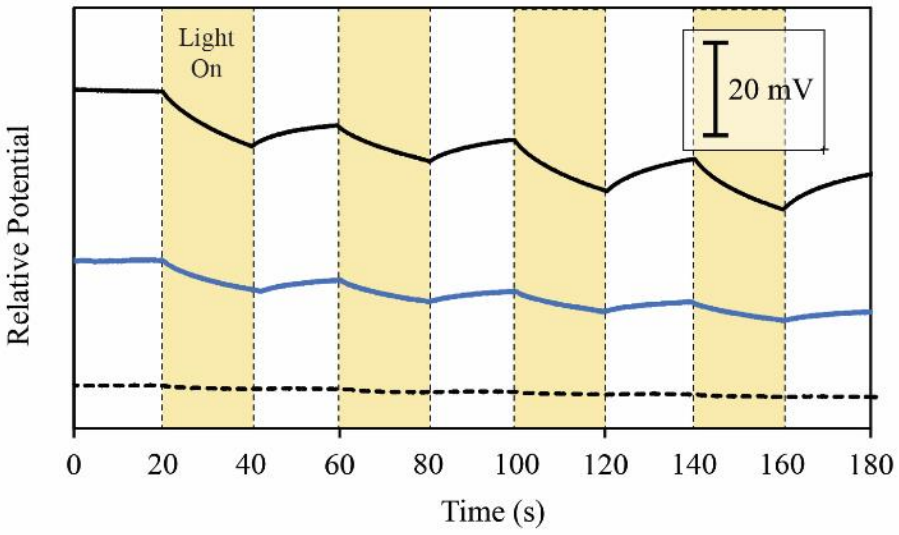

Figure 6.13. *Chopped light potentiometric study of PSI and ubiquinone-0. The potential at a gold working electrode was measured during illumination with a 100 mW/cm^2 white light source in the presence of 1 mL PSI solution and 1 mL 2 mM ubiquinone-0 (black), 1 mL elution buffer and 1 mL 2 mM ubiquinone-0 (blue), or 1 mL PSI and 1 mL 100 mM KCl (black, dashed).*

We also determined that the PEDOT:PSS interlayers act as a conductive framework, aiding in electron transfer to the underlying electrode and improving the photocurrent production of the LBL films. PEDOT:PSS acting as a conductive framework is supported by electrochemical impedance spectroscopy (EIS), which showed no observable increase in impedance with the addition of layer pairs (Figure 6.14). Figure 6.14 shows the results in Bode plot format in panel A and in a Nyquist plot in panel B. The lack of a dramatic change in impedance also supports our hypothesis that the maximal photocurrent for the 6-layer pair (see Figure 6.16) is not related to a transport barrier effect, but rather to a charging effect within the LBL films due to excited electrons produced by PSI only when the samples are illuminated.

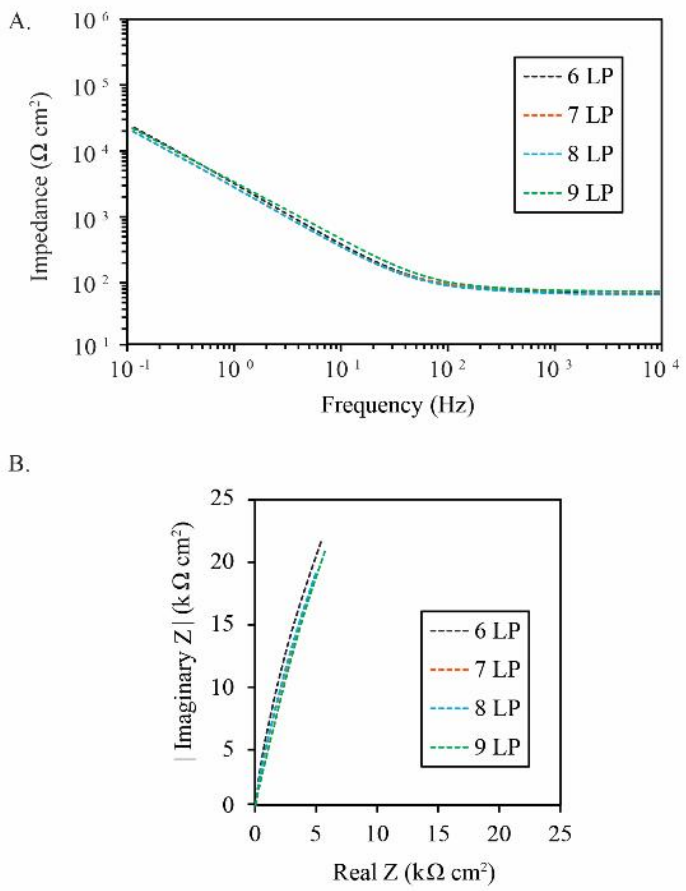

Figure 6.14. *Electrochemical impedance spectroscopy (EIS) was performed on a sample of 6-, 7-, 8-, and 9-layer pairs. EIS testing was performed at the open circuit potential over a frequency range of 0.1 to 10,000 Hz in a 100 mM KCl supporting electrolyte with a potential amplitude of 5 mV. Panel A gives a Bode plot representation of the data and panel B gives the same data in a Nyquist plot format. Note that in all tests the sample surface area was 0.21 cm².*

The LBL films were tested for photocurrent performance as soon as possible after the terminal PSI layer was deposited. Figure 6.15 shows representative PCA curves for samples with up to 9-layer pairs. The shape of the photocurrent curves indicates that two electron transfer processes are occurring. A photocurrent spike and diffusional loss is observed but the spike is hidden by a gradual increase in photocurrent. The spike behavior is typical of mediated electron transfer (MET) in a PSI film as reported by Robinson et al.[46] However, the diffusional loss or "diffusional tail" does not follow the typical shape for MET. Instead, an increase in current is

observed in the first 2 s of illumination, followed by a gradual decrease after ~2 s. We attribute this unique shape to a "saw-tooth" photocurrent limitation that has been observed in solid-state PSI devices.[10] In a saw-tooth response, the photocurrent increases gradually up to a maximum value and does not show signs of diffusional losses. An overlay of a "saw-toothed" photocurrent response and a typical MET response (a spike followed by a diffusional loss) yields the photocurrent shape observed in the LBL assemblies. We believe the combination of the photocurrent response shapes is due to the two modes of electron transfer. The first is MET from PSI to the PEDOT:PSS or underlying electrode (diffusional response) and the second is electron transfer through the PEDOT:PSS conductive framework (saw-tooth).

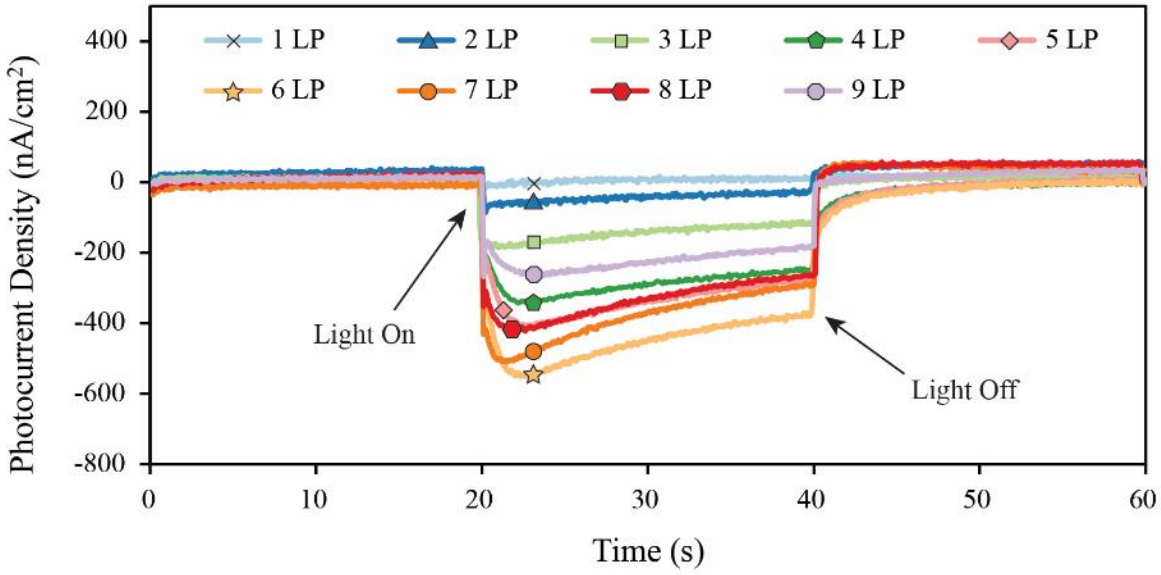

***Figure 6.15**. Representative PCA curves for each layer pair where the samples were illuminated from 20 to 40 s by a 100 mW/cm² white light source in the presence of 2 mM ubiquinone-0 and 100 mM KCl with the electrode held at the dark OCP.*

Figure 6.16 shows the average photocurrent after 15 s of illumination recorded for n = 3 samples of each type. The photocurrent of the LBL films increased in a linear manner up to 6-layer pairs, where a maximum value of 414 ± 13 nA/cm² was achieved, and then decreased with additional layers. We attribute the photocurrent maximum achieved at 6-layer pairs to charge

carrier trapping within the outer most PEDOT:PSS domains of the film.[23, 49-51] Charge carrier trapping has been observed in model LBL systems such as polybithiophene and polyviologen films.[51] As the number of layer pairs increases in the PSI-PEDOT:PSS films, electrons that have been excited by PSI may no longer have an energetically favorable path to the electrode due to film imperfections, inhomogeneity, and the resistance associated with the PSI interlayers. Instead of contributing to the observed photocurrent, these electrons will be trapped throughout the PEDOT:PSS framework where they impact the polymer's redox state and may lower conductivity. Based upon the trend in Figure 6.16, we believe the charging effect must increase as the distance from the electrode to the outermost layer increases and that charging within one layer can alter electron transfer from nearby layers. EIS data for 6- through 9-layer pairs (Figure 6.14) shows that no barrier effect to ion transfer is introduced with the additional layers, indicating that the charging effect occurs only during photocurrent production. The inability to collect these electrons and an overall decrease in film conductivity results in a tradeoff in performance at higher numbers of layer pairs, yielding a maximum photocurrent density between 5- and 7-layer pairs.

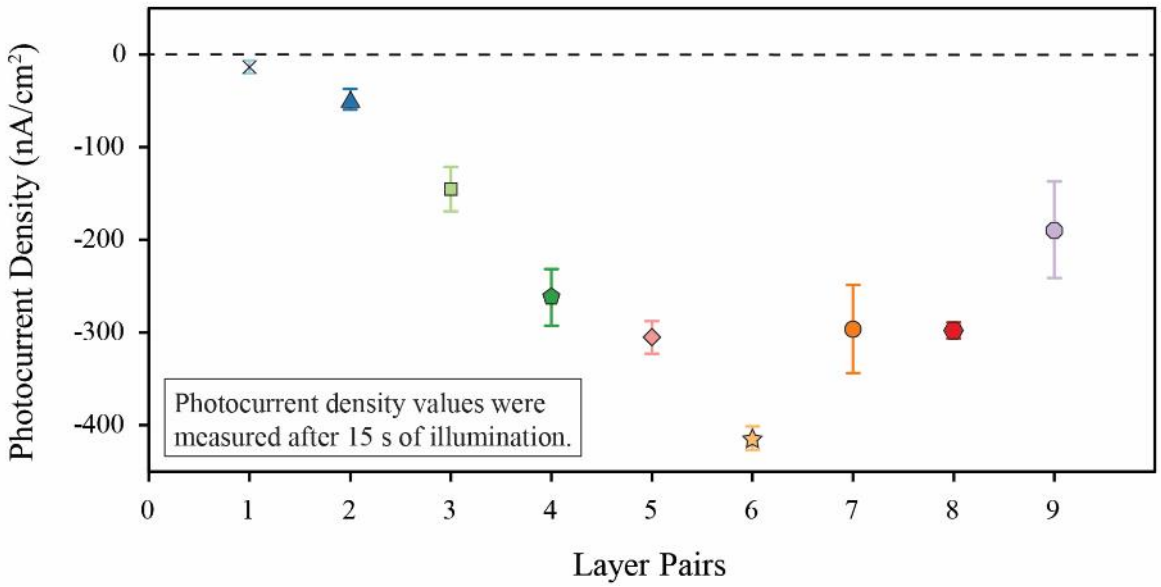

Figure 6.16. *Average photocurrent response after 15 s of illumination (at t = 35 s in Figure 6.15). Each data point represents 3 independently prepared samples (n = 3). All PCA data were obtained at open circuit potential (measured in the dark) and in the presence of 2 mM ubiquinone-0 and 100 mM KCl.*

Through a least-squares linear regression we determined that each additional layer pair (between 1- and 6-layer pairs) yields an increase of 83 ± 6 nA/cm^2 of anodic photocurrent. In comparison to previously reported PSI monolayers, which yielded approximately 90 nA/cm^2 when densely packed in a single monolayer on gold, the LBL system achieves a similar performance with each layer pair until saturation is reached at 6-layer pairs.[2] To our knowledge, this is the highest number of distinct PSI layers deposited in a layered film. Yehezkeli et al. reported a maximum in performance after just 3 layers of PSI deposition.[14] The ability to systematically build individual layers of PSI and conducting polymer is encouraging for the development of improved connectivity and higher loadings of PSI in films for both liquid electrochemical cells and solid-state PSI devices.

To ensure the observed photocurrent response can be directly attributed to the incorporation of PSI, an additional control test was conducted by preparing PSI that had been deactivated by ultraviolet light. Figure 6.17 shows UV-Visible absorbance spectra of PSI solutions that have been exposed to UV light (mercury UV lamp) for 0, 2, and 4 h. The characteristic PSI absorbance peaks at 680 and 440 nm diminish upon exposure and Rayleigh scattering increases (resulting in an increased background across all wavelengths).

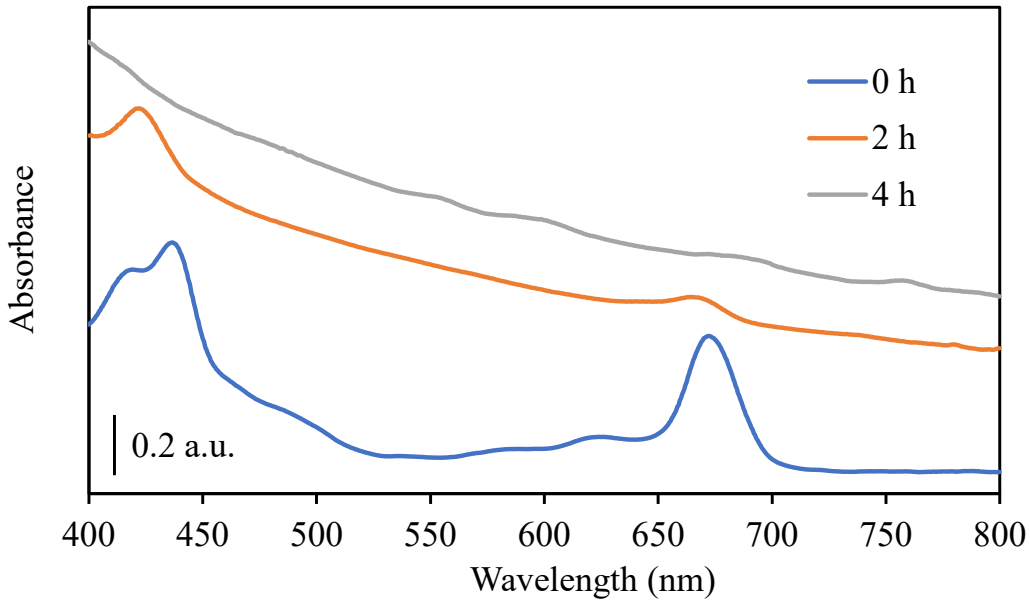

Figure 6.17. *UV-Vis Absorbance profiles of PSI before (0 h) and after exposure to a mercury UV lamp for 2 and 4 h. The characteristic PSI absorbance peaks at 680 and 440 nm disappear after exposure to UV and Rayleigh scattering across the visible spectrum is increased.*

The deactivated PSI was then used to prepare LBL films of 3-layer pairs. These samples were tested in a 2 mM ubiquinone-0 mediator solution, and the results are shown in Figure 6.18. A noisy and drifting background current was observed and no change in current occurred when the lamp illuminated the samples. Thus, we conclude that active PSI is required for photocurrent production in the LBL films reported in this manuscript.

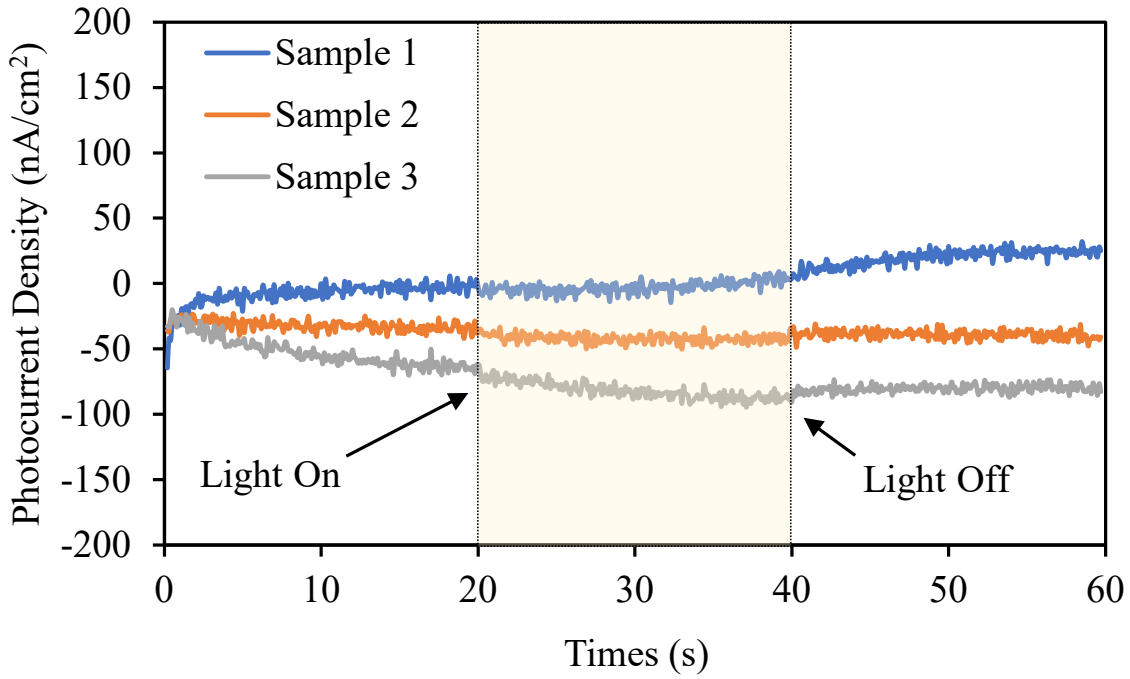

Figure 6.18. *Photochronoamperometric performance of 3-layer pair samples produced using deactivated PSI (exposed to UV light for 4 h). Each run represents an independently prepared film.*

The PSI LBL films exhibit a large photocurrent response for such a thin PSI film (~50 nm thickness at 6-layer pairs). To better understand how individual PSI complexes are performing in the LBL films, we analyzed the performance on a per PSI basis by calculating the turnover number (TN). The TN is calculated using Equation 6.1 and describes the photocurrent normalized to the quantity of PSI in the film.

$$TN\left(\frac{mol_{e^-}}{s * mol_{PSI}}\right) = \frac{i_{PCA}\left(\frac{A}{cm^2}\right)}{C_{PSI}\left(\frac{mol_{PSI}}{cm^2}\right) * F\left(\frac{C}{mol_{e^-}}\right)} \qquad \text{Eq. 6.1}$$

In Figure 6.19, the TN, as calculated from PCA data, is plotted for each number of layer pairs. When compared in terms of TN, a similar performance is achieved between 4- and 6-layer pairs. Thus, the negative impacts of loss of charge trapping result in similar TNs for 4-, 5- and 6-layer pairs before the TN decreases above 6-layer pairs. These results show that a trade-off in

performance is being made gradually, beginning at approximately 4-layer pairs. We also performed studies of densely packed, drop-cast PSI multilayer films atop a PEDOT:PSS film in the presence of 2 mM ubiquinone-0. Shown in red in Figure 6.19, multilayer films of PSI achieve a TN of 0.03 ± 0.01 $mol_{e^-}/(s\ mol_{PSI})$, an order of magnitude lower than the PSI-PEDOT:PSS LBL films that achieve 0.34 ± 0.03 $mol_{e^-}/(s\ mol_{PSI})$ for 4- to 6-layer pairs. Therefore, the LBL films not only increase the achievable loading of PSI but also enable more current to be produced by each PSI complex in the film when compared to a less organized PSI multilayer.

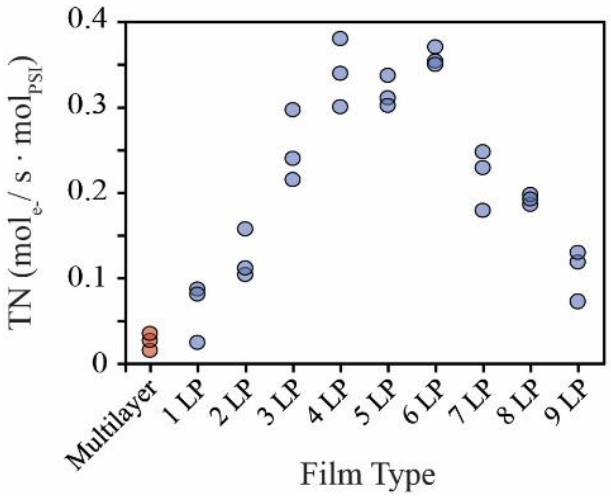

Figure 6.19. *Turnover numbers for LBL films based on photocurrent performance and quantity of PSI in the film. For multilayer films, the quantity of PSI was determined based on the concentration and volume of PSI solution deposited and for LBL films the amount of PSI was determined based on the number of densely packed monolayers present.*

Limitations of the current system include low light absorbance by such thin films and the MET by ubiquinone-0, both of which limit the amount of photocurrent. Circumventing the latter will require further study on the use of mixed mediators for enhanced electron and hole extraction from PSI. Nonetheless, the LBL films show linear increases in mediated photocurrent generation by ubiquinone-0 for each layer pair added up to 6-layer pairs and the achieved TN is also an order of magnitude greater than that of a densely packed PSI multilayer. These results along with the highly reproducible nature of the LBL assemblies show great promise for producing very thin and high performing PSI and PEDOT:PSS bioelectrodes.

Conclusions

The rapid deposition of alternating layers of PSI and PEDOT:PSS via LBL deposition was leveraged to produce layered assemblies up to 9-layer pairs thick. The ability to deposit these PSI-PEDOT:PSS LBL films is due to the favorable electrostatic interactions between the mixed charge surfaces of the PSI protein complex (Figure 6.1) and the PEDOT:PSS polymer. The LBL assemblies yielded alternating changes in contact angle throughout the deposition process along with a highly reproducible layer pair thickness of 8.11 ± 0.14 nm. An increase in photocurrent density of 83 ± 6 nA/cm^2 was observed with each additional layer pair from 1- to 6-layer pairs. The linear enhancement of the achieved photocurrent peaked at 6-layer pairs, producing 414 ± 13 nA/cm^2, and then decreased with additional layer pairs. We attribute the decrease in performance to charge carrier trapping within the outermost PEDOT:PSS layers due to an increase in resistance to electron transfer across or through the proteinaceous interlayers. The LBL films greatly outperform densely packed PSI multilayer films in terms of the turnover number (TN), proving that LBL assembly of PSI with an intrinsically conducting polymer provides benefits beyond increasing areal loading of the protein complex. Our results highlight the LBL process as an efficient and controllable means of depositing PSI films and show promise for tailoring of the PSI and PEDOT:PSS LBL system to produce a variety of biohybrid photovoltaic device architectures in the future.

References

1. Ciesielski, P. N.; Faulkner, C. J.; Irwin, M. T.; Gregory, J. M.; Tolk, N. H.; Cliffel, D. E.; Jennings, G. K., Enhanced Photocurrent Production by Photosystem I Multilayer Assemblies. *Adv. Funct. Mater.* **2010,** *20*, 4048-4054.

2. Faulkner, C. J.; Lees, S.; Ciesielski, P. N.; Cliffel, D. E.; Jennings, G. K., Rapid Assembly of Photosystem I Monolayers on Gold Electrodes. *Langmuir* **2008,** *24*, 8409-8412.

3. Kincaid, H. A.; Niedringhaus, T.; Ciobanu, M.; Cliffel, D. E.; Jennings, G. K., Entrapment of Photosystem I within Self-Assembled Films. *Langmuir* **2006,** *22* (19), 8114-8120.

4. Manocchi, A. K.; Baker, D. R.; Pendley, S. S.; Nguyen, K.; Hurley, M. M.; Bruce, B. D.; Sumner, J. J.; Lundgren, C. A., Photocurrent Generation from Surface Assembled Photosystem I on Alkanethiol Modified Electrodes. *Langmuir* **2013,** *29*, 2412-2419.

5. Mukherjee, D.; May, M.; Vaughn, M.; Bruce, B. D.; Khomami, B., Controlling the Morphology of Photosystem I Assembly on Thiol-Activated Au Substrates. *Langmuir* **2010,** *26* (20), 16048-16054.

6. Yan, X.; Faulkner, C. J.; Jennings, G. K.; Cliffel, D. E., Photosystem I in Langmuir–Blodgett and Langmuir–Schaefer Monolayers. *Langmuir* **2012,** *28* (42), 15080-15086.

7. Wang, P.; Frank, A.; Zhao, F.; Szczesny, J.; Junqueira, J. R. C.; Zacarias, S.; Ruff, A.; Nowaczyk, M. M.; Pereira, I. A. C.; Rögner, M.; Conzuelo, F.; Schuhmann, W., Closing the Gap for Electronic Short-Circuiting: Photosystem I Mixed Monolayers Enable Improved Anisotropic Electron Flow in Biophotovoltaic Devices. *Angew. Chem. Int. Ed.* **2020,** *n/a* (n/a).

8. Zhao, F.; Wang, P.; Ruff, A.; Hartmann, V.; Zacarias, S.; Pereira, I. A. C.; Nowaczyk, M. M.; Rögner, M.; Conzuelo, F.; Schuhmann, W., A photosystem I monolayer with anisotropic electron flow enables Z-scheme like photosynthetic water splitting. *Energy Environ. Sci.* **2019,** *12* (10), 3133-3143.

9. Robinson, M. T.; Simons, C. E.; Cliffel, D. E.; Jennings, G. K., Photocatalytic photosystem I/PEDOT composite films prepared by vapor-phase polymerization. *Nanoscale* **2017,** *9*, 6158-6166.

10. Gizzie, E. A.; Scott Niezgoda, J.; Robinson, M. T.; Harris, A. G.; Kane Jennings, G.; Rosenthal, S. J.; Cliffel, D. E., Photosystem I-polyaniline/TiO2solid-state solar cells: Simple devices for biohybrid solar energy conversion. *Energy Environ. Sci.* **2015,** *8*, 3572-3576.

11. Zhao, F.; Sliozberg, K.; Rögner, M.; Plumeré, N.; Schuhmann, W., The Role of Hydrophobicity of Os-Complex-Modified Polymers for Photosystem 1 Based Photocathodes. *J. Electrochem. Soc.* **2014,** *161*, H3035-H3041.

12. Badura, A.; Guschin, D.; Kothe, T.; Kopczak, M. J.; Schuhmann, W.; Rögner, M., Photocurrent generation by photosystem 1 integrated in crosslinked redox hydrogels. *Energy Environ. Sci.* **2011,** *4*, 2435-2440.

13. Dervishogullari, D.; Gizzie, E. A.; Jennings, G. K.; Cliffel, D. E., Polyviologen as Electron Transport Material in Photosystem I-Based Biophotovoltaic Cells. *Langmuir* **2018**.

14. Yehezkeli, O.; Tel-Vered, R.; Michaeli, D.; Nechushtai, R.; Willner, I., Photosystem I (PSI)/Photosystem II (PSII)-Based Photo-Bioelectrochemical Cells Revealing Directional Generation of Photocurrents. *Small* **2013,** *9* (17), 2970-2978.

15. Efrati, A.; Lu, C.-H.; Michaeli, D.; Nechushtai, R.; Alsaoub, S.; Schuhmann, W.; Willner, I., Assembly of photo-bioelectrochemical cells using photosystem I-functionalized electrodes. *Nat. Energy* **2016,** *1* (2), 15021.

16. Kazemzadeh, S.; Riazi, G.; Ajeian, R., Novel Approach of Biophotovoltaic Solid State Solar Cells Based on a Multilayer of PS1 Complexes as an Active Layer. *ACS Sustain. Chem. Eng.* **2017,** *5*, 9836-9840.

17. Barhom, H.; Carmeli, C.; Carmeli, I., Fabrication of Electronic Junctions between Oriented Multilayers of Photosystem I and the Electrodes of Optoelectronic Solid-State Devices. *J. Phys. Chem. B* **2021,** *125* (3), 722-728.

18. Gizzie, E. A.; LeBlanc, G.; Jennings, G. K.; Cliffel, D. E., Electrochemical Preparation of Photosystem I–Polyaniline Composite Films for Biohybrid Solar Energy Conversion. *ACS Appl. Mater. Interfaces* **2015,** *7* (18), 9328-9335.

19. Wolfe, K. D.; Dervishogullari, D.; Passantino, J. M.; Stachurski, C. D.; Jennings, G. K.; Cliffel, D. E., Improving the stability of photosystem I–based bioelectrodes for solar energy conversion. *Curr. Opin. Electrochem.* **2020,** *19*, 27-34.

20. Leaf, M. A.; Muthukumar, M., Electrostatic Effect on the Solution Structure and Dynamics of PEDOT:PSS. *Macromolecules* **2016,** *49* (11), 4286-4294.

21. Amunts, A.; Toporik, H.; Borovikova, A.; Nelson, N., Structure determination and improved model of plant photosystem I. *J. Bio. Chem.* **2010,** *285*, 3478-3486.

22. Crespilho, F.; Zucolotto, V.; Oliveira, O., Electrochemistry of Layer-by-Layer Films: a review. *Int. J. Electrochem. Sci.* **2006,** *1*.

23. DeLongchamp, D. M.; Kastantin, M.; Hammond, P. T., High-Contrast Electrochromism from Layer-By-Layer Polymer Films. *Chem. Mater.* **2003,** *15* (8), 1575-1586.

24. Lvov, Y. M.; Lu, Z.; Schenkman, J. B.; Zu, X.; Rusling, J. F., Direct Electrochemistry of Myoglobin and Cytochrome P450cam in Alternate Layer-by-Layer Films with DNA and Other Polyions. *J. Am. Chem. Soc.* **1998,** *120* (17), 4073-4080.

25. Ventrella, A.; Catucci, L.; Placido, T.; Longobardi, F.; Agostiano, A., Photosystem II based multilayers obtained by electrostatic layer-by-layer assembly on quartz substrates. *J. Bioenerg. Biomembr.* **2014,** *46* (3), 221-228.

26. Zhao, J.; Liu, B.; Zou, Y.; Xu, C.; Kong, J., Photoelectric conversion of photosynthetic reaction center in multilayered films fabricated by layer-by-layer assembly. *Electrochim. Acta* **2002,** *47* (12), 2013-2017.

27. Cao, Y.; Chen, D.; Wu, X.; Kong, J.; Zou, Y.; Xu, C., Probing Electron Transfer of the Redox Species in Wild-Type Rc Protein and its Pigment-Replaced Mutants Re-Constituted in Self-Assembly Monolayers. *Anal. Lett*. **2001**, 34 (5), 713-725.

28. Kong, J.; Sun, W.; Wu, X.; Deng, J.; Lu, Z.; Lvov, Y.; Desamero, R. Z. B.; Frank, H. A.; Rusling, J. F., Fast reversible electron transfer for photosynthetic reaction center from wild type Rhodobacter sphaeroides re-constituted in polycation sandwiched monolayer film. *Bioelectrochem. Bioenerg.* **1999,** *48* (1), 101-107.

29. Stieger, K. R.; Ciornii, D.; Kölsch, A.; Hejazi, M.; Lokstein, H.; Feifel, S. C.; Zouni, A.; Lisdat, F., Engineering of supramolecular photoactive protein architectures: the defined co-assembly

of photosystem I and cytochrome c using a nanoscaled DNA-matrix. *Nanoscale* **2016,** *8*, 10695-10705.

30. Ciesielski, P. N.; Scott, A. M.; Faulkner, C. J.; Berron, B. J.; Cliffel, D. E.; Jennings, G. K., Functionalized Nanoporous Gold Leaf Electrode Films for the Immobilization of Photosystem I. *ACS Nano* **2008,** *2*, 2465-2472.

31. Decher, G.; Eckle, M.; Schmitt, J.; Struth, B., Layer-by-layer assembled multicomposite films. *Curr. Opin. Colloid Interface Sci.* **1998,** *3* (1), 32-39.

32. Duc, C.; Malliaras, G. G.; Senez, V.; Vlandas, A., Long-term ageing of PEDOT:PSS: wettability Study. *Synth. Met.* **2018,** *238*, 14-21.

33. Tang, Z.; Donohoe, S. T.; Robinson, J. M.; Chiarelli, P. A.; Wang, H.-L., Film formation, surface character, and relative density for electrochromic PEI/(PSS:PEDOT) multilayered thin films. *Polymer* **2005,** *46* (21), 9043-9052.

34. Jurin, F. E.; Buron, C. C.; Martin, N.; Monney, S.; Filiâtre, C., Electrical conductivity enhancement and wettability modification of (PDDA/PEDOT:PSS)n multilayer film. *Thin Solid Films* **2018,** *664*, 33-40.

35. Laibinis, P. E.; Bain, C. D.; Nuzzo, R. G.; Whitesides, G. M., Structure and Wetting Properties of .omega.-Alkoxy-n-alkanethiolate Monolayers on Gold and Silver. *J. Phys. Chem.* **1995,** *99* (19), 7663-7676.

36. Seekaew, Y.; Lokavee, S.; Phokharatkul, D.; Wisitsoraat, A.; Kerdcharoen, T.; Wongchoosuk, C., Low-cost and flexible printed graphene–PEDOT:PSS gas sensor for ammonia detection. *Org. Electron.* **2014,** *15* (11), 2971-2981.

37. Yoo, D.; Kim, J.; Kim, J. H., Direct synthesis of highly conductive poly(3,4-ethylenedioxythiophene):poly(4-styrenesulfonate) (PEDOT:PSS)/graphene composites and their applications in energy harvesting systems. *Nano Research* **2014,** *7* (5), 717-730.

38. Friedel, B.; Keivanidis, P. E.; Brenner, T. J. K.; Abrusci, A.; McNeill, C. R.; Friend, R. H.; Greenham, N. C., Effects of Layer Thickness and Annealing of PEDOT:PSS Layers in Organic Photodetectors. *Macromolecules* **2009,** *42* (17), 6741-6747.

39. Bahry, T.; Cui, Z.; Deniset-Besseau, A.; Gervais, M.; Sollogoub, C.; Bui, T.-T.; Remita, S., An alternative radiolytic route for synthesizing conducting polymers in an organic solvent. *New J. Chem.* **2018,** *42* (11), 8704-8716.

40. de Barros, A.; Constantino, C. J. L.; da Cruz, N. C.; Bortoleto, J. R. R.; Ferreira, M., High performance of electrochemical sensors based on LbL films of gold nanoparticles, polyaniline and sodium montmorillonite clay mineral for simultaneous detection of metal ions. *Electrochim. Acta* **2017,** *235*, 700-708.

41. de Barros, A.; Ferreira, M.; Constantino, C. J. L.; Ferreira, M., Nanocomposites based on LbL films of polyaniline and sodium montmorillonite clay. *Synth. Met.* **2014,** *197*, 119-125.

42. Zhao, F.; Hardt, S.; Hartmann, V.; Zhang, H.; Nowaczyk, M. M.; Rögner, M.; Plumeré, N.; Schuhmann, W.; Conzuelo, F., Light-induced formation of partially reduced oxygen species limits the lifetime of photosystem 1-based biocathodes. *Nature Comm.* **2018,** *9*.

43. Zhao, F.; Ruff, A.; Rögner, M.; Schuhmann, W.; Conzuelo, F., Extended Operational Lifetime of a Photosystem-Based Bioelectrode. *J. Am. Chem. Soc.* **2019,** *141*, 5102-5106.

44. Friebe, V. M.; Swainsbury, D. J. K.; Fyfe, P. K.; van der Heijden, W.; Jones, M. R.; Frese, R. N., On the mechanism of ubiquinone mediated photocurrent generation by a reaction center based photocathode. *Biochim. Biophys. Acta Bioenerg.* **2016,** *1857*, 1925-1934.

45. Bard, A. J., Electrochemical methods : fundamentals and applications / Allen J. Bard, Larry R. Faulkner. Wiley: New York, New York. **1980**.

46. Robinson, M. T.; Cliffel, D. E.; Jennings, G. K., An Electrochemical Reaction-Diffusion Model of the Photocatalytic Effect of Photosystem I Multilayer Films. *J. Phys. Chem. B* **2018,** *122* (1), 117-125.

47. Gulaboski, R.; Markovski, V.; Jihe, Z., Redox chemistry of coenzyme Q—a short overview of the voltammetric features. *J. Solid State Electrochem.* **2016,** *20* (12), 3229-3238.

48. Morlock, S.; Subramanian, S. K.; Zouni, A.; Lisdat, F., Scalable Three-Dimensional Photobioelectrodes Made of Reduced Graphene Oxide Combined with Photosystem I. *ACS Appl. Mater. Interfaces* **2021,** *13* (9), 11237-11246.

49. Abruna, H. D.; Denisevich, P.; Umana, M.; Meyer, T. J.; Murray, R. W., Rectifying interfaces using two-layer films of electrochemically polymerized vinylpyridine and vinylbipyridine complexes of ruthenium and iron on electrodes. *J. Am. Chem. Soc.* **1981,** *103* (1), 1-5.

50. Ruths, J.; Essler, F.; Decher, G.; Riegler, H., Polyelectrolytes I: Polyanion/Polycation Multilayers at the Air/Monolayer/Water Interface as Elements for Quantitative Polymer Adsorption Studies and Preparation of Hetero-superlattices on Solid Surfaces. *Langmuir* **2000,** *16* (23), 8871-8878.

51. Hillman, A. R.; Mallen, E. F., Electroactive bilayers employing conducting polymers. Part 2.—Speciation by in situ spectroscopy. *J. Chem. Soc., Faraday Trans.* **1991,** *87* (14), 2209-2217.

Chapter 7 – Introduction to Electrochemical Nicotinamide Cofactor Regeneration

In collaboration with National Renew. Energy Laboratory (NREL) scientists Yannick J. Bomble, Michael E. Himmel, Marcus Alahuhta, Chapters 7-9 of this dissertation explores the electrochemical regeneration of NADH from NAD^+ for use in an enzymatic bioreactor to produce 2,3-butanediol (2,3-BD). Text and figures reported in the following sections are adapted or reproduced from update reports submitted to Yannick J. Bomble as partial fulfillment of subcontract number XEJ-9-92257-01 (prime contract number DE-AC36-08GO28308). All data, figures, and text were produced by the author (Kody D. Wolfe).

Nicotinamide cofactors (NAD^+/NADH/$NADP^+$/NADPH) are used in many biosynthetic processes and are a costly feedstock.[1-2] Specifically, the metabolic pathways of acetogenic microorganisms have been studied in an effort to diversify the available sources of 2,3-BD, a feedstock for the production of many commodity chemicals.[3,4] 2,3-BD is typically produced as a byproduct of the oil refining process and earns a market of 40+ billion dollars in sales each year.[4] As society transitions from a primarily fossil fuel based economy, we will need to find alternative sources of petroleum based products. Many microorganisms are capable of producing 2,3-BD.[3] However, isolating the specific enzymes that catalyze the production of 2,3-BD in these organisms may provide a pathway to a more efficient production process. While solely electrochemical methods of 2,3-BD synthesis have been developed, enzymatic routes benefit from the natural selectivity and efficiency of acetogenic organisms. Therefore, a combination of an enzymatic pathway with the control enabled by electrochemical methods of cofactor regeneration would enable the development of an electrochemically controlled enzymatic pathway with high yield and selectivity for 2,3-BD.[5]

The specific target application of this work is the production of 2,3-BD from a feedstock of pyruvate based on an electrochemical platform. In an ideal scenario, the reduction of NAD^+ to the cofactor NADH will be performed at an electrode, with three enzymes, which are necessary for the complete conversion of pyruvate to 2,3 butanediol, immobilized near the electrode surface, Figure 7.1.A. The complete enzymatic pathway of interest is given in Figure 7.1.B. NADH is consumed by acetoin reductase to convert acetoin to 2,3 butanediol. Because NADH is the energy source for this reduction reaction, control over the turnover of NAD^+ to NADH is highly desirable. Therefore, the foremost goal is to design an electrode that facilitates NAD^+ reduction and is suitable for the immobilization of the three enzymes necessary to produce 2,3-BD.

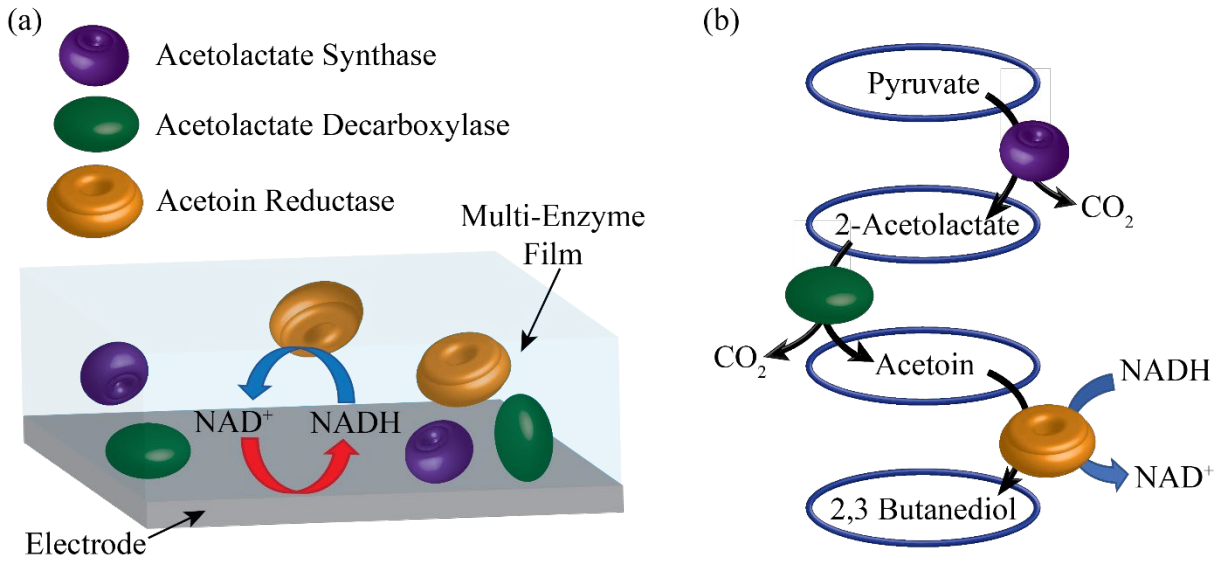

Figure 7.1. *(A) The proposed multi-enzyme electrode for the production of 2,3-butanediol. The electrode drives the production of 2,3-butanediol (2,3-BD) by replenishing the NADH cofactor to be consumed by acetoin reductase. (B) The production of 2,3-BD from pyruvate via a three-enzyme pathway.*

In comparison to purely enzymatic or cellular turnover of cofactors, electrochemical regeneration provides numerous advantages.[1-2, 6] The first is that the chemical energy for the reaction is cheaper. Non-electrochemical routes for regeneration require a chemical electron source or sink to provide the electron needed for the reduction or oxidation of a cofactor.

Electrochemical regeneration allows for the use of electricity provided directly to the electrode as the electron source or sink. Electricity is much cheaper than chemical feedstock, does not require storage, is much simpler to distribute or transport, and results in no waste stream to be separated and disposed.[2] Another advantage of electrochemical regeneration is the control over the regeneration rate.[6] The rate of reaction can be controlled by varying the current at the electrode, a streamlined approach compared to varying feedstock flow rates as in enzymatic or cellular turnover. Electrochemical cofactor regeneration has been long sought after and has the potential to enable the feasibility of biosynthesis of many desirable commodity chemicals.

Electrochemical reduction of NAD^+ to NADH is a two electron, single proton exchange.[7] Figure 7.2 shows the mechanism of NAD^+ reduction at an electrode. First, NAD^+ adsorbs to the electrode surface and accepts a single electron to produce a radical species, $NAD^\bullet$. Next, a proton attacks the $NAD^\bullet$, yielding $NADH^+$. Finally, a second electron reduces the positively charged $NADH^+$, resulting in the generation of NADH. The second electron transfer occurs at a much greater overpotential, reported at -1.6 V vs. SCE on a mercury electrode.[7] An alternative pathway is possible, in which $NAD^\bullet$ dimerizes forming $(NAD)_2$. However, it is suspected that dimer dissociation often results in the production of biologically inactive 1,6-NADH. Critical factors in the NAD^+ reduction reaction include the adsorption density, conformation of the adsorbed species, proton concentration, and rate of dimer dissociation.[7]

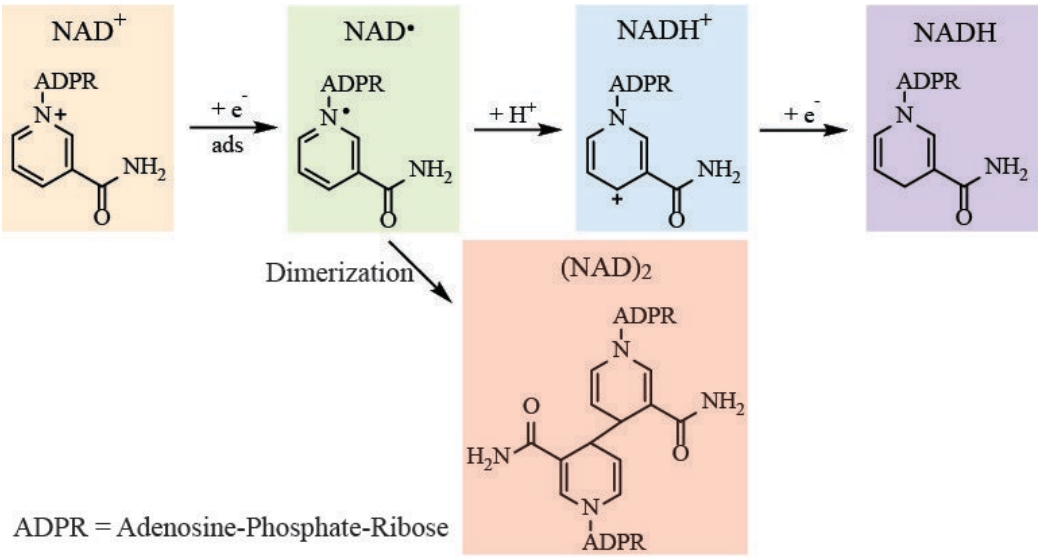

Figure 7.2. *Mechanism of electrochemical NAD^+ reduction. The desired overall reaction pathway is a two electron, single proton addition following the mechanism of ECE. Inactive $(NAD)_2$ dimers may form after the first electron transfer.*

Efforts aimed at the electrochemical regeneration of NADH form NAD^+ typically fall into two categories: the employment of organometallic catalysts or the use of surface immobilized metal catalysts.[2] The use of organometallic complexes, typically containing ruthenium, rhodium, osmium, or iridium, has been shown to catalyze the reduction of NAD^+ both in solution and immobilized or found in a redox polymer.[2, 8-10] This approach significantly lowers the reaction overpotential but is complicated by the necessity of synthesizing organometallics and tethering them to an electrode surface while retaining conductivity. Second, the use of nanostructured metals with high affinity for proton adsorption has been shown to improve the reaction by avoiding biologically inactive byproducts such as NAD dimers and 1,6-NADH.[2, 11,12] Others have used biological species known to bind to NAD^+ in attempt to lower the reduction overpotential by promoting surface adsorption of NAD^+.[13] As mentioned, the important metrics of improving the NAD^+ reduction is lowering the overpotential and avoiding the production of biologically inactive byproducts. The strategy used in this dissertation is the deposition of platinum monolayers to promote the NAD^+ reduction reaction by increasing the surface concentration of adsorbed hydrogen. Ali et al. and others have demonstrated high yields of active NADH production at

platinum-modified glassy carbon electrodes.[14-16] Inspired by their findings, the work presented in Chapter 9 uses carbon paper electrodes with platinum monolayers to lower the mass of platinum needed, therefore lowering the cost of production of NADH per cost of catalyst.

The following chapters highlight work toward the development of an efficient and applicable electrochemical NAD^+ to NADH regeneration scheme. First, Chapter 8 covers the stability of NAD^+/NADH in aqueous buffers of relevant conditions for bioreactors. While there are literature studies of cofactor stability, they are often incomplete and are not undertaken in conditions suitable for stability of both the oxidized and reduced forms of the cofactors, which is a requisite for a regeneration reaction. Chapter 8 highlights the long-term stability of both oxidized and reduced cofactors (NAD^+/NADH) in tris (tris(hydroxymethyl)aminomethane) buffer at a pH of 8.5. Then, Chapter 9 discusses work on the development of a low-cost carbon paper electrode modified with monolayer platinum for NAD^+ reduction. Both long-term stability and efficient electrochemical reduction at an electrode are necessary for cost-effective electrochemical cofactor regeneration and the efforts reported here are necessary steps toward the development of such a system for the enzymatic production of 2,3-BD.

References

1. Cravens, A.; Payne, J.; Smolke, C. D., Synthetic biology strategies for microbial biosynthesis of plant natural products. *Nature Comm.* **2019,** *10* (1), 2142.
2. Lee, Y. S.; Gerulskis, R.; Minteer, S. D., Advances in electrochemical cofactor regeneration: enzymatic and non-enzymatic approaches. *Curr. Opin. Biotechnol.* **2022,** *73*, 14-21.
3. Köpke, M.; Mihalcea, C.; Liew, F.; Tizard, J. H.; Ali, M. S.; Conolly, J. J.; Al-Sinawi, B.; Simpson, S. D., 2,3-butanediol production by acetogenic bacteria, an alternative route to chemical synthesis, using industrial waste gas. *Appl. Environ. Microbiol.* **2011,** *77* (15), 5467-5475.
4. Celińska, E.; Grajek, W., Biotechnological production of 2,3-butanediol—Current state and prospects. *Biotechnol. Adv.* **2009,** *27* (6), 715-725.
5. Ochoa-Gómez, J. R.; Fernández-Carretero, F.; Río-Pérez, F.; García-Luis, A.; Roncal, T.; García-Suárez, E. J., Electrosynthesis of 2,3-butanediol and methyl ethyl ketone from acetoin in flow cells. *Green Chemistry* **2019,** *21* (1), 164-177.
6. Chenault, H. K.; Simon, E. S.; Whitesides, G. M., Cofactor Regeneration for Enzyme-Catalysed Synthesis. *Biotechnol. Genet. Eng. Rev.* **1988,** *6* (1), 221-270.

7. Elving, P. J.; Bresnahan, W. T.; Moiroux, J.; Samec, Z., Nad Nadh as a Model Redox System - Mechanism, Mediation, Modification by the Environment. *Bioelectrochem. Bioenerg.* **1982,** *9* (3), 365-378.

8. Tan, B. X.; Hickey, D. P.; Milton, R. D.; Giroud, F.; Minteer, S. D., Regeneration of the NADH Cofactor by a Rhodium Complex Immobilized on Multi-Walled Carbon Nanotubes. *J. Electrochem. Soc.* **2015,** *162* (3), H102-H107.

9. Hollmann, F.; Witholt, B.; Schmid, A., [Cp*Rh(bpy)(H2O)](2+): a versatile tool for efficient and non-enzymatic regeneration of nicotinamide and flavin coenzymes. *J. Mol. Cat. B Enzym.* **2002,** *19*, 167-176.

10. Walcarius, A.; Nasraoui, R.; Wang, Z. J.; Qu, F. L.; Urbanova, V.; Etienne, M.; Gollu, M.; Demir, A. S.; Gajdzik, J.; Hempelmann, R., Factors affecting the electrochemical regeneration of NADH by (2,2 '-bipyridyl) (pentamethylcyclopentadienyl)-rhodium complexes: Impact on their immobilization onto electrode surfaces. *Bioelectrochemistry* **2011,** *82* (1), 46-54.

11. Kim, S.-H.; Chung, G.-Y.; Kim, S.-H.; Vinothkumar, G.; Yoon, S.-H.; Jung, K.-D., Electrochemical NADH regeneration and electroenzymatic CO2 reduction on Cu nanorods/glassy carbon electrode prepared by cyclic deposition. *Electrochim. Acta* **2016,** *210*, 837-845.

12. Damian, A.; Omanovic, S., Electrochemical reduction of NAD+ on a polycrystalline gold electrode. *J. Mol. Catal. A: Chem.* **2006,** *253* (1), 222-233.

13. Long, Y. T.; Chen, H. Y., Electrochemical regeneration of coenzyme NADH on a histidine modified silver electrode. *J. Electroanal. Chem.* **1997,** *440* (1-2), 239-242.

14. Ali, I.; Gill, A.; Omanovic, S., Direct electrochemical regeneration of the enzymatic cofactor 1,4-NADH employing nano-patterned glassy carbon/Pt and glassy carbon/Ni electrodes. *Chem. Eng. J.* **2012,** *188*, 173-180.

15. Ali, I.; Khan, T.; Omanovic, S., Direct electrochemical regeneration of the cofactor NADH on bare Ti, Ni, Co and Cd electrodes: The influence of electrode potential and electrode material. *J. Mol. Catal. A: Chem.* **2014,** *387*, 86-91.

16. Ali, I.; Ullah, N.; McArthur, M. A.; Coulombe, S.; Omanovic, S., Direct electrochemical regeneration of enzymatic cofactor 1,4-NADH on a cathode composed of multi-walled carbon nanotubes decorated with nickel nanoparticles. *Can. J. Chem. Eng.* **2018,** *96* (1), 68-73.

Chapter 8 – Long-Term Stability of NAD^+/NADH in Aqueous Buffers

The work included in this chapter is in collaboration with National Renew. Energy Laboratory (NREL) scientists Yannick J. Bomble, Michael E. Himmel, and Marcus Alahuhta under subcontract number XEJ-9-92257-01 (prime contract number DE-AC36-08GO28308). Marcus Alahuhta provided the nicotinamide oxidase enzyme used herein. Text and figures are adapted or reproduced from update reports submitted to Yannick J. Bomble. All data, figures, and text were produced by the author (Kody D. Wolfe).

Introduction

The stability of the NAD(H) cofactor in solution is a serious concern when considering the possibility of long-term cofactor regeneration.[1-3] Unfortunately, nicotinamide cofactors have complex degradation considerations. Specifically, the oxidized form (NAD^+) undergoes base-catalyzed degradation at high pH values while the reduced form (NADH) undergoes acid-catalyzed degradation at low pH values. Chenault and Whitesides have reported on the stability of nicotinamide cofactors including a summary figure showing that the NAD^+/NADH system may have an optimum pH of approximately 8.5, with respect to minimizing degradation of both species.[1] The total degradation rate of the reduced form of the cofactor can be summarized by Equation 8.1 where k_{obs} is the total first-order rate constant of NADH degradation, k_w is the rate constant for general degradation, k_{H+} is the rate constate for general acid-catalyzed degradation, and k_{HA} is the rate constant for specific acid-catalyzed degradation.[1] A similar equation may be written for the base catalyzed degradation of NAD^+.

$$k_{obs} = k_w + k_{H+} + k_{HA} \qquad \text{Equation 8.1}$$

General degradation (k_w) is predominantly a function of temperature while acid-catalyzed degradation (k_{H+}) is dependent on the pH of the solution. The specific acid-catalyzed degradation (k_{HA}) is dependent on the concentration of the specific acid (HA), which is a function of the solution pH and the pKa of the specific acid. Further, experimental studies have shown that the degradation rate is highly sensitive to the solution pH and the specific acid present.[2] Typically, the specific acid present is the conjugate acid found in the chosen buffer. Therefore, buffers with high

pKa values result in a lower concentration of HA and reduce the rate of NADH degradation. Note that the degradation of NAD^+ is base- and specific base-catalyzed and the opposite trend holds true.

Optimal conditions for solutions containing NAD^+ and NADH have been reported as pH = ~8.5, room temperature or cooler, and biologically relevant buffers with high pKa values such as HEPES and Tris buffers.[1] Additionally, phosphate containing buffers have been shown to have high rates of specific acid-catalyzed degradation of NADH.[1, 4-6] Methods used in previous reports for studying NAD^+/NADH degradation are largely limited to UV-visible spectroscopy.[2, 5] The reduced form (NADH) contains a dihydropyridine ring that absorbs strongly at both 260 and 340 nm while the oxidized form (NAD^+) contains a pyridine ring that absorbs at 260 nm and does not absorb at 340 nm (Figure 8.1).[2]

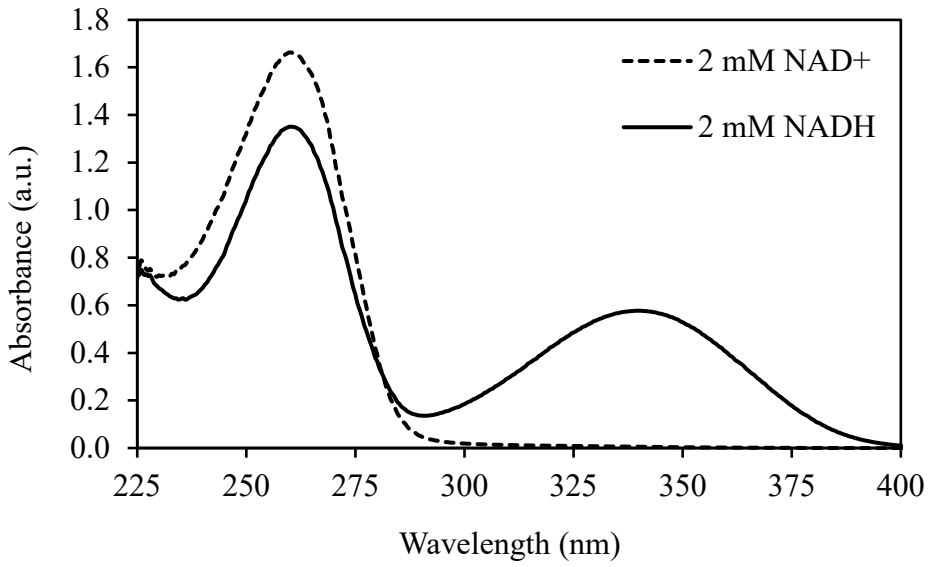

Figure 8.1. *Absorbance spectra of 2 mM NAD^+ and 2 mM NADH in HEPES buffer pH = 8.5. The absorbance peak at 340 nm is attributed to the reduced dihydropyridine ring of NADH. Note that the cuvette concentration is 100 μM NAD^+ or NADH.*

Degradation of NADH proceeds through acid-catalyzed protonation of the dihydropyridine ring followed by nucleophilic attack of the imine resulting in the addition of a hydroxyl group at either C_5 or C_6.[3] The expected products of NAD^+ degradation are D-ribose 5-phosphate ($C_5H_{11}O_8P$, MW = 230.1 g/mol), nicotinamide ($C_6H_6N_2O$, MW = 122.1 g/mol), adenylic acid or adenosine

monophosphate ($C_{10}H_{14}N_5O_7P$, MW = 347.2 g/mol), and nicotinamide mononucleotide ($C_{11}H_{15}N_2O_8P$, MW 334.2 g/mol).[4] Figure 8.2 shows the structure of NADH along with the three likely locations of degradation: 1.) Phosphate-phosphate linkage, 2.) nicotinamide-ribose linkage, and 3.) carbons C_5 and C_6 of the dihydropyridine ring. Efforts have been made to improve stability of nicotinamide cofactors in aqueous solutions including the use of organic, inorganic, and biological additives as well as modification of the pyridine ring.[5, 7-8] The work presented herein is aimed to determine the simplest optimum buffer conditions for long-term stability of both NAD^+ and NADH, upon which other more complex methods may be used to further improve the stability.

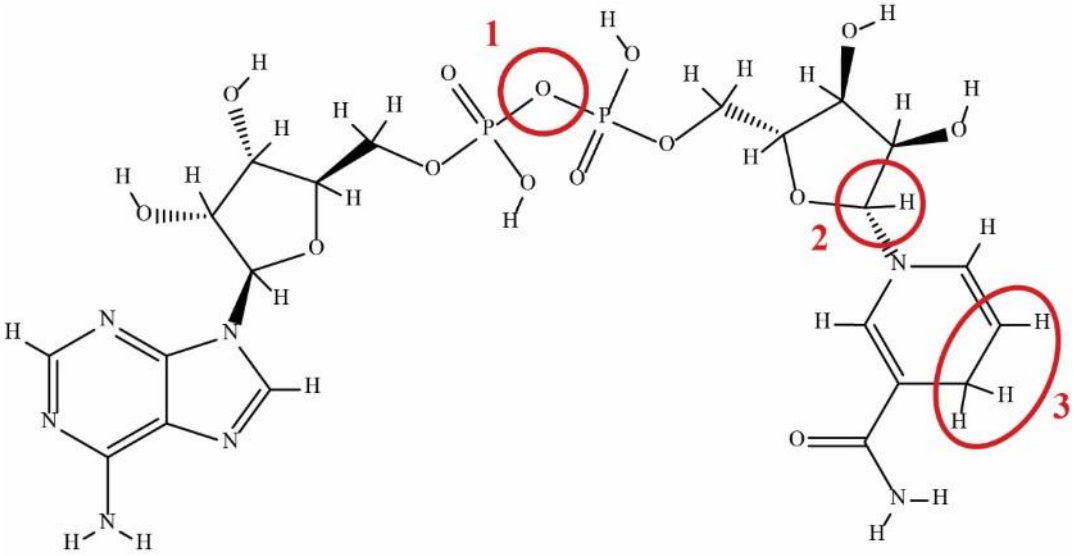

Figure 8.2. *Structure of NADH with the likely locations of degradation labeled: 1.) Phosphate-phosphate linkage, 2.) nicotinamide-ribose linkage, and 3.) carbons C_5 and C_6 of the dihydropyridine ring (subject to acid-catalyzed hydrolysis and nucleophilic attack). Note that the hydrolysis of the phosphate-phosphate linkage is base catalyzed and is the main degradation mechanism of the NAD^+ cofactor.*

Previous studies of nicotinamide cofactor stability have focused on specific applications or reported degradation rate constants for many conditions.[2, 5, 9] Based upon these reports, the conditions studied herein should result in long-term stability, which is necessary for the development of an NADH regeneration system. To show the ability to achieve long-term stability, in this chapter a long-term degradation study is conducted at optimal conditions for implementation in a bioreactor. The buffers used are 2-amino-2-(hydroxymethyl)propane-1,3-diol (tris), 4-(2-hydroxyethyl)-1-piperazineethanesulfonic acid (HEPES), and sodium phosphate all at

pH values of 8.5 and a buffer concentration of 50 mM. In addition to the typical UV-visible spectroscopic measure of stability, an enzymatic assay to show proof of biological activity is also utilized. The findings suggest that tris buffer is an attractive buffer system for the NAD^+/NADH system because it fosters cofactor stability for up to 43 days. In the test conducted, a loss of only 7 % NADH was observed in tris buffer over 43 days at a rate of 4 μM/day and although a quantitative value was not determined, NAD^+ appeared to be highly stable as well.

Results & Discussion

For the initial UV-visible spectroscopic stability study, sample solutions were prepared with a range of NADH concentrations from 0 to 2000 μM with the total NAD^+/NADH concentration being constant at 2000 μM (i.e. 800 μM NADH and 1200 μM NAD^+). The buffer conditions are pH = 8.5, temperature = 19 °C, and a total buffer concentration of 50 mM. UV-vis calibration curves were taken at t = 1 h from wavelengths of 400 nm to 200 nm in the range of 0-100 μM NADH. The curve for HEPES buffer is shown in Figure 8.3. Note that the slope varied slightly between the buffers with a value of 0.0056 in tris, 0.0057 in HEPES, and 0.0058 in sodium

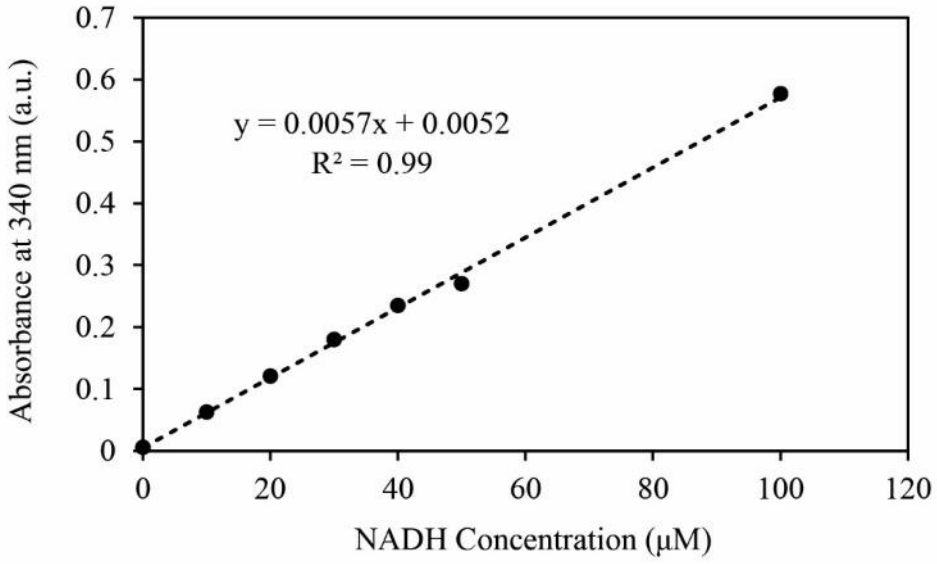

Figure 8.3. *Calibration curve for absorbance at 340 nm vs. NADH concentration in HEPES buffer. Identical tests were completed in Tris and sodium phosphate buffers as well, resulting in minimally different slopes. The calibration curves were used to determine the NADH concentration in the following figures.*

phosphate. The calibration performed in each buffer was used to determine concentration in that buffer for all successive testing.

Absorbance spectra were then taken at various time intervals spanning over two weeks at a 19:1 dilution of the stock solutions to determine the concentration of NADH over time. The 340 nm absorbance was used to track the concentration of NADH in each buffer (Figure 8.4). The measured concentration of NADH in the 2 mM or 2000 μM NADH samples did not change appreciably over the timespan of 24 h at pH = 8.5 and 19 °C in any of the three buffers. However, the testing was continued over days and the resulting degradation rates are shown in Figure 8.4. NADH degraded most rapidly in sodium phosphate buffer (Figure 8.4.C), at a rate of approximately 23 μM/day of loss. Both HEPES (Figure 8.4.B) and tris (Figure 8.4.A) were found to be more stable, with Tris showing the lowest rate of degradation at 4 μM/day. A comparison of all three buffers in Figure 8.4.D shows that when the temperature and pH are equal at 19 °C and pH = 8.5, tris buffer yields the lowest acid catalyzed rate of degradation of NADH. As determined from the slopes, the rates of degradation in HEPES and phosphate are higher by 3.9- and 5.5-times, respectively, than that measured in tris.

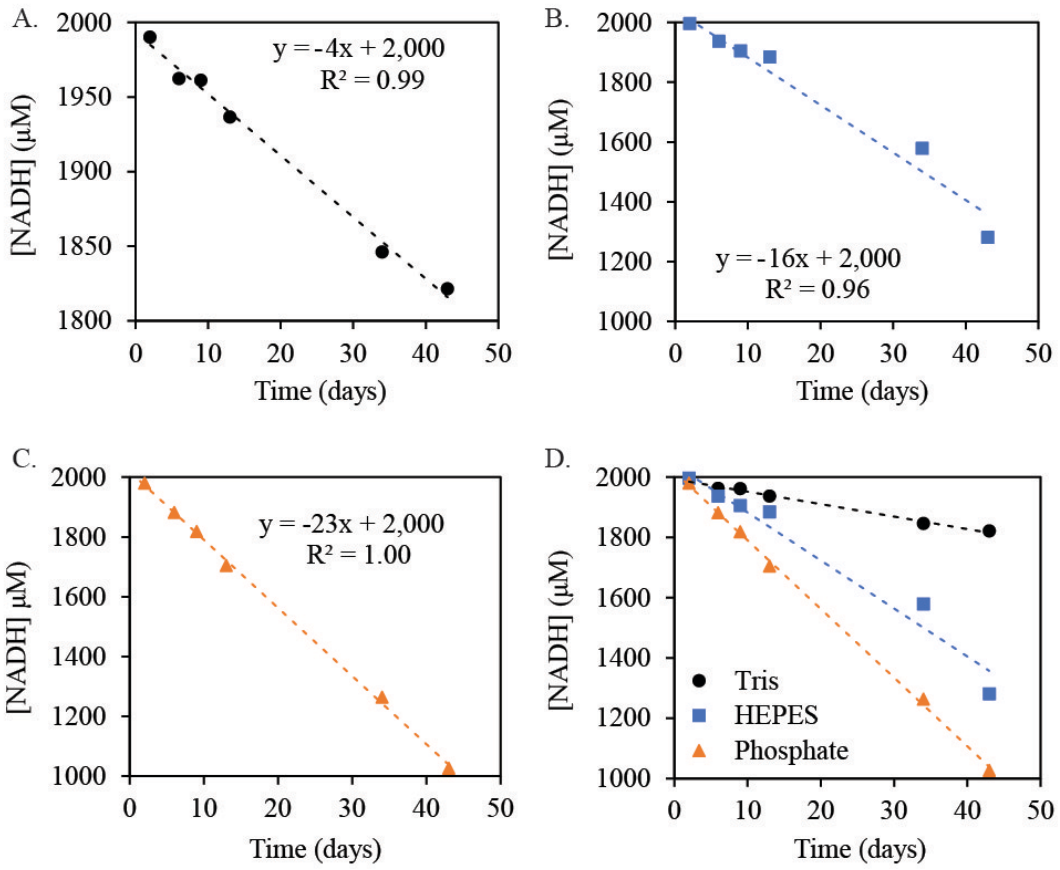

Figure 8.4. *Stability of NADH in A.) tris buffer, B.) HEPES buffer, C.) phosphate buffer, and D.) all three buffers shown in one figure. For each buffer, pH = ~8.5 and the temperature was 19 °C. The initial concentration of NADH was 2 mM and the stability was measured via the absorbance of NADH at 340 nm using UV-Vis spectroscopy and referring to a calibration curve made for each buffer.*

The effect of temperature on the degradation of NADH was also investigated. Samples of 2 mM NADH in 50 mM buffers at pH = 8.5 were stored in a water bath at 25 °C. The increased temperature (by 6 °C) increased the rate of degradation in each of the three buffers (Figure 8.5). The degradation rate in tris buffer (8.5.A) increased from 4 µM/day to 11 µM/day, the rate in HEPES buffer (8.5.B) increased from 18 µM/day to 51 µM/day, and the rate in sodium phosphate buffer (8.5.C) increased from 23 µM/day to 34 µM/day. Note that the 11-day data point in tris buffer was determined to be erroneous and was omitted. Temperature has a significant effect on

NADH stability and Figure 8.5.A shows that at 19 °C over 90% of the NADH is retained over 40 days while at 25 °C only 75% of the NADH remains. To summarize, 50 mM tris buffer at pH = 8.5 and lower temperatures (19 °C) are ideal conditions for long-term stability of NADH in solution.

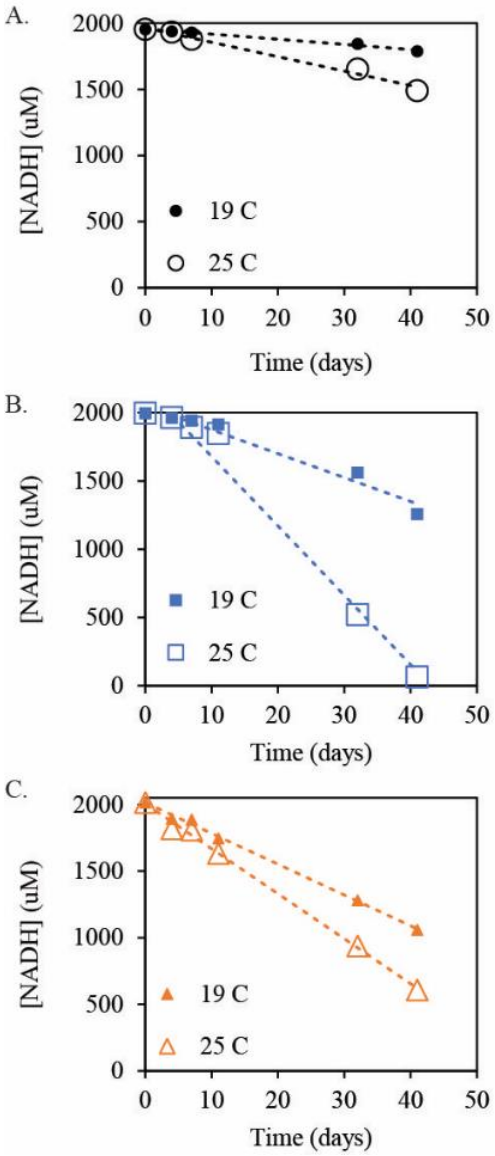

Figure 8.5. *Effect of temperature on the degradation rate of NADH in (A) tris, (B) HEPES, and (C) sodium phosphate buffers.*

The direct determination of the concentration of NAD^+ in solution is not straightforward due to the potential of NADH degradation products (mainly acid-catalyzed products with a hydroxyl addition on the dihydropyridine ring) also absorbing at 260 nm wavelength. Therefore, to qualitatively study the degradation of both NAD^+ and NADH, the absorbance spectra for 2 mM NAD^+, 1 mM NAD^+ and 1 mM NADH, and 2 mM NADH over 43 days were plotted for each of the three tested buffer systems. First, we will discuss the behavior in sodium phosphate buffer (Figure 8.6), which yields the most rapid rate of NADH degradation. As a reminder, in sodium phosphate buffer, we have observed a degradation rate of 23 μM/day for NADH. As shown in Figure 8.6.A, the reduction in the peak absorbance at 260 nm indicates that NAD^+ degrades slowly over the 43-day experiment. As previously mentioned, absolute degradation rates were not reported for NAD^+ as was for NADH due to other species absorbing at 260 nm. The next intriguing observation is shown in Figure 8.6.B; the peak at 260 nm first increases in magnitude, then decreases. This behavior indicates that two processes are occurring simultaneously, and one results in production of a pyridine-containing molecule while the other degrades such a molecule. The production of the pyridine is likely the acid-catalyzed attack of nicotinamide, which results in the addition of a hydroxyl group to dihydropyridine and a change in the electronic configuration of the ring. Lastly, in Figure 8.6.C, the peak at 260 nm increases over the course of the experiment while the peak at 340 nm decreases. To explain the two-process behavior shown in Figure 8.6.B, the pyridine must degrade at a slower rate than the dihydropyridine, resulting in a simultaneous increase and decrease in the intensity of the 260 nm peak when NADH and NAD^+ are present.

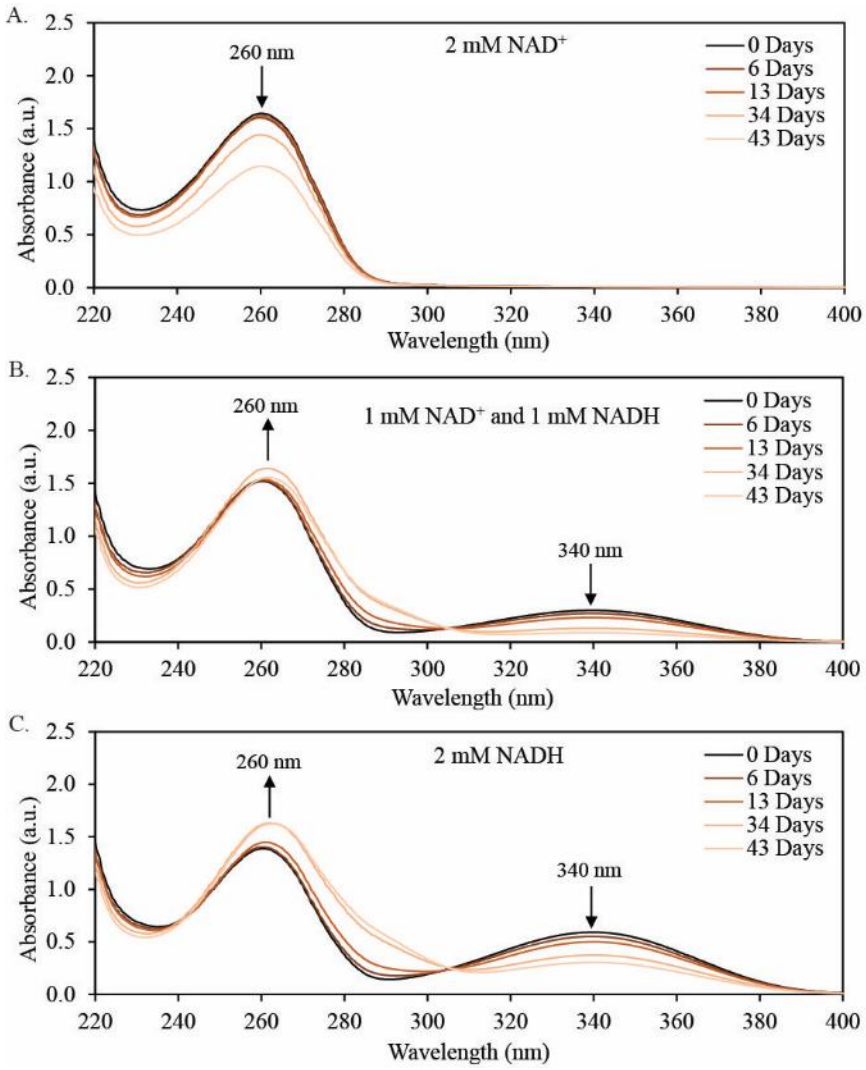

Figure 8.6. *UV-Vis spectra for A.) 2 mM NAD^+, B.) 1 mM NAD^+ and 1 mM NADH, and C.) 2 mM NADH in sodium phosphate buffer over a span of 43 days. The peak at 340 nm is assigned to dihydropyridine (characteristic of NADH) and the peak at 260 nm is assigned to pyridine (characteristic of NAD^+).*

In the HEPES buffer (Figure 8.7), the 2 mM NAD^+ solution (Figure 8.7.A) degraded nearly entirely over the 43-day period. Thus, while NADH is more stable in HEPES buffer than in sodium phosphate, the oxidized cofactor (NAD^+) degrades more rapidly in HEPES. There is also a clear red shift in the 260 nm peak as the NAD^+ degrades.

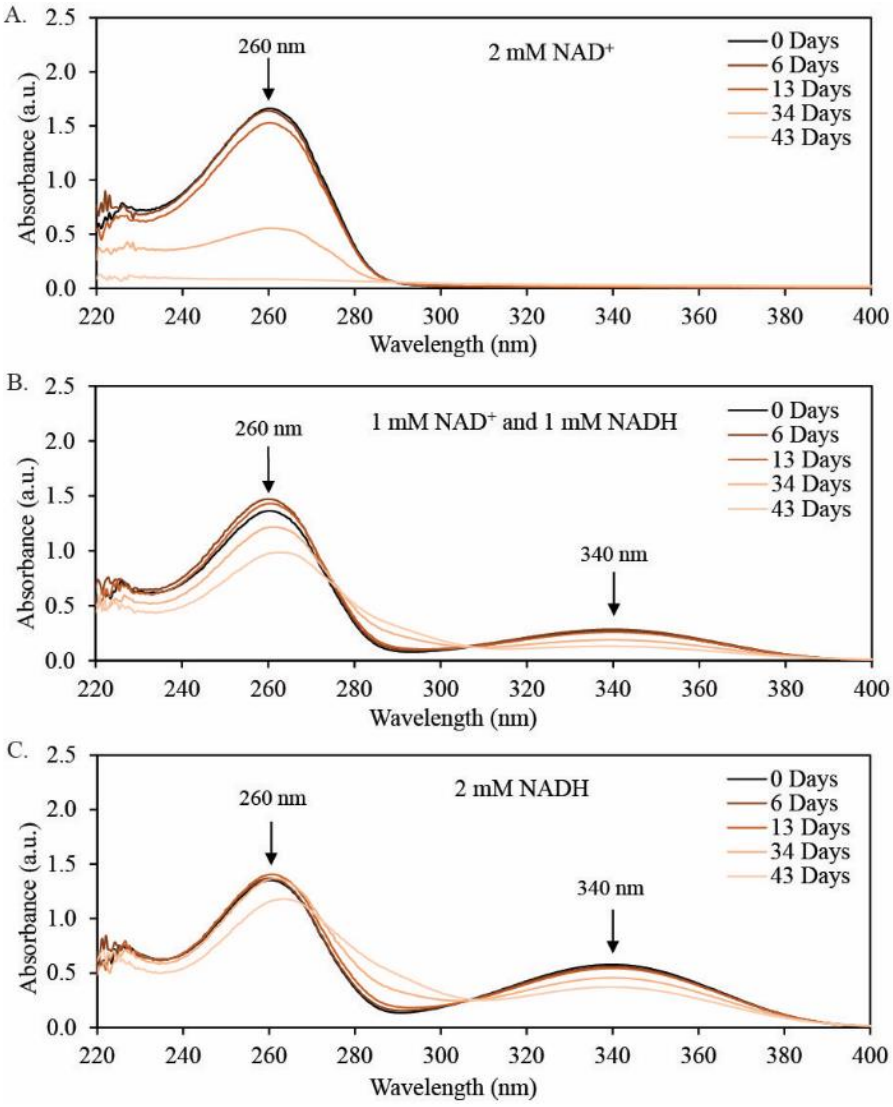

Figure 8.7. *UV-Vis spectra for A.) 2 mM NAD^+, B.) 1 mM NAD^+ and 1 mM NADH, and C.) 2 mM NADH in HEPES buffer over a span of 43 days. The peak at 340 nm is assigned to dihydropyridine (characteristic of NADH) and the peak at 260 nm is assigned to pyridine (characteristic of NAD^+).*

Lastly but critically, in Figure 8.8, we observed that both NAD^+ and NADH are very stable in tris buffer over several weeks, further supporting the use of pH = 8.5 tris buffer for an NAD^+/NADH reactor. The degradation of rate of NADH in tris was determined to be only 4 μM/day and a very small change in absorbance at 260 nm was observed following a similar trend as for HEPES buffer.

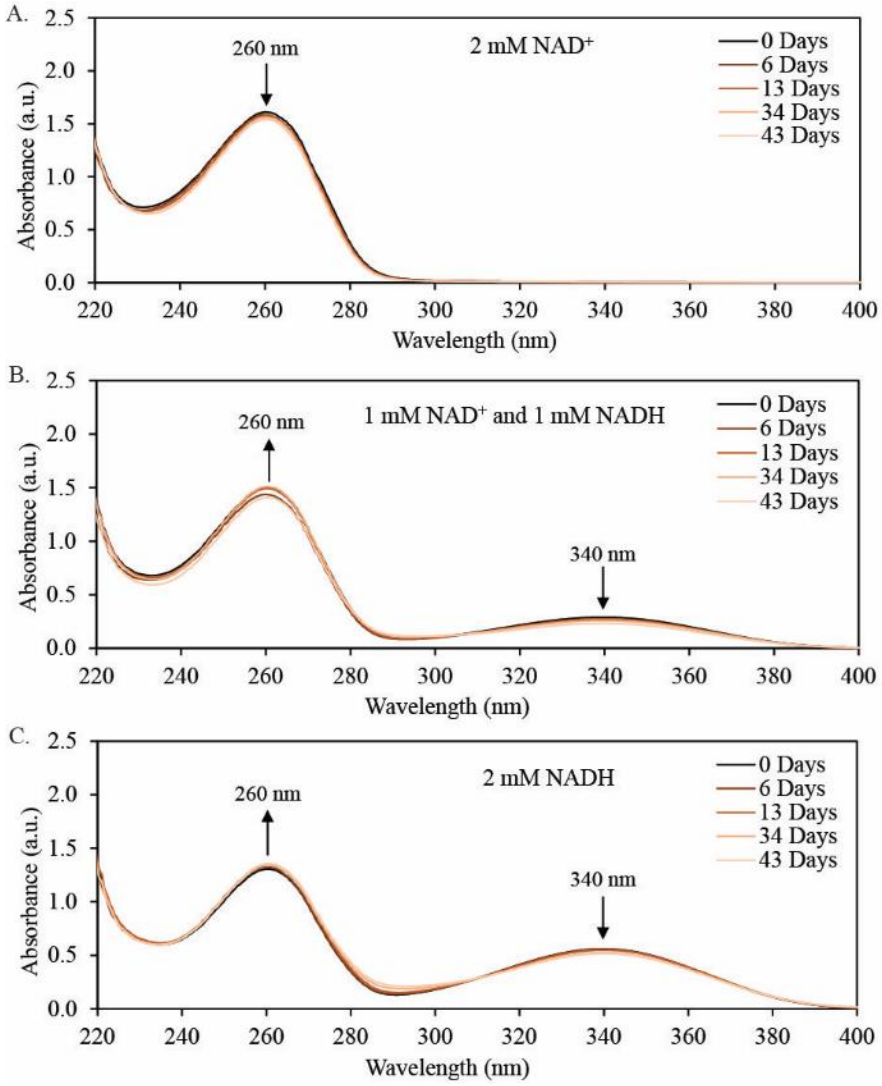

Figure 8.8. *UV-Vis spectra for A.) 2 mM NAD^+, B.) 1 mM NAD^+ and 1 mM NADH, and C.) 2 mM NADH in tris buffer over a span of 43 days. The peak at 340 nm is assigned to dihydropyridine (characteristic of NADH) and the peak at 260 nm is assigned to pyridine (characteristic of NAD^+).*

To better represent the stability of NAD^+, albeit without quantification, Figure 8.9 shows the UV-visible spectra for NAD^+ in the buffers (seen as the disappearance of the peak at 260 nm) over the same time points (from Figures 8.6.A, 8.7.A, and 8.8.A). The spectra show that the

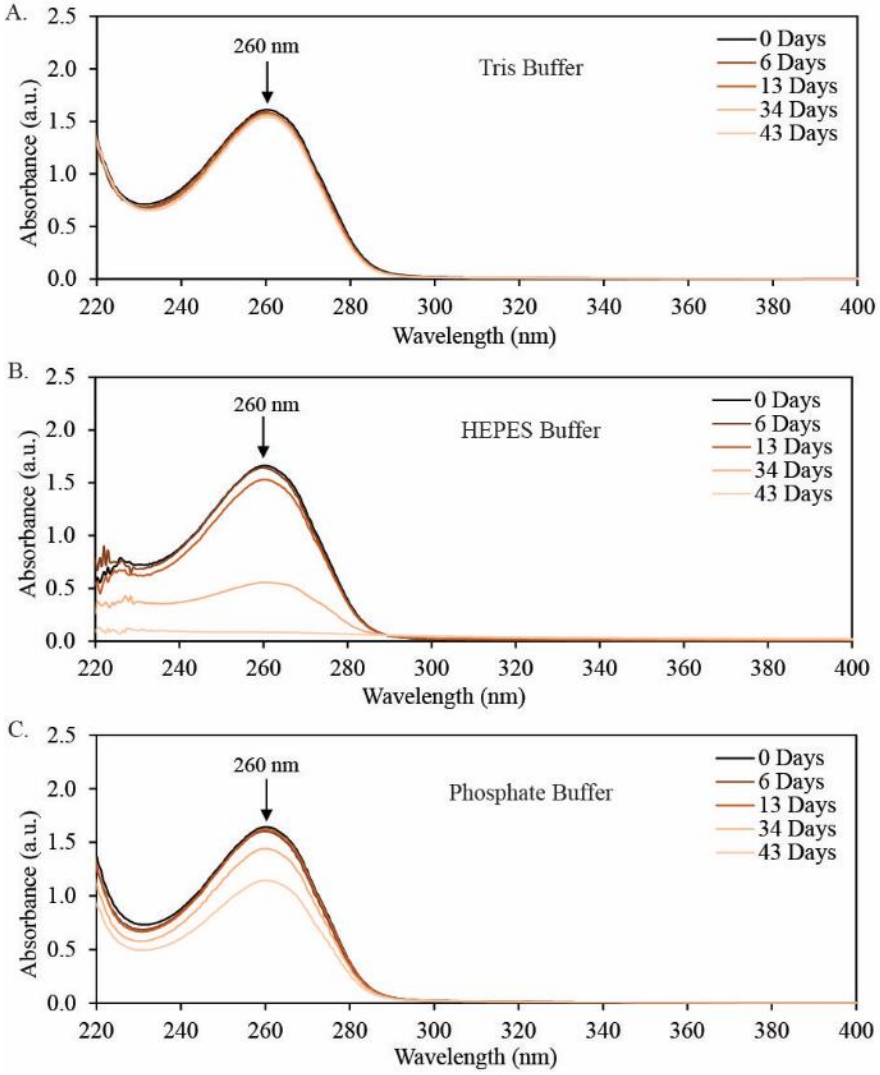

Figure 8.9. *Stability of NAD^+ in tris buffer (top), HEPES buffer (middle), and Phosphate buffer (bottom) over 43 days. The initial concentration was 2 mM NAD^+ and the buffers are prepared at pH = 8.5 and kept at 19 °C. The decrease in peak intensity at 260 nm is attributed to the degradation of NAD^+, but the degradation rate cannot be quantified from this data due to lack of a calibration curve for NAD^+ only solutions.*

degradation of NAD^+ in Tris is slow, with only slight (4%) drop in the 260 nm peak after 43 days, which is much slower than the degradation in phosphate or HEPES. The stability of NAD^+ in HEPES is poor, as indicated by the complete loss of the peak at 260 nm after 43 days.

Going beyond the often-used UV-vis method for NAD^+/NADH quantification, the stability results discussed above were followed by an enzymatic activity stability study. This follow up test using a highly specific enzyme is important because degradation products may contain either dihydropyridine or pyridine, thereby resulting in absorbance at 340 or 260 nm respectively and giving false positive stability data. We received NADH oxidase (NOX) from Markus Alahuhta of the National Renew. Energy Laboratory for use as an enzymatic assay for NADH activity. The NOX assay allows for quick and simple verification of activity of NADH due to its high activity and use of oxygen as a substrate. Upon receiving aliquots of NOX from Markus, an enzyme dilution series was performed in tris buffer (data not shown). Using a 1:2000 dilution of NOX from the ~29 mg/mL stock and a concentration of 50-100 uM NADH in a cuvette continuing tris buffer, the absorbance of the 340 nm peak is quenched in approximately 4 min. These conditions are suitable for performing both the stability test and enzymatic activity tests after bulk electrolysis (Chapter 9).

Next, the kinetics of the NOX assay were tested in each buffer using a 1:2000 NOX dilutant of a 29.43 mg/mL stock solution. Note that 30 µL of NOX dilutant was spiked into a 3 mL cuvette, making the total dilution 1:200,000 or 150 ng/mL NOX. Figure 8.10 shows full spectrum examples of the consumption of freshly prepared 100 uM NADH (150 µL of 2 mM NADH stock solution diluted to 3 mL in the cuvette) by NOX in A.) tris, B.) HEPES, and C.) phosphate buffers. The spectra in Figure 8.10 were taken by scanning every 30 s from 450 to 250 nm wavelength. Tris buffer yields the slowest NOX reaction rate while NOX in HEPES and phosphate buffers exhibits a similarly higher reaction rate. The slower reaction rate in tris is believed to be indicative of some interaction between either the tris buffer and NOX or the tris buffer and NADH, causing a slower binding and reaction rate. The metric for the stability test is the absorbance at 340 nm after the enzymatic reaction has gone to completion in comparison to the absorbance at the beginning of the test. If a significant absorbance is still observed after the reaction, then non-enzymatically active NADH (containing a dihydropyridine moiety) is present in the sample. Note that in the tests

shown in Figure 8.10, using freshly prepared NADH, the absorbance goes to a near-zero value and therefore approximately 100% of the NADH present is enzymatically active.

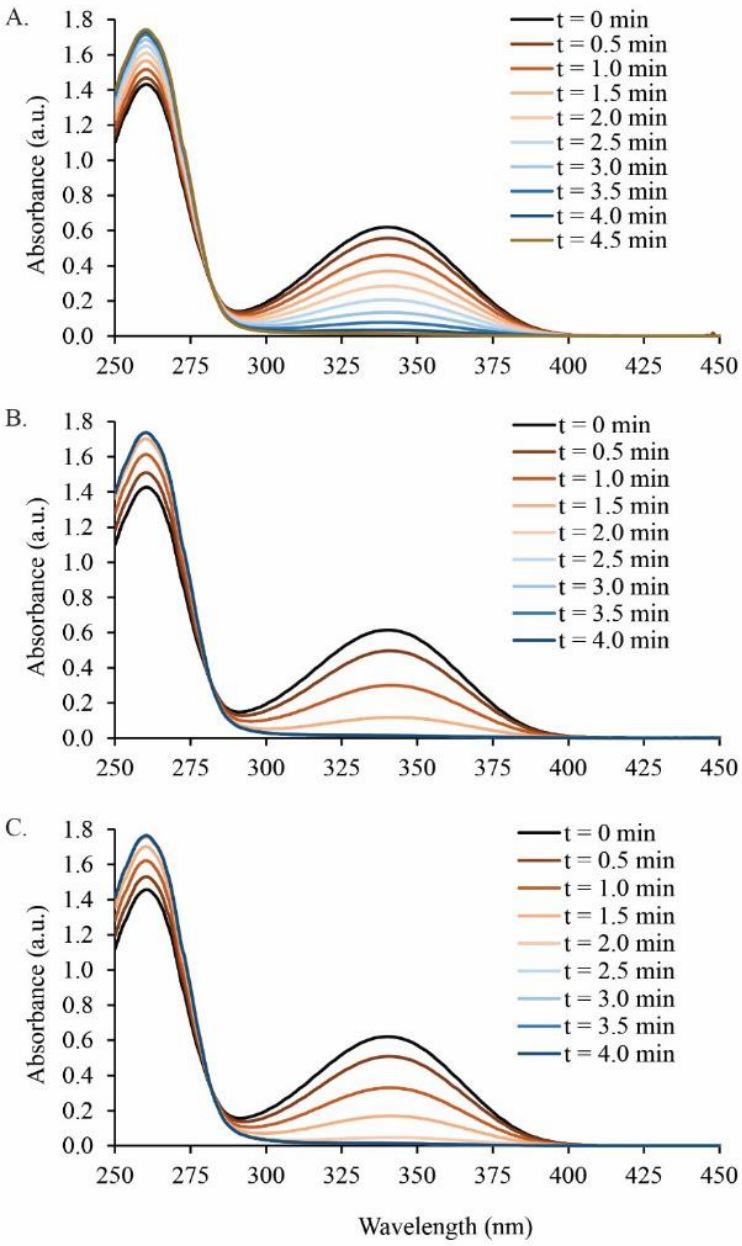

Figure 8.10. *Examples of NOX consuming 100 uM NADH as shown by a decrease in absorbance at 340 nm wavelength in A.) tris, B.) HEPES, and C.) Phosphate buffers at pH 8.5 and a buffer concentration of 50 mM.*

The enzymatic activity-based stability study of NADH over 30 days, as determined via the NOX assay, is shown for the three buffers in Figure 8.11. This data set is complementary to the previous stability analyses and demonstrates that the improved stability in tris buffer at pH = 8.5 (in comparison to HEPES or phosphate buffers) also preserves enzymatic activity. If inactive NADH degradation products containing an intact dihydropyridine ring were present, the absorbance at 340 nm would not have gone to zero or near zero values. Therefore, because NOX was able to consume the remaining NADH over 30 days in each buffer, we conclude that any remaining absorbance at 340 nm in the UV-Vis stability studies corresponds to active NADH. Thus, the NADH degradation rates shown in Figures 8.4 and 8.5 can be interpreted as enzymatically active NADH degradation rates.

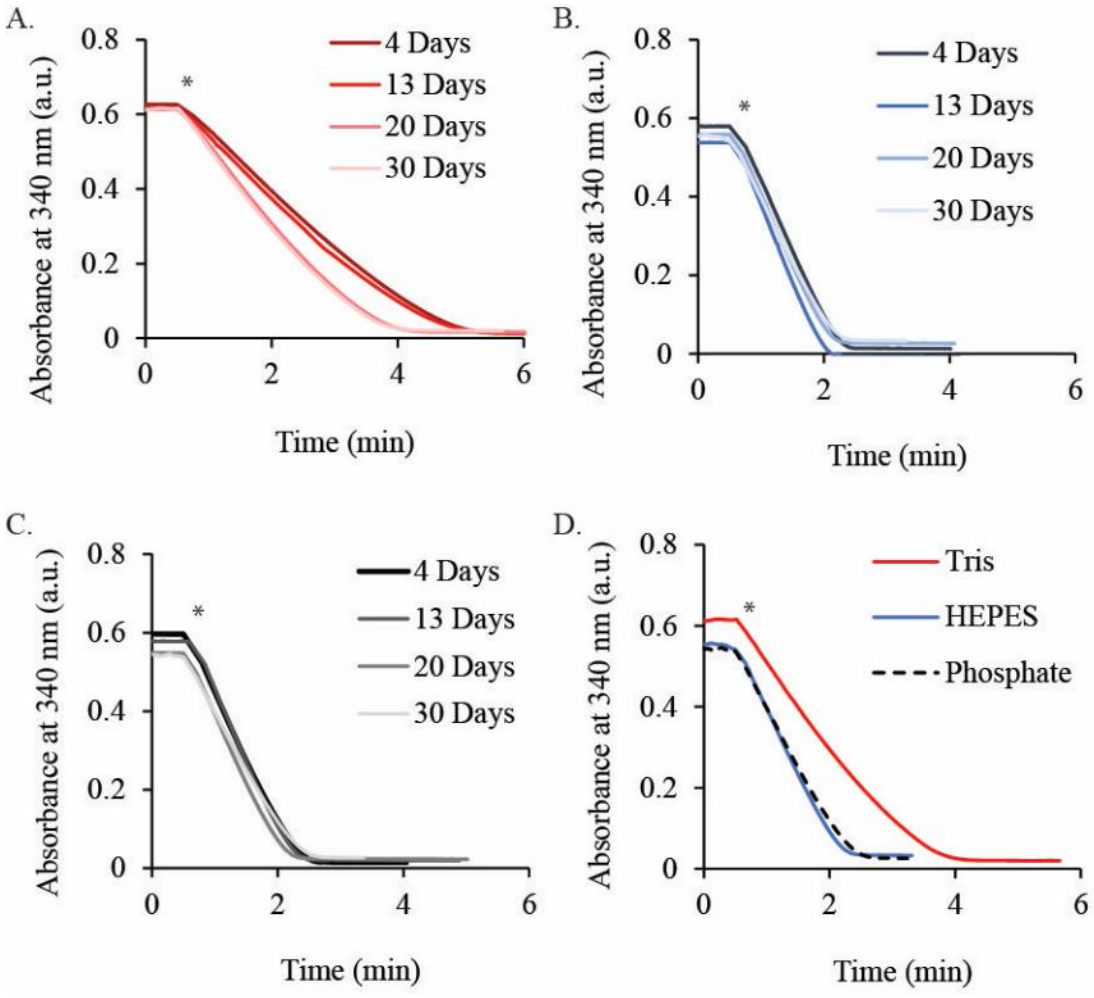

Figure 8.11. *Enzymatic activity testing data over 30 days for 2 mM NADH (diluted to 100 μM) solutions in A) Tris, B) HEPES, and C) Phosphate buffers. All buffer concentrations are 50 mM, pH =8.5, and solutions were stored at 19 °C. Panel D shows the 30-day curve for each buffer. Enzymatic activity was tested by spiking a dilute solution of NADH oxidase (NOX) into the cuvette at t = 0.5 min (marked by an asterisk) and measuring the decrease in absorbance at 340 nm wavelength.*

Conclusions

The long-term stability testing of NAD^+/NADH showed that 50 mM tris buffer at pH = 8.5 and 19 °C is a favorable aqueous buffer for storing NAD^+/NADH solutions for up to 40 days. This condition is an important finding because although the stability of nicotinamide cofactors has been previously reported for various aqueous solutions, current studies employing NAD/NADH as

reactants for electrochemical or biochemical reactions often use ill-fit buffers.[10-15] As seen in Figure 8.4, tris buffer yields a low degradation value for NADH of 4 μM/day. In Figure 8.8, the stability of both NADH and NAD^+ is qualitatively proven, a requisite for systems in which turnover of the cofactors is necessary. Lastly, Figure 8.11 shows that the spectroscopic measurements of NADH stability are upheld by an enzymatic activity assay, ensuring that the long-term stability of NADH in tris buffer also maintains biological activity. The stability test reported herein may be expanded upon by identifying the degradation mechanisms and further studying the effect of temperature on the degradation rates. If the degradation products and degradation mechanisms were better understood, alternative methods for improving the stability may be explored.

References

1. Chenault, H. K.; Simon, E. S.; Whitesides, G. M., Cofactor Regeneration for Enzyme-Catalysed Synthesis. *Biotechnol. Genet. Eng. Rev.* **1988,** *6* (1), 221-270.
2. Rover, L.; Fernandes, J. C. B.; Neto, G. d. O.; Kubota, L. T.; Katekawa, E.; Serrano, S. l. H. P., Study of NADH Stability Using Ultraviolet–Visible Spectrophotometric Analysis and Factorial Design. *Anal. Biochem.* **1998,** *260* (1), 50-55.
3. Hentall, P. L.; Flowers, N.; Bugg, T. D. H., Enhanced acid stability of a reduced nicotinamide adenine dinucleotide (NADH) analogue. *Chem. Commun.* **2001,** (20), 2098-2099.
4. Anderson, B. M.; Anderson, C. D., The effect of buffers on nicotinamide adenine dinucleotide hydrolysis. *J. Biol. Chem.* **1963,** *238*, 1475-8.
5. Shabir, G. A.; Forrow, N. J., Development and validation of a HPLC method for 4,7-phenanthroline-5,6-dione I and identification of its major impurity by HPLC-MS-APCI. *J. Chromatogr. Sci.* **2005,** *43* (4), 207-12.
6. Alivisatos, S. G. A.; Ungar, F.; Abraham, G., Non-enzymatic Interactions of Reduced Coenzyme I with Inorganic Phosphate and Certain Other Anions. *Nature* **1964,** *203* (4948), 973-975.
7. Buckmann, A. F.; Kula, M. R.; Wichmann, R.; Wandrey, C., An Efficient Synthesis of High-Molecular-Weight Nad(H) Derivatives Suitable for Continuous Operation with Coenzyme-Dependent Enzyme Systems. *J. Appl. Biochem.* **1981**, *3* (4), 301-315.
8. Adachi, S.; Ogata, M.; Tobita, H.; Hashimoto, K., Effects of molecular weight of dextran and NAD+ density on coenzyme activity of high molecular weight NAD+ derivative covalently bound to dextran. *Enzyme Microb. Technol.* **1984,** *6* (6), 259-262.

9. Lee, Y. S.; Gerulskis, R.; Minteer, S. D., Advances in electrochemical cofactor regeneration: enzymatic and non-enzymatic approaches. *Curr. Opin. Biotechnol.* **2022,** *73*, 14-21.

10. Tan, B. X.; Hickey, D. P.; Milton, R. D.; Giroud, F.; Minteer, S. D., Regeneration of the NADH Cofactor by a Rhodium Complex Immobilized on Multi-Walled Carbon Nanotubes. *J. Electrochem. Soc.* **2015,** *162* (3), H102-H107.

11. Yuan, M.; Kummer, M. J.; Milton, R. D.; Quah, T.; Minteer, S. D., Efficient NADH Regeneration by a Redox Polymer-Immobilized Enzymatic System. *ACS Catalysis* **2019,** *9* (6), 5486-5495.

12. Ali, I.; Gill, A.; Omanovic, S., Direct electrochemical regeneration of the enzymatic cofactor 1,4-NADH employing nano-patterned glassy carbon/Pt and glassy carbon/Ni electrodes. *Chem. Eng. J.* **2012,** *188*, 173-180.

13. Ali, I.; Khan, T.; Omanovic, S., Direct electrochemical regeneration of the cofactor NADH on bare Ti, Ni, Co and Cd electrodes: The influence of electrode potential and electrode material. *J. Mol. Catal. A: Chem.* **2014,** *387*, 86-91.

14. Ali, I.; Ullah, N.; McArthur, M. A.; Coulombe, S.; Omanovic, S., Direct electrochemical regeneration of enzymatic cofactor 1,4-NADH on a cathode composed of multi-walled carbon nanotubes decorated with nickel nanoparticles. *Can. J. Chem. Eng.* **2018,** *96* (1), 68-73.

15. Damian, A.; Omanovic, S., Electrochemical reduction of NAD+ on a polycrystalline gold electrode. *J. Mol. Catal. A: Chem.* **2006,** *253* (1), 222-233.

Chapter 9 – Platinum-Modified Carbon Paper Electrodes for NAD^+ Reduction

The work included in this chapter is in collaboration with National Renew. Energy Laboratory (NREL) scientists Yannick J. Bomble, Michael E. Himmel, and Marcus Alahuhta under subcontract number XEJ-9-92257-01 (prime contract number DE-AC36-08GO28308). Marcus Alahuhta provided the nicotinamide oxidase enzyme used herein. Text and figures are adapted or reproduced from update reports submitted to Yannick J. Bomble. All data, figures, and text were produced by the author (Kody D. Wolfe).

Introduction

In comparison to other recent efforts toward electrochemical reduction of NAD^+ to NADH, the work reported herein explores the production of a low-cost and high surface area alternatives to previously reported modified glassy carbon or carbon nanotube electrodes.[1-5] The deposition of metal catalysts that promote NAD^+ reduction on glassy carbon has been proven as a means of increasing the amount of biologically active product.[1-3, 5-8] However, the deposition method reported in this chapter is more versatile and decreases the amount of platinum used by leveraging the ability to create a platinum monolayer on gold nanostructures. Specifically, proton donating catalysts including platinum, nickel, titanium, and cadmium deposited as nanoparticles onto an electrode surface facilitate the reduction of NAD^+ by providing active adsorbed protons on the electrode surface.[2-3] Using these catalysts does not reduce the overpotential of the reaction, it simply pushes the reaction forward by providing the reactant for the rate limiting protonation step. The monolayer platinum catalysts will be deposited onto a high surface area carbon paper electrode that should both increase the rate of NADH production per footprint area and lower the cost in comparison to other carbon electrodes. The goal of the research in this chapter is to develop a procedure for producing low-cost carbon paper-based electrodes with monolayer platinum catalysts and to study their viability as electrodes for NAD^+ reduction.

The deposition of metallic nanostructures onto carbon electrodes has been studied and shown to be highly adaptable.[1-3, 9] Various size and morphological features are achievable by tuning the surfactant concentration and deposition time and potential. In this study, chloroauric

acid ($HAuCl_4 \bullet 3H_2O$) solutions are prepared with 1.4 wt % cetyltrimethylammonium chloride (CTAC) as a cationic surfactant. The CTAC forms finger-like micelles in solution that encapsulate the gold salt, and upon reduction of the gold salt at the electrode surface, the formation of coral-shaped gold nanostructures is achieved.[9] Next, a monolayer of copper atoms is deposited onto the gold nanostructures via underpotential deposition (UPD) and then exchange for platinum atoms via electroless exchange (Reaction 9.1).[10-11] The copper UPD and electroless exchange for platinum must be repeated multiple times to produce a platinum monolayer due to the 2:1 copper:platinum stoichiometry seen in reaction 9.1.[12] Figure 9.1 shows a schematic of the catalyst deposition procedure. Variable gold nanostructures were produced using different deposition potentials and all could undergo copper UPD and the deposition of platinum.

$$2Cu\ (s) + PtCl_4^{2-}\ (aq) \rightarrow Pt\ (s) + 2Cu^{2+}\ (aq) + 4Cl^-\ (aq) \qquad \text{Rxn 9.1}$$

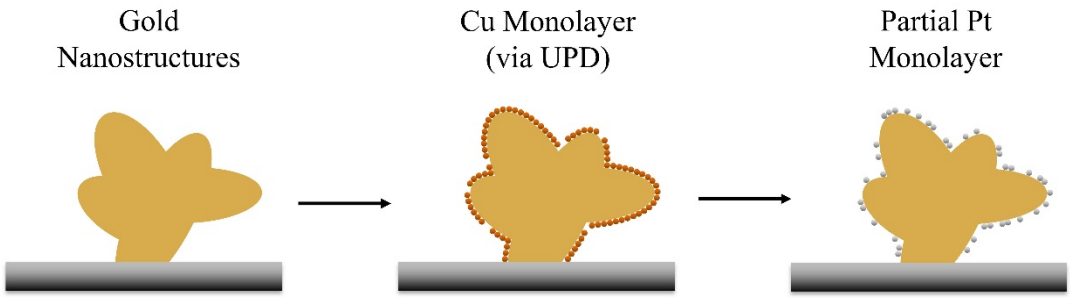

Figure 9.1. *Schematic illustration showing the deposition of copper monolayers onto gold nanostructures and the exchange of copper for platinum monolayers.*

After preparation of the platinum-modified electrodes, they were tested for their ability to reduce NAD^+ to NADH. A stirred batch reactor was used with 2 mM NAD^+ as the feedstock. Because the oxygen reduction reaction is known to consume adsorbed proton, therefore competing with NAD^+, the solution was thoroughly deoxygenated using N_2 purging. The production of NADH was measured via both UV-visible spectroscopic monitoring of the 340 nm wavelength

(corresponding to dihydropyridine in NADH) and an enzymatic assay to show biological activity. Although reasonably high rates of NADH production were found using UV-vis spectroscopy, the resulting solutions showed little biological activity. The low biological activity is attributed to the production of NAD dimers or 1,6-NADH (a typical problem in electrochemical NAD^+ reduction) and is hypothesized to occur on the bare carbon-paper, between the catalysts.[4, 6, 13] Therefore, the reported method for high surface area platinum-modified carbon paper electrodes may be improved via backfilling of some molecule or layer onto the bare carbon paper or through chemical modification of the carbon paper surface.

Results & Discussion

The process of depositing the platinum monolayers begins with depositing gold nanostructures. Following a procedure by Tung et al., gold nanostructures were first potentiostatically deposited onto the carbon paper at a potential of -1.8 V vs. a graphite rod counter and reference electrode.[9] The deposition time was varied to determine the time required to achieve a uniform coating. The deposited gold was analyzed using scanning electron microscopy and the images taken of bare carbon paper and gold deposited for 10 s, 100 s, and 1000 s are shown in Figure 9.2. The gold nanostructures appear to deposit by sintering or tacking to one another after the initial reduction of gold onto the carbon paper surface. This behavior is shown best at a higher magnification. The carbon paper with gold nanostructures after a 10 s deposition and after a 1000 s deposition are shown at 100,000 X magnification in Figure 9.3. The 1000 s deposition provided an even covering of the gold nanostructures; however, the nanostructures did begin to deposit in larger clumps and grow away from the surface.

The deposition of gold nanostructures from CTAC solution is considered an electrochemical templating method. CTAC forms elongated micelles around solvated gold, and therefore, as a reducing potential is applied, finger-like or coral-like gold nanostructures are produced.[9] In an effort to produce smaller gold nanostructure feature sizes, we have varied the reducing potential and the time of applied potential to study their effects on nanostructure morphology. First, Figure 9.4 shows the effect of electrode potential at two length scales. In this study, the potential was held constant at -1.1, -1.8, or -2.5 V vs a graphite rod counter electrode

for 100 s. At the lowest potential, the gold nanostructures deposited as few, but large coral-like structures and as the potential was increased, the feature size, or size of the individual structures, decreased significantly.

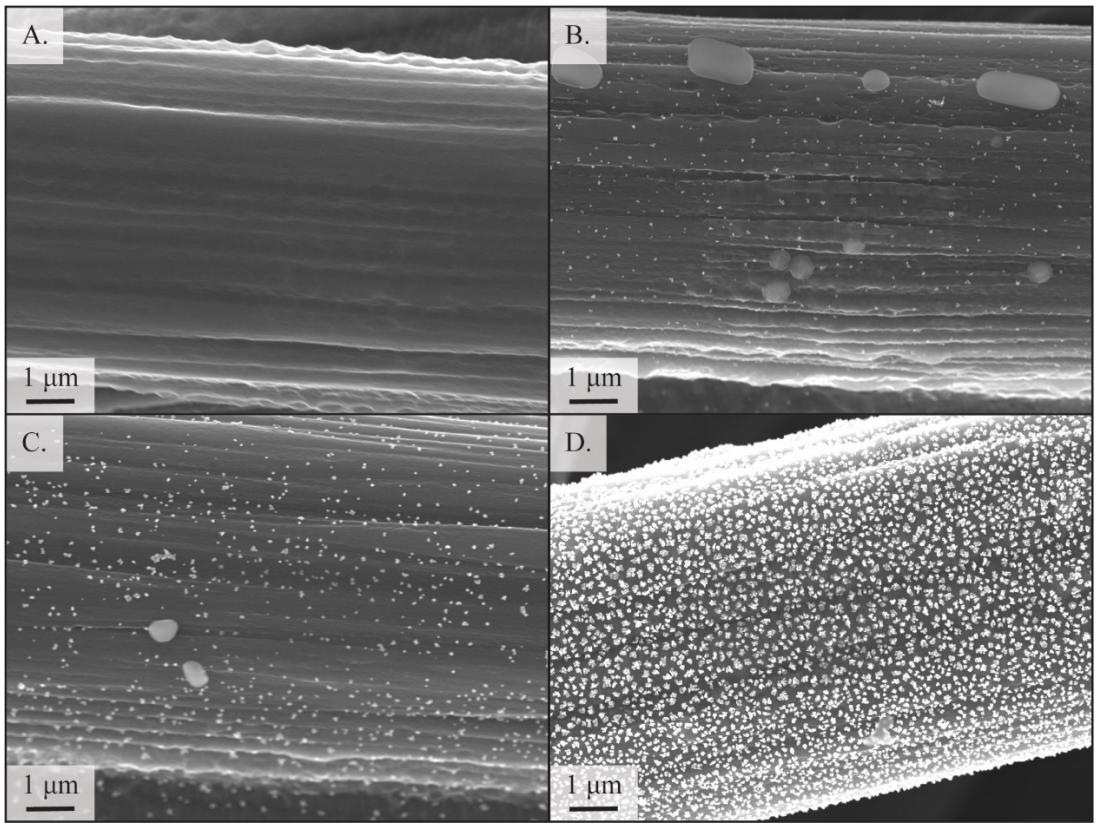

Figure 9.2. *Scanning electron micrographs of (A) bare carbon paper and carbon paper after gold nanostructure deposition for (B) 10 s, (C) 100 s, and (D) 1000 s. The micrographs were taken at an accelerating voltage of 10.0 keV and a magnification of 25,000 X.*

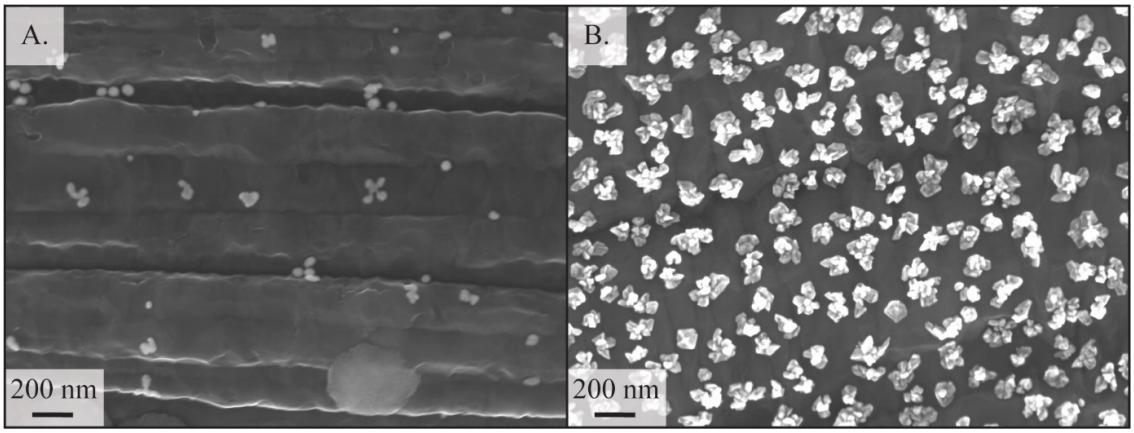

Figure 9.3. *Scanning electron micrographs of (A) 10 s and (B) 1000 s gold nanostructure depositions at 100,000 X magnification.*

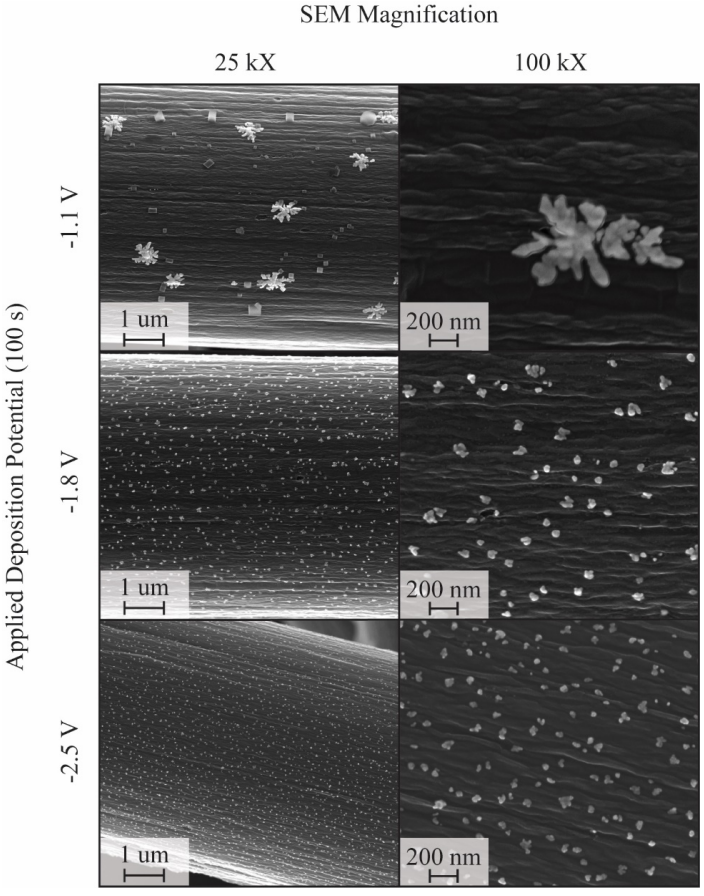

Figure 9.4. *Changse in morphology of gold nanostructures deposited from CTAC solution at -1.1, -1.8 and -2.5 V vs graphite for 100 s.*

Next, the effect of the length of time of applied potential was studied by applying a pulsed potential for 1 s and allowing the solution and electrode to rest for 9 s before the next pulse. This waveform allows the gold nanostructures to be deposited only on the timeframe of the diffusional "drop" where the current is changing from kinetic to diffusional limitation (Figure 9.5). After approximately 1 s the current changed dramatically (believed to be the change from "seeding" or nucleation to gold nanostructure growth) and after ~50 s the deposition rate was constant, limited by only diffusion of gold to the electrode.

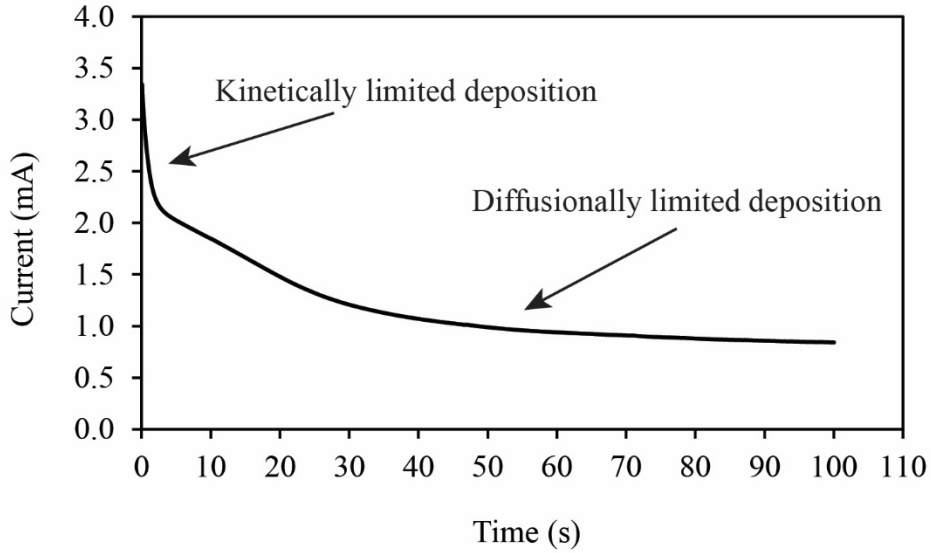

Figure 9.5. *Electrochemical deposition of gold nanostructures at carbon paper electrode. A potential of -1.8 V vs. a graphite rod counter/reference electrode was applied for 100 s.*

Figure 9.6 shows the effect of 1 s pulsed deposition at the 3 chosen potentials. The nanostructure morphology was altered at each of the three potentials. However, there was not a specific trend observed in the morphological change. At the -2.5 V potential, a high areal coverage of nanostructures was produced. Additionally, we hypothesize that the nanostructures produced at high pulsed potential are very thin due to their low contrast with the carbon electrode.

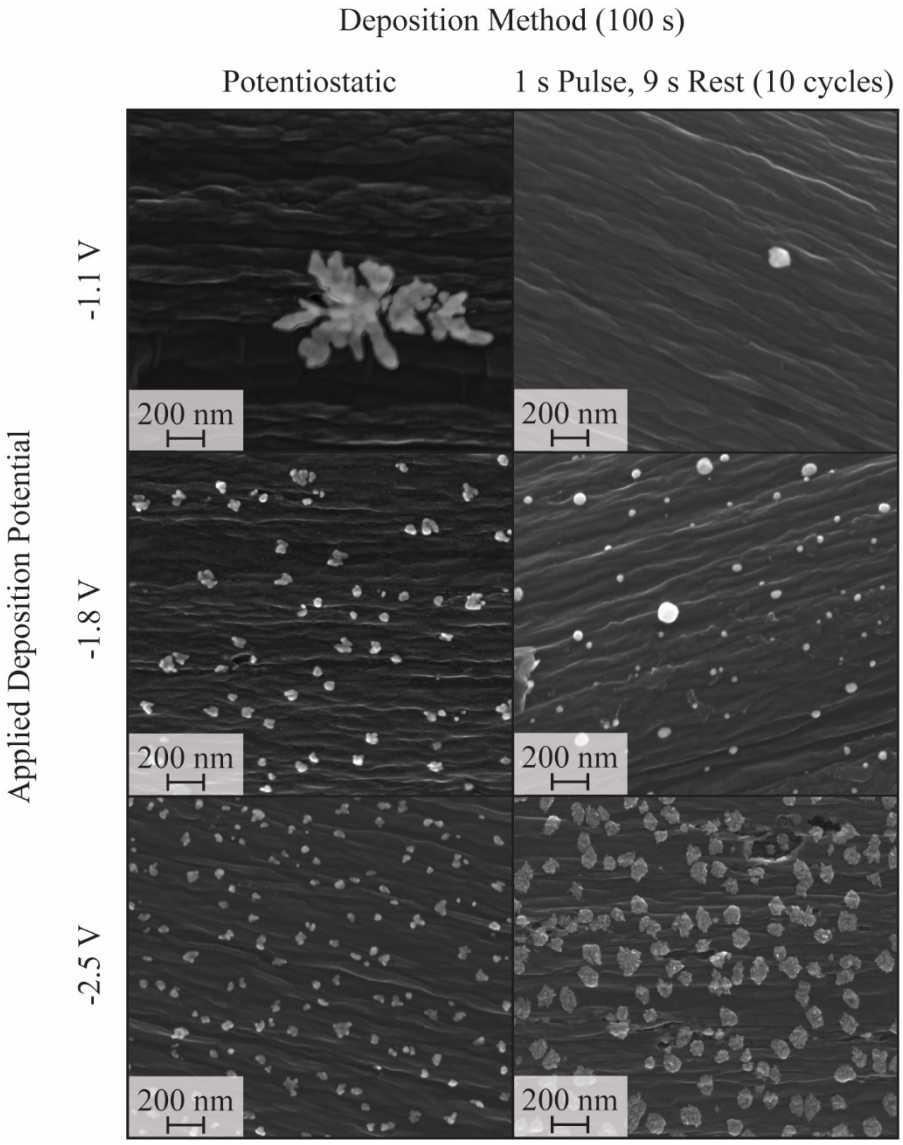

Figure 9.6. *Changes in morphology of gold nanostructures deposited from CTAC solution at -1.1, -1.8 and -2.5 V vs graphite for 100 s via either a potentiostatic deposition or a 1 s pulse, 9 s rest deposition.*

After the deposition of the gold nanostructures, a monolayer of copper must be deposited at a potential under, as in more positive, the potential required for bulk copper deposition. This is termed underpotential deposition or UPD. UPD enables a monolayer of metal to be deposited by

leveraging the lower energetic barrier to depositing single atoms on a heterogeneous surface vs. depositing a bulk metal.[11] To study the ability to UPD a copper monolayer onto the gold nanostructures, copper UPD was performed from a copper salt on bare carbon paper, planar gold, and carbon paper coated with gold nanostructures. For this experiment, a gold deposition time of 30 min was used to ensure a surface area of gold that would be observable on the obtained cyclic voltammograms (CVs). Figure 9.7 shows CVs of the deposition and stripping of copper monolayers of bare carbon paper, planar gold, and gold nanostructure coated carbon paper. The bare carbon paper does not facilitate the UPD of copper (Figure 9.7.A), which results in the two smaller and broad peaks seen near 0.55 and 0.40 V vs. Ag/AgCl. Both the planar gold and the gold nanostructure-coated carbon paper (Figures 9.7.B and 9.7.C) exhibit these peaks corresponding to the deposition of monolayer copper (~0.40 V vs. Ag/AgCl) and the stripping of the monolayer (~0.55 V vs. Ag/AgCl). The observation of UPD peaks on gold nanostructured carbon paper is an indication that the gold deposition was performed correctly and that the copper will be deposited as expected in the next step.

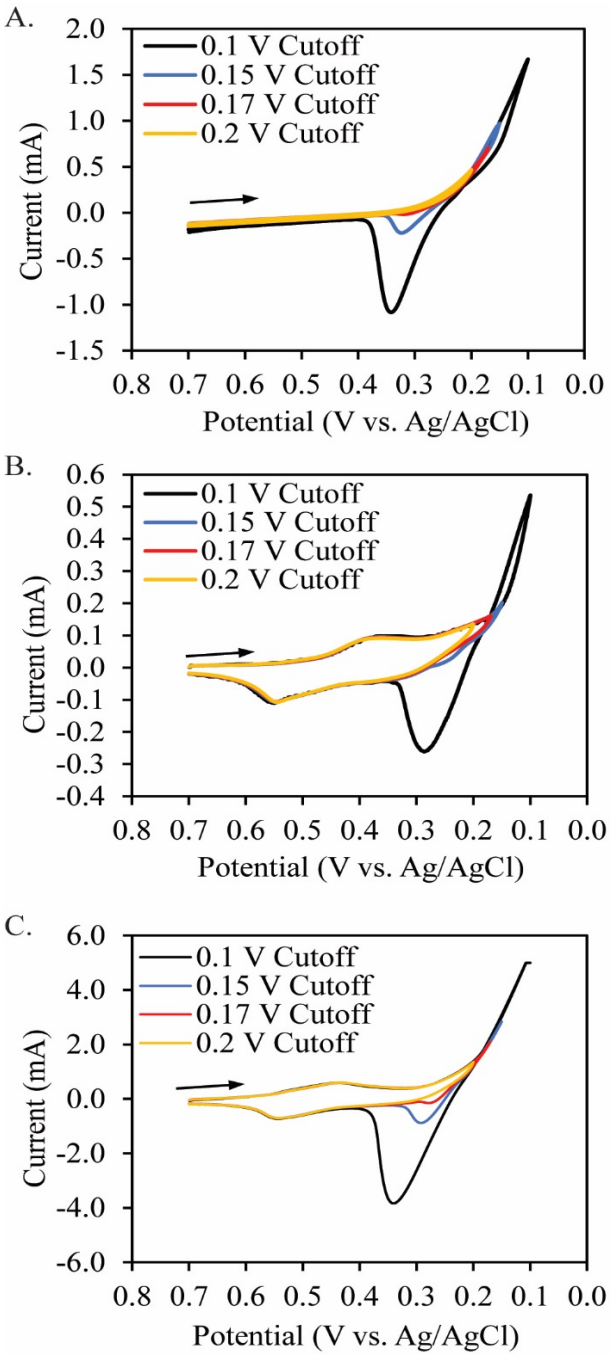

Figure 9.7. *Cyclic voltammograms (CVs) of the UPD of copper monolayers onto (A) bare carbon paper, (B) planar gold, and (C) gold nanostructure coated carbon paper.*

The large oxidation peak seen near 0.3 V vs. Ag/AgCl is the stripping of deposited bulk copper. This peak does not correspond to the UPD process and is only observed when the potential

is scanned sufficiently positive, allowing for the deposition of bulk copper as opposed to monolayer copper (See Figure 9.8). Potentials resulting in the presence of this stripping peak should be avoided when performing UPD, so the potential window was varied for each sample to determine where the onset of bulk deposition occurs. Seen in Figure 9.7.C, the bulk stripping peak is not present when the potential cutoff was 0.20 V vs. Ag/AgCl, but there is a small peak when scanned just 30 mV further to 0.17 V vs. Ag/AgCl. This shows that the onset of bulk copper deposition is between 0.20 and 0.17 V vs. Ag/AgCl. When UPD is performed, the electrode will be held at a potential that is more positive than 0.20 V vs. Ag/AgCl to avoid bulk copper deposition.

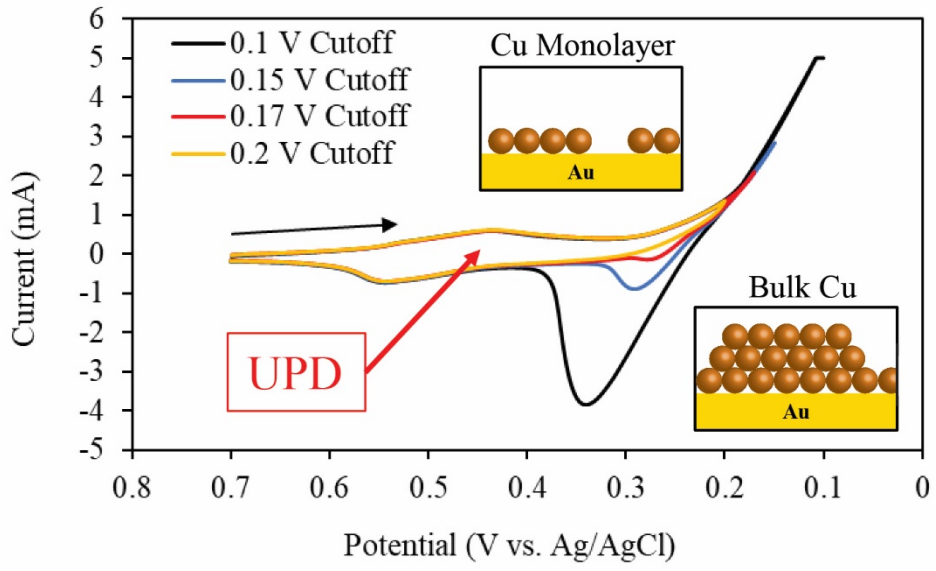

Figure 9.8. *Schematic showing copper UPD in comparison to deposition of bulk copper.*

The UPD of copper was performed by holding the electrode at 0.3 V vs. Ag/AgCl for 100 s. As seen in Figure 9.9, the current drops off quickly after ~5 s. This is attributed to the rapid deposition of a copper monolayer. As previously mentioned, if the applied potential was slightly more negative, bulk copper deposition may occur (see Figure 9.8).

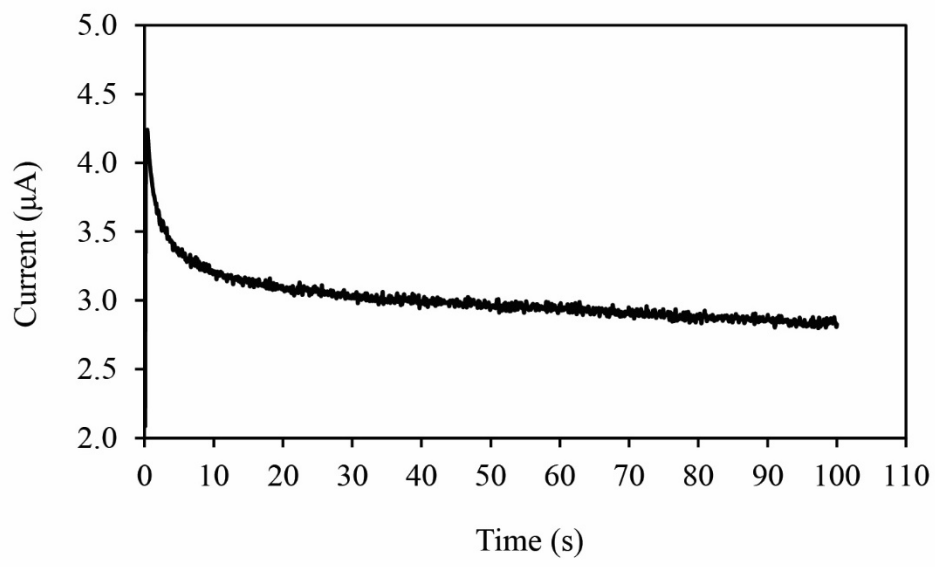

Figure 9.9. *Copper UPD curve. Solution conditions 1 mM copper(II) sulfate in 0.1 M sulfuric acid. The 1 cm x 1 cm modified carbon paper electrode was held at 0.3 V vs. Ag/AgCl for 100 s.*

After the UPD of the copper monolayer is performed, the sample is quickly immersed in a platinum salt solution, resulting in the electroless exchange of the copper atoms for platinum. The platinum salt solution must be deoxygenated via N_2 purging to avoid the fast oxidation of copper to copper oxides, which would hinder the electroless exchange process.[12, 14] The electroless exchange of copper for platinum follows a 2:1 copper:platinum stoichiometry.[14] Therefore, the UPD and electroless exchange process must be repeated multiple times to achieve a high coverage of monolayer platinum.

The oxygen reduction reaction (ORR) results in the electrochemical conversion of dissolved oxygen into water and typically occurs at high cathodic potentials (negative potentials vs. Ag/AgCl). However, due to the affinity for adsorbed protons on platinum and other metal surfaces, the ORR occurs at more positive potentials. To show the ability to introduce monolayer platinum onto the carbon paper, Figure 9.10 shows the onset of the ORR at the various steps in the electrode preparation in 1 M H_2SO_4 saturated with oxygen. After the electroless exchange of copper for platinum, the onset of the ORR shifts to a more positive potential (blue), and after three

repetitions of the electroless exchange (red), the ORR onset potential is comparable to a bulk platinum electrode (grey). In the cases of bare carbon paper (black), gold nanostructure-modified carbon paper (yellow), and copper monolayer-modified carbon paper (orange), the ORR onset is at a much more positive potential. Note that the slope of the ORR is dependent on the surface area, and in Figure 9.10 the currents have not been normalized to active surface area. This result shows that the platinum monolayer deposition process improves the electrode's ability to provide active adsorbed protons, which is also necessary for the NAD^+ reduction reaction.

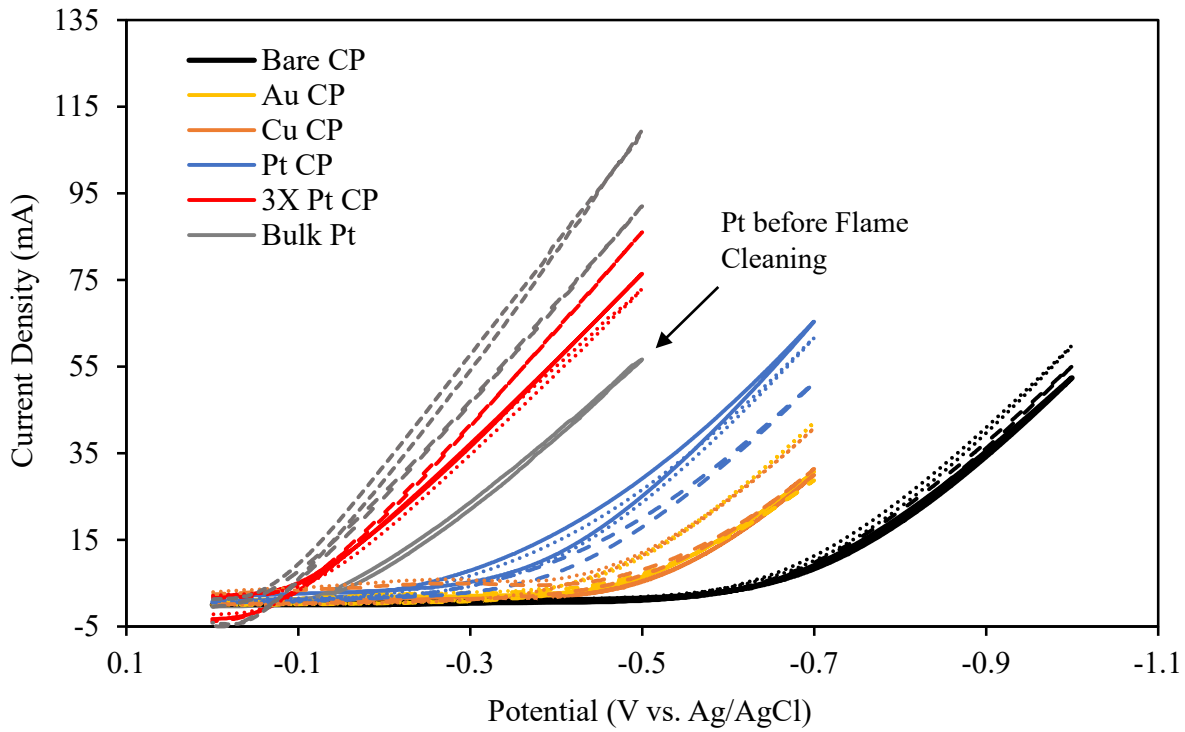

Figure 9.10. *Shifting onset of the ORR at various steps in the deposition of platinum monolayers onto carbon paper (CP). Scans taken in 1 M H_2SO_4 under saturated O_2 conditions at a scan rate of 100 mV/s. The dashed and solid lines of the same color indicate replicates of the same electrode type.*

Batch electrochemical testing of the carbon paper electrodes was begun by first testing a sample with a high likelihood of success to gain a better idea of the achievable conversion rates.

Platinum nanostructures were deposited onto the carbon paper similarly to our previous gold depositions. Platinum was deposited for 100 s at -1.2 V vs. Ag/AgCl onto a 1 cm^2 carbon paper electrode. The platinum nanostructure-decorated carbon paper was then cycled in 0.1 M H_2SO_4 (Figure 9.11) to clean the surface and show catalytic activity for the ORR reaction. Catalytic activity for the oxygen reduction reaction is important because it indicates that the introduced platinum nanostructures increase the concentration of surface adsorbed hydrogen on the electrode surface, thereby facilitating catalysis of the ORR. Note that the bulk platinum nanostructures, as opposed to a platinum monolayer on a gold nanostructure, were prepared to show proof-of-concept NAD^+ reduction and to determine the achievable NADH production rate on a complete platinum surface. The onset of the ORR at a more positive potential for the platinum-modified electrode is evidence for the successful deposition of platinum and the presence of adsorbed proton.

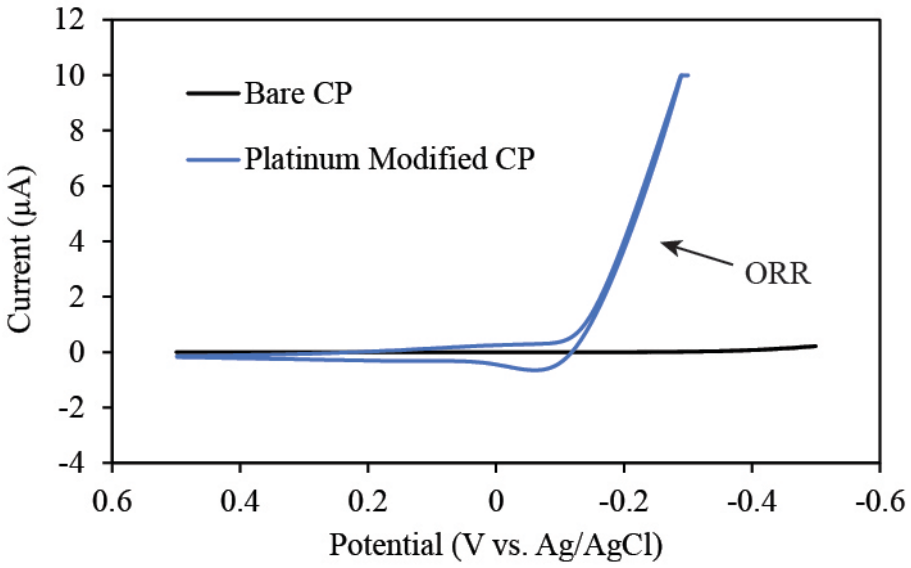

Figure 9.11. *Cyclic voltammograms of a bare CP electrode and a carbon paper electrode modified with platinum nanostructures (100s deposition) in 0.1 M H_2SO_4. The onset of the oxygen reduction reaction (ORR) is observed only on the platinum-modified sample due to platinum's ability to catalyze the ORR by providing active adsorbed hydrogen.*

Batch electrochemical testing for the reduction of NAD^+ to NADH was performed in 50 mM tris buffer (pH = 8.5) under deoxygenated conditions. The reaction solution was first purged with N_2 in a separated round-bottom flask, then transferred to the reaction chamber that had been purged with N_2 as well. Discussed in Chapter 8, stability tests performed on buffers suitable for NAD^+/NADH electrochemistry over 43 days showed that tris(hydroxymethyl)aminomethane (Tris buffer) is an ideal candidate for our studies. At 19 °C, a concentration of 50 mM, and pH = 8.5, Tris buffer retains over 90% of the original NADH concentration (as measured via absorbance at 340 nm) and shows little to no NAD^+ degradation. These conditions differ from previously reported NAD^+ reduction testing in that the most stable buffer (tris) has been used in place of the previously used phosphate buffer. The reaction was run for 1 h to produce a measurable amount of NADH and the reaction solution was continuously stirred to remove any mass transfer limitations. Figure 9.12 shows the batch electrochemical reaction setup.

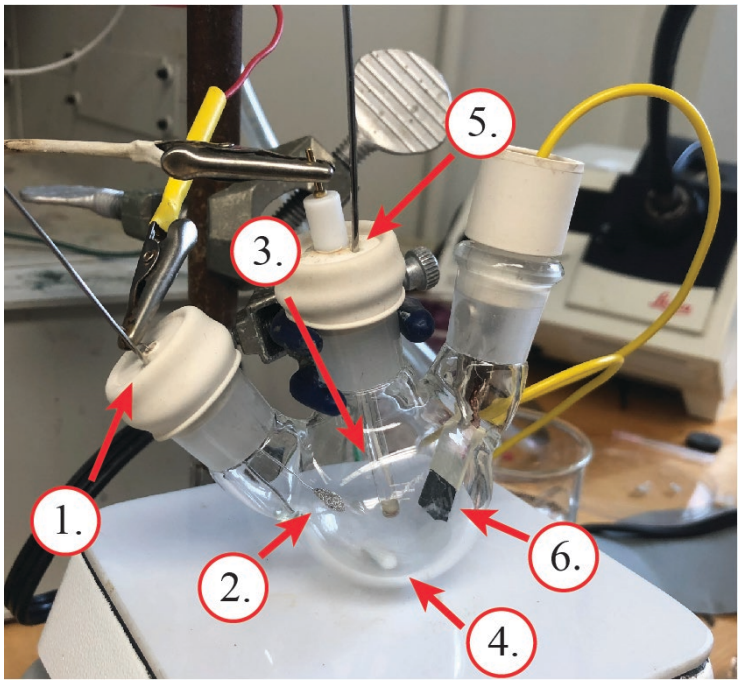

Figure 9.12. *Electrochemical batch reaction setup: 1.) Counter electrode connection and N_2 inlet needle, 2.) platinum mesh counter electrode, 3.) Ag/AgCl reference electrode, 4.) stir bar, 5.) N_2 outlet needle, 6.) carbon paper working electrode (held with alligator clip inside of reaction vessel).*

The UV Vis spectra of the reaction solution before and after the reaction at the bulk platinum-modified carbon paper electrode are shown in Figure 9.13.A and a calibration curve for the NADH absorbance at 340 nm is given in Figure 9.13.B. To obtain an absorbance spectrum within the absorbance range of the calibration curve, the reaction solution was diluted by 10X to yield the curve shown in Figure 9.13.A. From the peak absorbance of 0.13 a.u. and the calibration equation shown in Figure 9.13.B, the concentration of NADH in the diluted reaction solution was approximately 22 μM. After multiplying by the dilution factor and accounting for the 15 mL volume of the reaction cell, the NADH production rate was 3.3 μM h^{-1} cm^{-2}. Based on this preliminary data, obtaining a full and homogenous coverage of platinum on deposited gold nanostructures is key in achieving a high reaction rate.

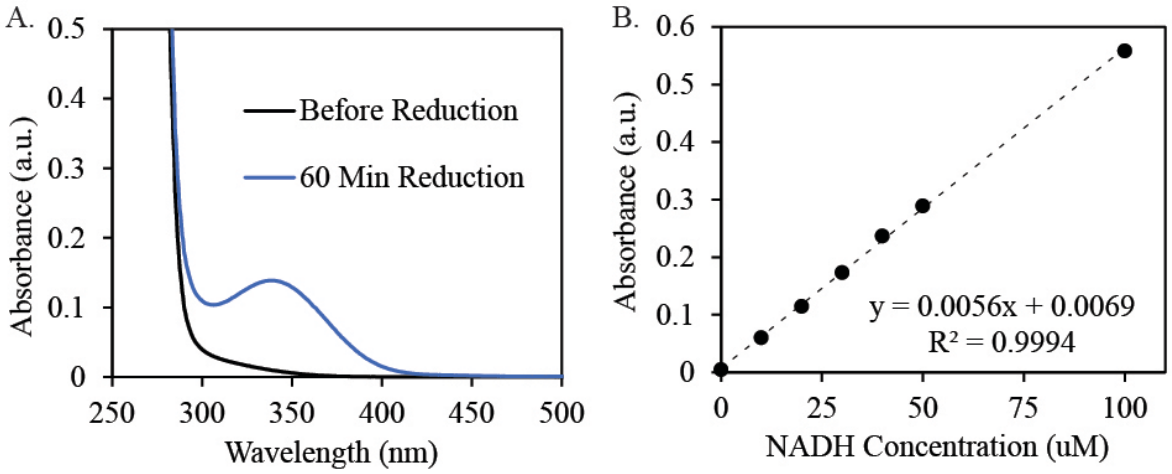

Figure 9.13. *A.) UV-Vis spectra of a 2 mM NAD^+ solution in 50 mM tris buffer (pH = 8.5) before reaction at a platinum modified carbon paper electrode and after 60 min of reaction at an applied voltage of -1.2 V vs. Ag/AgCl. The peak at 340 nm corresponds to the presence of NADH and the solution was diluted by 10X to obtain an absorbance spectrum within the bounds of the calibration curve. B.) A calibration curve for peak absorbance at 340 nm by NADH in 50 mM tris buffer.*

Next, batch electrochemical reduction of NAD^+ to NADH was performed at four types of 1 cm x 1 cm carbon paper electrodes including bare carbon paper (CP), carbon paper that was modified with gold nanostructures (denoted as Au), carbon paper modified with both gold nanostructures and a copper monolayer atop the gold (denoted as Cu), and an electrode in which the copper monolayer was electrolessly exchanged with platinum to form a platinum monolayer on the gold (denoted as Pt). A deposition potential of -2.5 V (Figure 9.14.B) was used for gold depositions due to the ability to produce smaller gold structures with a greater surface coverage at the more negative potential (compared to-1.8 V vs Ag/AgCl shown in 9.14.A). And, as previously reported, cyclic voltammetry in 1 M H_2SO_4 was used as a means of validating the presence of platinum monolayers via a catalytic activity of the oxygen reduction reaction.

The four sample types were tested in a 10 mL deoxygenated and stirred electrochemical cell containing 2 mM NAD^+ and 50 mM Tris buffer (pH = 8.5), see Figure 9.12. Samples were held at -1.2 V vs. Ag/AgCl for 15 min and an aliquot of the resulting solution was transferred to a cuvette for UV-Vis spectroscopy. Absorbance was measured between 300 and 450 nm wavelengths and the peak value near 340 nm was then used to determine the concentration of

NADH produced. Figure 9.15 shows the results of these tests, each electrode type having 3 individually prepared samples except for the Au samples (n = 2).

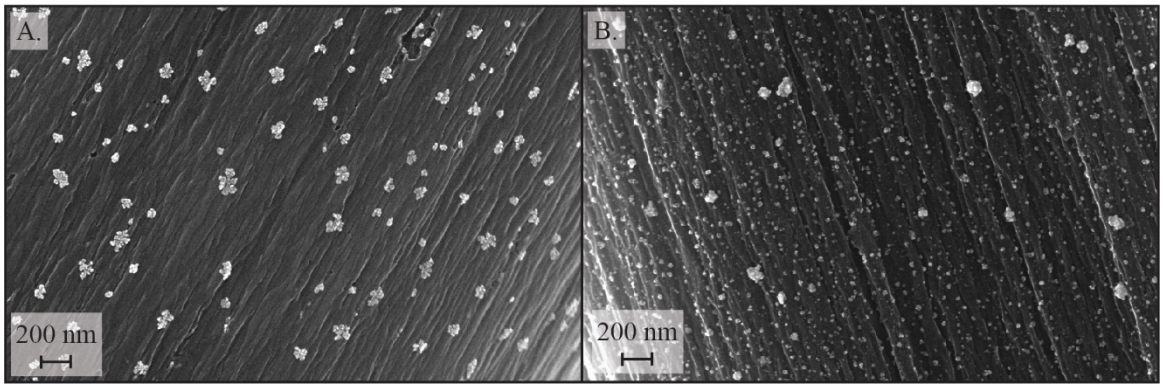

Figure 9.14. *Scanning electron micrographs of A.) gold nanostructures deposited at a potential of -1.8 V vs. graphite and B.) gold nanostructures deposited at -2.5 V vs. graphite. Gold nanostructures were deposited for 100 s from a gold acid and cetyltrimethylammonium chloride (CTAC) solution due to the higher surface coverage achieved at -2.5 V.*

The results in Figure 9.15 show that modification of the carbon paper electrodes increases both their average activity for NAD^+ reduction and the variability among samples. The bare carbon paper electrodes (CP) yielded a reproducible rate of NADH production (4.4 ± 0.3 μmol NADH h^{-1} cm^{-2}). The platinum-modified electrodes produced 5.1 ± 1.3 μmol NADH h^{-1} cm^{-2} and were more reproducible than either the gold (Au) or copper (Cu) electrodes. However, on average, the Au and Cu control electrodes exhibited higher apparent concentrations of NADH than the Pt did. Literature on electrochemical NAD^+ reduction indicates that a platinum surface produces high yields of biologically active NADH while many other metals suffer from high rates of NAD dimerization.[2, 15-16] Thus, the Pt may have produced lower concentrations of products but high concentrations of the active product. We hypothesize that the decrease in NADH production on the Pt electrodes (in comparison to Au and Cu) is due to a competitive effect of the oxygen reduction reaction (ORR) that occurs readily on platinum surfaces.

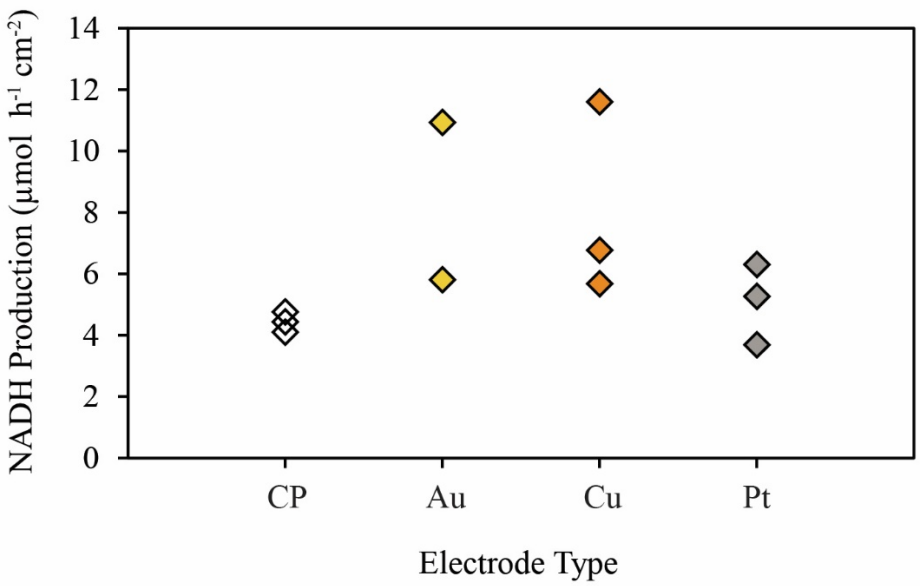

Figure 9.15. *NADH production rate for carbon paper (CP), gold nanostructure coated carbon paper (Au), copper underpotential deposited onto gold nanostructures (Cu), and monolayer Pt deposited onto gold nanostructures via electroless exchange with copper (Pt). The NADH production rates are based on increased absorbance at 340 nm wavelength measured via UV Vis spectroscopy. Tests were conducted in a 10 mL deoxygenated and stirred solution of 2 mM NAD^+ in 50 mM Tris buffer (pH 8.5) for 15 min at a reducing potential of -1.2 V vs. Ag/AgCl.*

A follow up experiment was conducted to provide additional data to the data set shown in Figure 9.15. Figure 9.16 shows the additional data points (red circles) in comparison to the data shown in Figure 9.15 (black diamonds). Similar rates of NADH production were observed with the platinum-modified electrodes yielding a slightly lower rate than previously reported. Additionally, Chapter 8 discusses the use of an enzymatic assay based on NADH oxidase (NOX) to validate NADH biological activity. The new samples (red circles) were also used to perform the NOX assay for biological activity.

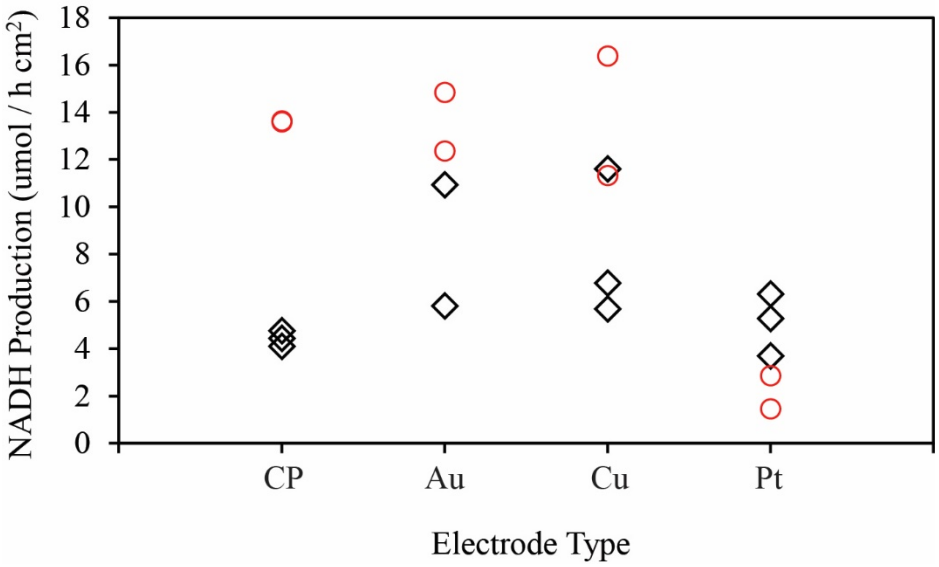

Figure 9.15. *An updated figure of the NADH production rate for previously reported samples (black diamonds) and newly prepared samples (red circles). The NADH production rate reported here is determined by the absorbance of dihydropyridine (present only in reduced NADH, not in NAD^+) in the reaction effluent.*

Using the NOX assay as the enzymatic probe for biological activity, Figure 9.16 shows scanning kinetics UV-vis curves for bare carbon paper (9.16.A), gold nanostructure-modified carbon paper (9.16.B), and platinum monolayer-modified carbon paper (9.16.C). Unfortunately, the scanning kinetics curves using NOX enzyme do not show biological activity. The peak at 340 nm wavelength (seen clearly in 9.16.B) should disappear as the NOX enzyme consumes the produced NADH. We attribute the lack of activity to the production of either NAD dimers or 1,6 NADH, which both contain dihydropyridine but are not enzymatically active.[17] Opportunities for improving the current system include chemical modifications of the carbon fiber surface or switching to a primarily sp^2 hybridized carbon electrode.

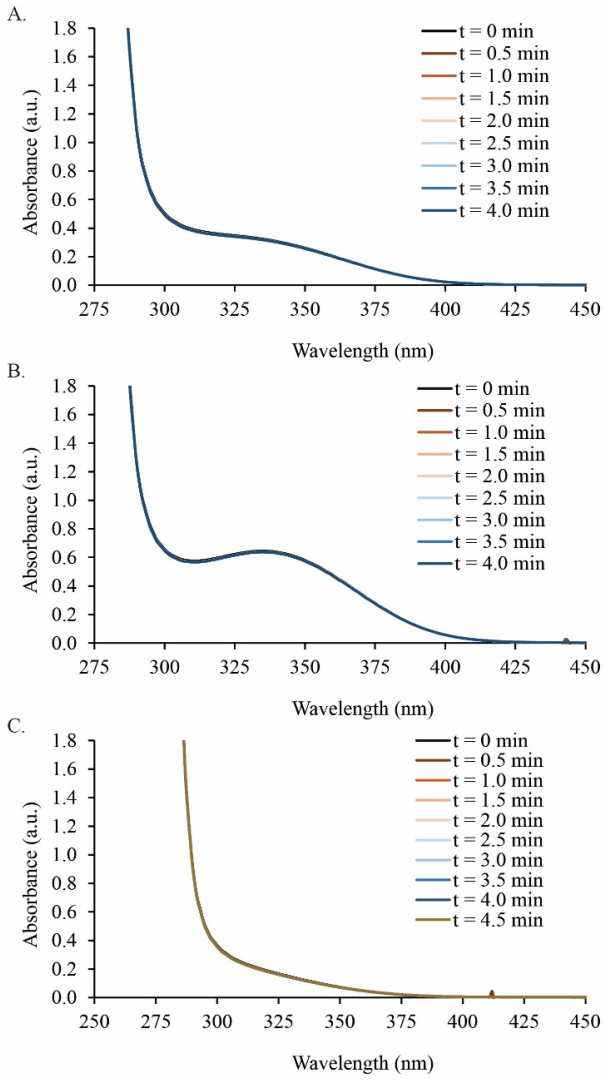

Figure 9.16. *Enzymatic activity testing of the product of NAD^+ batch electrolysis reactions performed in deoxygenated 2 mM NADH in Tris buffer for 15 min on A.) bare carbon paper, B.) gold nanostructure-modified carbon paper, and C.) platinum nanostructure-modified carbon paper electrodes. Dilute NADH oxidase (NOX) was spiked into the cuvette containing the reaction product at t = 0.5 min. Note that the scans trace themselves and no change in absorbance was observed.*

Conclusions

This chapter shows a reproducible and versatile method for the production of platinum monolayer-modified carbon paper electrodes. The size of the gold nanostructures can be tuned through deposition time and deposition potential. Some control over nanostructure morphology is also achievable. Aside from use as NAD^+ reduction catalyst, these electrodes may be used for other applications such as incorporation with PSI (see chapters 4-7) for use as a biohybrid hydrogen evolution scheme.[18-19]

When employed for the reduction of NAD+ to NADH via batch electrolysis, the electrodes produce some dihydropyridine-containing product that is not enzymatically active. Likely products are either 1,6-NADH or NAD_2 (NAD dimers).[16-17] Further work on facilitating the catalysis of NAD^+ to NADH at the produced electrodes is necessary with a key area of focus being the underlying carbon paper electrode and the remaining bare carbon paper surface. Ali et al. have reported glassy carbon electrodes modified with bulk platinum nanostructures and show NADH activity as high as 96%.[2] Therefore, the foremost conclusion from the findings reported herein is that the carbon support or underlying electrode must influence the reduction of NAD^+. Switching to sp^2 hybridized carbon or chemically modifying the carbon surface are recommended first steps in studying this shortcoming.

References

1. Ali, I.; Gill, A.; Omanovic, S., Direct electrochemical regeneration of the enzymatic cofactor 1,4-NADH employing nano-patterned glassy carbon/Pt and glassy carbon/Ni electrodes. *Chem. Eng. J.* **2012,** *188*, 173-180.
2. Ali, I.; Khan, T.; Omanovic, S., Direct electrochemical regeneration of the cofactor NADH on bare Ti, Ni, Co and Cd electrodes: The influence of electrode potential and electrode material. *J. Mol. Catal. A: Chem.* **2014,** *387*, 86-91.
3. Ali, I.; Ullah, N.; McArthur, M. A.; Coulombe, S.; Omanovic, S., Direct electrochemical regeneration of enzymatic cofactor 1,4-NADH on a cathode composed of multi-walled carbon nanotubes decorated with nickel nanoparticles. *Can. J. Chem. Eng.* **2018,** *96* (1), 68-73.

4. Tan, B. X.; Hickey, D. P.; Milton, R. D.; Giroud, F.; Minteer, S. D., Regeneration of the NADH Cofactor by a Rhodium Complex Immobilized on Multi-Walled Carbon Nanotubes. *J. Electrochem. Soc.* **2015,** *162* (3), H102-H107.

5. Kim, S.-H.; Chung, G.-Y.; Kim, S.-H.; Vinothkumar, G.; Yoon, S.-H.; Jung, K.-D., Electrochemical NADH regeneration and electroenzymatic CO2 reduction on Cu nanorods/glassy carbon electrode prepared by cyclic deposition. *Electrochim. Acta* **2016,** *210*, 837-845.

6. Lee, Y. S.; Gerulskis, R.; Minteer, S. D., Advances in electrochemical cofactor regeneration: enzymatic and non-enzymatic approaches. *Curr. Opin. Biotechnol.* **2022,** *73*, 14-21.

7. Damian, A.; Omanovic, S., Electrochemical reduction of NAD+ on a polycrystalline gold electrode. *J. Mol. Catal. A: Chem.* **2006,** *253* (1), 222-233.

8. Long, Y. T.; Chen, H. Y., Electrochemical regeneration of coenzyme NADH on a histidine modified silver electrode. *J. Electroanal. Chem.* **1997,** *440* (1-2), 239-242.

9. Tung, S.-P.; Huang, T.-K.; Lee, C.-Y.; Chiu, H.-T., Electrochemical growth of gold nanostructures on carbon paper for alkaline direct glucose fuel cell. *RSC Advances* **2012,** *2* (3), 1068-1073.

10. Oyamatsu, D.; Nishizawa, M.; Kuwabata, S.; Yoneyama, H., Underpotential deposition of silver onto gold substrates covered with self-assembled monolayers of alkanethiols to induce intervention of the silver between the monolayer and the gold substrate. *Langmuir* **1998,** *14* (12), 3298-3302.

11. Herrero, E.; Buller, L. J.; Abruña, H. D., Underpotential Deposition at Single Crystal Surfaces of Au, Pt, Ag and Other Materials. *Chem. Rev.* **2001,** *101* (7), 1897-1930.

12. Mohl, M.; Dobo, D.; Kukovecz, A.; Konya, Z.; Kordas, K.; Wei, J.; Vajtai, R.; Ajayan, P. M., Formation of CuPd and CuPt Bimetallic Nanotubes by Galvanic Replacement Reaction. *J. Phys. Chem. C* **2011,** *115* (19), 9403-9409.

13. Yuan, M.; Kummer, M. J.; Milton, R. D.; Quah, T.; Minteer, S. D., Efficient NADH Regeneration by a Redox Polymer-Immobilized Enzymatic System. *ACS Catalysis* **2019,** *9* (6), 5486-5495.

14. Khosravi, M.; Amini, M. K., Carbon paper supported Pt/Au catalysts prepared via Cu underpotential deposition-redox replacement and investigation of their electrocatalytic activity for methanol oxidation and oxygen reduction reactions. *Int. J. Hydrogen Energy* **2010,** *35* (19), 10527-10538.

15. Bresnahan, W. T.; Elving, P. J., The role of adsorption in the initial one-electron electrochemical reduction of nicotinamide adenine dinucleotide (NAD+). *J. Am. Chem. Soc.* **1981,** *103* (9), 2379-2386.

16. Elving, P. J.; Bresnahan, W. T.; Moiroux, J.; Samec, Z., Nad Nadh as a Model Redox System - Mechanism, Mediation, Modification by the Environment. *Bioelectrochem. Bioenerg.* **1982,** *9* (3), 365-378.

17. Rover, L.; Fernandes, J. C. B.; Neto, G. d. O.; Kubota, L. T.; Katekawa, E.; Serrano, S. l. H. P., Study of NADH Stability Using Ultraviolet–Visible Spectrophotometric Analysis and Factorial Design. *Anal. Biochem.* **1998,** *260* (1), 50-55.

18. Badura, A.; Kothe, T.; Schuhmann, W.; Rögner, M., Wiring photosynthetic enzymes to electrodes. *Energy Environ. Sci.* **2011,** *4*, 3263-3274.

19. LeBlanc, G.; Chen, G.; Jennings, G. K.; Cliffel, D. E., Photoreduction of Catalytic Platinum Particles Using Immobilized Multilayers of Photosystem I. *Langmuir* **2012,** *28* (21), 7952-7956.

Chapter 10 – Summaries & Perspectives

A summary of each research chapter along with a perspective and outlook for PSI bioelectrodes and electrochemical NADH regeneration is given below. Thank you for your interest and time spent reading this dissertation.

Summary of PSI Bioelectrode Research

The PSI bioelectrodes produced in Chapters 4, 5, and 6 show great promise in improving MET within PSI biohybrid devices. First, the challenges of improving protein loading and capturing converted mediator were addressed by developing porous, translucent, and conductive ITO electrodes. The protein complexes, trapped within the inverse opal pores of the ITO cathode, produced oxidized DCPIP that diffuses through the porous structure and reacts at the high surface area mesoporous pore wall (Figures 4.5 & 4.6). The porous ITO cathodes produced 42.4 ± 5.2 μA cm^{-2} at a protein loading of 66 μg cm^{-2} and avoided the "pore blockage" effects observed for mesoporous cathodes. In future works, porous electrodes may be incorporated into full PSI devices or solid-state biohybrid photovoltaics. Additionally, the use of porous, conductive, and transparent electrodes for photoactive protein complex based bioelectrodes could be extended to other fields such as biophotocatalysis or biosynthesis. Lastly, the finding that 5 μM pores performed best in comparison to both smaller and larger pores calls for further research into the diffusion of reactive, soluble species through porous electrode architectures because even 3-dimensional diffusional models do not account for the porosity of the electrode material.

Chapter 5 lays out a method for preparing PSI complexes with stromal-side only chemical modifications. The modified PSI complexes were then used to prepare PSI monolayers with distinct deposition rates and wetting properties. The distinct surface properties imply that the PSI complexes may be oriented on the surface. However, when photochronoamperometry was conducted in an aerobic solution, similar photocurrents were observed for each of the distinct monolayers. The presence of oxygen and similarity of the performance of the PSI control and modified PSI monolayers leads to the conclusion that oxygen mediated electron transfer (MET) was prevalent and that additional surface or protein complex modification is necessary to facilitate DET.

Chapter 6 explores a method for increasing the loading of PSI monolayers beyond a single monolayer, addressing some of the challenges faced in Chapter 5 by increasing the areal loading of the protein complex. A layer-by-layer assembly process was employed with PSI monolayers deposited in between PEDOT:PSS layers. Up to 9-layer pairs were produced with highly reproducible layer thicknesses (8.11 ± 0.14 nm per layer pair). A maximum in photocurrent performance, 414 ± 13 nA/cm^2, was achieved at 6-layer pairs with a trade-off being made between protein complex loading and loss of connectivity of the PEDOT:PSS conductive matrix at higher layer pairs. PSI and PEDOT:PSS LBL assemblies show an order of magnitude greater turnover numbers than PSI multilayers in the same mediator, proving that the PEDOT:PSS conductive matrix is beneficial to MET in PSI bioelectrodes.

Perspectives and Outlook for PSI-Based Biohybrids

The current challenges in PSI biohybrid energy conversion are developing a better understanding of oxygen effects in MET, developing strategies for achieving DET, and producing solid state PSI biohybrid devices. Many research efforts have been aimed at understanding oxygen interactions in PSI bioelectrodes, but the importance of oxygen should be included in all reports of novel PSI studies.[1-4] One critical area of research is the effect of oxygen on solid-state and quasi-solid-state PSI devices.[1, 5]

Research efforts in determining the typical modes of electron transfer based on photochronoamperometry or photocurrent curve shape would be greatly beneficial. For example, the diffusional limited current achieved in Chapter 4 (Figure 4.13) varies greatly in appearance from the curves in the LBL assembly in Chapter 6 (Figure 6.15). However, these systems both undergo MET. Until a comprehensive understanding of the many electron transfer mechanisms encountered in PSI bioelectrodes is available, modelling studies may be the best resource for better understanding photocurrent curve shapes and meanings.[5-7]

Lastly, the move toward solid-state PSI devices is greatly promising and challenging, in that a solid device weighs less than an electrochemical cell and requires the ability to achieve DET

if the solvent is removed (mediators require a solvent). Many reports have shown the promise of solid-state PSI devices.[1, 8-12] A few interesting prospects based upon the work discussed in this dissertation include the use of porous electrodes in solid-state devices, leveraging modified PSI for use in solid-state films, and the ability to systematically deposit individual monolayers, which may enable the fabrication of solid-state films with alternating or specified compositions.

Summary of NADH Regeneration Research

Developing an electrochemical means of recycling NADH as an enzymatic cofactor will require considerations of long-term stability (Chapter 8) and the production of biologically active NADH from NAD^+ at a specialized electrode (Chapter 9). Chapter 8 shows that tris buffer at a pH of 8.5 is an ideal buffer for enabling the stability of both NAD^+ and NADH over 40+ days with a degradation rate of only 4 μM NADH per day at 19 °C and 11 μM NADH per day at 25 °C. Unfortunately, the NADH oxidase (NOX) enzyme also reacted with slower kinetics in the tris buffer system. Regardless of the specific application, careful selection of the buffer is necessary if the solution should be used for more than several hours and should be considered in all electrochemical cofactor regeneration efforts.[13]

Chapter 9 gives a detailed protocol to produce platinum monolayer-modified carbon paper electrodes. The procedure is highly tunable and can produce various nanostructure sizes and morphologies. Briefly, gold nanostructures were electrochemically deposited from gold acid and CTAC solutions with various potentials, times, and potential waveforms. The nanostructures deposited as “coral-like” structures at more positive potentials, and the structure size decreased drastically at more negative potentials (Figure 9.4). Pulsed depositions resulted in greater areal coverage of nanostructures (Figure 9.6). Then, copper monolayers were deposited using underpotential deposition and exchange via electroless or galvanic exchange for platinum monolayers. The success of the fabrication procedure was then shown via catalysis of the oxygen reduction reaction (Figure 9.10). Platinum-modified carbon paper electrodes achieved a similar potential onset of the ORR to bulk platinum.

The platinum-modified carbon paper electrodes produced dihydropyridine containing reaction products that were not biologically active 1,4-NADH when used in a batch NAD^+ reduction reaction. The product is most likely 1,6-NADH or NAD_2 dimers.[14] Based on the success of other reports with similar catalysis strategies, the cause of the inactivity is most likely the underlying carbon paper electrode.[15-17] Future studies utilizing this deposition procedure should focus on changing the carbon substrate for an sp^2 hybridized carbon or chemically modifying the carbon paper surface.

Perspectives & Outlook for Electrochemical NADH Regeneration

Many challenges remain in improving the electron transfer between biomolecules and electrode materials with the frontiers of this field working on enabling direct electron transfer and better understanding of proton coupled electron transfer. While others have reported up to 97% biological activity of NADH produced at bare metal catalysts, alternative means of electrochemical NAD+ reduction are available.[16] These include both MET with an organometallic catalyst or DET between a surface, an organometallic catalyst, and NAD^+.[18-20] Prospects regarding NAD^+ based on Chapters 8 and 9 of this dissertation include the use of highly stable buffer systems for the cofactors and the use of high-surface area electrodes. Note that the first step in the NAD^+ reduction mechanism is adsorption and electron transfer (Figure 7.2); therefore, high-surface area electrodes are critical for improving the production rate per footprint area. Potential also exists for the success of techniques reported in Chapters 4 & 6 (porous and conductive electrodes and layer-by-layer assembly) to produce electrodes for NAD^+ reduction. The most important future work based upon Chapter 9 is the study of the effects of the underlying carbon electrode hybridization and surface chemistry on the adsorption and reduction of NAD^+ to NADH.

References

1. Wolfe, K. D.; Dervishogullari, D.; Passantino, J. M.; Stachurski, C. D.; Jennings, G. K.; Cliffel, D. E., Improving the stability of photosystem I–based bioelectrodes for solar energy conversion. *Curr. Opin. Electrochem.* **2020,** *19*, 27-34.

2. Zhao, F.; Hardt, S.; Hartmann, V.; Zhang, H.; Nowaczyk, M. M.; Rögner, M.; Plumeré, N.; Schuhmann, W.; Conzuelo, F., Light-induced formation of partially reduced oxygen species limits the lifetime of photosystem 1-based biocathodes. *Nature Comm.* **2018,** *9*.

3. Zhao, F.; Ruff, A.; Rögner, M.; Schuhmann, W.; Conzuelo, F., Extended Operational Lifetime of a Photosystem-Based Bioelectrode. *J. Am. Chem. Soc.* **2019,** *141*, 5102-5106.

4. Nguyen, K.; Bruce, B. D., Growing green electricity: Progress and strategies for use of Photosystem I for sustainable photovoltaic energy conversion. *Biochim. Biophys. Acta Bioenerg.* **2014,** *1837*, 1553-1566.

5. Passantino, J. M.; Wolfe, K. D.; Simon, K. T.; Cliffel, D. E.; Jennings, G. K., Photosystem I Enhances the Efficiency of a Natural, Gel-Based Dye-Sensitized Solar Cell. *ACS Appl. Bio. Mater.* **2020**.

6. Buesen, D.; Hoefer, T.; Zhang, H.; Plumeré, N., A kinetic model for redox-active film based biophotoelectrodes. *Faraday Discuss.* **2019,** *215*, 39-53.

7. Robinson, M. T.; Cliffel, D. E.; Jennings, G. K., An Electrochemical Reaction-Diffusion Model of the Photocatalytic Effect of Photosystem I Multilayer Films. *J. Phys. Chem. B* **2018,** *122* (1), 117-125.

8. Barhom, H.; Carmeli, C.; Carmeli, I., Fabrication of Electronic Junctions between Oriented Multilayers of Photosystem I and the Electrodes of Optoelectronic Solid-State Devices. *J. Phys. Chem. B* **2021,** *125* (3), 722-728.

9. Gizzie, E. A.; Scott Niezgoda, J.; Robinson, M. T.; Harris, A. G.; Kane Jennings, G.; Rosenthal, S. J.; Cliffel, D. E., Photosystem I-polyaniline/TiO2solid-state solar cells: Simple devices for biohybrid solar energy conversion. *Energy Environ. Sci.* **2015,** *8*, 3572-3576.

10. Gordiichuk, P. I.; Wetzelaer, G. J. A. H.; Rimmerman, D.; Gruszka, A.; De Vries, J. W.; Saller, M.; Gautier, D. A.; Catarci, S.; Pesce, D.; Richter, S.; Blom, P. W. M.; Herrmann, A., Solid-state biophotovoltaic cells containing photosystem i. *Adv. Mater.* **2014,** *26*, 4863-4869.

11. Kazemzadeh, S.; Riazi, G.; Ajeian, R., Novel Approach of Biophotovoltaic Solid State Solar Cells Based on a Multilayer of PS1 Complexes as an Active Layer. *ACS Sustain. Chem. Eng.* **2017,** *5*, 9836-9840.

12. Zeynali, A.; Ghiasi, T. S.; Riazi, G.; Ajeian, R., Organic solar cell based on photosystem I pigment-protein complex, fabrication and optimization. *Org. Electron.* **2017,** *51*, 341-348.

13. Chenault, H. K.; Simon, E. S.; Whitesides, G. M., Cofactor Regeneration for Enzyme-Catalysed Synthesis. *Biotechnol. Genet. Eng. Rev.* **1988,** *6* (1), 221-270.

14. Bresnahan, W. T.; Elving, P. J., The role of adsorption in the initial one-electron electrochemical reduction of nicotinamide adenine dinucleotide (NAD+). *J. Am. Chem. Soc.* **1981,** *103* (9), 2379-2386.

15. Ali, I.; Gill, A.; Omanovic, S., Direct electrochemical regeneration of the enzymatic cofactor 1,4-NADH employing nano-patterned glassy carbon/Pt and glassy carbon/Ni electrodes. *Chem. Eng. J.* **2012,** *188*, 173-180.

16. Ali, I.; Khan, T.; Omanovic, S., Direct electrochemical regeneration of the cofactor NADH on bare Ti, Ni, Co and Cd electrodes: The influence of electrode potential and electrode material. *J. Mol. Catal. A: Chem.* **2014,** *387*, 86-91.

17. Ali, I.; Ullah, N.; McArthur, M. A.; Coulombe, S.; Omanovic, S., Direct electrochemical regeneration of enzymatic cofactor 1,4-NADH on a cathode composed of multi-walled carbon nanotubes decorated with nickel nanoparticles. *Can. J. Chem. Eng.* **2018,** *96* (1), 68-73.

18. Lee, Y. S.; Gerulskis, R.; Minteer, S. D., Advances in electrochemical cofactor regeneration: enzymatic and non-enzymatic approaches. *Curr. Opin. Biotechnol.* **2022,** *73*, 14-21.

19. Tan, B. X.; Hickey, D. P.; Milton, R. D.; Giroud, F.; Minteer, S. D., Regeneration of the NADH Cofactor by a Rhodium Complex Immobilized on Multi-Walled Carbon Nanotubes. *J. Electrochem. Soc.* **2015,** *162* (3), H102-H107.

20. Yuan, M.; Kummer, M. J.; Milton, R. D.; Quah, T.; Minteer, S. D., Efficient NADH Regeneration by a Redox Polymer-Immobilized Enzymatic System. *ACS Catalysis* **2019,** *9* (6), 5486-5495.

Appendix A – Photosystem I Extraction & Quantification Procedures

Prior to use in Photosystem I (PSI) biohybrid devices or for PSI-electrode interface studies, the PSI complex must be isolated and quantified. PSI can be isolated from a variety of sources including species of cyanobacterium and higher plants to be used in the conversion of solar to chemical or electrical energy.[1-4] The following procedure is designed for the isolation of PSI from baby spinach (young leaves harvested from *Spinacia oleracea.)* Baby spinach should be purchased at a local grocer for PSI isolation. The isolation of PSI complexes, also called PSI extraction, is a stepwise procedure taking place over several hours, followed by storage, and quantification. Additionally, the resulting PSI solution may be dialyzed against deionized (DI) water to remove surfactant, depending on the desired application of the PSI complexes. Dialysis is typically performed just before the PSI is to be used in an experiment. The procedure herein was adapted from Reeves and Hall, Shiozawa et al., Millsaps et al., Kincaid et al., and Baba et al.[5-9] Figure A.1 shows the general extraction steps, and the following sections give the solution recipes and the step-by-step extraction procedure.

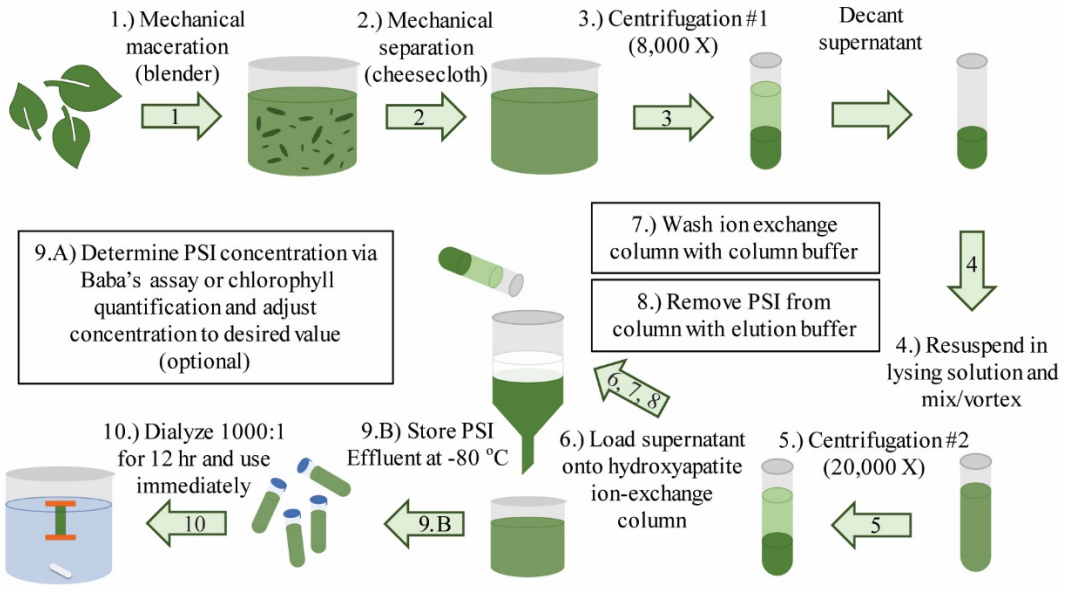

Figure A.1. *Schematic of the PSI extraction procedure from baby spinach. Steps 7, 8, and 9.A are not shown but are described in the written procedure below.*

For best results, the solutions required for the extraction should be prepared in advance and chilled to at least 4 °C. This allows for a streamlined workflow during the extraction while also maintaining a cold temperature at each step. The solution recipes provided below are sufficient for a typical extraction from 100-150 g of baby spinach leaves and the expected yield of PSI is 50-100 mL of 1-3 mg/mL PSI. This extraction may be modified in several ways. Namely, the centrifugation step using grinding medium may be repeated to increase the concentration of PSI by increasing the total number of separated thylakoid membranes. It is important to note that this procedure is often performed in the absence of ambient light (lights turned off). However, no significant variation in results of extracted PSI has been observed and, therefore, this choice is left to a matter of personal preference. Important safety considerations during the extraction procedure include the use of a high-velocity desktop centrifuge. The centrifuge vials (including the vial, cap, and contents) must be balanced before each centrifugation step. Please refer to the centrifuge's operating manual for balance tolerances. The maximum tolerance reported for the Allegra X-30R Centrifuge by Beckman Coulter when using either the F-0850 or F-0630 rotor is +/- 6 g. It is strongly recommended that all vials are balanced to within +/- 100 mg when using these rotors.

Column Buffers

The two sodium phosphate buffers used for the ion affinity column are responsible for the washing of other proteins and organic matter from the column (Column Buffer) and then the elution or removal of PSI from the column (Elution Buffer). The hydroxyapatite ion affinity column works based on both a change in pH and a change in ionic concentration or ionicity of the buffer.[10] The column buffer is a 10 mM sodium phosphate buffer with a pH of 7 and the elution buffer is a 200 mM sodium phosphate buffer with a pH of 6.5. The elution buffer also contains 0.05 wt % Triton X-100 to promote desorption and solubilization of PSI during elution. Note that the pH values of the buffers should be checked and slightly adjusted, but they should be very near the expected value. The Henderson-Hasselbach equation and the pKa of the sodium monobasic and dibasic buffer system (6.82) may be used to prepare buffers of differing ionic strengths or pH values.

Extraction Solutions

Grinding Medium (300 mL)

- Sorbitol 18.040 g
- Na-Pyrophosphate 1.340 g
- $MgCl_2 \cdot 6H_2O$ 0.240 g
- (L) Ascorbic Acid 0.110 g

*Adjust pH to 6.5 with HCl

Lysing Solution (100 mL)

- HEPES 1.192 g
- Sorbitol 6.012 g
- EDTA 0.058 g
- $MgCl_2 \cdot 6H_20$ 0.020 g
- $MnCl_2 \cdot 4H_2O$ 0.020 g
- Triton X-100 1.000 g
  1.00% (w/v)

- $NaH_2PO_4 \cdot H_20$ (Monobasic) 0.549 g
- Na_2HPO_4 anhydrous (Dibasic) 0.855 g

*Adjust pH to 7.0

Elution Buffer (1 L)

- $NaH_2PO_4 \cdot H_20$ (Monobasic) 18.656 g
- Na_2HPO_4 anhydrous (Dibasic) 9.199 g
- Triton X-100 0.500 g
  0.05% (w/v)

*Adjust pH to 6.5

Procedure

The PSI extraction procedure is composed of multiple steps that must be followed sequentially (Figure A.1). To maximize efficiency, upcoming steps can be prepped while waiting on the current step to be completed. Note that all extraction solutions should be prepared well in advance (usually the day before the extraction) and stored in a refrigerator at 4 °C. Also be sure that ice is available to chill the column and a bucket and circulation pump to use for several hours. The centrifuge should be turned on and chilled to 4 °C (it will take several hours to cool, and the first rotor (F-0850) should be loaded while it is cooled). Before beginning check that the blender, centrifuge tubes (both sizes for each rotor), and column are clean and dry. Also check that plastic vials for PSI storage are available (~100 mL of volume total, typically in 2 mL aliquots). If PSI quantification and dilution to a desired concentration will be performed before storage, be sure

that a UV-Vis spectrometer is available for use immediately after the extraction and that the quantification solutions have been prepared.

1. **Mechanical Maceration**

First the baby spinach leaves must be deveined and weighed. Remove the stems and any large veins or harder plant materials and discard. This is easily done by holding a leaf with the thumb of one hand across the center vein coming from the stem and ripping the softer and dark green section from the opposite side. Then switch hands and rip the other side from the central vein and stem. Discard the vein and stem. Devein approximately 100 – 150 g of baby spinach leaves and load them into the blender. Pour 200 mL of grinding medium into the blender and blend until the contents appear homogenous (well blended so that no large pieces of leaf remain).

2. **Mechanical Separation**

Large (unmacerated) leaf material must now be removed via mechanical separation using a cheesecloth filter. Before proceeding, check that the centrifuge is on and cooled to 4 °C with the F-0850 rotor loaded.

Place two layers of cheesecloth within a funnel and position the funnel so that it empties into a beaker of at least 300 mL volume. Pour the contents of the blender into the cheesecloth slowly. You may have to stop and change the cheesecloth if it becomes clogged. After the first pass of the solution, switch the cheesecloth filter to eight layers and pour the collected volume through the cheesecloth into another 300 mL beaker. You may need to gently squeeze the cheesecloth to promote solution to pass through during these separation steps. You should collect approximately 150-200 mL of solution after the eight-layer separation.

3. **Centrifugation #1 (Thylakoid Separation)**

After maceration and mechanical separation, the thylakoids will be isolated by centrifugation. The thylakoids and thylakoid stacks are heavier than other organelles and plant cell debris in solution and will therefore pellet when centrifuged at the appropriate angular velocity.

After this centrifugation, the pellet will be kept and the supernatant discarded. Before proceeding check that the centrifuge is prepared with the correct rotor (F-0850), it is cooled, and the settings are set to RCF = 8,000 and Time = 1 min. Be sure that the rotor setting on the centrifuge is correct! The rotor setting corresponds to the rotor number (the "F" is omitted). If the rotor setting is incorrect the angular velocity necessary to obtain the correct RCF will be incorrectly calculated by the centrifuge.

Locate the centrifuge tubes/vials that are sized to fit the F-0850 rotor (they are larger than the tubes for the F-0630 rotor) and place them in a holder or rack. Divide the filtered solution into the tubes. They should be filled approximately halfway (20-25 mL each). Now balance the tubes by eyesight. Use a Pasteur pipet to transfer solution from the tubes with a greater volume to those with less. Be sure that the tubes are straight vertically and that they are sitting in their stands at equal heights. You may want to look at eye level to the menisci to check for equally level filling. Next, take the mass of each tube (including the cap) and write the masses down on a scrap piece of paper. They can be labeled on the cap for notetaking. After weighing, check that the maximum difference between any two tubes is not greater than 100 mg. If you are using a centrifuge other than the Allegra X-30R Centrifuge by Beckman Coulter, check the manufacturer's balance tolerance guidelines. Once the vials are balanced, place them in the F-0850 rotor. Be sure that you fill the rotor or (if using less vials for an alternative extraction) the rotors are loaded in a balanced manner. Search "balanced loading of centrifuge holders" for more information.

After the vials are properly loaded, tighten the rotor cap (do not overtighten, finger tight is sufficient) and close the centrifuge lid. Check the settings (Rotor = 0850, RCF = 8,000 and Time = 1 min) and begin the centrifugation by pressing start. The centrifuge will make a humming noise. If you hear a rattle as the centrifuge is ramping up, immediately press stop. While you wait, you may locate the centrifuge tubes for the second centrifugation and the lysing solution. After the centrifugation, remove the samples and discard the supernatant. The pellet can be left in the vials for the next step.

4. Lysing the Thylakoid Membrane

A surfactant containing solution will now be used to lyse the thylakoid membranes (located in the pellet). The surfactant acts by inserting into the hydrophobic regions of the lipid bilayer membrane, solubilizing the lipids, and releasing membrane bound proteins. The surfactant also solubilizes proteins by binding to their hydrophobic equatorial regions that are typically embedded within the thylakoid membrane. Herein the surfactant will be Triton X-100. Other surfactants may be used, and significant amounts of research have been conducted on surfactant properties and effects on isolated PSI activity.[4, 11] From this step forward (until dialysis) the PSI complex will be solubilized by some amount of Triton X-100 so that it will remain suspended in solution (if the surfactant is removed, PSI may "crash out" of solution). Note that prior to this step, modifications of the stromal side of the PSI complex may be achieved by introducing amine reactive molecules before lysing the membrane. More detail on PSI stromal side modifications is given in a later section of this procedure.

Begin by changing the centrifuge rotor to the F-0630 rotor in preparation for the next centrifugation step and changing the centrifuge settings to Rotor = 0630, RCF = 20,000, and Time = 15 min. With a Pasteur pipet, load a few mL (2-3 mL) of lysing solution into each of the eight centrifuge tubes containing pellets from the previous step. Vortex each tube for ~30 s (or shake vigorously) and empty the contents into the tubes for the next centrifugation step (the smaller tubes for the F-0630 rotor). Note that the F-0630 rotor can only hold six tubes, so the solution from the previous eight tubes must be equally distributed among the six for the next step. Place these tubes open on a holder or rack.

5. Centrifugation #2 (Removal of Cell Material)

The second centrifugation will separate any thylakoids that were not successfully lysed or any heavier organelles and cell material from the now solubilized PSI complexes. Remember that there is also solubilized lipids and other proteins in the solution as well. Any solubilized cell material that is not heavier than PSI will not be separated at this step. The solubilized PSI complexes will not "fall-out" into the pellet, they will remain in the supernatant. Therefore, after this centrifugation the supernatant will be collected, and the pellets discarded. Because the

supernatant will be collected, it is advisable to use as little lysing solution as possible during this step. Approximately 25-40 mL total volume or 3-6 mL per R-0630 centrifuge tube (six tubes) is a good benchmark.

Begin by ensuring that the centrifuge is cool, the rotor has been changed to the F-0630 rotor, and the settings are correct for this step (Rotor = 0630, RCF = 20,000, Time = 15 min). Now, balance the six tubes with a few additional mL of lysing solution. Balance by eyesight as described in step 3 and weight the tubes (including caps) to verify the largest discrepancy in mass is less than 1 mg between any two tubes. Vortex or shake each tube vigorously, again, for 30 s. Load the tubes and begin the centrifugation.

This step will take over 15 min, so this time should be used to prepare the column. Place a circulation pump with the outlet connected to a hose in a bucket and fill it with ice. Then fill the void space in the bucket with cold tap water. Secure a straight jacketed extraction column (with a valve) upright using glassware clamps. Attach the outlet of the pump to the lower inlet of the column jacket and attach another piece of tubing to the upper jacket opening. This tube should return the water to the bucket so that the flow of the cooling water is up through the jacket. Weigh 15 g of hydroxyapatite (fast-flow) and place it in a 300 mL beaker. Add enough column buffer to this beaker to cover the hydroxyapatite with an excess of a few cm above. Stir the mixture and allow it to settle for 30-60 s then discard the column buffer without losing much of the hydroxyapatite. Repeat this procedure once more. This is a washing/activation step that removes very small hydroxyapatite particles that may slow down flow through the column and allows the hydroxyapatite to become properly charge for the column loading procedure. Fill the beaker with column buffer again and pour the mixture into the column with the valve closed. After the hydroxyapatite settles, open the valve, and allow the excess column buffer to drain into a waste beaker until the meniscus is exactly level with the top of the now packed hydroxyapatite layer. Turn the valve off, discard the column buffer waste, and turn on the circulation pump to cool the column.

Return to the centrifuge to collect the tubes after the centrifugation has finished. Remove the tubes, decant the supernatant into a small beaker or Erlenmeyer flask (there should be

approximately 25-30 mL), and turn off the centrifuge. The tubes and pellets can be set aside for cleaning later.

6. Loading the Extraction Column

The loading of the hydroxyapatite extraction column with PSI is achieved by collecting the negatively charged, solubilized PSI complexes via hydrostatic interactions with the hydroxyapatite particles.[12] Note that the PSI complex's net negative charge is due to the collective charge of surface amino acid residues that are mostly primary amines (found in lysine residues) and carboxylic acids. The surface charge of PSI complexes in solution is dependent on the solution pH and the pKa's of the surface amino acid residues. The isoelectric point of solubilized PSI was reported as 4.4, making PSI negatively charged at neutral pH.[12] During the column loading, acidic proteins (including PSI) will adhere to the hydroxyapatite electrostatically.[12]

Using a Pasteur pipet, carefully load the supernatant from the second centrifugation step onto the column. The solution can be applied to the inner column wall, 1-3 cm above the top of the hydroxyapatite layer, and allowed to run down the wall to avoid disrupting the hydroxyapatite surface. Load all the solution while keeping the column valve in the off position. Open the valve and allow the solution to flow through the column, catching the waste in a beaker, until the meniscus is again level with the top of the hydroxyapatite. The column is now loaded with PSI and should be visibly dark green.

7. Washing the Extraction Column

Washing the extraction column with a low ionic concentration buffer (the column buffer) will remove any weakly bound or positively charged species. These species may include other proteins or protein complexes or micelles of thylakoid membrane lipids. While washing the column, a green effluent will be removed and should be discarded. However, the column should either remain green or a green band should remain. After washing the column, PSI complexes will be removed in the next step by using a high ionic concentration buffer that also contains a surfactant.

With the valve in the off position, and in the same manner that the PSI solution was loaded onto the column, careful load column buffer onto the column. After the buffer is filled several centimeters above the hydroxyapatite layer, the valve can be opened, and the effluent caught in a waste beaker. Continue to add column buffer, keeping the level several centimeters above the hydroxyapatite (even filling the column is alright), until the effluent is completely clear. The washing process may take 1-2 h. After the effluent becomes clear, allow the remaining column buffer to pass through the column until the meniscus is level with the hydroxyapatite, then turn the valve off. The column buffer can be kept on ice to keep it chilled while loading it onto the column during the washing procedure.

8. Eluting the Extraction Column/Collecting PSI

By changing the buffer to a high ionic concentration and slightly lowering the pH, the electrostatic attraction of negatively charged species to the column will be decreased due to charge shielding by the ions in solution.[10] Additionally, the excess Triton X-100 solubilizes PSI complexes adsorbed to the hydroxyapatite that may have lost a portion of their surfactant during the washing procedure. A combination of these driving forces results in the release of PSI from the column when the elution buffer is used.

Load elution buffer onto the column carefully as described above in steps 6 and 7. After an excess of elution buffer is loaded, open the valve. Keep a waste collection beaker under the column until the effluent becomes a dark green. Some extractions result in lighter effluent colors, but there will be a change in effluent color and even the appearance of a downward moving “band” of PSI in the column. Continue adding elution buffer. When the dark effluent or band reaches the outlet of the column switch to a PSI collection beaker. Continue adding elution buffer and collecting the darker PSI effluent until the color begins to change back toward clear. After a sufficient volume of darker PSI effluent is collected (typically 50-100 mL), the valve can be turned off. The pump can be turned off as well and the column left for cleanup after the PSI solution is stored. At this point in the extraction an unknown concentration of PSI has been isolated and is ready to store at -80 °C. The next step (9) includes an optional quantification and dilution step (9.A) followed by the storage instructions.

9. Quantify and Store PSI

9.A) PSI Quantification and Dilution (Optional)

Before storing, the concentration of the isolated PSI may be quantified to allow for dilution to a chosen concentration. This step is optional, but it is very beneficial as well. First, adjusting the PSI concentration to a known (presumably round and easily remembered) number will allow for easy reporting of the concentration used in future studies. Second, if the concentration is known, dilution studies can be easily designed without further concentration analyses. The expected PSI concentration based on past results is between 1-3 mg PSI/mL. There are two procedures typically used for PSI concentration quantification, Baba's assay and chlorophyll quantification.[5] For best results, both can be used and contrasted. While performing the quantification procedure(s) the PSI solution should be kept covered in a refrigerator at 4 °C. After using one or both quantification procedures, the determined concentration can be used to dilute the remaining PSI solution to any chosen value via $C_1V_1 = C_2V_2$ using the remaining elution buffer. The procedure for Baba's assay is outlined in the "Baba's Assay" section of this document.

9.B PSI Storage

The isolated PSI concentration (regardless of whether Step 9.A was taken) is now prepared to be stored at -80 °C in the elution buffer. Use a Pasteur pipet to transfer aliquots of PSI solution into small vials. Typically, 2 mL vials are chosen although smaller aliquots may be suitable for certain projects. Place the capped vials into a box or other storage container and label well with your name and date of extraction. The concentration should be noted as well if it is known. Place the box in a -80 °C freezer and begin cleanup of the glassware/equipment used. Remember to turn off the centrifuge.

10. Dialyze PSI for Experimental Use (Optional)

PSI solution can be taken from storage, thawed, and used immediately. However, because the frozen PSI solution contains a high concentration of Triton X-100, this solution cannot be used to prepare PSI multilayers.[13] Non-dialyzed PSI, or PSI solution containing high concentrations of

free surfactant, has been shown to enable the facile preparation of PSI monolayers on some electrode materials.[14] Briefly, to prepare PSI monolayers, simply incubate a cleaned electrode in the non-dialyzed PSI solution or use vacuum assisted deposition to dry non-dialyzed PSI solution on an electrode and rinse excessively with deionized water to remove PSI that is not strongly adsorbed to the surface.[14] Alternatively, to prepare PSI multilayers, the PSI solution must be dialyzed against deionized water to remove excess surfactant.[13] A complete dialysis of PSI solution obtained using this extraction procedure should be performed at a dilution ratio of at least 1000:1 and should be given a minimum of 12 h to complete. A topic of concern when performing PSI dialyses is exposure to ambient light and temperature. This may be mitigated by dialyzing the PSI inside a designated refrigerator equipped with a stir plate. If dialysis is to take place on the bench top, aluminum foil should be used to shield the dialysis setup from ambient light.

To begin dialysis, remove the desired PSI aliquots from the freezer and allow to thaw. Fill a bucket or other sufficiently large container with deionized water. Use 1000 times the volume of PSI solution to be dialyzed to fill the container for dialysis (typically 2 x 2 mL (4 mL total) aliquots are dialyzed per bucket, so 4000 mL or 4 L of deionized water is needed). Place a large stir bar in the bucket and position the bucket securely on a stir plate. Cut a 5-8 cm portion of 8 kDa molecular weight cut-off (MWCO) regenerated cellulose dialysis tubing (use the version with a 15 mm inner diameter from Spectrum Labs). Clamp one end shut using a specialized dialysis clamp or a binder clip. Hold the opposite end open with one hand and pipet in your aliquot of thawed PSI solution using the other hand. Load the PSI solution to be dialyzed and clamp the second end of the dialysis tubing. Place a float (Styrofoam or dialysis float) on one clamp and check for leaks. If there are no leaks, place the tubing, clamps, and float into the bucket. Start the stir plate on a low to medium speed and check that the dialysis setup remains in the center of the bucket, spinning in the vortex created by the stir bar. Cover the entire dialysis setup with aluminum foil and leave for at least 12 h. Remove the PSI solution from the dialysis tubing using a Pasteur pipet and transfer it to a container for storage at 4 °C until used in experimentation. The dialyzed solution can now be pipetted onto a surface and dried using vacuum assisted deposition to produce a PSI multilayer.

Photosystem I Quantification

This procedure has been adapted from the procedure reported by Baba et al. for the quantification of P700 reaction centers.[5] The solutions for Baba's assay should be prepared in advance of beginning the extraction. Baba's assay is based on collecting absorbance spectra from two samples containing PSI of equal concentration; one that is treated with a reducing agent and one that is treated with an oxidizing agent. The difference in the absorbance of these samples at a wavelength of 725 nm (the isosbestic point) can be used to determine the concentration of PSI in the samples by way of determining the concentration of P700 reaction centers. The assumption must be made that all P700 reaction centers are fully reduced and oxidized, and that each PSI complex contains exactly one P700 reaction center. As mentioned in step 9.A, a chlorophyll quantification procedure may also be used to validate the results found via Baba's assay. In any case, a sample size of at least three is recommended to obtain an accurate concentration, because Baba's assay has been found to vary greatly between trials. The required buffer (Baba's Assay Buffer), the reduction solution, and the oxidation solution are given below followed by brief instructions for performing the assay and an example of the expected results.

Baba Assay Buffer (100 mL)

- Tricine (50 mM) 0.896 g
- Sorbitol (0.1 M) 1.822 g
- NaCl (10 mM) 0.059 g
- Triton (0.05 % w/v) 0.050 g

Oxidation Solution (10 mL)

- Ferricyanide (1 M) 3.293 g

Reduction Solution (1 mL)

- Na Ascorbate (0.5 M) 0.099 g
- Dithiothreitol (5 mM) 0.001 g

Baba's Assay Procedure

First check that the UV-Vis spectrometer is turned on and the lamp is warmed up. Set the instrument to take scans between wavelengths of 750-650 nm. The UV-Vis scans must either be done using a double beam experiment with one sample cuvette being the "Reference" cuvette and the other being the "Sample" cuvette or separate reference scans must be taken individually for later calculation. This brief procedure is written for a double beam experimental setup but can be easily adapted to a single beam test.

1. Take a baseline scan with 3000 µL of Baba's Assay Buffer.

2. Test the concentration of PSI by adding 100 µL of the extracted PSI solution to a cuvette filling with 2800 µL of Baba's Assay Buffer and taking a scan from 750-400 nm. The absorbance of the peak near 700 nm should be between 0.4 to 0.7 for Baba's Assay to work properly. If the absorbance is not in this range, adjust the volume of PSI added accordingly and retest.

3. Prepare two cuvettes with 2275 µL of Baba's Assay Buffer and 100 µL of PSI (assuming 100 µL resulted in an appropriate absorbance) solution from the extraction. Mix by inverting.

4. Place the two cuvettes in the UV-Vis spectrometer and collect the absorbance spectrum. Save the scan. When using a double beam setup, the machine may save the data as "Sample" cuvette minus "Reference" cuvette, so the data for this scan can be interpreted as the baseline scan and can be used to qualitatively determine the background noise of the experiment. The data should be very near zero. If the data is reported as two different spectra, they should be nearly identical, and their difference can be taken as the baseline scan.

5. Add 120 µL of deionized water and 5 µL of reduction solution to the reference cuvette. Note that the volume of reduction solution will need to be adjusted if the volume of PSI was changed.

6. Add 125 µL of the oxidation solution to the "Sample" cuvette. Quickly cap and invert the cuvettes to mix. Note that the volume of oxidation solution will need to be adjusted if the volume of PSI was changed. Wait 15 min for reaction to complete.

7. Collect the absorbance spectrum from 750-650 nm. You may also use a wider range to see the full PSI absorbance spectrum if desired. Save the scan.

8. Export the "reaction" scan and the baseline scan and open in Microsoft Excel or other data processing software. Subtract the baseline scan from the reaction scan and plot.

9. Locate the peak absorbance in the differential scan, the peak should be near 700 nm. Record the peak absorbance value.

10. Record the absorbance value at 725 nm (isosbestic point) and subtract the isosbestic point value from the peak absorbance value. Record the difference.

11. Calculate the PSI concentration in the sample cuvette using the extinction coefficient of P700 (64 mM^{-1} cm^{-1}). Equation A.1 shows the necessary calculation.

$$C_{PSI,\ sample\ cuvette}(mM) = \frac{[A_{peak} - A_{isobestic}]}{64\ (mM^{-1}\ cm^{-1}) \times L\ (cm)} \qquad \text{Eq. A.1}$$

$C_{PSI,\ sample\ cuvette}$ = PSI Concentration in the Sample Cuvette (mM)

A_{peak} = Peak absorbance from the differential spectrum (unitless)

$A_{isobestic}$ = Isosbestic point absorbance (unitless)

$L\ (cm)$ = Pathlength in the cuvette (cm), typically 1 cm

12. Back calculate the PSI solution concentration from the determined concentration in the sample cuvette using Equation A.2. Additionally, the concentration can be converted to the more common units of mg PSI/mL by using the molecular weight of PSI (500 kDa).

$$C_{PSI}(mM) = \frac{C_{PSI,sample\ cuvette}(mM) \times V_{cuvette}}{V_{PSI\ solution}} \qquad \text{Eq. A.2}$$

C_{PSI} = PSI Concentration in the bulk PSI solution (mM)

$C_{PSI,\ sample\ cuvette}$ = PSI Concentration in the Sample Cuvette (mM)

$V_{cuvette}$ = Total volume of the sample cuvette (µL), typically 2500 µL

$V_{PSI\ solution}$ = Volume of PSI solution added to the cuvette (µL), typically 100 µL

The expected results from Baba's assay are outlined in Figure A.2. Please note that regardless of the exact procedural steps, the goal is to obtain a scan of PSI + reduction solution and a scan of PSI + oxidation solution so the difference in absorbance between fully reduced and fully oxidized PSI can be measured.

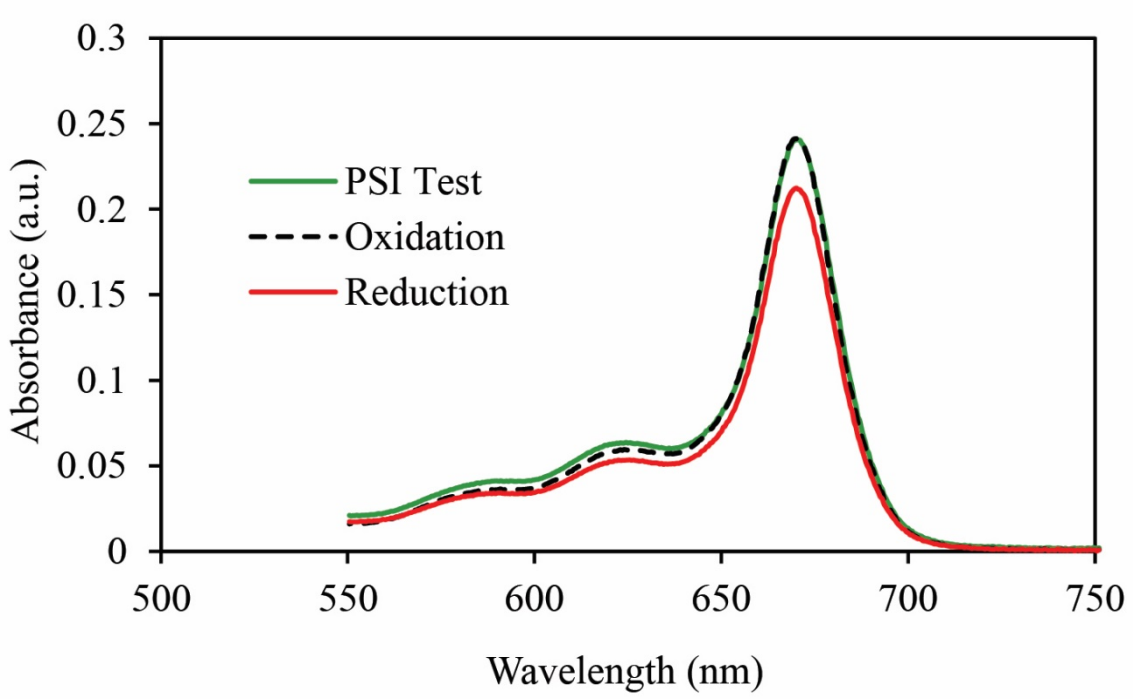

Figure A.2. *Example curves for the Baba's Assay. The oxidation curve traces the example PSI only curve taken without the addition of either oxidation or reduction solution. The absorbance at 680 nm is quenched for reduced PSI (red curve). And the absorbance at the isosbestic point (720 nm) is unchanged. Note that this sample did not yield a high enough absorbance because the PSI concentration in the cuvette was lower than recommended.*

References

1. Nguyen, K.; Bruce, B. D., Growing green electricity: Progress and strategies for use of Photosystem I for sustainable photovoltaic energy conversion. *Biochim. Biophys. Acta Bioenerg.* **2014,** *1837*, 1553-1566.

2. Wolfe, K. D.; Dervishogullari, D.; Passantino, J. M.; Stachurski, C. D.; Jennings, G. K.; Cliffel, D. E., Improving the stability of photosystem I–based bioelectrodes for solar energy conversion. *Curr. Opin. Electrochem.* **2020,** *19*, 27-34.

3. Friebe, V. M.; Frese, R. N., Photosynthetic reaction center-based biophotovoltaics. *Curr. Opin. Electrochem.* **2017,** *5*, 126-134.

4. Musazade, E.; Voloshin, R.; Brady, N.; Mondal, J.; Atashova, S.; Zharmukhamedov, S. K.; Huseynova, I.; Ramakrishna, S.; Najafpour, M. M.; Shen, J.-R.; Bruce, B. D.; Allakhverdiev, S. I., Biohybrid solar cells: Fundamentals, progress, and challenges. *Journal of Photochemistry and Photobiology C: Photochemistry Reviews* **2018,** *35*, 134-156.

5. Baba, K.; Itoh, S.; Hastings, G.; Hoshina, S., Photoinhibition of Photosystem I electron transfer activity in isolated Photosystem I preparations with different chlorophyll contents. *Photosynth. Res.* **1996,** *47*, 121-130.

6. Reeves, S. G.; Hall, D. O., [8] Higher plant chloroplasts and grana: General preparative procedures (excluding high carbon dioxide fixation ability chloroplasts). In *Photosynthesis and Nitrogen Fixation - Part C*, Ed. Academic Press: San Pietro, **1980**; Vol. 69, pp 85-94.

7. Shiozawa, J. A.; Alberte, R. S.; Thornber, J. P., The P700-chlorophyll a-protein: Isolation and some characteristics of the complex in higher plants. *Arch. Biochem. Biophys.* **1974,** *165* (1), 388-397.

8. Kincaid, H. A.; Niedringhaus, T.; Ciobanu, M.; Cliffel, D. E.; Jennings, G. K., Entrapment of Photosystem I within Self-Assembled Films. *Langmuir* **2006,** *22* (19), 8114-8120.

9. Millsaps, J. F.; Bruce, B. D.; Lee, J. W.; Greenbaum, E., Nanoscale photosynthesis: Photocatalytic production of hydrogen by platinized photosystem I reaction centers. *Photochem. Photobiol.* **2001,** *73* (6), 630-635.

10. Gorbunoff, M. J., The interaction of proteins with hydroxyapatite: I. Role of protein charge and structure. *Anal. Biochem.* **1984,** *136* (2), 425-432.

11. Korotych, O.; Mondal, J.; Gattás-Asfura, K. M.; Hendricks, J.; Bruce, B. D., Evaluation of commercially available styrene-co-maleic acid polymers for the extraction of membrane proteins from spinach chloroplast thylakoids. *Eur. Polym. J.* **2019,** *114*, 485-500.

12. Åkerlund, H.-E.; Andersson, B.; Persson, A.; Albertsson, P.-Å., Isoelectric points of spinach thylakoid membrane surfaces as determined by cross partition. *Biochim. Biophys. Acta Biomembr.* **1979,** *552* (2), 238-246.

13. Ciesielski, P. N.; Faulkner, C. J.; Irwin, M. T.; Gregory, J. M.; Tolk, N. H.; Cliffel, D. E.; Jennings, G. K., Enhanced Photocurrent Production by Photosystem I Multilayer Assemblies. *Adv. Funct. Mater.* **2010,** *20*, 4048-4054.

14. Faulkner, C. J.; Lees, S.; Ciesielski, P. N.; Cliffel, D. E.; Jennings, G. K., Rapid Assembly of Photosystem I Monolayers on Gold Electrodes. *Langmuir* **2008,** *24*, 8409-8412.

Appendix B – Preparation of Porous Indium Tin Oxide Electrodes

Porous and conductive electrodes comprised of indium tin oxide (ITO) nanoparticles have proven themselves to be highly beneficial in biohybrid electrodes.[1-4] Generally, porous ITO electrodes are prepared by sintering ITO nanoparticles together that have been cast onto some desired template. The following fabrication guidelines will describe the process for preparing reproducible electrodes with 5 μm inverse opal pores, herein described as macropores or macroporous electrodes. The procedure may be adapted to produce electrodes with larger or smaller pore sizes. The procedure can be adapted to produce electrodes with mesopores or mesoporous electrodes. The mesoporous electrodes do not have an inverse opal structure and the pore size is defined by the random packing of ITO nanoparticles that are nominally 25 nm in diameter, and yield pores between 10-100 nm with varying morphology. It should be noted and considered when analyzing experimental results, that the macroporous electrodes contain some degree of mesoporosity as well. This is due to the macropore wall being composed of sintered ITO nanoparticles. Therefore, the macroporous electrodes have a hierarchical structure with both meso- and macropores that result in a great increase in active electrode surface area.

The preparation of macroporous ITO electrodes follows a templating procedure in which a polystyrene microsphere (PSM) template is first deposited, followed by the deposition of ITO nanoparticles that cover and fill the void space of the template, and the simultaneous removal of the PSM and sintering of ITO nanoparticles to yield a mechanically stable and electrically conductive porous electrode. The electrodes can then be filled via vacuum assisted deposition with, for example, Photosystem I (PSI) protein complexes. Figure A.3 shows the stepwise procedure for the preparation of macroporous ITO electrodes. Alternatively, the PSM template can be omitted to produce mesoporous ITO electrodes. The procedure given below has been adapted and optimized from Wenzel et al.[3]

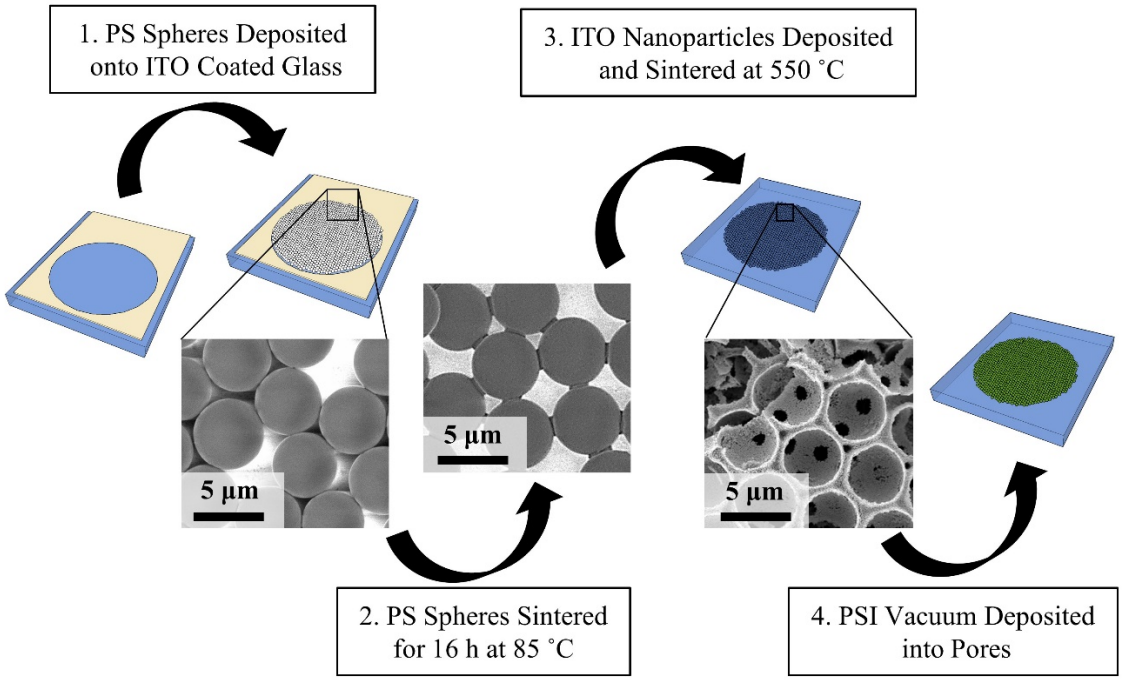

Figure A.3. *Procedure for the preparation of macroporous ITO electrodes infiltrated with Photosystem I (PSI) protein complexes.*

Procedure

The preparation of inverse opal porous ITO electrodes requires the use of a sonication bath, hotplate, and tube furnace equipped with argon gas and the ability to reach 500 to 600 °C. Other required materials (not included in stock solutions above) include ethanol, acetone, nitric acid, ITO coated glass slides, a scribe or glass scorer, and tape or other material to prepare masks. The procedure takes approximately two to three days due to two slow drying steps and the sintering process. Below the procedure is given as a series of sequential steps, including the characterization of the produced electrodes. The crystal structure can be determined via powder x-ray diffraction (XRD), the conductivity via four-point probe analysis, and the transmittance via transmission absorbance spectroscopy. Additionally, the procedure for determining the electrochemically active surface area via cyclic voltammetry, adapted from Voiry et al., is given.[5] The characterization of the active surface area is incredibly useful and can also be used to analyze other electrode

materials. Lastly, the method for introduction of Photosystem I (PSI) into the electrodes is given, because the incorporation of PSI within porous and translucent electrodes is the primary goal of this work.[4]

1. ITO Coated Glass Cleaning and Preparation

First determine the desired electrode size. The final electrode area must lie within a masked area during the following deposition processes, so the actual area must be larger to accommodate the mask. Approximately 1.5 cm x 3 cm is a suitable size to prepare circular porous electrodes with an area of 0.71 cm^2. Leaving a space for holding the sample is also advised. Figure A.4 shows a schematic of the typical masked electrode before any deposition has begun. The ITO coated surface will need to be well cleaned to remove any adsorbed species that would prevent good ITO nanoparticle adhesion during later steps. Lastly the masks will be prepared and applied to the ITO coated glass slides.

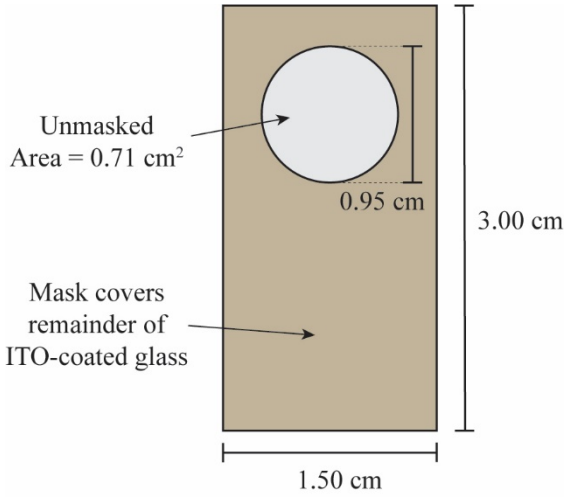

Figure A.4. *Schematic of typical ITO coated glass dimensions with a circular, 0.71 cm^2 mask applied. The circular, unmasked area, which will define the final electrode area, can be prepared by punching a hole in the mask using a 3/8 inch in diameter hole punch.*

Begin by cutting the ITO coated glass slides to the desired dimensions. Using a multimeter, determine which side is conductive and place that side face down on a Kim Wipe or other non-abrasive surface. Score the slide using a scribe or glass cutting wheel. Position the larger portion of the slide, on either side of the score, on top of another piece of glass or other thin object that has

been covered with a Kim Wipe. Allow the smaller section to hang off the ledge with the score aligned on the edge. Hold the larger section down firmly and crack the smaller section off. Pressing the larger side down with a ruler or straight edge is helpful for larger pieces. Remove any glass debris and continue to the next cut.

Sonicate the cut ITO pieces for 5 min in acetone, ethanol, 30% nitric acid, and water sequentially. Using a bath sonicator and a vial or beaker, sonicated now more than 2-3 pieces at a time and dry with an inert gas between each sonication. Refrain from touching the surfaces and instead hold the pieces using wafer tweezers or hold by the edges. After the water sonication and drying, lay the ITO pieces on a dry Kim Wipe. Using a multimeter, check again for the conductive side. Leave the conductive side face up.

Prepare your masks so that they will cover the entire ITO piece, leaving only the area desired for electrode deposition bare. Electrochemical masking tape (Gamry) works well. Paper hole punches are helpful for circular electrode masks. Be careful to center the punched hole in the middle of the mask so that it is not too near an edge. Carefully apply the masks to the conductive sides of the ITO pieces with touching the bare ITO surface. Labeling samples by marking on the mask is helpful.

2. Deposition of Polystyrene Microsphere (PSM) Template

The polystyrene microspheres (PSMs) should be well dispersed in a slow drying solvent. Herein deionized water is used, but other solvents such as terpineol were investigated. In this step the PSM solution will be cast onto the unmasked ITO-coated glass surface and allowed to dry slowly. The slow drying step allows for the PSMs to self-organize in a close packed hexagonal structure (Figure A.5). The drying procedure will be followed by an overnight sintering step in which the PSMs will become interconnected with each other. The sintering provides mechanical stability of the PSM template and also results in good pore connection within the final electrode.

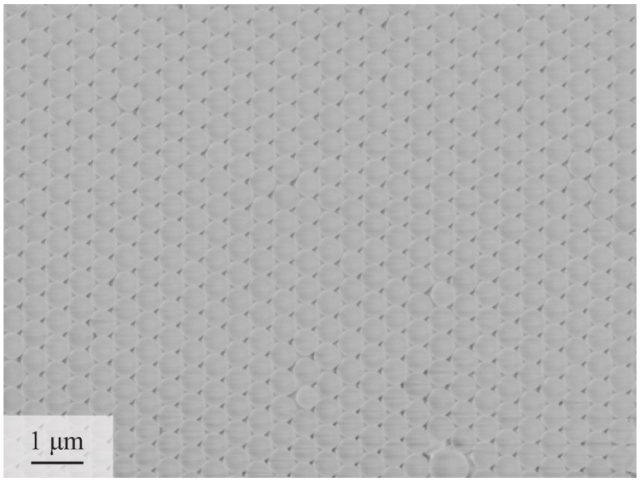

Figure A.5. *Scanning electron micrograph of well packed 500 nm PSMs yielding a close-packed hexagonal structure.*

Dilute the stock solution of PSMs to less than 1 wt %. For PSMs of different sizes, a different weight percent may be necessary to achieve a uniform film after drying. Using 5 μm PSMs, a dilution of 13:1 of deionized water to 5 μm PSMs (10 wt %) was found to produce well-behaving films. The diluted PSM stock can be stored for repeated use. Using a micropipette, agitate the diluted PSM solution by pipetting several times without removing the pipet from the solution. Now, apply enough PSM solution to cover the unmasked area. For a 0.71 cm^2 area, 85 μL is sufficient. If the solution does not wet the entire area, gently use the pipette tip to spread the solution. Set the PSM coated ITO aside to dry for several hours under ambient conditions. Note that the airflow in a fume hood may cause the films to dry too fast and therefore produce non-uniform films.

After fully dry, check for cracking, peeling, or the "coffee-ring-effect". If the films look uniform, place the ITO-coated glass pieces on a hot plate set to 85 °C and leave overnight (~18 h). The pieces should be kept near the center of the hotplate to maintain uniform heating. After this step, the PSM template should be sintered and mechanically stable. A scanning electron micrograph can be taken before and after leaving overnight on the hotplate to check for sintering

and even packing (Figure A.6). Use a low accelerating voltage (0.5 keV) and close working distance (5 μm) to image the non-conductive PSMs. If a charging effect is observed during imaging, lower the probe current or use inert gas flow to mitigate the charging of the particles.

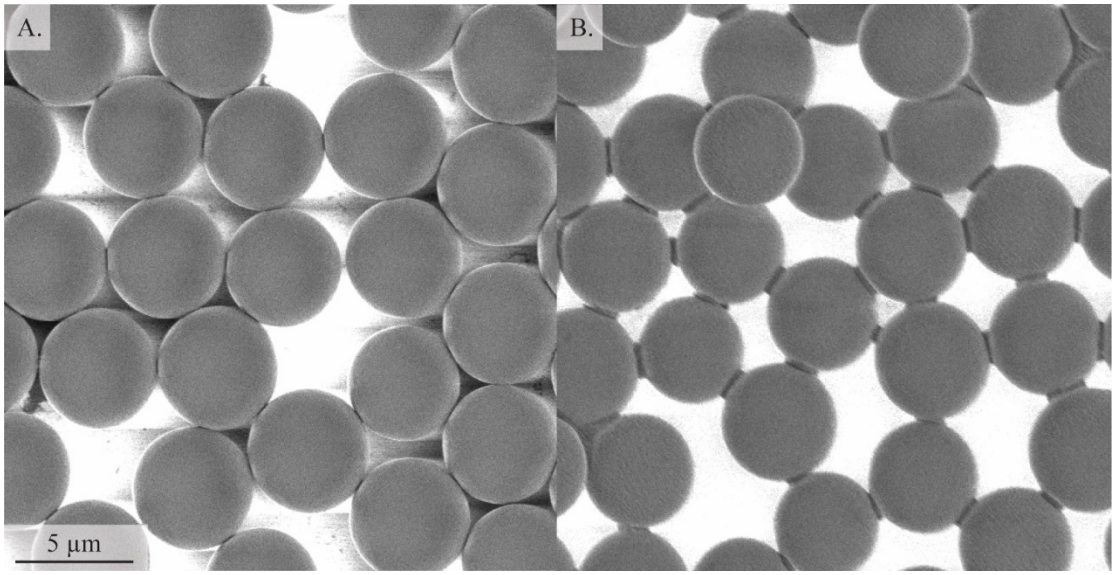

Figure A.6. *Scanning electron micrographs of the PSM template before (A) and after (B) sintering. Accelerating voltage = 0.5 keV, Working distance = 5.0 μm. A low accelerating voltage and probe current is necessary to avoid charging of the non-conductive PSMs.*

3. Deposition of Indium Tin Oxide (ITO) Nanoparticles

After the PSM template has been sintered, ITO nanoparticles must be deposited to fill the void space in the template. ITO nanoparticles of 100 nm nominal diameter can be purchased in solution (Sigma). ITO nanoparticles are typically suspended in an alcohol-based solvent and therefore a solvent exchange is necessary for the deposition, which requires a slow drying or less volatile solvent. After exchanging the solvent, the nanoparticles are deposited and the excess solution above the masked area is removed via a doctor blade or tape casting procedure. The nanoparticles are then allowed to dry fully overnight.

Exchange the stock solvent for a less volatile one such as terpineol by removing the solvent using a rotary evaporator and resuspending the collected nanoparticles in terpineol. Note the mass

fraction of the original suspension, determine the mass of nanoparticles after the initial solvent is removed, and add an appropriate volume or mass of terpineol so that the new mass fraction of ITO nanoparticles is known. For example, an exchange from a 30 wt % ITO nanoparticle suspension in isopropanol was performed by rotary evaporation of 10.6 mL of solution (2.5 g of nanoparticles based on the density of isopropanol, 0.786 g/mL). The 2.5 g of dried nanoparticles were then resuspended in 10.7 mL of terpineol to provide a 20 wt % ITO suspension in terpineol.

Next, deposit enough of the ITO nanoparticle suspension onto the PSM template with the mask still in place. 100 µL will sufficiently cover 0.71 cm^2 of PSM template. Allow the solution to settle for 30-60 s, then quickly slide a straight-edged object such as a glass slide across the masked area to remove any solution that is above the mask. The mask acts as a guide to set the height of the straight edge. This procedure is known as doctor blading or tape casting. Be careful not to scratch the PSM template. The removal of excess solution accelerates the drying process and reduces the "coffee-ring effect". Now let the ITO nanoparticle coated PSM templates dry overnight in ambient conditions. After fully dried, the films should appear very slightly tacky but not wet.

4. Sintering the ITO Nanoparticles and Removal of PSM Template

The last step in the preparation of the inverse-opal ITO electrodes is the simultaneous sintering of the ITO nanoparticles and the removal of the PSM template. This is done by heating the samples to 550 °C under an argon atmosphere. It is hypothesized that the PSMs melt and evaporate and the ITO becomes sintered. The order of these two occurrences is not known. The argon atmosphere reduces excess oxidation of the ITO nanoparticle surface, resulting in more conductive electrodes.

Remove the mask from the dried samples and keep them in some order if they were not all prepared identically. If the samples must be labeled, it is recommended that numbers be inscribed on the glass away from the electrode area. Load 5 to 10 samples into a tube furnace. Either a 1" or 4" tube will work, but the samples should be kept near the center of the furnace to avoid

temperature fluctuations. Seal the tube and begin argon flow to evacuate the tube. Wait 10-30 min for the tube to be fully cleared of residual air.

Using a gradual ramp-up procedure or recipe, program the furnace to increase the furnace temperature to 550 °C over several hours with short periods of rest. The rest periods allow for temperature variations within the tube to dissipate. It is recommended that the temperature ramp be no greater than 5 °C/min. An example recipe is as follows:

1. Room temperature (25 °C) to 300 °C over 3 h
2. 300 °C to 350 °C over 30 min
3. Rest at 350 °C for 10 min
4. 350 °C to 400 °C over 30 min
5. Rest at 400 °C for 10 min
6. 400 °C to 450 °C over 30 min
7. Rest at 450 °C for 10 min
8. 450 °C to 500 °C over 30 min
9. Rest at 500 °C for 10 min
10. 500 °C to 550 °C over 30 min
11. Rest at 550 °C for 15 min
12. Cool to room temperature (25 °C)

The samples may be removed after the temperature has dropped below 100 °C. After sintering, the electrode area should appear a translucent blue (Figure A.7). If there is a black soot-like color, the PSMs were burned. This should be mitigated by adjusting the ramp-up procedure to

be more gradual or be ensuring the tube is sealed and full of argon when the sintering process is performed.

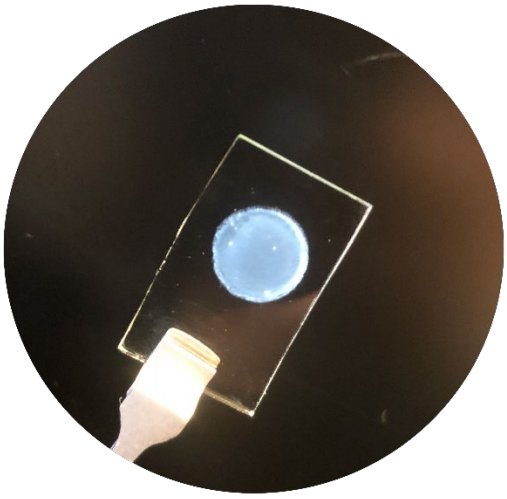

Figure A.7. *Image of a sintered 5 μm inverse opal porous ITO electrode.*

5. Determining the Crystal Structure of the Sintered ITO

The conductivity of the sintered electrodes is dependent on good intra-nanoparticle connections provided by the sintering, absence of surface contaminants (such as burned PSMs due to the presence of oxygen), and the crystal structure of the ITO nanoparticles themselves. ITO is most conductive when it is in a body centered cubic structure (space group = Ia-3, no. 206). The crystal structure of the prepared electrodes can be verified and compared to the unsintered ITO nanoparticles using powder x-ray diffraction (XRD). Powder XRD works by collecting a diffracted x-ray signal over a range of angles (Θ). The powder sample will yield the greatest signal at angles corresponding to the diffraction within specific crystal planes. The diffraction spectra over a range of Θ can then be used in comparison to a database to confirm the crystal structure of the powder sample.

Start by preparing a set of electrodes and choosing one or more to analyze using XRD. Carefully scrape the sintered nanoparticles from the prepared electrode onto a glass slide or an XRD powder holder. Prepare a control sample by evaporating the solvent from the as received ITO nanoparticles and collecting the dried nanoparticles. Perform an XRD scan from $\Theta = 20°$ to 70° and plot the results. Reference an x-ray diffraction database to find the diffraction pattern of body centered cubic ITO. Figure A.8 gives the diffraction spectra of body centered cubic ITO and an example spectra obtained from ITO nanoparticles.[3, 6]

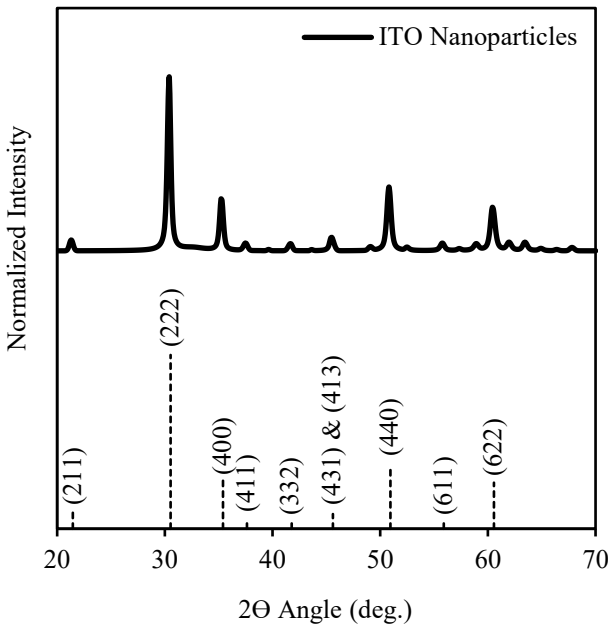

Figure A.8. *Diffraction spectra of body centered cubic indium tin oxide (ITO) from tabulated data (dashed).[6] Space group = Ia-3, No. 206. Example diffraction spectra obtained from ITO nanoparticles (solid).*

6. Four-Point-Probe Analysis of Electrode Conductivity

Another method for verifying the production of conductive porous electrodes is the four-point-probe technique. Four-point-probe measures the surface resistance of a sample as the applied

potential is varied. The main advantage of this technique is that it decouples the current and potential measurements using four probes instead of two as in a typical voltmeter. A critical assumption that is violated when using four-point-probe on a porous sample is the assumption that the film is continuous and uninterrupted. By definition, porous electrodes do not meet these criteria. Therefore, four-point-probe is a useful tool because it will determine the general conductivity or resistivity of the film, however, a quantitative resistivity or conductivity value cannot be determined.

7. Transmission Absorbance Measurements for Electrode Translucency

A major advantage to producing porous ITO electrodes is that ITO remains partially transmissive across the visible light spectrum. It can be clearly seen that the resulting electrode is blue (Figure A.7), meaning it absorbs lower wavelength visible light. Transmission absorbance spectroscopy can be used to determine how transmissive the prepared electrodes are over a range of wavelengths. Using a standard UV-visible spectrophotometer, and a transmission sample holder, scan from approximately 400 to 800 nm. Be sure the sample holder being used allows the beam to pass through the electrode area. The control or background sample should be a piece of ITO coated glass. Figure A.9 shows the transmission spectra of a typical porous ITO electrode

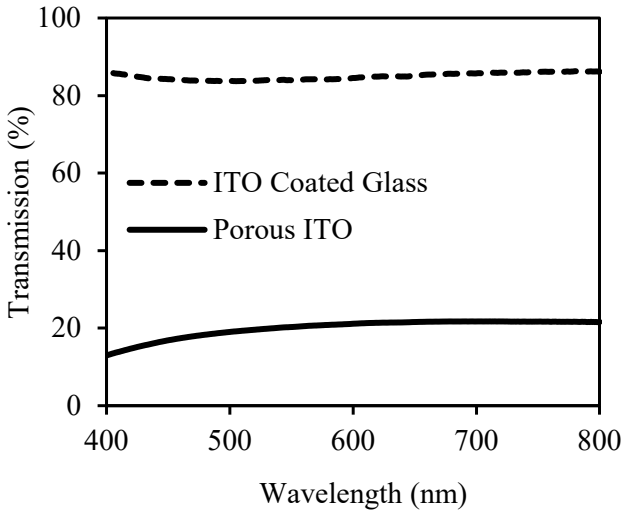

Figure A.9. *Transmission spectra of a typical 5 μm inverse opal porous ITO electrode. Note that Rayleigh scattering causes decreased transmission near the UV wavelengths.*

prepared with a 5 μm PSM template. The average transmission is approximately 20% across the visible spectrum. Note that considerable Rayleigh scattering occurs at low wavelengths.

8. Characterizing the Electrochemically Active Surface Area

The electrochemically active surface area of the prepared porous electrodes is much greater than the geometric, or footprint, surface area. The increase in electrochemically active surface area is beneficial because it increases the overall rate of reaction at the electrode by increasing the surface area.[7] This, however, causes a problem if the active surface area is unknown. For example, a figure reporting current with respect to the footprint area of the electrode may mislead the reader to believe an improvement is being made with respect to the kinetic rate or another rate limiting step of the reaction when, in fact, it may be solely due to an increase in active surface area. To address this issue, the electrochemically active surface area can be determined and should be reported for porous electrodes as described by Voiry et al.[5]

The electrochemically active surface area can be determined experimentally by comparing the magnitude of the capacitive current, observed in cyclic voltammetry, of the porous electrode to the capacitive current of a planar electrode. The planar electrode must be composed of the same material and have a known surface area.[18] To determine the active surface area of the prepared porous ITO electrodes, first mask an area of an ITO coated glass slide and collect a cyclic voltammogram in a high concentration supporting electrolyte, such as 500 mM potassium chloride. The same 0.71 cm^2 mask is recommended and a piece of copper tape can be used as a connection. Using Ag/AgCl reference, platinum mesh counter, and ITO coated glass working electrode obtain scans over a potential window yielding a nearly flat capacitive current. Obtain the same voltammogram with varied scan rates (10 to 500 mV/s). Switch the working electrode to a porous ITO electrode with the 0.71 cm^2 porous area exposed and the remainder covered by an electrochemical mask. Repeat the same cyclic voltammetry conditions as for the planar sample.

Choose a point within the flat region of the capacitive current (0.00 V vs. Ag/AgCl works well) and extract either the cathodic or anodic current values at this potential for one scan from

each cyclic voltammogram. Plot the current magnitude vs. scan rate. Create this plot for the porous electrode also. Determine the slope of capacitive current vs. scan rate for each electrode by applying a linear fit or trendline. Now, divide the slope obtained from the porous electrode by the slope from the planar electrode. This value is deemed the electrochemical surface area factor or ECSAF of the porous electrode. The ECSAF can be multiplied by the known surface area of the planar electrode to find the electrochemically active surface area of the porous electrode. Replicate this test with several porous electrodes to achieve an average value for the electrochemically active surface area of the prepared electrodes. There should not be a high variance in the obtained ECSAF values. Figure 8 (A) shows two cyclic voltammograms highlighting the large increase in capacitive current between the planar ITO and the porous ITO electrodes. Panel (B) shows the capacitive current vs. scan rate for a planar and porous ITO electrode along with the slope values needed to calculate the ECSAF and the active surface area of the porous electrode (shown in inset text boxes).

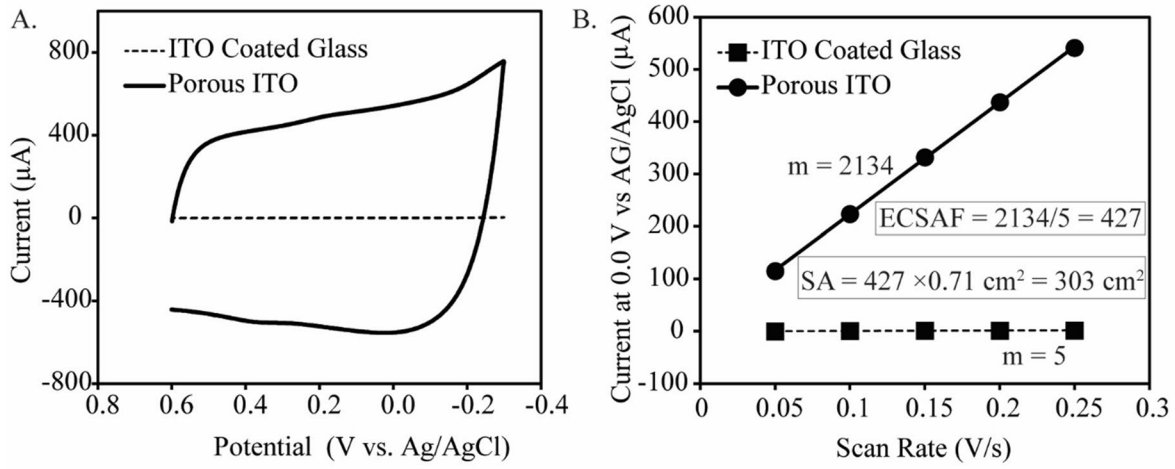

Figure A.10. *(A) Cyclic voltammograms obtained at a scan rate of 250 mV/s on planar (solid) and porous (dashed) ITO. (B) Capacitive current vs. scan rate for a typical planar (solid squares) and porous dashed circles) ITO electrode. The slope (m) of the porous electrode divided by the slope of the planar electrode yields the ECSAF of the porous electrode. The ECSAF can then be multiplied by the known surface area of the planar electrode to determine the active surface area (SA) of the porous electrode.*

9. Loading the Porous Electrode

The prepared porous ITO electrodes can be filled with PSI or another biological molecule via vacuum assisted deposition. Vacuum assisted deposition is a simple method that allows the quantity of deposited material to be easily determined based on the volume deposited and the known concentration. To fill the electrode with PSI, deposit a small volume (25 µL) of dialyzed PSI onto the electrode with the 0.71 cm^2 mask applied. Apply low vacuum for approximately 30 min to remove the solvent and deposit another small aliquot of dialyzed PSI and repeat, if desired. The series of small volumes allows the PSI solution to fill the porous electrode and then dry, leaving the PSI well dispersed.[3, 8] If a large volume is deposited at once, the electrode will be overfilled and any PSI solution above the electrode surface will be dried on top of the electrode and result in blocking of the upper pores. Figure A.11 shows an electrode filled with approximately 75 µg of PSI.

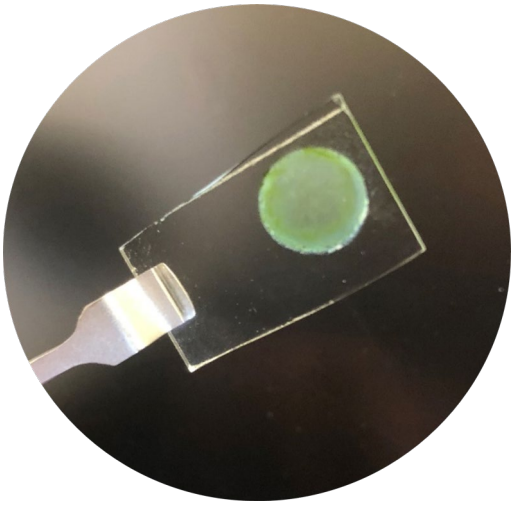

Figure A.11. *Image of PSI filled porous ITO electrode (approximately 75 µg PSI).*

References

1. Kato, M.; Cardona, T.; Rutherford, A. W.; Reisner, E., Photoelectrochemical Water Oxidation with Photosystem II Integrated in a Mesoporous; Indium Tin Oxide Electrode. *J. Am. Chem. Soc.* **2012,** *134* (20), 8332-8335.

2. Stieger, K. R.; Feifel, S. C.; Lokstein, H.; Hejazi, M.; Zouni, A.; Lisdat, F., Biohybrid architectures for efficient light-to-current conversion based on photosystem i within scalable 3D mesoporous electrodes. *J. Mater. Chem. A* **2016,** *4*, 17009-17017.

3. Wenzel, T.; Härtter, D.; Bombelli, P.; Howe, C. J.; Steiner, U., Porous translucent electrodes enhance current generation from photosynthetic biofilms. *Nature Comm.* **2018,** *9*, 1299.

4. Wolfe, K. D.; Dervishogullari, D.; Stachurski, C. D.; Passantino, J. M.; Kane Jennings, G.; Cliffel, D. E., Photosystem I Multilayers within Porous Indium Tin Oxide Cathodes Enhance Mediated Electron Transfer. *ChemElectroChem* **2020,** *7* (3), 596-603.

5. Voiry, D.; Chhowalla, M.; Gogotsi, Y.; Kotov, N. A.; Li, Y.; Penner, R. M.; Schaak, R. E.; Weiss, P. S., Best Practices for Reporting Electrocatalytic Performance of Nanomaterials. *ACS Nano* **2018,** *12*, 9635-9638.

6. González, G. B.; Cohen, J. B.; Hwang, J.-H.; Mason, T. O.; Hodges, J. P.; Jorgensen, J. D., Neutron diffraction study on the defect structure of indium–tin–oxide. *J. Appl. Phys.* **2001,** *89*, 2550-2555.

7. Bard, A. J., Electrochemical methods : fundamentals and applications / Allen J. Bard, Larry R. Faulkner. Wiley: New York, New York. **1980**.

8. Ciornii, D.; Kölsch, A.; Zouni, A.; Lisdat, F., A precursor-approach in constructing 3D ITO electrodes for the improved performance of photosystem I-cyt c photobioelectrodes. *Nanoscale* **2019**.

Appendix C – Layer-by-Layer Assembly of Photosystem I and PEDOT:PSS

Layered films on the nanometer and sub-nanometer scale can be produced on a surface through careful use of attractive molecular charges. In a traditional layer-by-layer (LBL) film, molecular cations and anions are deposited repeatedly by introducing a surface to one molecule in solution then rinsing and exposing it to the next. The molecules adsorb to the surface due to a strong attraction to an opposite charge and if two molecules of opposite charge are used, they can be layered, often up to 50-100 layers.[1-2] Before the first layer is deposited, the surface must be cleaned and be suitable for good adsorption of the first molecule. Many LBL procedures begin with the formation of a self-assembled monolayer (SAM) to prepare the surface. SAMs also allow the surface charge to be tailored to promote the first layer of deposition. Of course, the molecules of interest must be compatible.

Utilizing LBL assembly to deposit proteins is a growing field of interest. Traditional LBL molecules are small and have strong charges relative to their size. In contrast, proteins are bulky, and their charge is dependent on functional groups that have different pKa values and are present in varied quantities on the protein surface. Still, many protein LBL systems have been studied and have shown promise in the development of organized protein thin films. Below a procedure is given for producing LBL assemblies of PSI and PEDOT:PSS. Under the proper conditions, films of PSI and PEDOT:PSS can be produced with up to 10 layer pairs or bilayers.

Deposition Solutions:

- Aminoethane thiol (AET) solution
    - 1 mM aminoethane thiol (AET) in ethanol
- PSI Solution (used “as extracted”)
    - 0.5 mg PSI/mL in 200 mM sodium phosphate buffer at pH = 7.0 and containing 1 wt % Triton X-100
- PEDOT:PSS Solution
    - 0.5 mg/mL PEDOT:PSS and 0.15 M NaCl

1. Gold Preparation

A gold surface is used to facilitate the deposition of an aminoethane thiol (AET) SAM. Before deposition of the SAM, the gold surface must be cleaned appropriately. If a gold surface prepared through physical vapor deposition is to be used, and the surface has not been exposed to any other environment than air, the gold is already mostly clean. Simply rinse the gold with water then ethanol and dry with nitrogen. If a gold disc electrode is to be used, the electrode surface should be polished using 0.25 μm alumina slurry polish then rinsed with deionized water and sonicated in deionized water for 2-3 min. Next, the electrode should be cleaning via cyclic voltammetry in 1 M H_2SO_4 to remove any chemical contaminants from prior uses or storage. Cycle the electrode from 1.0 to -1.0 V vs. Ag/AgCl using a scan rate of 100 mV/s for at least 10 full cycles. The cyclic voltammogram will have peaks, but after a few cycles, the scans will trace over themselves indicating that no changes are being made to the electrode surface by the potential cycles.

2. Formation of an Aminoethane Thiol (AET) SAM

Simply place the cleaned gold surface into a 1 mM AET solution and allow the SAM to form. For the sake of this procedure, a one-hour deposition is sufficient. Note that the formation of a densely packed SAM can take many hours depending on the carbon chain or tail length and the degree or organization or packing desired. The purpose of the AET SAM in this procedure is to provide a positively charged surface for the initial deposition of PEDOT:PSS. After the one-hour deposition, the sample should be rinsed with ethanol and dried. The contact angle can be checked and should be much lower than before the deposition to verify formation of the AET SAM.

3. Deposition of PEDOT:PSS and PSI

Immediately after the formation of the AET SAM, the sample can be immersed in the PEDOT:PSS solution. The best method of immersion is dependent on the sample shape and the amount of PEDOT:PSS prepared. Options include small petri dishes, small beakers, standard screw top vials, or centrifuge tubes. The AET coated gold should be left in the

PEDOT:PSS solution for 15 min. Then rinse the sample with deionized water and dry. No visible change will be seen due to the thin nature of the film. Both contact angle and spectroscopic ellipsometry are viable methods for determining if PEDOT:PSS was deposited but the clearest evidence is only present after the PSI deposition.

In the same manner, simply incubate the sample in PSI solution for 30 min. Extra care or planning may be necessary for the PSI deposition due to the large volume of PSI necessary to sufficiently cover the sample(s). A small petri dish is very useful. Another option is to mask an area of the sample using electrochemical tape (Gamry), pipette a volume of PSI solution onto the masked area, and to allow the deposition to take place while the solution rests as a drop. The excess solution can be rinsed off. After the PSI deposition the sample should be rinsed and dried again. The deposition of PSI results in a drastic change in hydrophobicity. The sample should now have a contact angle of near 80° (using deionized mater) and when placed back into the PEDOT:PSS solution (for the next deposition step) the surface should be noticeably hydrophobic. If using gold coated silicon wafers and a petri dish, the samples will likely float atop the PEDOT:PSS solution after the PSI deposition due to the hydrophobicity. But after the PEDOT:PSS deposition, they will easily be wetted when introduced to the PSI solution. This repetitive change in contact angle is good evidence that the deposition is proceeding well. To produce many layer pairs, simply incubate the sample in PEDOT:PSS solution for 15 min, rinse and dry, incubate in PSI solution for 30 min, rinse and dry, and repeat as many times as desired.

References

1. Abruna, H. D.; Denisevich, P.; Umana, M.; Meyer, T. J.; Murray, R. W., Rectifying interfaces using two-layer films of electrochemically polymerized vinylpyridine and vinylbipyridine complexes of ruthenium and iron on electrodes. *J. Am. Chem. Soc.* **1981,** *103* (1), 1-5.
2. Crespilho, F.; Zucolotto, V.; Oliveira, O., Electrochemistry of Layer-by-Layer Films: a review. *Int. J. Electrochem. Sci.* **2006,** *1*.

Appendix D – Square Wave Voltammetry of Thiol-Modified Photosystem I

Square wave voltammetry (SWV) was used to study the thiol-modified Photosystem I protein complexes reported in Chapter 5. Following a report by Ciobanu et al., PSI complexes were deposited via solution adsorption onto a hydroxyl terminated self-assembled monolayer (SAM) on a gold electrode.[1] Ciobanu et al. reported that the P_{700} reactive site can be observed through electrochemical oxidation and reduction at a potential of 0.30 V vs. Ag/AgCl by SWV atop short-chain hydroxyl terminated SAMs.[1] A mercaptohexanol SAM was shown to yield the greatest current corresponding to P_{700} oxidation/reduction due to the suppression of the gold oxide peak, which has a potential near that of P_{700}. The results reported in this appendix agree with the findings of Ciobanu et al.; however, the observation of the oxidation/reduction of the P_{700} site was not highly reproducible. Approximately 1/6 of the tested samples yielded the results shown below and therefore the SWV analysis was not included in the main text (Chapter 5). Additionally, various chain-lengths of hydroxyl-terminated SAMs were studied.

Following Ciobanu et al.'s protocol, hydroxyl-terminated SAMs were prepared by first cleaning the gold electrode through both polishing with alumina slurry and cycling in sulfuric acid, then immersing the electrode into a 2 mM mercaptoethanol solution in ethanol for approximately 12 h. The SAM-coated gold electrode was then immersed into either the PSI extraction elution buffer (control), an unmodified PSI solution, or a thiol-modified PSI (T-PSI) solution for 24 h. The samples were removed, rinsed, and used for SWV testing in a 100 mM KCl solution. Performing the test in only a supporting electrolyte solution (no active mediator present) allows for the direct oxidation and reduction of the reaction centers themselves. We hypothesized that downward oriented films (T-PSI with the stromal side nearest the electrode) would show an increase in oxidation/reduction peaks of the F_B cluster due to its close proximity to the electrode surface. Figure A.12 shows the SWV results for the positive scan direction of both unmodified PSI and T-PSI. Note that during SWV either a positive scan direction or a negative scan direction may be used. During a positive scan, the electrode becomes increasingly positively charged and species near the electrode surface are oxidized, resulting in anodic current at the electrode. In the case of Figure A.12, the peak observed 0.35 V vs. Ag/AgCl may be attributed to the oxidation of P_{700} as

reported by Ciobanu et al. at 0.30 V vs. Ag/AgCl. The peak at -0.75 was also present in the buffer only control samples and is therefore not a result of the deposition of PSI.

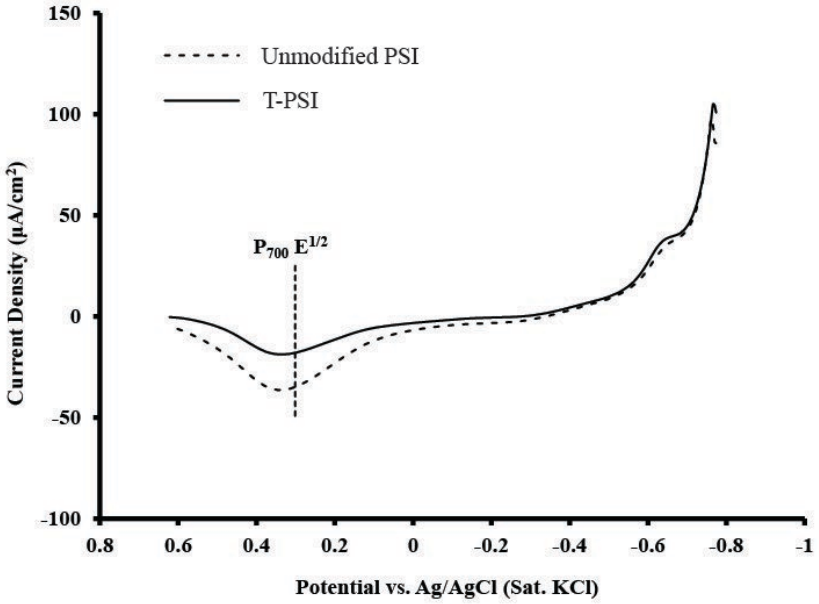

Figure A.12. *Positive scan square wave voltammograms showing peaks for the direct oxidation of the P_{700} site on a mercaptoethanol SAM.*

The voltammograms in Figure A.12 show a decrease in the presence of the P_{700} reaction center in T-PSI protein complexes. This may be taken as indirect evidence for the expected downward orientation; however, the argument is not strong due to the lack of reproducibility and known variance in the modified PSI monolayers (see Chapter 5). Interestingly, the peak attributed to P_{700} was observed on both mercatoethanol and mercaptohexanol SAMs, which further supports findings by Ciobanu et al.[1] In conclusion, SWV may be a beneficial tool in determining the effects of side-selectively modifying PSI protein complexes; however, the procedure must be optimized to greatly improve reproducibility.

References

1. Ciobanu, M.; Kincaid, H. A.; Lo, V.; Dukes, A. D.; Kane Jennings, G.; Cliffel, D. E., Electrochemistry and photoelectrochemistry of photosystem I adsorbed on hydroxyl-terminated monolayers. *J. Electroanal. Chem.* **2007,** *599* (1), 72-78.